IMPERIAL COLLEGE OF SCIENCE, TECHNOLOGY & MEDICINE

University of London

Centre for Vibration Engineering

Aeroelasticity in Turbomachinery

by

Reza Mostofi

A thesis submitted to the University of London for the degree of Doctor of Philosophy and for the Diploma of Imperial College

Dynamics Section
Department of Mechanical Engineering
Imperial College of Science, Technology and Medicine
Exhibition Road
London SW7 2BX

Completed December 1994
Submitted April 1995

Acknowledgements

I would like to express my deepest appreciation to Professor D. J. Ewins and Dr. M. Imregun for their supervision and guidance, and for putting up with me. At times, it even surprised me.

I would like to thank all the members of Centre for Vibartion Engineering for their help. Special thanks are due to Dr. A. Stochniol who readily answered my daily "computing questions" and kept his calm in face of the strange, and unexplained, happenings on the computing environment. I wish to thank Mr. J. G. Marshall and Dr. M. Vahdati, the aeroelasticity group, for hours of interesting topical discussions, including those on aeroelasticity. It has been an eye-opener! Finally, my deepest thanks to Mr. H. Yiu for helping me to finish this manuscript in the last hours towards one of the final deadlines.

This work was sponsored by Rolls-Royce Plc, Derby. I would like to thank Dr. B. Bellamy and Dr. P. Stow for their helpful suggestions.

Hamlet has put on the crown, but is now wondering why he exists.

Régis Debray

Abstract

The use of high aspect ratio compressor blades operating at transonic flow regimes has highlighted the non-linear features of the flutter phenomenon. The traditional methods of flutter prediction often assume flutter to be a linear stability problem. This linear assumption is then used to decouple the flutter problem into separate fluid and structural analyses, the results of which are subsequently combined in a coupling procedure. The uncoupled and linear nature of the traditional methods are judged to be responsible for their failure to predict the flutter boundaries for modern turbomachinery compressor blades.

In this work, a three-dimensional, integrated and non-linear flutter prediction model is introduced. The method is integrated since the fluid and the structural components are modelled and solved for simultaneously, a feature that avoids simplifying assumptions at the fluid/structure interface and models the energy transfer at this interface exactly. The method is also nonlinear since it models the non-linear behaviour of the flow and the fluid/structure interaction. In this study, the structural model remains linear. The fluid flow is modelled by an inviscid Euler model. The structure is represented by a reduced modal model obtained from a structural eigensolution. The spatially discretized aeroelastic equations are solved simultaneously in time using an explicit multi-stage Runge-Kutta scheme. The method is second-order accurate in both time and space. To increase the allowable time step, residual smoothing and multi-grid techniques are used in the fluid flow model. The allowable time step for the structural model is not restrictive due to modal reduction.

The aeroelasticity model and its fluid and structural components are rigorously tested and validated against series of numerical and experimental data available in the literature. The integrated non-linear method is then successfully employed to determine the untwist and flutter boundary of a real fan blade.

The disadvantage of the integrated method proposed is in its large computational requirements when used for flutter calculations. (as opposed to the untwist calculations which are computationally cheap) This is not a major obstacle to its routine use as more and more powerful computers are becoming available.

The advantage of the integrated non-linear model, apart from giving the right answer, is in its ability to produce a large amount of information on the flutter boundary investigated. While the method does not require any prior information on the flutter problem, it gives the amplitude of limit cycles as well as the mode of flutter experienced. This is a major step forward compared to the traditional methods that most often require so much information on the flutter problem that makes their use superfluous.

Contents

	Page
Chapter 1 **A Literature Survey**	1
1.1 What is Aeroelasticity?	1
1.1.1 Flutter	2
1.1.2 Forced Response	3
1.2 Aeroelasticity in Turbomachines	3
1.3 Flutter Prediction Methods	4
1.3.1 Traditional Methods	5
1.3.2 Integrated Methods	7
1.4 Research Objectivess	8
Chapter 2 **Traditional Methods**	9
2.1 Background	9
2.2 Theory	11
2.3 A Case Study	13
2.4 Discussion	250
Chapter 3 **An Integrated Non-Linear Aeroelastic Model**	27
3.1 Theory	27
3.2 Structural Vibration Model	29
3.3 Aerodynamic Model	31
3.3.1 Fluid Flow in Turbomachinery	31
3.3.2 Equations of Fluid Flow	31
3.3.3 Lagrangian-Eulerian Model of Fluid Flow	33
3.3.4. Discretization of Flow Equations	35
3.4 Aeroelasticity Model	45
3.4.1 Time-Marching Solution	48
3.4.1a Stability of Time Integration Process	49
3.4.1b Time Step Limit	52
3.4.2 Boundary Conditions	53
3.4.3 Fluid Mesh Kinematics	54
Addendum - Non-Reflective Boundary Conditions	57
A.1 Theory	57
A.2 Implementation	60

Chapter 4 **Validation of Aerodynamic Model**	62
4.1 Shock Tube Flow	62
4.2 Steady Flow	63
4.2.1 Channel Flow	63
4.2.2 Single Airfoil	65
4.2.2.1 NACA-0012 Airfoil, Non-lifting Case	65
4.2.2.2 NACA-0012 Airfoil, Lifting Case	66
4.3 Unsteady Flow	67
4.3.1 Case 1	67
4.3.2 Case 2	68
4.3.2 Case 3	68
4.4 Conclusions	78
Chapter 5 **Validation of Aeroelastic Model**	108
5.1 Problem Definition	108
5.2 Steady Flow Model	109
5.3 Structural Model	112
5.4 Aeroelasticity Analysis	118
5.5 NACA-64a006 Flutter Boundary	156
5.6 Conclusions	159
Chapter 6 **Three-Dimensional Modelling in Turbomachinery**	161
6.1 Introduction	161
6.2 Fluid Flow Model	162
6.2.1 Flow Boundary Conditions	167
6.2.2 Non-Reflective Boundary Conditions in 3D Flow	173
6.2.3 Multi-Passage Flow Modelling	175
6.3 Structural Dynamics Model	179
6.4 Aeroelasticity Model	180
6.5 Time-Marching Acceleration	182
6.5.1 Residual Averaging	182
6.5.2 Multi-Grid Method	185
Chapter 7 **Blade Untwist**	190
7.0 About this Chapter	190
7.1 Introduction	190

7.2 Case Study 191
7.2.1 Structural Model 191
7.2.2 Steady Flow 192
7.2.3 Blade Untwist 193
7.3 Time Accuracy for Untwist Calculations 194
7.4 Effects of Mesh Density 194
7.5 Effects of Geometrical Non-linearity 195
7.6 Blade Unrunning 196
7.7 Conclusions 197

Chapter 8 **Blade Flutter** 210

8.1 Introduction 210
8.2 Case Study 211
8.3 Structural Model 211
8.4 Steady Flow 212
8.5 Blade Flutter Results 217
8.6 Discussion and Conclusions 221

Chapter 9 **Conclusions and Further Work** 224

9.1 Conclusions 224
9.2 Recommendations for Further Work 225

References 227

Appendix - **A Dictionary of Aeroelasticity** 232

Chapter 1

A Literature Survey

Beginnings are always difficult in all sciences.
Karl Marx - Capital

1.0 About this Chapter

A broad definition of aeroelasticity as an independent branch of engineering is given in part (1.1). This is followed by outlining the current aeroelasticity problems encountered in turbomachines (1.2). Part (1.3) enumerates the main categories of numerical techniques for predicting aeroelastic instabilities. The obectives of this research work are presented in part (1.4).

1.1 What is Aeroelasticity?

Aeroelasticity is a branch of engineering that deals with the interaction of structural and fluid dynamics. This mutual interaction between the aerodynamic forces and the structural deformations is of prime importance in both the design and the performance of the structure which, typically, may be a suspension bridge, a helicopter blade, or an aero-engine [1,2].

It is clear from the above definition that the field of aeroelasticity is a crossing where different engineering disciplines meet, a feature that can explain various misunderstandings occuring from different practices and definitions. With this in mind, it is felt that a concise definition of the main aeroelasticity terms, will be of some help. A dictionary of aeroelasticity, is thus provided to help those relatively new to the field in the Appendix.

In literature, two different but related classes of fluid/structure interaction have been identified, namely forced response and flutter. Flutter is a free vibration phenomenon while forced response is the excitation of the structure by non-uniformities of the flow. This fundamental difference in the nature of flutter and forced response has, in turn, led to different numerical techniques in their prediction. Let us look at these two categories of the aeroelasticity phonomenon in more detail.

1.1.1 Flutter

A structure, because of its inertial and elastic properties, is prone to freely oscillate if disturbed from its equilibrium position and released. These oscillations occur at certain frequencies, known as natural frequencies, which represent the rate at which the structure exchanges its kinetic energy (due to elasticity) and its potential energy (due to inertia). These frequencies and the corresponding form of deformation of the structure are characteristic of that structure.

The same structure, if is in contact with a flow, can still exhibit the above tendency to vibrate at its natural frequencies. However, the fluid flow can now effect the way the structure vibrates. This is because the flow also has elasticity and inertia. It also has the capacity to dissipate energy (i.e. damping). Once the structure is disturbed, the aerodynamic forces, which are a function of the structure's oscillatory motion, as well as the flow dynamics, strongly interact with the structure. Flutter occurs when the aerodynamic forces, thus generated, enhances the structural oscillations leading to sustained fluid/structure vibration. This definition implies that flutter is a stability problem [3]. It also implies that, as a free vibration problem, flutter tends to occur at lower fluid/structure vibration modes.

The presence of flow and its interaction with the structure will lead to structural frequencies and deformations which are different from the "structure-alone" modes of vibration.

It is important to note that the main mechanism for flutter is the presence of unsteadiness in the flow which is generated by the vibratory motion of the structure. If the fluid flow were to remain steady, the structure would deform under the steady fluid loads and reach a new equilibrium position but no flutter occurs. This static fluid/structure interaction is known as untwist.

1.1.2 Forced Response

Forced response of structures is due to the disturbances on the incoming flow. These can be gusts, turbulence or wakes that hit the blade periodically and force it to vibrate. The effect of forced response becomes significant if the frequency of the arrival of the incoming disturbances coincides with one or more of the natural frequencies of the structure. Therefore, the problem is one of determining the frequency content of the incoming disturbances and of checking if any of the excitation frequencies coincide with the natural frequencies of the structure.

The above definition explains the inherent differences between numerical prediction techniques for flutter and forced response investigations. In flutter cases, fluid flow characteristics and its unsteady behaviour is essential. This determines whether the flow is absorbing energy from the structure and has a stabilizing effect on the structure, or is enhancing the structural vibrations by transmitting its unsteady energy to it. Therefore, fluid flow is an inseparable part of the flutter phenomenon and the nature of its behaviour needs to be determined. This is not the case with forced response. In the latter case, the fluid flow acts as a medium for the external disturbances to reach the structure. This can be best described by an elastic string whose one end is tucked at suddenly. A wave is generated which travels through the string. Each point along the path of the wave is disturbed only to allow the wave to be transmitted. To determine what happens at the other end of the string, the dynamic behaviour of the string itself will not be required.

This has meant that techniques for simulation of forced response problems usually use very simple fluid models as opposed to flutter prediction techniques.

1.2 Aeroelasticity in Turbomachines

The problem of aeroelastic instability in turbomachinery is a long-standing problem which has become more significant as compressor blades of light-weight and low aspect ratio have become the norm. Furthermore, the much higher operation range of these blades, has increased the influence of flutter considerations in blade design. Today, the flutter boundaries are the actual operation limiters in the performance of turomachines, and specifically aero-engines [4,5]

This may be seen on a typical compressor map of figure 1.1, derived from reference [6]. The presence of different flutter regimes surrounding the operational line for the compressor are shown in some detail. Deviations from the working line due to landing, take-off, or manouvers during flight can lead to flutter instabilities. Presence of different flutter mechanisms both below and above the operational line clearly explains the need for understanding the mechanics of different flutter regimes and the ability to predict them at the design stage.

It should be pointed out that figure 1.1 is only a generic representation of the various flutter boundaries, the actual flutter boundaries being dependent on the specific blade design and operational requirements. However, it is interesting to note that flutter boundaries create more stringent limits on performance than purely aerodynamic considerations, notably, the surge line where the engine stalls. More worringly, figure 1.1 shows that flutter regimes can occur along the operational line of the engine itself.

The main cause of forced response in turbomachines is the coincidence of the assembly natural frequencies with that of the engine-orders, i.e. harmonics of engine rotational frequencies. The flow disturbances forcing the blades to vibrate are formed due to obstructions present in the path of the flow. These can be other stages upstream or, indeed, other bodies present downstream of the blade. Upstream obstructions create wakes that hit the blade while those downstream of the blade can influence the blade by potential flow effects. For a safe design, the structural modes of vibration should be well away from the engine-orders. In this research , forced response is not considered.

1.3 Flutter Prediction Methods

There are a large number of numerical techniques for prediction of flutter. These can be classified in variety of ways based on different criteria. One can consider the type of aerodynamic or structural modelling that is being employed. The solution domain (time vs frequency), is another basis for classification. The range of applicability, linear vs. non-linear or range of blade amplitudes, is yet another candidate. There are a variety of special techniques employed in coupling the fluid flow and the structural vibrations and these can also form a basis for distinguishing different strategies of flutter prediction. The list of choices is not endless but certainly extensive. It seems, however, that a logical route is to classify the variety of numerical techniques available, based on the aeroelastic assumptions inherent in each model. This means one can identify a given technique according to the modelling of the fluid/structure interaction rather than to the specifics of the numerical treatment.

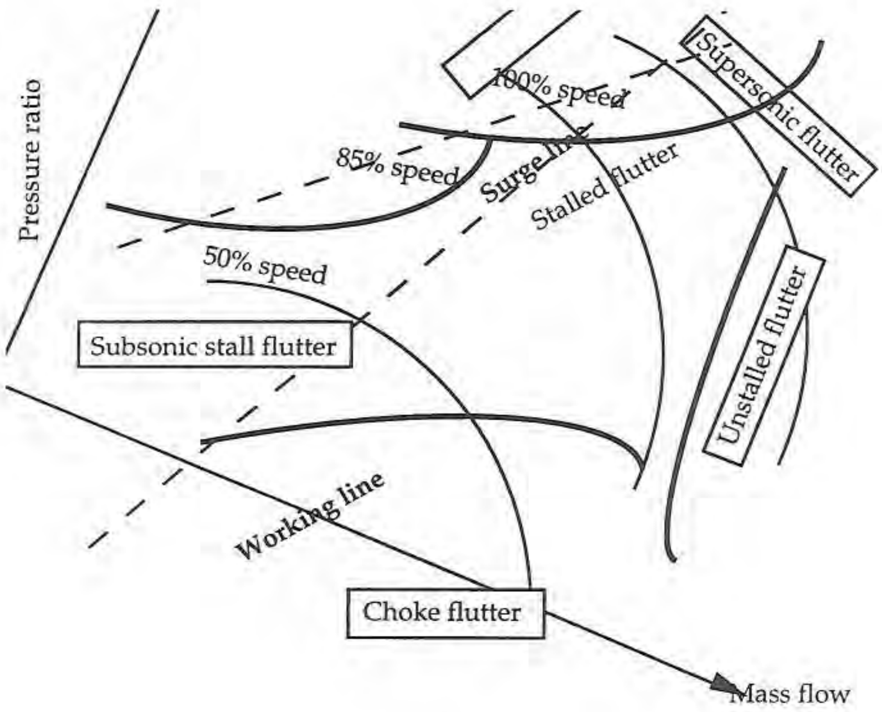

Figure 1.1 - A typical fan blade compressor map

Based on this criterion, two main strategies can be discerned from the literature. The first strategy is to perform the analysis of the two components of the flutter phenomenon, i.e. the unsteady aerodynamics and the structural vibrations, separately and combine the outcome of each analysis via the surface pressures in an integration procedure, hereafter referred to as the traditional method. The second strategy is to retain the fluid/structural coupling and treat the fluid and the structure as one continuum, hereafter referred to as the integrated method. Both strategies and the different numerical nuances in each are described in more detail below.

1.3.1 Traditional Methods

Traditional methods start by decoupling the fluid flow and the structural vibrations from each other. These two parts are then analysed separately. The structural analysis is simply the determination of the natural frequencies and mode shapes of the structure, i.e. solution of the governing equations of motion for free vibration. The fluid flow solution proceeds in two stages. First, the steady flow past the structure is determined. The unsteady fluid forces acting on the structure are then determined for infinitesimal blade oscillations. As blade oscillations are very small the unsteady flow can be regarded as a harmonic variation about a mean which is the steady flow condition. This implies a linearisation of the unsteady flow model about the steady flow. The unsteady aerodynamic loads are determined for all the structural vibration modes of interest. The unsteady work done by the flow on the structure is then determined from the unsteady fluid loads and the structural modes of vibration using the principle of virtual work. If this work is positive, the flow is transmitting energy to the structure and the fluid/structure system is inherently unstable. On the other hand if the work is negative, the flow is absorbing energy from the structure and acts as a damping mechanism for the structure. The system is then said to be stable.

This strategy is the one used by Whitehead [7-8] and Verdon [9-10], as well as many other researchers in the field of aeroelasticity [11-14].

The linearisation of the unsteady fluid about its mean steady condition results in a major simplification in the model. It also results in a significant reduction in the computational work. Furthermore, a linear unsteady model can be handled in the frequency domain which is very convenient.

The decoupling of the fluid and the structure at the start is based on the assumption that flutter is a stability problem and hence linear. All we are concerned with is whether the flow is destabilizing when the structure is infinitesimally displaced.

The other assumption in these methods is that flutter will occur at one of the blade natural frequencies. This is justified since the mass ratio of the flow to the structure is very small and the structure is, evidently, much stiffer than the fluid. Hence, while in reality the flutter frequencies are somewhat different from that of the "structure-alone" modes of vibration , this difference must be very small.

It should be pointed out that, in traditional methods, the fluid modelling itself can be non-linear in the steady flow stage. Indeed, the fluid flow models used in for the steady flow calculations can be very sophisticated.

The major shortcoming of the traditional methods is their inability to handle finite amplitude blade vibrations [15]. The aeroelastic non-linearities in the transonic flow regimes, ignored by traditional methods, may be significant. This means that the assumption of linearity of unsteady flow is not valid at high reduced frequencies [16-17]. Furthermore, the traditional methods are unable to handle flutter regimes based on mode coupling or when unsteady flow is significantly different due to flow separation. In this latter case the traditional methods singularly fail. Also, when transonic unsteady behaviour is present, e.g. formation and disapearance of shocks during blade vibrations, the linearisation process becomes completely invalid [15,17,18,19].

In passing, it should be also pointed out that the amount of information provided by the traditional methods is very limited. In practice, one would like to know about the level of instability, how close one is to the flutter boundary and, more importantly, one needs to know the probable regime of flutter. Most of the traditional methods require this to be known in advance [1].

1.3.2 Integrated Methods

The limitations found in the traditional methods have led many researchers to the conclusion that coupling between the structure and the flow needs to be incorporated in the flutter prediction method [15-24] so that the fluid and the structure are treated as a continuous medium. The governing equations of motion for both the structure and the fluid flow along with the necessary compatibility conditions at the fluid/structure interface can then be solved together. The solution is invariably in the time domain, although a recent exception is the non-linear model developed by Dowell [1] which attempts to solve the coupled problem in the frequency domain.

The outcome of the integrated models is often a time history of the structural vibrations. If the amplitude of vibrations grows in time, the structure is unstable but for most non-linear cases, the outcome is in the form of a limit cycle.

The simultaneous solution of the fluid flow and the structural vibration models means that the compatibility conditions at the fluid/structure interface are to be satisfied at each instant in time. This simply means that at each instant in time, the flow should know where the structure is and how it is moving and, in turn, the structure should know the instantaneous aerodynamic loads. Those integrated methods that use different time-marching solution procedures for the flow and the structure satisfy this condition iteratively. Those integrated models that use the same time-marching solution procedure for both the flow and the structure satisfy the compatibility condition directly.

The fluid flow modelling in such methods is typically Euler or Navier-Stokes in order to take into account the highly non-linear nature of the flow. Structural models tend to be based on the modal representation technique. Although this allows a major reduction in the structural data, it means that the structural model is linear and, in effect, only valid for small vibration amplitudes. However, attempts at solving the non-linear structural equations of motion for flutter have been recently reported in the literature [24-25]. This is essential for aircraft wing problems because of the large amplitudes of vibrations involved. In turbomachinery problems, the vibration amplitudes are much lower and the use of modal representation, although not entirely satisfactory, might be considered as adequate. This argument in favour of modal models is further augmented if one consideres the size of structural models required to represent the whole bladed-disc assemblies.

1.4 Research Objectives

The main motivation behind this work is to develop an integrated model for the prediction of flutter of aero-engine blades via an objective critique of the traditional models that are currently in use for this purpose.

A variety of integrated models are available for wing flutter modelling. The general capabilities in the realm of aircraft flutter seem to be well ahead of their counterparts in turbomachines. This is partly explained by the more complex physical phenomena encountered in turbomachinery along with the more complicated modelling issues that are present when dealing with turbomachinery blades. Therefore, it is sensible to try to transfer the more advanced aircraft flutter techniques to the field of turbomachinery. The feasibility of such a transfer and the applicability of an integrated method for routine flutter calculations on turbomachinery blades in transonic flow regimes is the objective of this research.

Chapter 2

Traditional Methods

The past was safe in its cage, why not have a look?
Vladimir Nabokov - Laughter in the Dark

2.0 About this Chapter

The background to this investigation of a traditional method for flutter calculations is given in part (2.1). This is followed by a description of the theory of the model in part (2.2). Part (2.3) gives the results of the numerical studies on a case study considered. This is followed, in part (2.4), by a general discussion of the limitations of the model with a view towards the next generation of the aeroelasticity methods outlined in the subsequent chapters of this document.

2.1 Background

As part of the process of familliarization with the flutter stability problems in the field of turbomachinery, it is appropriate to start by an investigation of the current numerical techniques used for both design and problem solving in industry. A series of test cases for turbine and compressor blades operationg in transonic flow regimes have been chosen for this study. These cases represent the current challenges to the flutter prediction tools. Here, the traditional methods fail in providing an adequate answer to the problem. This is mainly due to the simplifications implicit, or explicit, in these models. For this very reason, regardless of the quantative results, the traditional models tend to command little confidence, amongst designers and numerical analysts.

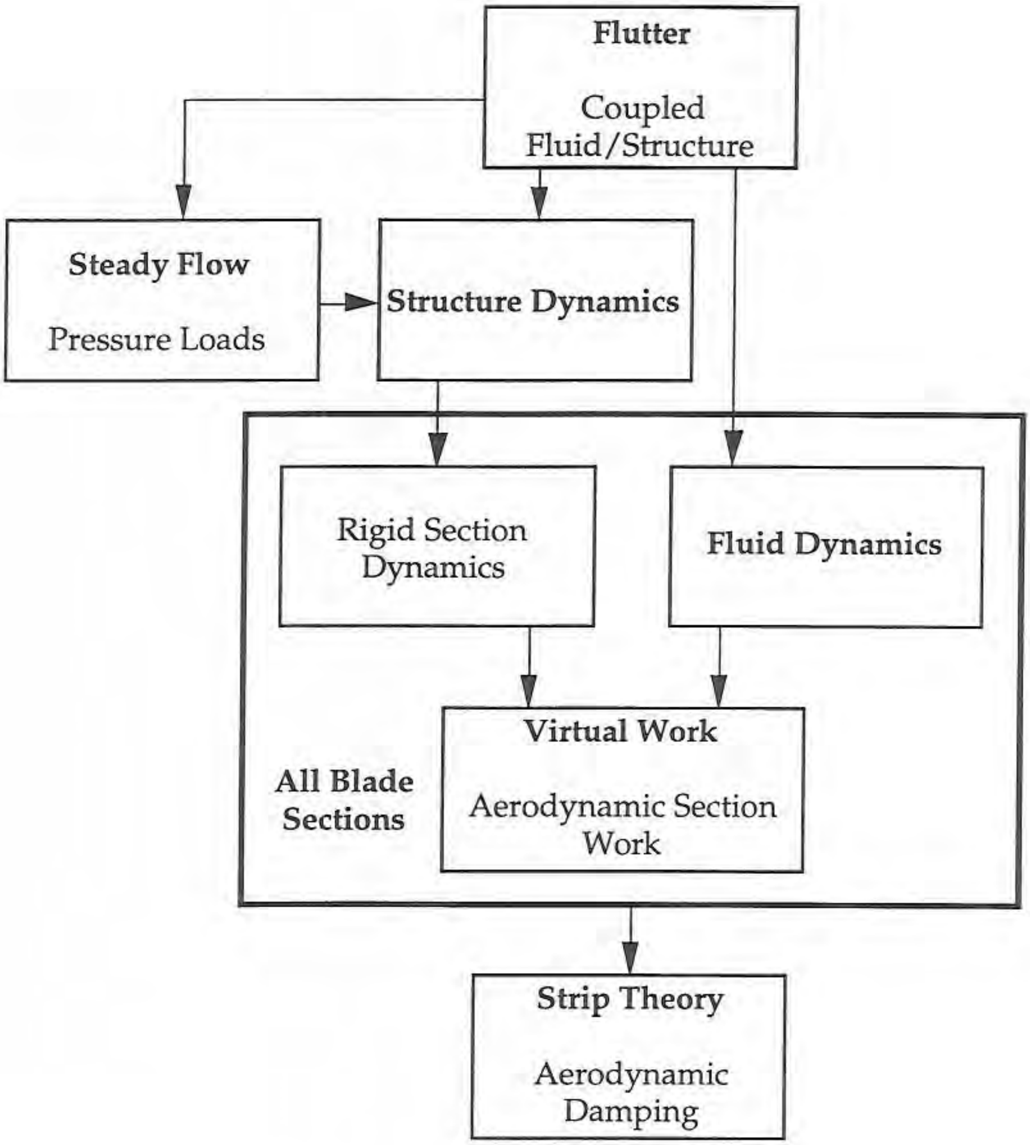

Figure 2.1 - A Schematic Representation of Flutter Model

2.2 Theory

The model used here is that provided by Rolls-Royce Plc and is shown schematically in figure 2.1. The system comprises from a finite element structural analysis package, SADIE, which performs the eigen-solution of the rotating bladed-disc assembly. The effect of the stress stiffening due to blade rotation is included by first performing a stress analysis on the blade at the required rotational speed. The stiffness matrix for the vibration analysis is subsequently modified using the results of the stress analysis. The effect of static fluid load is also incorporated in the stress analysis calculation. The static pressure load is obtained from a 3-D steady flow analysis performed separately.

The resultant mode shapes from the eigen-solution are then reduced to translational and rotational displacement for a series 2-D rigid blade sections which are then used for aeroelastic analysis. A typical section is shown in figure 2.2. The important factor is the determination of the torsional section displacement. This is determined as follows:

$$\theta_z = \frac{d_{LE} - d_{TE}}{\text{chord}} \qquad (2\text{-}1)$$

where

d_{LE} = Displacement at the Leading Edge

d_{TE} = Displacement at the Trailing Edge

This expression means that the flexibility of the section is lost in the subsequent analysis.

The steady and unsteady flow calculations for 2-D rigid blade sections is performed using a finite element fluid flow program called FINSUP [7,8,26,27,28]. FINSUP is a two-dimensional, compressible, potential fluid flow model. Quasi-three-dimensional effects due to stream tube height effects are included.

To perform the steady flow analysis, inlet and outlet Mach numbers and flow angles are specified. These are usually obtained from experimental data or are values for which the blade has been designed for.

For a potential flow model, a solution that satisfies the boundary conditions at inlet and outlet exists, provided the circulation around the body is fixed. If not, the conditions at inlet and outlet and the blade geometry of the blade section do not determine the flow uniquely. In FINSUP, the magnitude of the circulation around the body is fixed by imposing a cusped trailing edge (to satisfy the Kutta-Joukowski condition) and introducing a jump in potential at the trailing edge point and across the wake line.

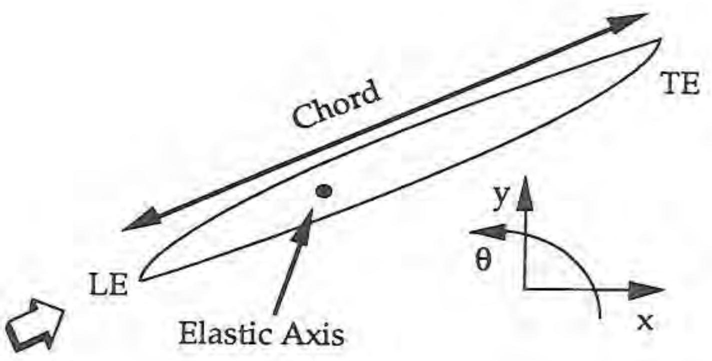

Figure 2.2 - A typical Rigid Body Section

To enable the prediction of transonic flow regime and capturing of shock waves, an artificial viscosity is added to the model. The use of the artificial viscosity is to bias the potential flow equations (which are otherwise elliptical) to handle small hyperbolic regions of the flow around the blade profile.

Unsteady calculations are based on the small periodic perturbation technique which is a linearisation of the unsteady flow about a mean which is the steady flow solution. Perturbing the flow along each of the three degrees of freedom for the rigid blade section (i.e. X,Y,θ_z directions), in turn, results in an unsteady fluid pressure force tensor.

The product of this force tensor and the rigid section mode-shapes, obtained from the structural analysis, gives the work done on the section by the unsteady flow i.e.

$$\begin{Bmatrix} W_x \\ W_y \\ W_\theta \end{Bmatrix} = \begin{bmatrix} C_{xx} & C_{xy} & C_{x\theta} \\ C_{xy} & C_{yy} & C_{y\theta} \\ C_{x\theta} & C_{y\theta} & C_{\theta\theta} \end{bmatrix} \begin{Bmatrix} x \\ y \\ \theta \end{Bmatrix} \tag{2-2}$$

The total section work done is

$$W_{total} = W_x + W_y + W_\theta \tag{2-3}$$

The total work on the blade is obtained by integrating these section works along the blade according to the strip theory, a procedure known as the worksum[29]. This total aerodynamic work on the blade is then scaled by the average kintetic energy of the blade, giving:

$$\delta_{aero} = \frac{-\text{Work}}{4\text{KE}} \tag{2-4}$$

The outcome is the aerodynamic damping, known also as the log dec, on the blade. If it is positive, the flow transmits energy to the blade and the system in unstable. In reality the aerodynamic damping should be more than the mechanical damping for the instability to occur. However, a conservative estimate is to regard the mechanical damping to be zero.

Alternatively, if the aerodynamic damping is negative, the flow absorbs energy and has a stabilizing effect on the blade.

2.3 A Case Study

A number of case studies have been chosen for this study of the traditional methods for flutter predictions [30-31]. One of these is a real fan geometry (hereinafter known as fan A) [32]. Experimental tests on this blade revealed flutter instability.

The structural analysis of the fan A is performed at 0%, 80%, 85% and 90% engine speeds. The finite element model of the blade is shown in figure 2.3. The model is made of twenty node brick elements which is the standard element assumed by

SADIE. The calculation of the aerodynamic forces is performed at three heights of 74%, 88% and 94% along the blade.

The convergence criterion for the FINSUP calculations is satisfying the inlet boundary condition (namely, the input Mach number and the input flow angle). Initially, calculations are performed at a low Mach number and are subsequently modified by increasing the inlet Mach number to its actual value. In order to avoid overshoots in the flow speed ahead of the shock, rather large levels of numerical damping are required. Lower damping levels tend to produce a spike in flow speed ahead of the shock wave.

From the experiments performed on a test rig [33] it has been observed that, in terms of flutter instability, the main area of interest is at the first flap mode. Therefore, the unsteady FINSUP calculations are performed at this frequency. Table 2.1 gives a list of the sections that are used for the purpose of the stability analysis (the blade is divided to 18 sections in total). The position of these cases on the compressor map is shown in figure 2.4.

The natural frequencies obtained from the structural analysis are given in Table 2.2. Figure 2.5 shows the modeshapes for the first four modes at the 85% speed. The agreement between the the natural frquencies of the blade at zero speed obtained from the rig tests given in reference [33] and the numerical results from SADIE is satisfactory. The experimental natural frequency at 0% speed was found to be 92.7 Hz. The numerical analysis predicts a value of 93.7 Hz. Experimental results for blade natural frequencies are available only at the zero speed.

The flutter experienced by the blade during testing was observed to occur at 30 degrees inter-blade phase angle. Therefore this mode is used in the numerical analysis.

Conditions	Sections	heights(%)	Speeds(%)	Working line
1	16	88	85	Max Flow
2	14,16,17	74,88,94	85	SLS
3	16	88	85	above SLS
4	14,16,17	74,88,94	85	Flutter

Table 1.1 - Summary of Blade Sections and Conditions

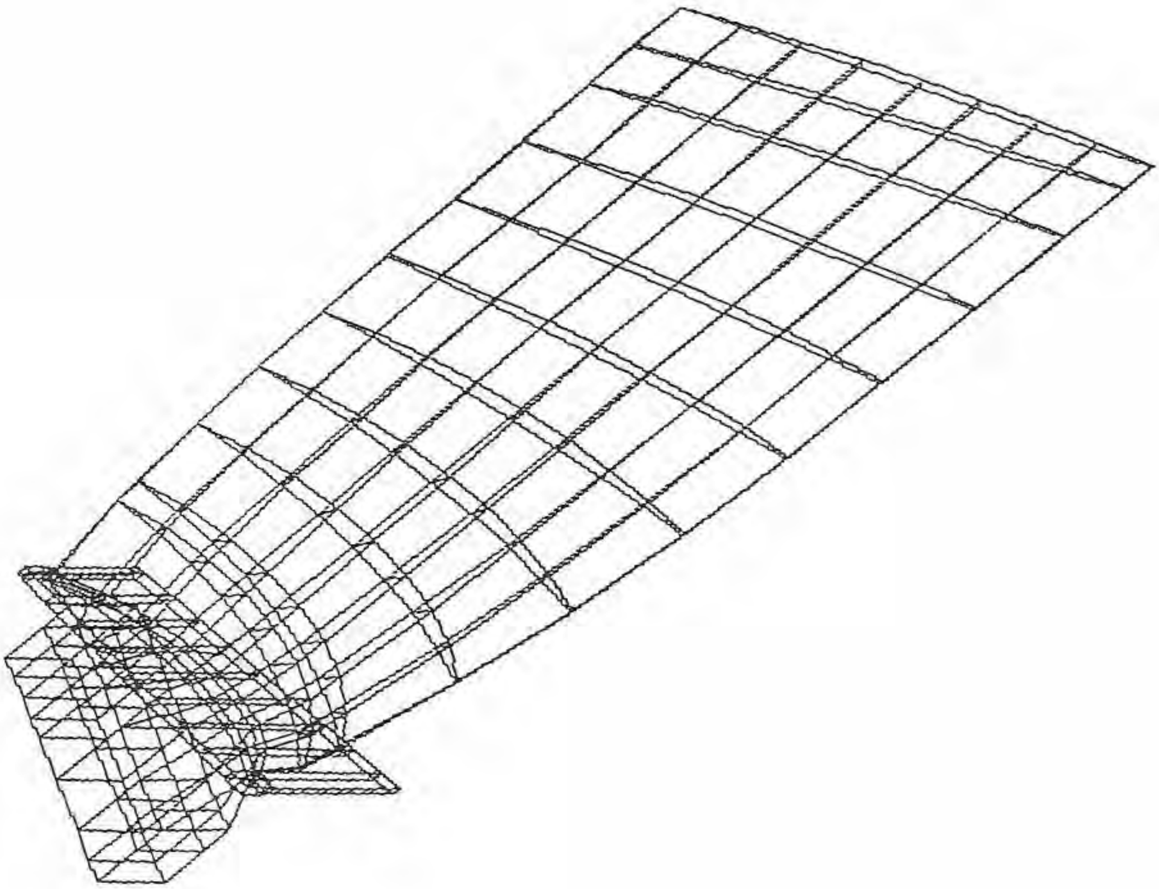

Figure 2.3 - Finite Element Mesh for Fan A Used in SADIE

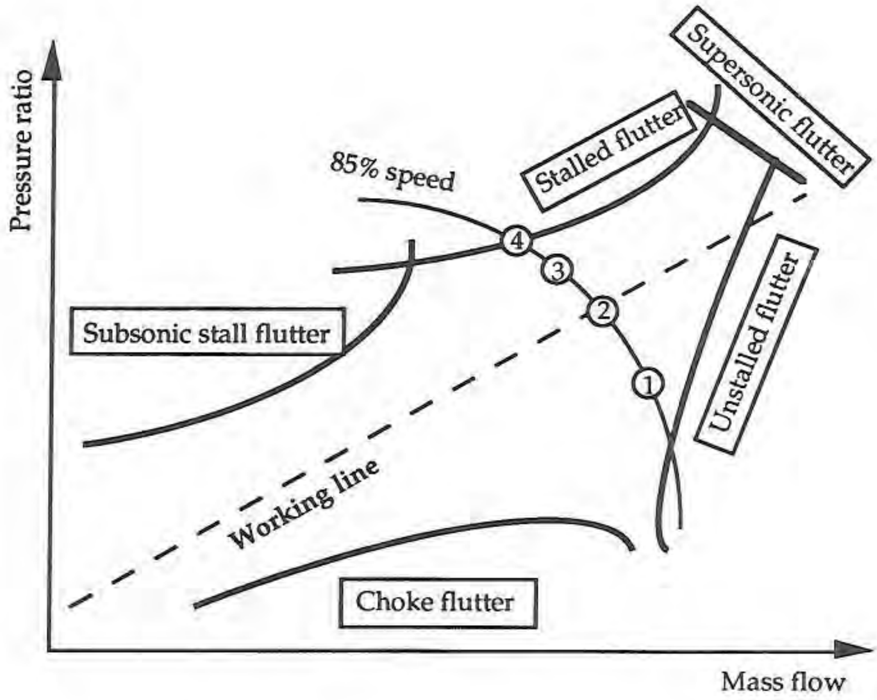

Figure 2.4 - Flutter Cases on the Compressor Map

MODE	Frequency(Hz)		
	80% Speed	85% Speed	90% Speed
1F	173.926	180.521	187.130
Coupled *	404.300	417.936	431.834
1T	674.995	675.320	675.659
2F	898.753	915.233	932.227
2T	1302.25	1303.980	1305.64
3F	1481.53	1489.730	1498.24
3T	1582.66	1584.720	1586.85
Plate mode	1810.21	1817.760	1825.91

* First flap and second edgewise

Table 2.2 - Natural frequencies for fan A

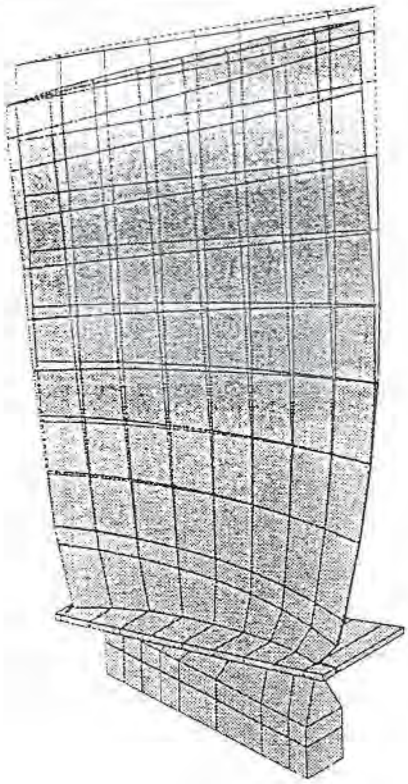

a) Mode one, f=180.521 Hz

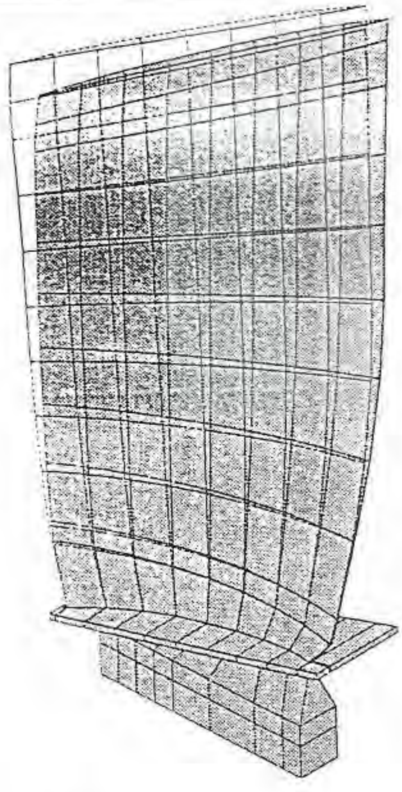

b) Mode two, f=417.936 Hz

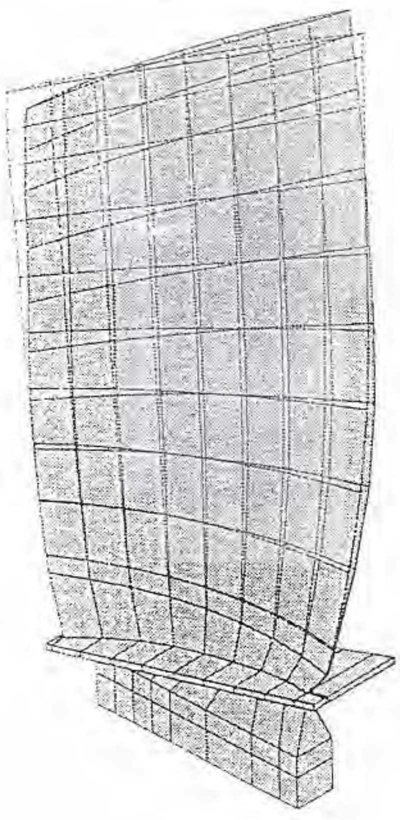

c) Mode three, f=675.30 Hz

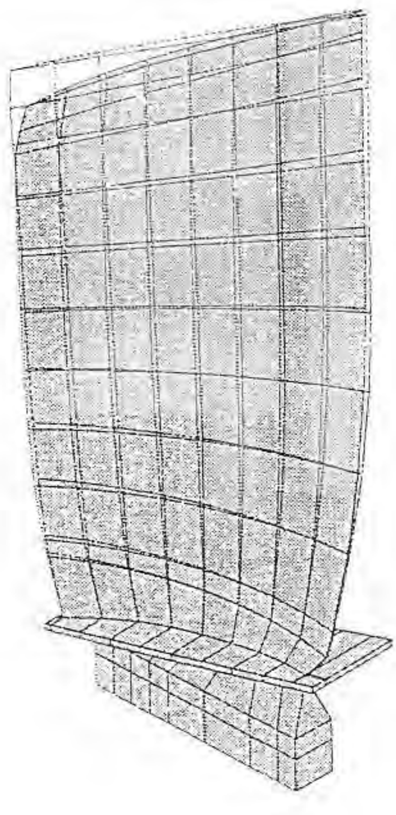

d) Mode four, f=915.233 Hz

Figure 2.5 - Modeshapes for Fan A at 85% Speed

Figure 2.6 shows the variation in the steady surface Mach numbers for the various operational conditions at the 85% speed. As expected, the position of the shock moves downstream along the blade height for all conditions. Furthermore, as we move towards the stall flutter boundary the position of the shock moves upstream. This is corresponding to the increase in the pressure ratio, i.e. a higher back pressure. The main implication of this is an increase in the steady lift on the blade an a decrease in the torsional load. Figure 2.7 shows the variation in the pattern of the steady surface Mach numbers with the speed along the Sea Level Static (SLS) working line. The main feature observed is the forward movement of the shock position with speed (from 42% of the axial chord at 80% speed to 55% of the chord at 90% speed). This, again, means an increase in the steady lift and a reduction in the torsional load on the blade.

Figures 2.8 shows the variation of the unsteady surface pressures along the blade surface for the SLS condition. The graphs of interest are those of unsteady pressures for Y-motion and the torsional motion of the blade sections. From figure 3.8b it can be seen that imaginary unsteady pressures, coressponding to blade velocity in the Y-direction, shows that as the blade section moves upward (i.e. positive Y-direction) the unsteady pressure on the suction surface increases and creates a downward unsteady force on the blade section. Therefore, the blade section is stable when in translational motion. The same is true of the unsteady pressures for rotational motion shown in figure 2.8c. For a positive motion in the θ-direction, i.e. anti-clockwise motion, the unsteady pressure field creates a clockwise moment on the blade to counteract the motion of the blade section. Therefore, the unsteady pressures on the blade section act in the the opposite direction to the blade motion. Hence, the blade section is stable at the SLS operating condition at 85% speed. The same is true for all the other sections of the blade chosen for this study.

Figures 2.9 shows the variation of the unsteady surface pressures at the 88% blade height for the condition 4 which is on the flutter boundary. As it can be seen the unsteady pressure load on the blade section for the Y-motion is again in the opposite direction to the blade section motion. The increase in the unsteady pressure on the suction surface creates a downward force as the the blade is moving upwards. On the other hand, the resultant moment is only marginally stable. In passing, it is interesting to note that the presence of the shock tends to have a destabilizing effect on the blade, as observed by the unsteady pressure spike at the position of the shock wave.

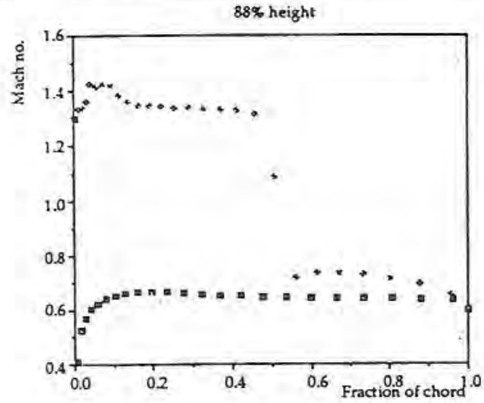

a) Condition 1, Maximum flow

b) Condition 2, Working line

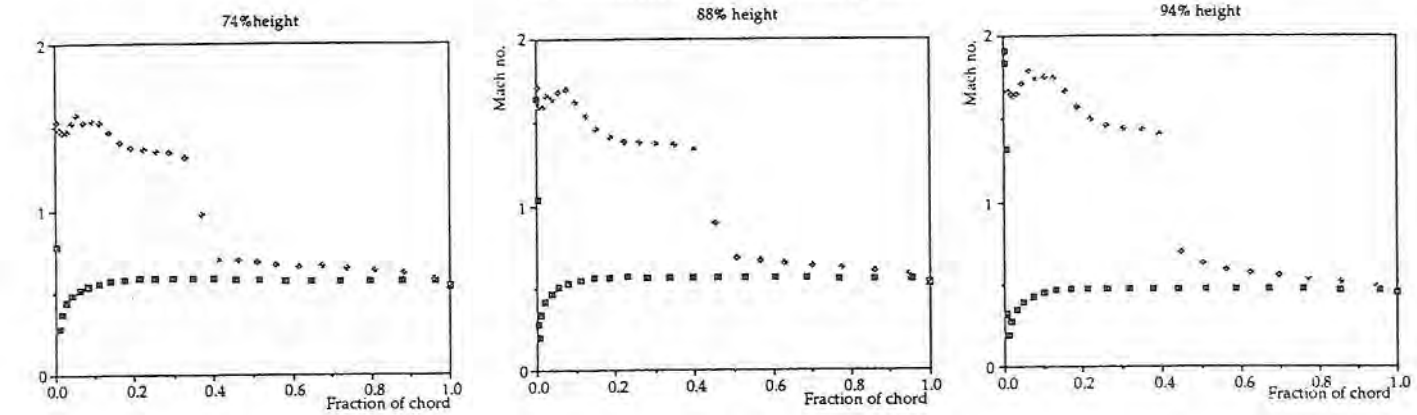

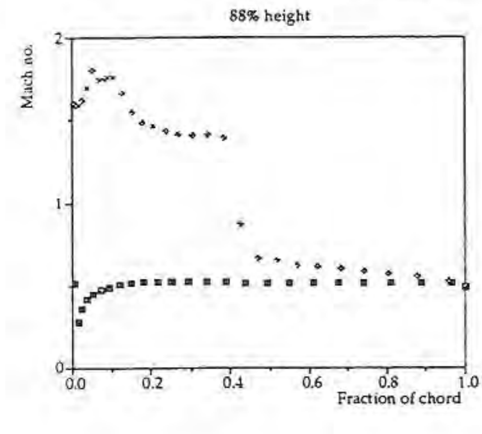

c) Condition 3, Above working

d) Condition 4, Flutter point

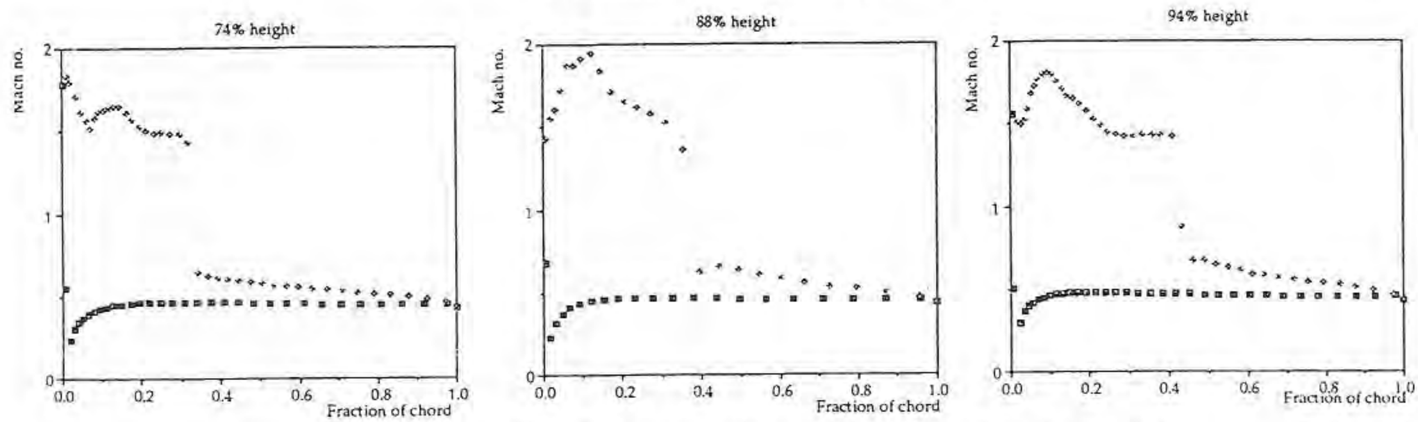

Figure 2.6 - Steady Surface Mach numbers at 85% speed

a) SLS Working Line, 80% speed

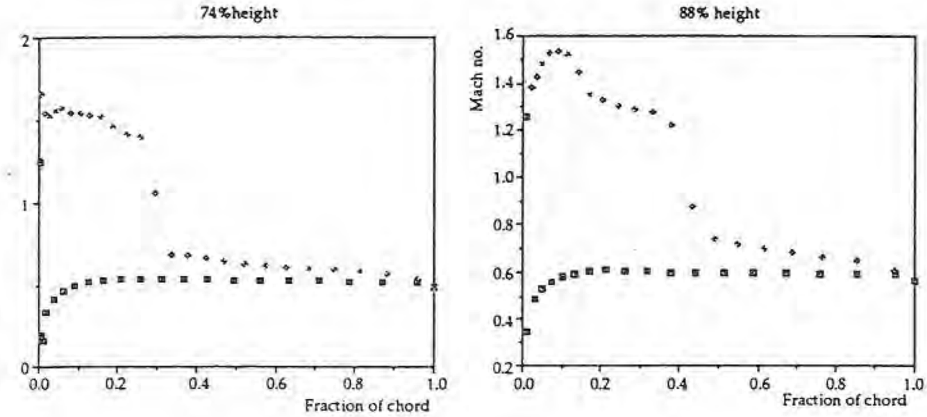

b) SLS Working Line, 85% speed

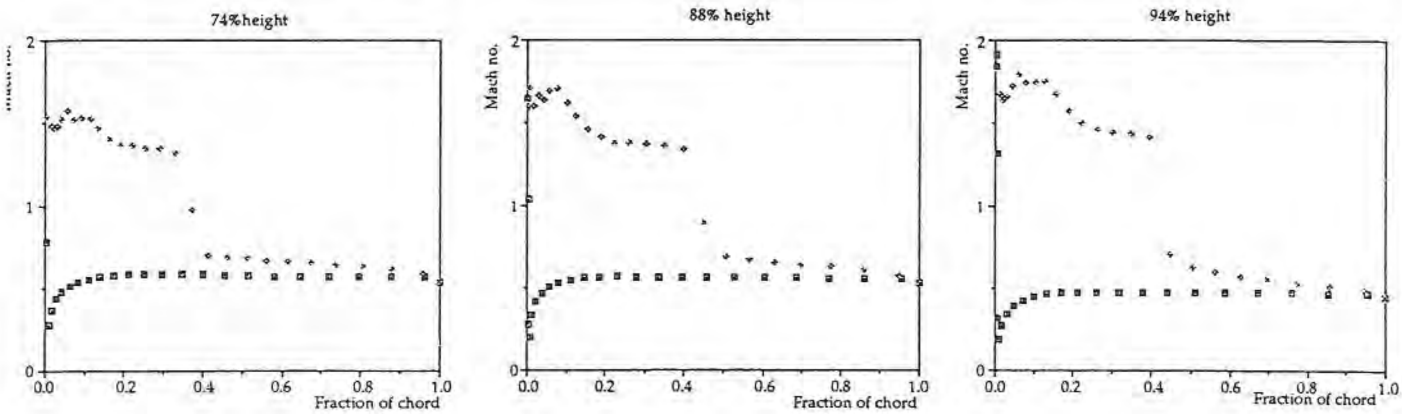

c) SLS Working Line 90% speed

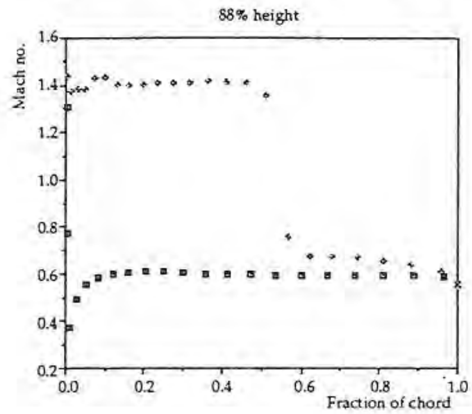

Figure 2.7 - Steady Surface Mach Numbers at 80%, 85% and 90% speeds, SLS

a) Unsteady surface pressure due to X-motion of blade section

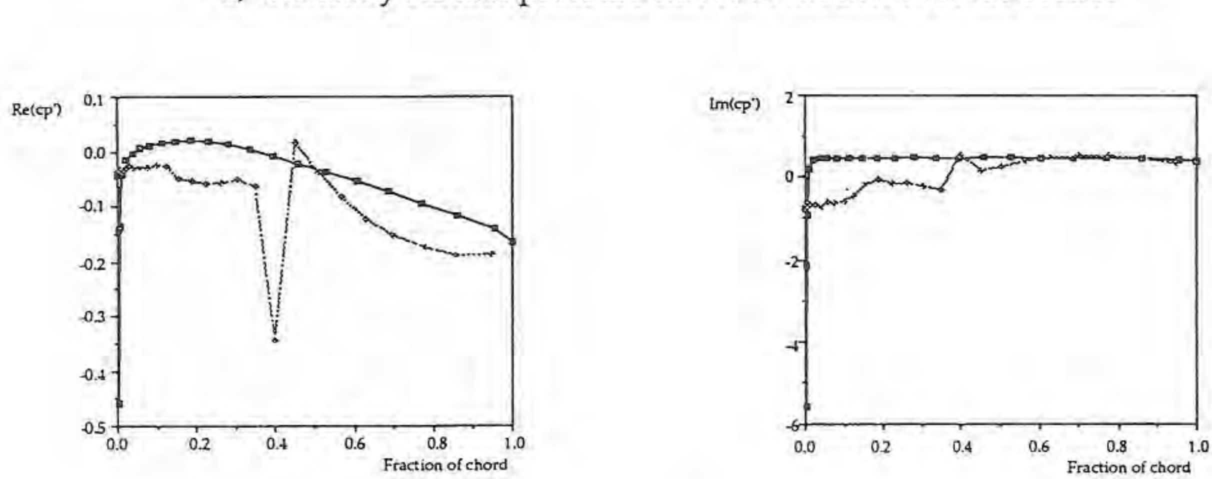

b) Unsteady surface pressure due to Y-motion of blade section

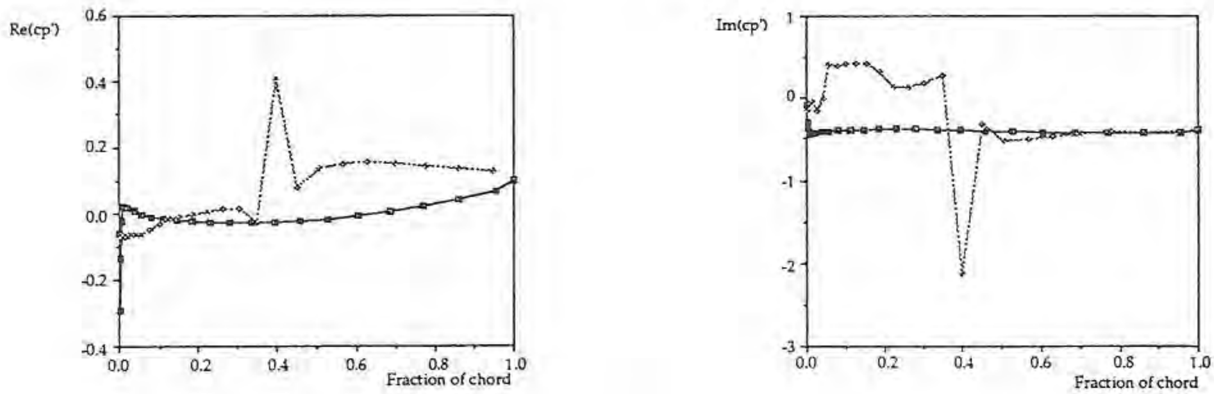

c) Unsteady surface pressure due to blade section torsion

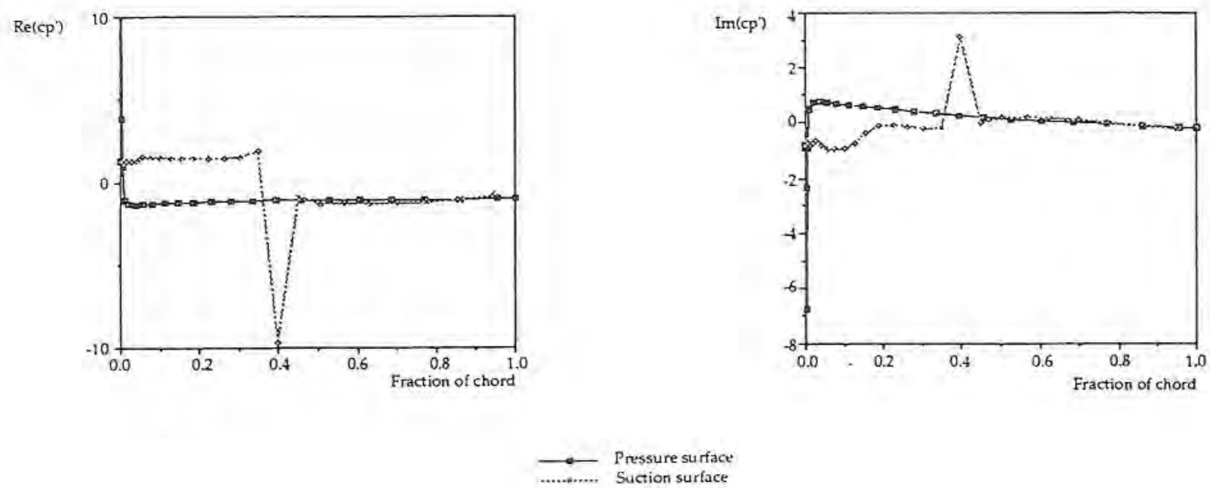

Figure 2.8 - Unsteady Surface Pressures for 88% height, Condition 2, 85% Speed

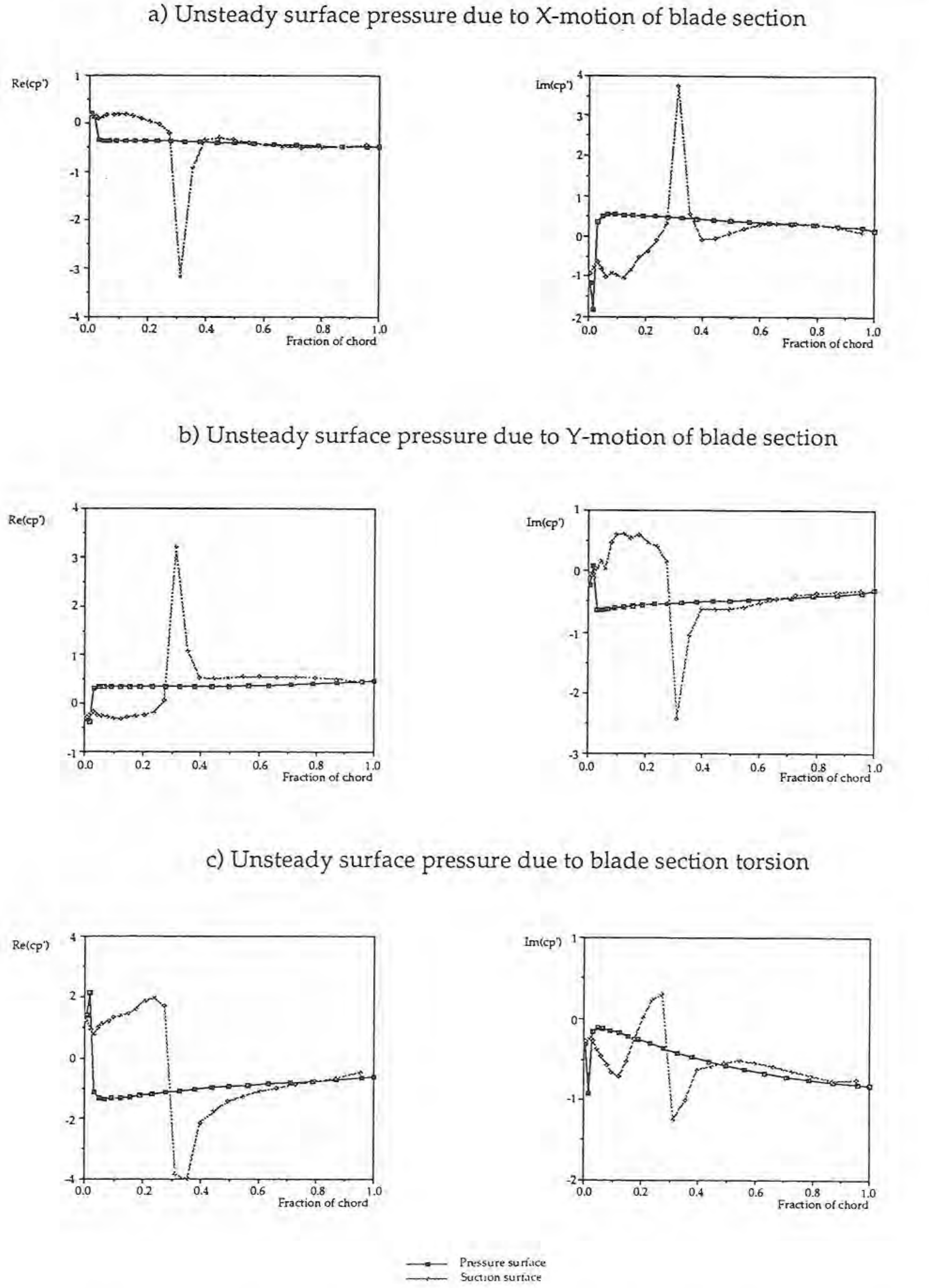

Figure 2.9 - Unsteady Surface Pressures for 88% height, Condition 4, 85% Speed

Figure 2.10 shows the variation of the section log dec along the blade height for the SLS and the flutter conditions. Two points can be discerned from this plot; the first is that the blade is less stable on the flutter boundary and, the second point is that the blade is more stable for higher blade heights. In fact this plot resembles the blade mode-shape for the first flap mode. This is expected from the above discussion; the larger the blade displacement, which occurs as we move along the blade height, the larger unsteady pressure opposing its motion. An outcome which is completely in contrast to the physics of the problem.

Figure 2.11 shows the variation of the blade log dec value for all the conditions considered here. It can be seen that the method is sensitive to the stall flutter boundary but it fails to determine the onset of stall flutter.

The effect of the hade angle is ignored in the standard worksum procedure. The above calculations were repeated by including the effect of the hade angle. This means that for each section of the blade, the motion at the trailing edge, centre of mass and the leading edge are determined at their true radial position. Figure 2.12 shows that the effect of this modification is to marginally reduce the value of the predicted section log dec. However, the result remains very stable[34].

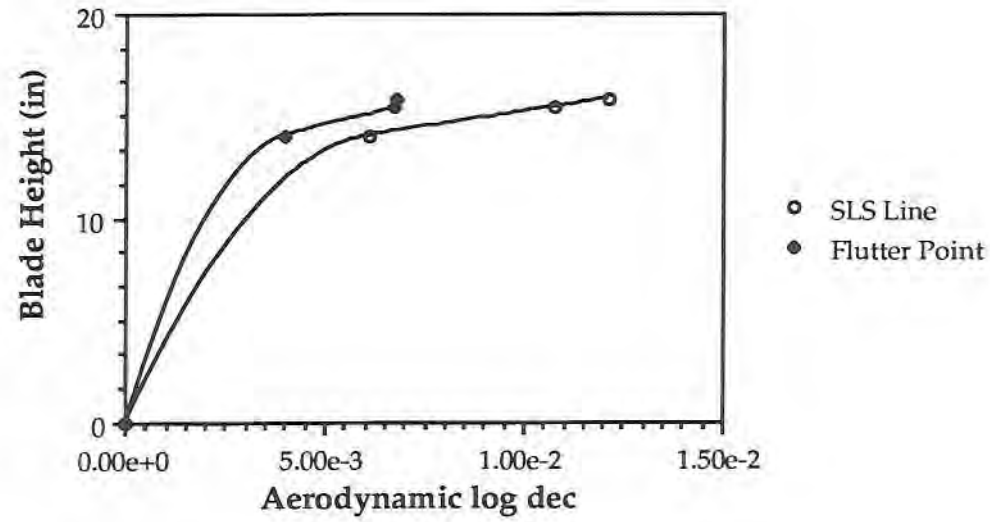

Figure 2.10 - Aerodynamic Damping at 85% speed

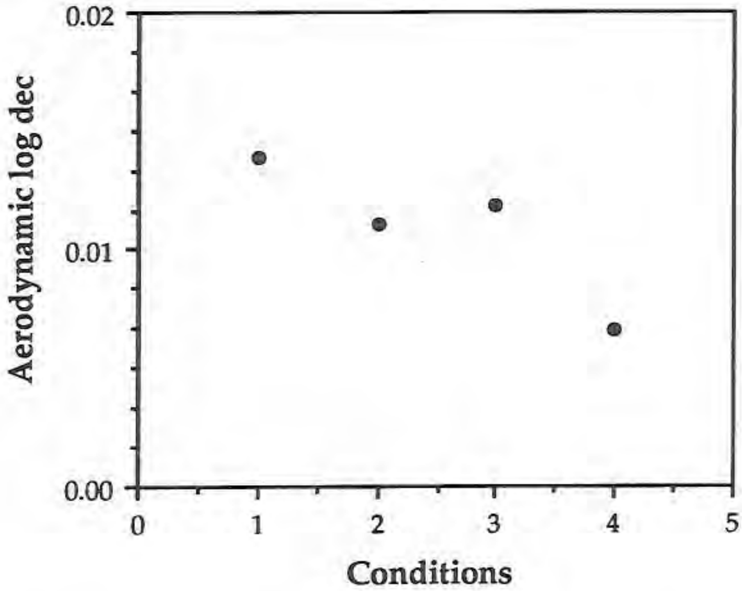

Figure 2.11 - Aerodynamic log dec for all Conditions at 85% speed

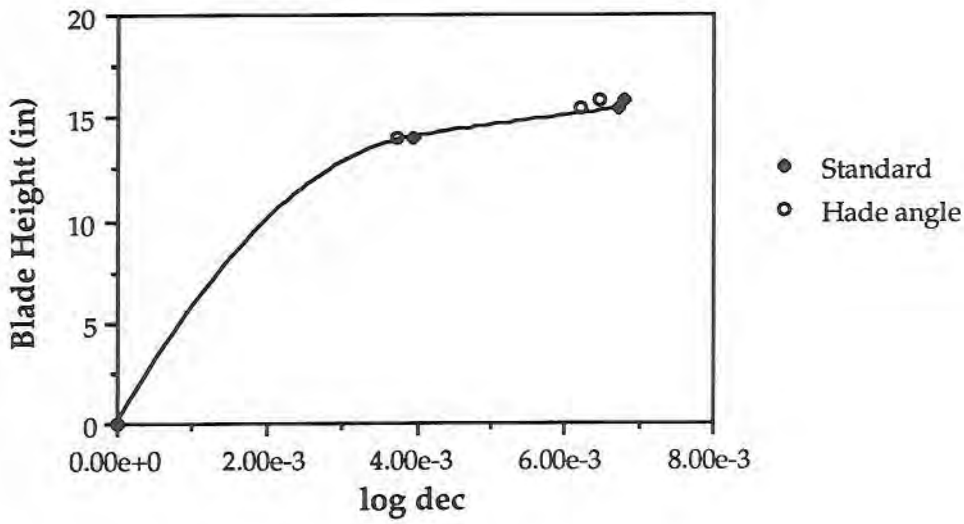

Figure 2.12 - Effect of Hade angle at Flutter Point

In conclusion, due to the very stable response of the flow to the heaving motion (i.e. Y-motion) of the blade section, the uncoupled method returns a stable solution on the flutter boundary.

2.4 Discussion

The inability of the uncoupled analysis to predict flutter boundaries for fan blades can be attributed to a number of factors. These are mainly the inviscid assumption in the aerodynamic analysis, three dimensional effects, shock-boundary layer interaction and the inability to model shock instability accurately which is better described by integrated models.

It can be argued that the traditional method used here is not a suitable tool for predicting most of fan blade flutter regimes (see figure 2.4). Choke flutter modelling within the current method of analysis is not possible since choke flutter is dominated by the presence of strong shock waves which can not exist in a potential flow model. Supersonic flutter is governed by shock instabilities which is beyond the scope of small perturbation theory. Prediction of this type of flutter requires an accurate model of the shock wave structure and its movement due to blade vibration.

In the case of stall flutter, either subsonic or transonic, the main mechanism for flutter is the complete or partial flow separation from the blade suction surface [5]. Obviously, this can not be modelled by an attached flow model. Furthermore, prediction of flow separation due to blade vibrations is not possible by linear perturbation models. Therefore, even with a viscous flow model, the traditional methods are unable to predict stall flutter which, in its many guises, is mainly governed by the non-linear aerodynamic reaction to the blade motion [1]. The uncoupled analysis neglects the non-linearity of the unsteady aerodynamic response. Therefore it seems essential that in order to be able to predict the onset of stall flutter, non-linearity of the flow response to blade vibrations and the flow separation should be modelled correctly.

Finally, in the above analysis, it was observed that the traditional method fails to detect the unstalled flutter boundary below the SLS working line. This is expected as this mode of flutter is due to structural mode coupling through the fluid. The above linear method is a single mode analysis hence it is insensitive to flutter due to mode coupling.

Therefore, it appears that the main limitation of the traditional methods is in their inability to model the unsteady flow due to finite amplitude blade vibrations. In reality, the flow field responds in a nonlinear fashion to blade displacements and the numerical simulation of the problem should represent this feature. The uncoupled flutter analysis, in effect, does not simulate the unsteady pressure forces properly and , hence, is unable to predict fan blade flutter. In the following chapter, a flutter prediction model is presented which allows for the nonlinear response of the flow to the structural vibrations by fully accounting for the fluid/structure coupling .

Chapter 3

An Integrated Non-Linear Aeroelastic Model

The thing, not the way, is important, says true wisdom.
Vladimir Nabokov, Lips to Lips

3.0 About this Chapter

The general theory of the integrated modells are given in part 3.1. Structural vibration model is described in part 3.2. A detailed description of the aerodynamic model is provided in part 3.3. Finally, an integrated and non-linear aeroelasticity model, used in this study, is developed in part 3.4.

3.1 Theory

The failure of traditional methods in dealing with non-linear aspects of the flutter phenomenon has highlighted the need for formulating the coupling between the structure and the fluid in a more rigourous fashion. This means avoiding the tendency of considering the two components of the interaction, i.e. the unsteady flow and the structural dynamics, separately despite the obvious advantages of this decoupling in the numerical treatment. The coupling and subsequent simultaneous solution of the flutter problem has its difficulties. A major concern is the historically different modelling techniques used in fluid flow and structural dynamics. Fluid flow modelling is usually based on an Eulerian formulation which does not trace the flow particles but defines a flow field. Therefore, at each point in the flow the dependent variables are defined on a spatially fixed domain through which the flow moves, as shown in figure 3.1a. Structural dynamics modelling, on the other hand, is based on a Lagrangian formulation which means the spatial domain moves with the structure. Therefore, the solution procedure traces each point on the structure and moves with it as shown in figure 3.1b.

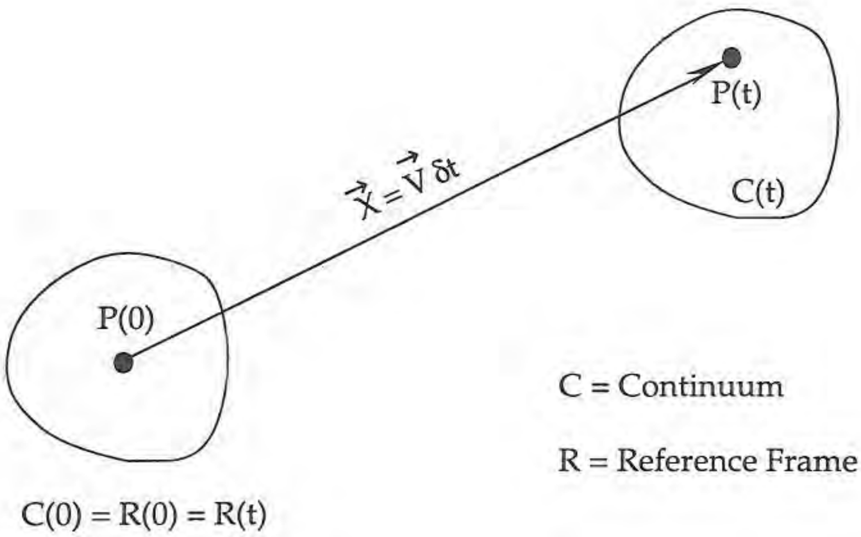

a - Kinematics of Eulerian Modelling

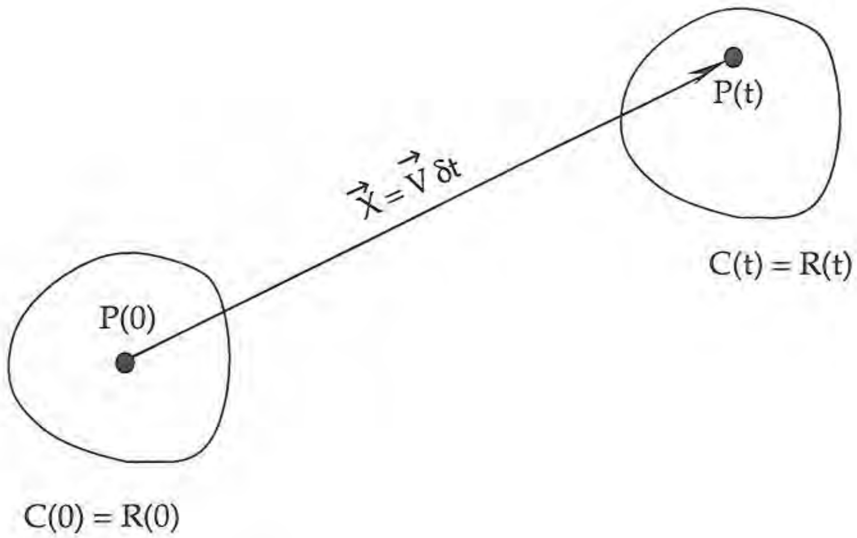

b - Kinematics of Lagrangian Modelling

Figure 3.1 - Different Modelling Terminologies

Evidently, this difference in methodology originates from the difference in the nature of the problems being dealt with. In a coupled or integrated modelling of flutter we would like to retain the advantages pertaining to each approach.

There are at least two different ways of formulating an integrated non-linear flutter model. The first one is a Lagrangian-Eulerian model in which the general formulation is Lagrangian and an Eulerian modification is added to the model to adjust for the fluid convection. A well-known version of this model is the ICED-ALE technique [20-21] in which the solution for structural motion in a fluid flow is advanced iteratively in time using a series of pressure corrections. The main advantage lies in its ability of obtaining a solution in terms of pressure since the coupling between the structure and the fluid is pressure driven. However, the iterative nature of the solution procedure tends to be computationally expensive.

The alternative approach, which will be employed in this work, is an Eulerian-Lagrangian model in which the Eulerian fluid formulation is adjusted by a Lagrangian modification to allow for structural motion. This, unlike the ICED-ALE model, is a direct time-marching model which simplifies the implementation of the compatibility conditions at the fluid-structure interface.

In the following sections, a description of the structural and the fluid flow models are given along with a detailed description of the integrated aeroelasticity model developed.

3.2 Structural Vibration Model

The equations of motion of a structure with N degrees of freedom can be written as [35]:

$$[M]\{\ddot{X}\} + [C]\{\dot{X}\} + [K]\{X\} = \{F\} \tag{3-1}$$

where {F} is a vector containing all the external forces acting on the structure. In flutter calculations this force vector is simply due to the instantaneous fluid pressure acting on the structure.

Although this equation can be used directly in aeroelastic calculations, it is preferable to transform it into N uncoupled structural equations by using a transformation of the form:

$$\{X\} = [\Psi]\,\{q\} \tag{3-2}$$

where the matrix $[\Psi]$ contains the mass-normalised mode shapes of the system described in equation (3-1). Using equations (3-1) and (3-2) one obtains:

$$[\Psi]^T [M]\,[\Psi]\,\{\ddot{q}\} + [\Psi]^T [C]\,[\Psi]\,\{\dot{q}\} + [\Psi]^T [K]\,[\Psi]\,\{q\} = [\Psi]^T \{F\} \tag{3-3}$$

Using the well-known property of modal orthogonality:

$$[\Psi]^T [M]\,[\Psi] = [I] \tag{3-4a}$$

$$[\Psi]^T [C]\,[\Psi] = 2\,\zeta\,[\omega] \tag{3-4b}$$

$$[\Psi]^T [K]\,[\Psi] = [\omega^2] \tag{3-4c}$$

the final form of the equation of motion in the generalised co-ordinates becomes:

$$\{\ddot{q}\} + 2\,\zeta\,[\omega]\,\{\dot{q}\} + [\omega^2]\,\{q\} = [\Psi]^T\{F\} \tag{3-5}$$

Equation (3-5) is a second-order equation in time. This form of the structural model is not compatible with the final form of the fluid flow model which are of order one in time. Therefore, equation (3-5) must be broken down into a set of first-order differential equations, as follows:

$$\frac{\partial}{\partial t}\{\dot{q}\} = [\Psi]^T\{F\} - 2\,\zeta\,[\omega]\{\dot{q}\} + [\omega^2]\,\{q\} \tag{3-6a}$$

$$\frac{\partial}{\partial t}\{q\} = \{\dot{q}\} \tag{3-6b}$$

The main advantage of using as modal representation lies in its amenability to reduction: one can retain any number of modes from the full modeshape matrix $[\Psi]$ and hence reduce the computational effort.

However, it should be stressed that the use of the modal model of structural vibrations means that mass, stiffness and damping properties of the structure in equation (3-1) are constant and do not vary in time, i.e. the structure is linear. Although, this might be valid when structural displacements are small, it remains only an approximation.

3.3 Aerodynamic Model

3.3.1 Fluid Flow in Turbomachinery

One of the main difficulties in turbomachinery aeroelasticity analyses is the transonic nature of the fluid flow encountered. The term "transonic flow" refers to flow regimes in which subsonic and locally supersonic regions are both present in the flow domain. In most cases, the supersonic pocket is terminated with a shock wave across which there is a large change in flow properties. Transonic flows are nonlinear and, as a result, extremely sensitive to slight changes.

In this section we describe the Euler equations as a model for obtaining a more accurate prediction of the flow field in a coupled aeroelastic analysis.

3.3.2 Equations of Fluid Flow

The fundamental equations of fluid dynamics are based on the following three conservation laws [36]:

I. Conservation of Mass,
II. Conservation of Momentum, and
III. Conservation of Energy.

The equation that results from implementing the Conservation of Mass law to a fluid is the continuity equation. Applying the Conservation of Momentum law to fluid flow results in a vector equation known as the momentum equation. The Conservation of Energy law, which is another form of the First Law of Thermodynamics, leads to the energy equation in the fluid domain. In addition to these equations, it is required to close the system of equations by establishing a relationship between various fluid properties, usually, the equation of state which relates the thermodynamic variables pressure (P), density (ρ) and temperature (T).

The Conservation of Mass law applied to a fluid passing through an infinitesimal, *fixed* control volume (see figure 3.2) yields the following equation of continuity:

$$\frac{\partial \rho}{\partial t} + \nabla \bullet (\rho \mathbf{V}) = 0 \tag{3-7}$$

where ρ is the fluid density and $\mathbf{V}$ is the fluid velocity. The first term in the equation represents the rate of density increase in the control volume and the second term represents the rate of mass flux passing out of the control surface per unit volume. For a Cartesian co-ordinate system, where u,v represent the x,y components of the velocity vector, equation (3-7) becomes:

$$\frac{\partial \rho}{\partial t} + \frac{\partial}{\partial x}(\rho u) + \frac{\partial}{\partial y}(\rho v) = 0 \tag{3-8}$$

Newton's Second Law applied to a fluid passing through an infinitesimal, fixed control volume results in the following momentum equation:

$$\frac{\partial}{\partial t}(\rho \mathbf{V}) + \nabla \bullet \rho \mathbf{V}\mathbf{V} = \rho \mathbf{f} \tag{3-9}$$

The first term in this equation represents the rate of momentum increase per unit volume in the control volume. The second term represents the rate of momentum lost by convection (per unit volume) through the control surface. The right-hand side term is the body force per unit volume.

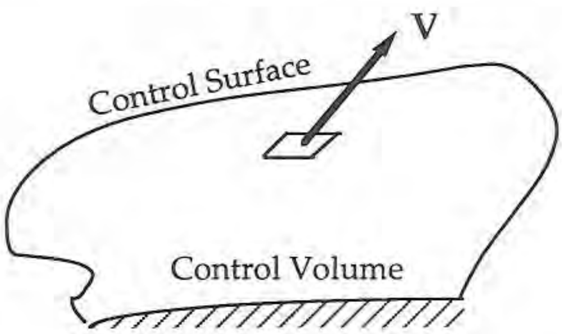

Figure 3.2 - Fixed Control Volume (Eulerian methodology)

Using equations (3-8) and (3-9), the momentum equation can be written in the Cartesian co-ordinate system as

$$\frac{\partial \rho u}{\partial t} + \frac{\partial}{\partial x}(\rho u^2 + p) + \frac{\partial}{\partial y}(\rho uv) = \rho f_x \tag{3-10a}$$

$$\frac{\partial \rho v}{\partial t} + \frac{\partial}{\partial x}(\rho uv) + \frac{\partial}{\partial y}(\rho v^2 + p) = \rho f_y \tag{3-10b}$$

The First Law of Thermodynamics applied to a fluid passing through an infinitesimal, fixed control volume results in the following energy equation

$$\frac{\partial \rho E}{\partial t} + \nabla \bullet \rho E \mathbf{V} = \frac{\partial Q}{\partial t} + \rho \mathbf{f} \bullet \mathbf{V} \tag{3-11}$$

where E is the total energy per unit mass and is equal to:

$$E = I + \frac{1}{2} V^2 \tag{3-11a}$$

and I is the internal energy per unit mass.

The first term on the left-hand side of the equation (3-11) represents the rate of increase of total energy per unit volume in the control volume while the second term shows the rate of total energy lost by convection through the control surface. The first term on the right-hand side shows the rate of heat applied to the control volume while the second term represents the work done on the control volume by the body forces. For a Cartesian co-ordinate system, equation (3-11) becomes

$$\frac{\partial \rho E}{\partial t} - \frac{\partial Q}{\partial t} - \rho(f_x u + f_y v) + \frac{\partial}{\partial x}(\rho E u + p u) + \frac{\partial}{\partial y}(\rho E v + p v) = 0 \tag{3-12}$$

In order to close the system of fluid dynamic equations it is necessary to form a relationship between the thermodynamic variables. Here we assume that the fluid is a perfect gas and the form of the equation state to be used can be written as follows:

$$p = (\gamma\text{-}1)\,\rho\, I \quad \text{and} \quad T = \frac{(\gamma\text{-}1)\, I}{R} \tag{3-13}$$

where $\gamma = \frac{c_p}{c_v}$ is the ratio of the specific heats and R is the gas constant.

3.3.3 Lagrangian-Eulerian Model of Fluid Flow

Equations (3-8), (3-10) and (3-12) constitute the basic fluid flow model used in this work. These equations are formed based upon the assumption of an Eulerian flow model. This implies that the control volumes are fixed in space and flow is convected across their boundaries. For the purpose of an aeroelasticity analysis this is not a satisfactory model since solid boundaries (i.e. the structure), and with them the control volumes, are in motion. Therefore, a

Lagrangian modification of the equations of the flow must be implemented which means vertices of control volumes are allowed to move in time.

Figure 3.3 shows the effect of this modification in the case of a one-dimensional flow. If the control volume for node P is fixed in space, any flow variable ϕ is convected across the boundary (w) at a relative speed of u. However, if the control volume surface is moving at a speed x_t, then ϕ is convected across (w) at a relative speed of $(u-x_t)$. For $x_t=u$, the model is called Lagrangian. This is equivalent to the discretization methodology used for the structural dynamics, i.e. mass of each control volume contains a fixed mass of fluid.

Implementing this modification in the system of Euler equations and re-writing these equations in a more convenient vector form results in the following:

$$\frac{\partial \mathbf{U}}{\partial t}+\frac{\partial \mathbf{E}}{\partial x}+\frac{\partial \mathbf{F}}{\partial y}=0 \tag{3-14}$$

where **U**, **E**, **F** are vectors given by

$$\mathbf{U}=\begin{bmatrix}\rho\\ \rho u\\ \rho v\\ \rho E\end{bmatrix} \qquad \mathbf{E}=\begin{bmatrix}\rho(u-x_t)\\ \rho u(u-x_t)+p\\ \rho v(u-x_t)\\ \rho E\,(u-x_t)+pu\end{bmatrix} \qquad \mathbf{F}=\begin{bmatrix}\rho(v-y_t)\\ \rho u(v-y_t)\\ \rho v(v-y_t)+p\\ \rho E\,(v-y_t)+pv\end{bmatrix}$$

and x_t , y_t are the Cartesian velocity components of the moving control volume surface.

The derivation of equations (3-14) described above, is equivalent to a general transformation of the fixed coordinate system to a moving coordinate system given by:

$$\mathbf{x}=\mathbf{x}\,(x,y,t), \quad \mathbf{y}=\mathbf{y}\,(x,y,t), \quad \mathbf{t}=t \tag{3-15}$$

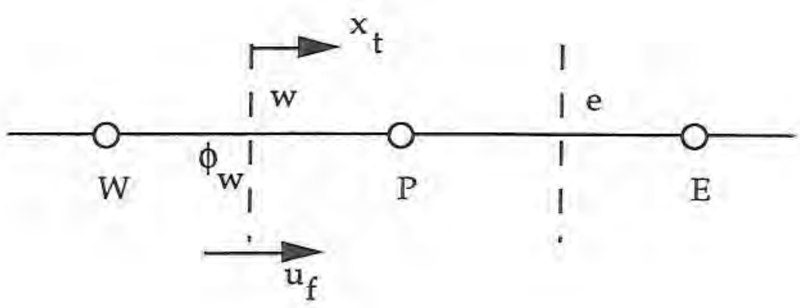

a) Eulerian if $x_t = 0$: Flux across (w) = $\rho u_f \phi_w$

b) Mixed if $x_t \neq 0$: Flux across (w) = $\rho(u_f - x_t) \phi_w$

c) Lagrangian if $x_t \neq 0 = u_f$: Flux across (w) = 0

Figure 3.3 - Grid-point cluster for one-dimensional flow

3.3.4. Discretization of Flow Equations

The discretization of the fluid equations are performed on a structured quadrilateral mesh. The mesh itself can be C-, H- or O-type, although no calculations have been performed on the last type, the key point being that the fluid discretization does not assume any specific type of mesh. The fluid mesh is generated separately by using a standard elliptic mesh generator with forcing terms at the solid boundaries for a nearly-orthogonal mesh, as described in reference [37].

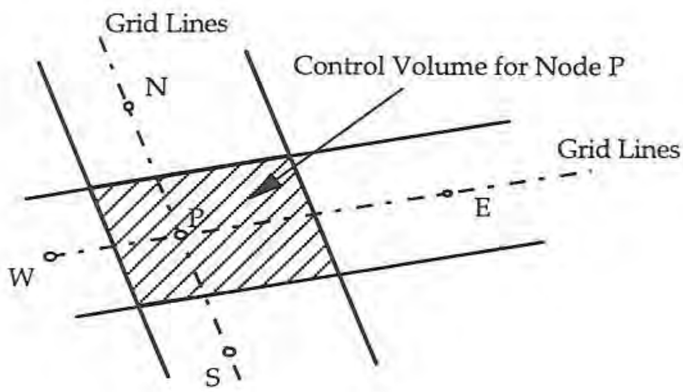

Figure 3.4 - A typical control volume

The discretization procedure follows closely that proposed by Jameson et al. [38]. An integral form of the flow equations (also known as weak conservation form) is formed for a typical cell (or control volume) such as that shown in figure 3.4. This is performed by first transferring the flow equations from the physical domain (x,y,t) into the generalised body fitting co-ordinates (ε,η,t) as shown in figure 3.5, the transformation matix being:

$$(x,y,t) = [\,J\,]\,(\varepsilon,\eta,t) \tag{3.16}$$

In practice the above relationship cannot be established explicitly, hence the inverse of the Jacobian transformation is used, i.e.

$$(\varepsilon,\eta,t) = J^{-1}\,(x,y,t) \tag{3.16a}$$

or, equivalently

$$\begin{Bmatrix} \varepsilon \\ \eta \\ t \end{Bmatrix} = \begin{bmatrix} x_\varepsilon & x_\eta & 0 \\ y_\varepsilon & y_\eta & 0 \\ 0 & 0 & 1 \end{bmatrix} \begin{Bmatrix} x \\ y \\ t \end{Bmatrix} \tag{3.16b}$$

This allows the numerical solution to be performed on a uniformly spaced computational grid. The form of the fluid flow equations in the computational domain, derived from (3-14), are as follows:

$$\frac{\partial\,(S \cdot \rho)}{\partial t} + \sum \{\, \rho U_c + \rho V_c \,\} = 0 \tag{3-17a}$$

$$\frac{\partial\,(S \cdot \rho u)}{\partial t} + \sum \{\, (\rho u U_c + p\beta_{11}) + (\rho u V_c + p\beta_{12}) \,\} = 0 \tag{3-17b}$$

$$\frac{\partial\,(S \cdot \rho v)}{\partial t} + \sum \{\, (\rho v U_c + p\beta_{21}) + (\rho v V_c + p\beta_{22}) \,\} = 0 \tag{3-17c}$$

$$\frac{\partial\,(S \cdot \rho E)}{\partial t} + \sum \{\, (\rho E U_c + p(u\beta_{11} + v\beta_{12})) + (\rho E V_c + p(u\beta_{21} + v\beta_{22})) \,\} = 0 \tag{3-17d}$$

where

$$S = \text{Area of control volume} = J^{-1}$$

$$U_c = J^{-1}\,\{\, (u - x_t)\varepsilon_x + (v - y_t)\varepsilon_y \,\}$$

$$V_c = J^{-1}\,\{\, (u - x_t)\eta_x + (v - y_t)\eta_y \,\}$$

and

$$\beta_{11} = J^{-1}\varepsilon_x \quad \beta_{12} = J^{-1}\varepsilon_y \quad \beta_{21} = J^{-1}\eta_x = \beta_{12} \quad \beta_{22} = J^{-1}\eta_y$$

Discretization is usually based on cell-centred or cell-vertex schemes. In a cell-centred scheme, flow variables are not stored at the vertices of the fluid grid, but in the middle of each grid cell which acts as the control volume, as shown in figure 3.6. This means that the flow variables, especially pressure, are not calculated on the fluid/structure interface but extrapolated from inside the flow domain. Such an approximation is incompatible with the spirit of an integrated aeroelasticity analysis method as the pressure surface distribution is the coupling mechanism between the structure and the fluid. Consequently, the fluid flow discretization is performed using a cell-vertex scheme which means a direct solution of the flow on solid surfaces. So the computations are carried out on a grid lattice as shown in figure 3.7. where the nodes are defined at grid intersections. There are various options as how to locate the fluid variables on this mesh. The strategy adopted in this work is a non-staggered arrangement in which all the depedent variables are stored at the grid nodes. This approach leads to de-coupling of pressure and velocities in incompressible flow, however, in turbomachinery cases the flow is invariably compressible (M>0.3) a feature that ensures the adequacy of the non-staggered arrangement adopted. The spatial integration performed on the computational grid consists of forming all the terms in the equations (3-17) on the control volumes surfaces and adding them together.

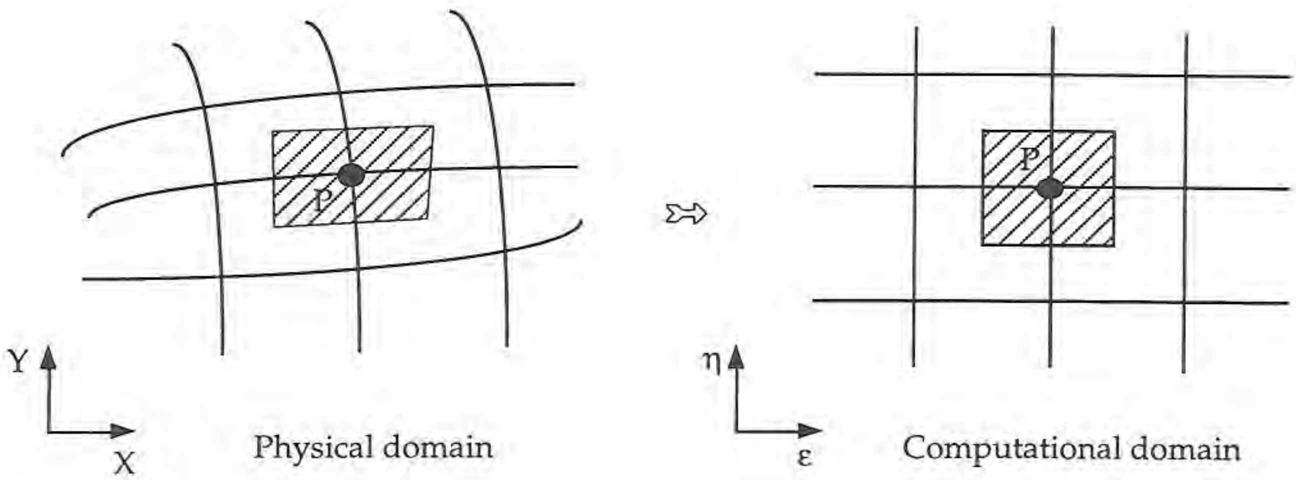

Figure 3.5 - Transformation from physical to computational domain

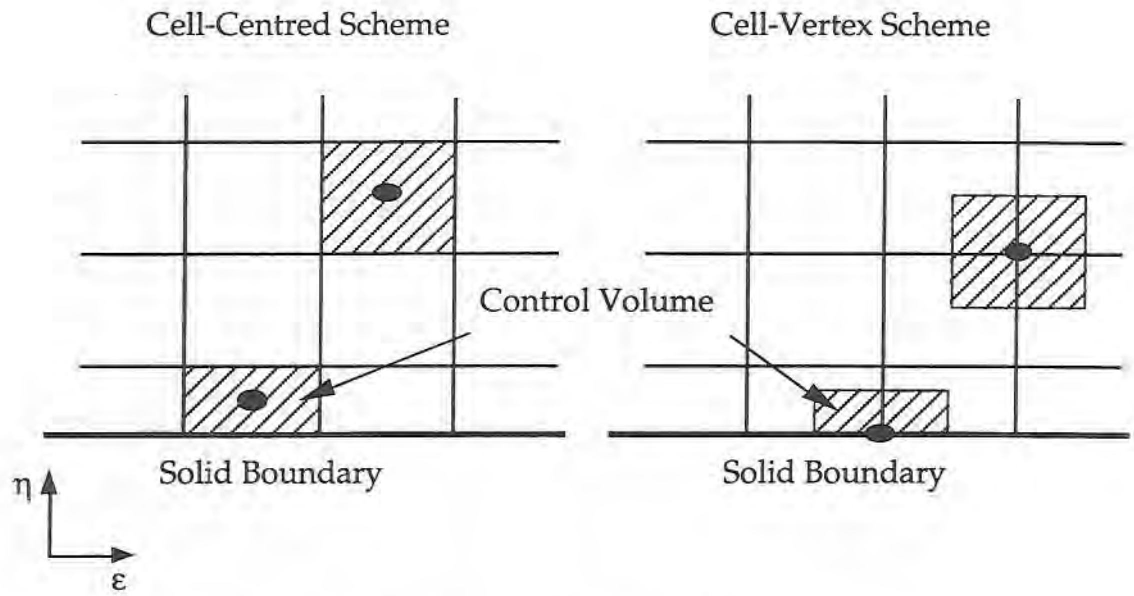

Figure 3.6 - Cell-Centred vs. Cell-Vertex schemes

It is important to note that the Jacobians required for this transformation do not appear explicitly in the discretization process and performing calculations in the computational domain does not produce any additional "errors".

To calculate the fluxes and pressure forces, flow variables are required on each boundary of the control volumes. These are obtained by averaging flow variables on either side of the boundary. Refering to figure 3.8, velocities on face (n) are

$$u_n = 0.5\,(\,u_P + u_N) \tag{3-18a}$$

similarly

$$v_n = 0.5\,(\,v_P + v_N). \tag{3-18b}$$

Higher forms of averaging such as:

$$u_n = \frac{0.5\,(\,\rho_P^{0.5}\,u_P + \rho_N^{0.5}\,u_N)}{\rho_P^{0.5} + \rho_N^{0.5}} \tag{3-18c}$$

which takes into account the compressibility of the flow can also be considered. but no noticable improvements in the results are observed.

The resulting velocities on the each face of the computational cell are subsequently used to obtain the contra-variant velocities on each face. So, for face (n), The following results

$$(\beta_{11})_n = J^{-1}\,\varepsilon_x = (x_{ne} - x_{nw})$$

$$(\beta_{12})_n = J^{-1}\,\varepsilon_y = (y_{ne} - y_{nw})$$

$$(\beta_{21})_n = \text{not used}$$

$$(\beta_{22})_n = \text{not used}$$

$$(U_c)_n = (\beta_{11})_n(u - x_t)_n + (\beta_{12})_n(v - y_t)_n, \; (V_c)_n = 0$$

shouldn't be here because of [illegible]

Similarly at face (e)

$$(\beta_{11})_e = \text{not used}$$

$$(\beta_{12})_e = \text{not used}$$

$$(\beta_{21})_e = J^{-1}\,\varepsilon_x = (x_{ne} - x_{se})$$

$$(\beta_{22})_e = J^{-1}\,\varepsilon_y = (y_{ne} - y_{se})$$

$$(U_c)_e = 0$$

$$(V_c)_e = (\beta_{21})_e(u - x_t)_e + (\beta_{22})_e(v - y_t)_e$$

The area of the control volume, i.e. the determinant of the Jacobian matrix $|J^{-1}|$, is

$$S_P = \frac{1}{2}\,|\,(x_{ne} - x_{sw})(y_{nw} - y_{se}) - (x_{nw} - x_{se})(y_{ne} - y_{sw})\,| \qquad (3\text{-}19)$$

The resulting flux at face (n) is therefore determined as follows:

$$FLUX_n = (U_c)_n \cdot \Phi_n \qquad (3\text{-}20)$$

where Φ_n is the value of the dependent variable on face (n), defined as

$$\Phi_n = \frac{1}{2}(\Phi_P + \Phi_N). \qquad (3\text{-}21)$$

The procedure for calculating the pressure forces is exactly the same. Again pressures on the boundaries of the control volume are determined by simple averaging.

The explicit discretization of the fluid flow equations in the spatial domain reduces the system of equations (3-17) to a set of ordinary differential equations of the form:

$$\frac{d}{dt}\{ S. \Phi_P \} + F(\Phi_P) - D(\Phi_P) = 0 \qquad (3\text{-}22)$$

where Φ_P is the dependent variable being solved for at grid node P, F is the net flux out of the cell and the resultant of pressure forces, and D is the numerical dissipation (see below).

Since a central-differencing technique is employed to calculate the value of Φ_n, some form of numerical diffusion is required to avoid spurious numerical oscillations in the vicinity of the shocks and large gradients. This is provided by a dissipative term of order one (i.e. order of accuracy in the spatial discretization on the **computational** grid) which is added in the vicinity of shock waves. Furthermore, to avoid odd-even de-coupling, an extra term consisiting of fourth-order spatial differences must be added to the model. This extra term has an order of accuracy of three (based on Taylor series truncation error (TSTE) in the computational grid) and does not affect the accuracy of the spatial discretization which is not greater than two (again based on TSTE). The mechanism of adding these diffusive terms is as follows [39]

$$\text{Numerical dissipation} \equiv \; D(\Phi) = \varepsilon^{(2)} \frac{S}{\delta t} \nabla^2 \Phi + \varepsilon^{(4)} \frac{S}{\delta t} \nabla^4 \Phi \qquad (3\text{-}23)$$

where δt is the local allowable time step based on convective fluxes.

The differential form of the equation (3-23) is given for the sake of brevity. In applying these to the numerical model, an integral form of the dissipation is employed to be consistent with the weak conservation form of the discretized equations of motion. This is essential for obtaining a correct position of the shock waves in transonic calculations.

Numerical dissipation should be of first-order near a shock and of second-order in the smooth regions of the flow. This is achieved by taking into account the pressure variations when evaluating the coefficients of the dissipation terms in equation (3-23). For example, at face (e) of the control volume shown in figure 3.8, these coefficients can be determined as:

$$\varepsilon^{(2)} = k^{(2)} \max (\upsilon_{EE}, \upsilon_{E}, \upsilon_{P}, \upsilon_{W}) \tag{3-24}$$

where

$$\upsilon_P = \left| \frac{p_E - 2\, p_P + p_W}{p_E + 2\, p_P + p_W} \right| \tag{3-25}$$

and p_W is the pressure at grid node P.

Fourth-order differences are switched off at the shock vicinity since their inclusion tends to cause oscillatory behaviour. This is achieved by choosing $\varepsilon^{(4)}$ as follows:

$$\varepsilon^{(4)} = - \max (0 , k^{(4)} - \varepsilon^{(2)}) \tag{3-26}$$

Typical values for the coefficients are $k^{(2)} = 0.25$ and $k^{(4)} = 0.005$. Of couse the actual values are dependent on the specific problem being considered. For lower mesh densities higher values for these coefficients are recommended. ($k^{(2)} = 0.5$ and $k^{(4)} = 0.015$)

This combination of adjusting numerical dissipation components means that at the vicinity of flow gradients, such as shock waves, pressure switch turns on the second-order disspator which itself switches off the fourth-order dissipator according to equation (3-26). This ensures a non-oscillatory shock wave. In the smooth regions of the flow, the pressure switch of equation (3-24) turns off the second-order smoothing and, in turn, the fourth-order smoothing prevents odd-even decoupling in the flow.

The scaling factor of $\frac{S}{\delta t}$ used in the dissipation equation is an isotropic one, though other choices are also possible [40]. An anisotropic scaling factor, which uses the allowable time step in each direction of the body-fitted co-ordinates, gives a better convergence rate for steady flow calculations and it is more stable for unsteady flow calculations. The local time step Δt, used for scaling the numerical smoothing $D(\Phi)$, is for the CFL number of 1. This avoids any dependance of the numerical smoothing on the CFL number chosen for the fluid flow calculations.

So, the final form of the numerical dissipation for face (n) of figure 3.8 is

$$D_e = \frac{S}{\delta t}\{ \varepsilon^{(2)} (\Phi_E - \Phi_P) + \varepsilon^{(4)} (\Phi_{EE} - 3\, \Phi_E + 3\, \Phi_P - \Phi_W) \} \tag{3-27}$$

and the total numerical dissipation at node P becomes

$$D_P = D_n - D_s + D_e - D_w \tag{3-28}$$

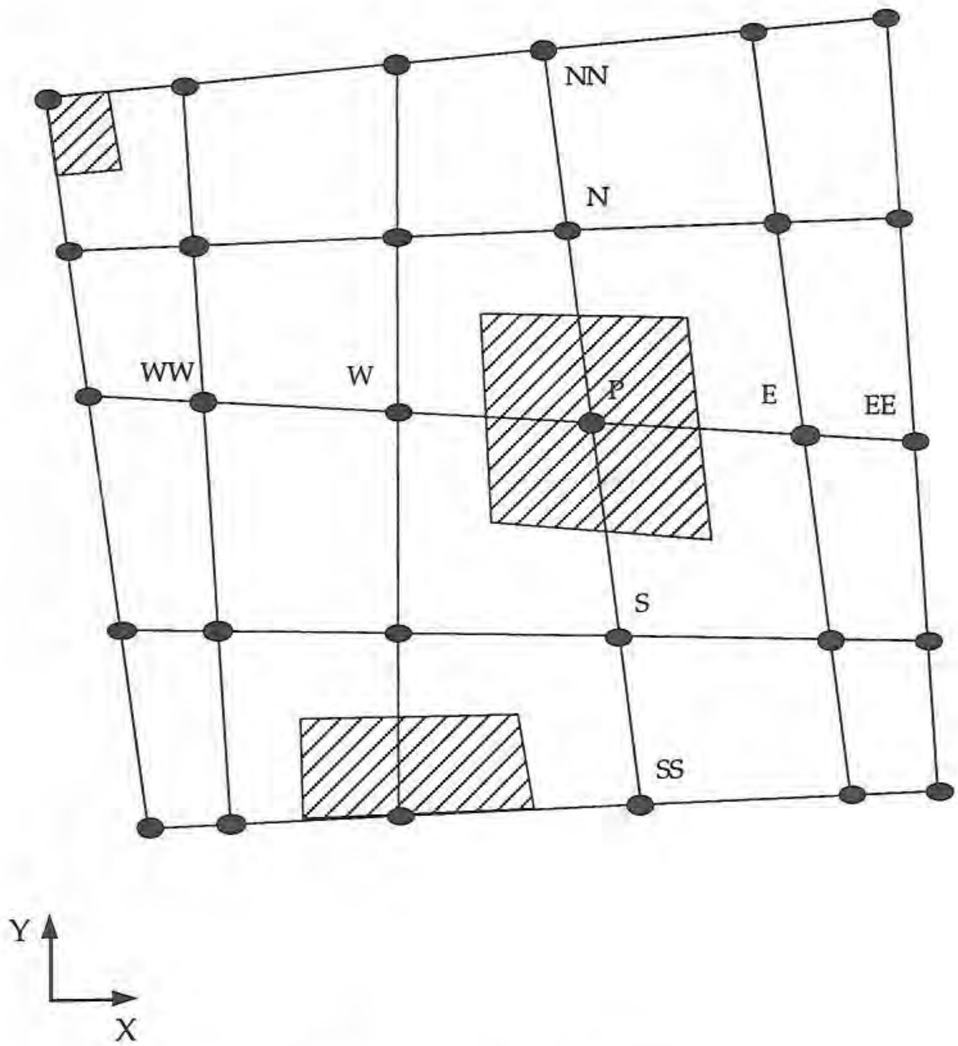

Figure 3.7 - Fluid flow lattice

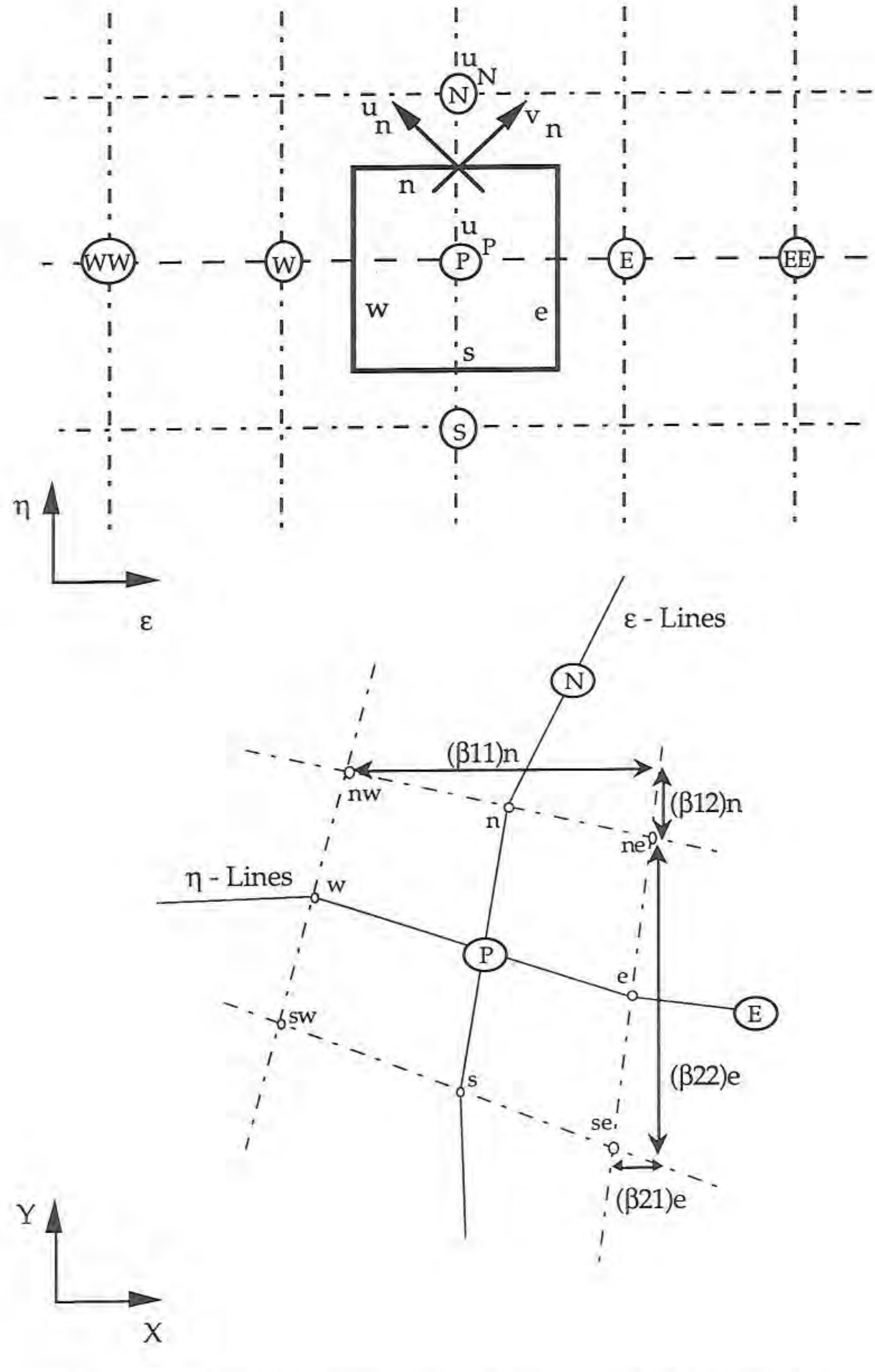

Figure 3.8 - Variable arrangement and geometrical properties

Obviously, the form of numerical dissipation given in (3-27) is not valid at nodes on and adjacent to the computational domain. The proper treatment of numerical dissipation on the boundaries is evidently very crucial for the stability of the overall scheme. The approach adopted here to overcome this problem is to use one-sided differencing on the boundaries. So at node (P), adjacent to the boundary, D_e becomes

$$D_e = \frac{S}{\delta t}\{\, \varepsilon^{(2)}\,(\, \Phi_E - \Phi_P\,) + \varepsilon^{(4)}\,(\, \Phi_E - 2\,\Phi_P + \Phi_W\,)\,\} \tag{3-29}$$

and for a node on the boundary D_e is taken to zero. This amounts to a one-sided differencing for the second-order dissipation on the boundaries and is important is ensuring a stable solution for the fluid flow as reported by Gerolymos[41].

The above scheme is fully dissipative and robust. Pulliam[42] has made an extensive investigation on the possible options for the treament of numerical dissipation on the boundaries of the computational domain. He suggests that the above treatment can be unstable because the matrix comprising the fourth-order numerical dissipation terms, i.e.

$$D^4 = \begin{bmatrix} -1 & +2 & -1 & — & — & — & — & — & — & — \\ +2 & -5 & +4 & -1 & — & — & — & — & — & — \\ -1 & +4 & -6 & +4 & -1 & — & — & — & — & — \\ — & -1 & +4 & -6 & +4 & -1 & — & — & — & — \\ — & — & -1 & +4 & -6 & +4 & -1 & — & — & — \\ — & — & — & -1 & +4 & -6 & +4 & -1 & — & — \\ — & — & — & — & -1 & +4 & -6 & +4 & -1 & — \\ — & — & — & — & — & -1 & +4 & -6 & +4 & -1 \\ — & — & — & — & — & — & -1 & +4 & -5 & +2 \\ — & — & — & — & — & — & — & -1 & +2 & -1 \end{bmatrix} \tag{3-30}$$

has zero eigenvalues since the sum of all the rows of the matrix is zero, so there is at least one zero eigenvalue. (there are in fact two such eigenvalues). Therefore, the dissipation scheme is not fully dissipative. However, the stability analysis in [42] is not very rigorous and, inherently, assumes a uniform mesh and a unifom flow, an unlikely case. Furthermore, the alternatives suggested are all very dissipative. Therefore the form in (3-29) has been retained in this work.

The original intention for flow modelling was to use a standard total variable diminishing (TVD) scheme which does not require any numerical dissipation and is based upon a more physical foundation. However, it was found that TVD schemes tend to increase the computational time by a factor of two. (Partly because the highest multi-stage Runge-Kutta scheme for TVD schemes is the four-stage scheme (RK4) with a CFL value of 2.1, the allowable CFL number for the Jameson scheme being 2.82) The other disadvantage of the TVD scheme is that it is not compatible with residual averaging (chapter 6) which is of utmost importance in reducing the computational time for aeroelasticity calculations. Hence, the central differencing (CD) scheme outlined above is judged to be preferable to the TVD scheme.

The final form of equations (3-22), including the numerical diffusion terms becomes:

$$\frac{d}{dt}\{ S.\,\Phi \} = -F(\Phi) + D(\Phi) \tag{3-31}$$

or

$$S\frac{d}{dt}\{ \Phi \} + \Phi\frac{d}{dt}\{S\} = -F(\Phi) + D(\Phi) \tag{3-32}$$

which results in the following set of ordinary differential equations in terms of the dependant flow variables;

$$\frac{d}{dt}\{ \Phi \} = \frac{1}{S}\,[\,-F(\Phi) + D(\Phi)\,] - \frac{\Phi}{S}\,\frac{d}{dt}\{S\} \tag{3-33}$$

The last term on the RHS of equation (3-33) includes the effect of the change in the fluid mesh due to motion of the structure.

3.4 Aeroelasticity Model

The most important charateristic of an integrated aeroelastic model is its ability to solve the governing fluid/structural equations simultaneously. In the present formulation, the following constraints are used to ensure solution compatibility across the two domains.

(i) There should be a one-to-one correspondence between the fluid and structural nodes at the fluid/structure interface.

(ii) Fluid nodes and structural nodes need to remain attached at all times.

(iii) The system of combined differential equations should be solved together using the same time-marching routine.

The first constraint might seem objectionable. It is a fact that the mesh density required for structural dynamics analyses are much less than that for fluid flow problems. However, in aeroelasticity, the sensitivity of the flow to a poorly defined structural geometry can be severe. Consider, for example, flow past the plate shown in figure 3.9, The resultant unsteady flow past the structure defined by the coarser mesh would be drastically different from what happens in reality. So, what might be considered as an adequate model for a purely structural problem is certainly not proper for aeroelasticity analyses.

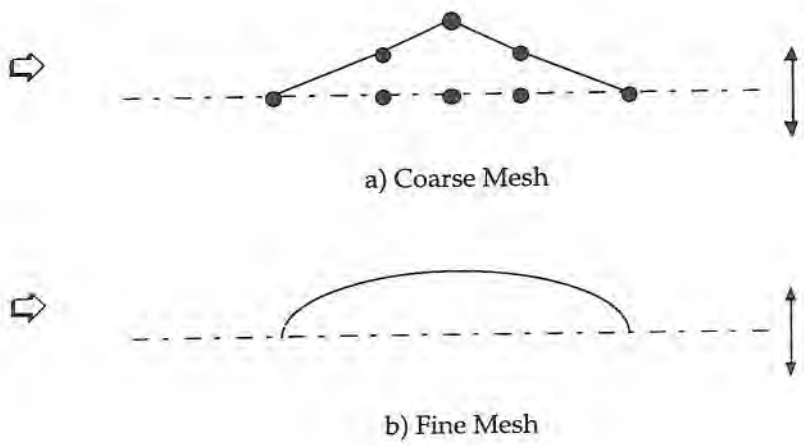

Figure 3.9 - Effect of structural mesh density

This argument supports the case of a fine enough structural grid without meanning identical meshing at the interface. The case of the constraint (i) lies in the satisfaction of the kinetic compatibility at the interface. If there is not a one-to-one correspondence between the two meshes, the computed stresses at the interface for the structure and the fluid will not be the same. The flow provides a pressure profile, such as that shown in figure 3.10 and the structure simply does not see it. Hence, a one-to-one correspondence is an essential feature for an integrated aeroelastic model. This argument also implies that the same shape function should be used in the modelling of the stucture and the flow.

The second constraint is much easier to justify. It ensures the kinematics compatibility at the interface automatically as it means that the fluid and structural velocities should be the same at each instance in time. Therefore, the position and the motion of the interface is automatically defined for the flow.

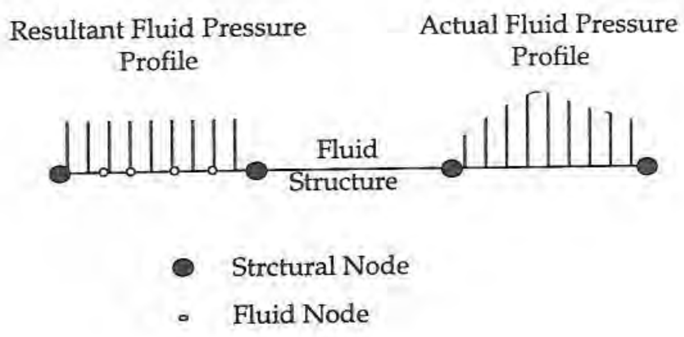

Figure 3.10 - Effect of structural mesh and pressure profile

The final constraint is the most contentious. Various numerical solution techniques, that have been tailored to the specific nature of the structural dynamics models, are available. The same is true of fluid dynamics. It would be natural to solve the fluid and structural parts of aeroelasticity by their own appropriate solvers. Such an approach would mean that the aeroelastic model is not solved directly. However, an iterative strategy would achieve the same result. Let us look at this point in more detail.

Schematically, the aeroelasticity model can be shown in the following form:

$$\begin{bmatrix} \begin{bmatrix} \text{(I)} \\ \text{FLUID FLOW} \\ \text{MODEL} \end{bmatrix} & \begin{bmatrix} \text{(II)} \\ \text{FLUID/STRUCTURE} \\ \text{COUPLING} \end{bmatrix} \\ \begin{bmatrix} \text{(III)} \\ \text{STRUCTURE/FLUID} \\ \text{COUPLING} \end{bmatrix} & \begin{bmatrix} \text{(IV)} \\ \text{STRUCTURAL} \\ \text{MODEL} \end{bmatrix} \end{bmatrix} \begin{Bmatrix} \text{Flow} \\ \text{Variables} \\ \cdots\cdots \\ \text{Structural} \\ \text{Variables} \end{Bmatrix} = 0 \quad (3\text{-}34)$$

The fully-integrated method, proposed here, solves the whole model simultaneously. Therefore, it requires only one solver. The alternative approach, the partially-integrated method, relying on the weak-coupling of fluid and structure (coupling through an interface), breaks (3-34) in to its fluid and structural components, solves them separately, and iterates through this procedure using II and III. Therefore, unlike the fully-integrated method, the partially-integrated method satisfies the fluid and the structural constraints (submatrices I & IV) directly and relies on the iteration process to satisfy the coupling constraints (submatrices II, III) indirectly. An obvious case for such an approach is when an implicit solution technique is used. An implicit and time-accurate solution of equation (3-34) is simply out of the question as there are too many variables. However, implicit solution techniques for fluid or structural problems are used routinely.

Despite the obvious advantages of a partially-integrated method, specially in view of the independent development of structure dynamics and fluid dynamics methods of analysis, this approach is not guaranteed to work in practice. In some cases, iterative techniques either do not reach a converged solution or require a prohibitively large number of iterations. The reason behind this is simple: the fluid model with known structural boundary is a well-posed problem (I). The same is true of the structural model with known fluid loads (IV). The addition of the iterative process, which is an added constraint, makes both these models over-determined. Therefore, a partially-integrated model cannot satisfy the coupling constraints (II & III) completely.

The fully-integrated aeroelasticity model is basically a procedure by which semi-discretized equations (3-6) and (3-33) are solved simultaneously in time to determine the aeroelastic behaviour of the fluid/structure system. This procedure can be divided into three parts :

1. Numerical integration or time-marching,
2. Imposition of boundary conditions and compatibility conditions,
3. Fluid mesh kinematics.

These three components of the solution procedure are described in the following sections.

3.4.1 Time-Marching Solution

The equations of (3-6) and (3-33) can be re-written in the following form :

$$\frac{d}{dt}\{\,\Phi\,\} = R\,(\Phi) \tag{3-35}$$

The system of ordinary differential equations given by (3-35) is solved simulataneously by employing an explicit multi-stage Runge-Kutta (RK) time marching scheme of the form:

$$\Phi^{0} = \Phi^{t=t_o} \tag{3-36a}$$

$$\Phi^{t=t_o+\alpha_i \delta t} = \Phi^{0} + CFL\ \alpha_i\ \delta t\, R_{i-1} \tag{3-36b}$$

$$\Phi^{t=t_o+\delta t} = \Phi^{t=t_o+\alpha_n \delta t} \tag{3-36c}$$

For transient response calculations in which accuracy in time is crucial, a five stage Runge-Kutta scheme (RK5) is found to be ideal. This scheme is second-order accurate in time has a very low level of numerical damping and allows a CFL = 3.2. The coefficients of the five stage RK scheme are as follows:

$$\alpha_1 = \frac{1}{4},\ \alpha_2 = \frac{1}{6},\ \alpha_3 = \frac{3}{8},\ \alpha_4 = \frac{1}{2},\ \alpha_5 = 1.0 \tag{3-37}$$

the value of α_5 has to be unity and the choice of $\alpha_4 = 0.5$ ensures second-order accuracy in time. The values of α_1, α_2 and α_3 are determined from numerical stability considerations.

3.4.1a Stability of Time Integration Process

The stability and damping properties of the RK5 scheme has been investigated by considering the solution of a one-dimensional linear model problem [43-44] of:

$$\frac{\partial \Phi}{\partial t} + c\ \frac{\partial \Phi}{\partial x} + \mu\ \delta x^{3}\ \frac{\partial d^{4}\ \Phi}{\partial^{4} x} = 0 \tag{3-38}$$

which represents the propagation of a wave of speed c with dissipation μ.

Following our solution procedure, equation (3-38) can be reduced to the form of equation (3-35). Considering a solution of the form $\Phi(x,t) = e^{ipx}$ and applying (3-36) for one time step yields:

$$\Phi^{n+1} = A(z)\ \Phi^{n} \tag{3-39}$$

and

$$z = -\lambda\ i \sin(\Omega) - 4\ \lambda\ \mu\ (1 - \cos(\Omega))^{2} \tag{3-39a}$$

with

$$\lambda = \frac{c \cdot \delta t}{\delta x} \qquad \text{and} \qquad \Omega = p\,\delta x \tag{3-39b}$$

where z is the Fourier residual and A(z) is the amplification factor.

[note:

To arrive at the equations (3-39a) one should first discretize the model problem (3-38) on a uniform mesh, i.e.

$$\frac{d}{dt}\Phi_i + c \cdot \frac{1}{2\delta x}(\Phi_{i+1} - \Phi_{i-1}) + \frac{\mu}{\delta x}(\Phi_{i+2} - 4\Phi_{i+1} + 6\Phi_i - 4\Phi_{i-1} + \Phi_{i-2}) \tag{E3-1}$$

Derivation of the discretized form for the convective part is as follows:

$$\begin{aligned} \Phi_{i+1} - \Phi_{i-1} &= e^{ip(x+\delta x)} - e^{ip(x-\delta x)} \\ &= \{ \sin(px+\Omega) + i\cos(px+\Omega) \} - \{ \sin(px-\Omega) + i\cos(px-\Omega) \} \\ &= \{ \sin(px+\Omega) - \sin(px-\Omega) \} + i\{ \cos(px+\Omega) - \cos(px-\Omega) \} \\ &= \{ 2\sin(\Omega)\cos(px) \} - i\{ 2\sin(\Omega)\sin(px) \} \\ &\cancel{= 2A\sin(\Omega)\{\cos(px) - i\sin(px)\}} \\ &= 2i\sin(\Omega)\{-i\cos(px) + \sin(px)\} \end{aligned} \tag{E3-2}$$

got the sign wrong?

$$\Phi_{i+1} - \Phi_{i-1} = 2i\sin(\Omega)\,e^{ipx}$$

$$\Phi_{i+1} - \Phi_{i-1} = 2i\sin(\Omega)\,\Phi_i \tag{E3-3}$$

therefore,

$$c \cdot \frac{1}{2\delta x}(\Phi_{i+1} - \Phi_{i-1}) = i\,\frac{c}{\delta x}\sin(\Omega)\,\Phi_i \tag{E3-4}$$

which after being multiplied by the time step the expression given in (3-39a) results as $\frac{c\,\delta t}{\delta x}$ is the CFL number or λ.]

For the RK5 scheme with above coefficients the amplification factor becomes:

$$A(z) = 1 + z + \frac{1}{2}z^2 + \frac{3}{8}\cdot\frac{1}{2}\cdot z^3 + \frac{1}{6}\cdot\frac{3}{8}\cdot\frac{1}{2}\cdot z^4 + \frac{1}{4}\cdot\frac{1}{6}\cdot\frac{3}{8}\cdot\frac{1}{2}\cdot z^5 \tag{3-40}$$

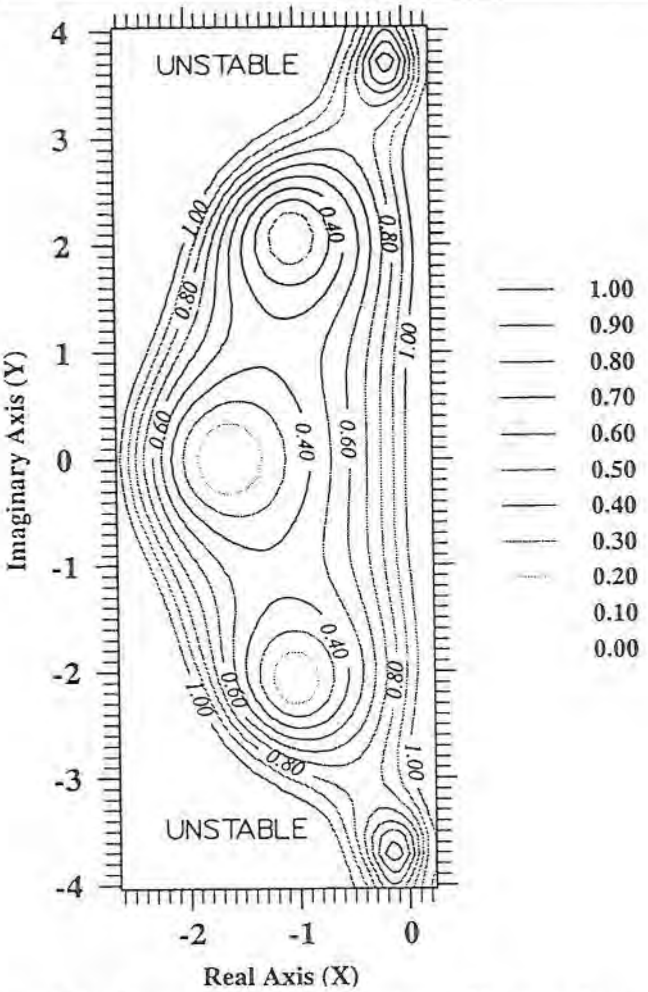

Figure 3.11 - Stability of five-stage Runge-Kutta scheme

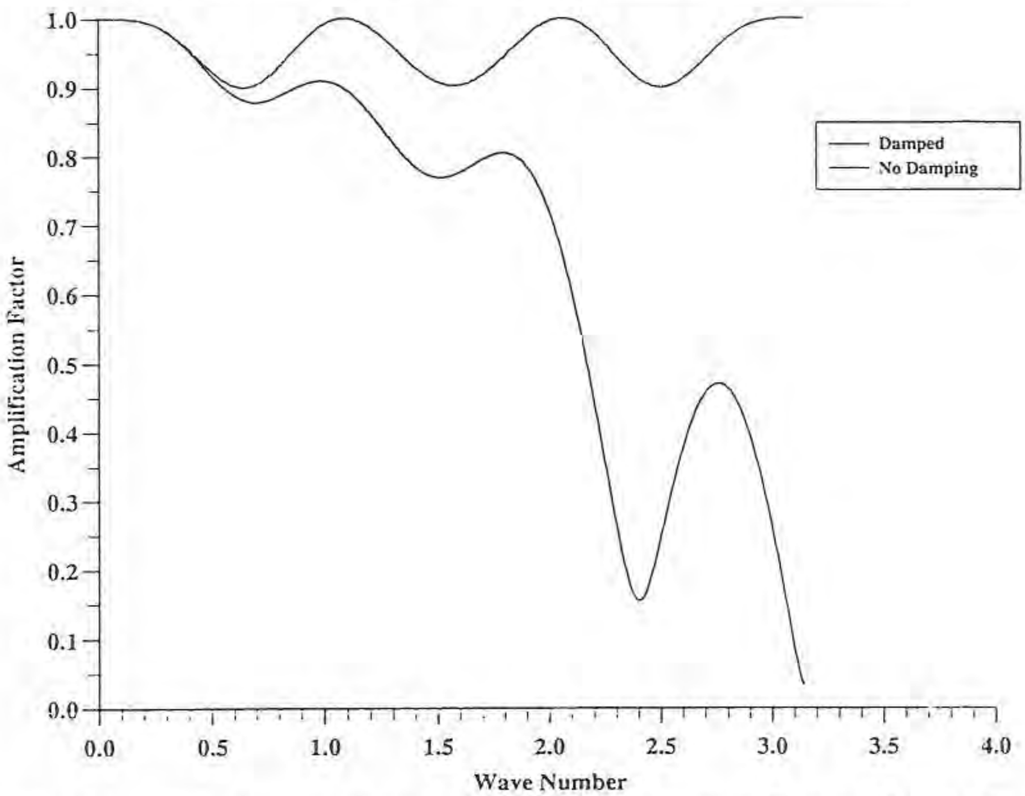

Figure 3.12 - Amplification factor diagram for five-stage Runge-Kutta scheme

The stability of the RK5 scheme is ensured if $| A(z) | \leq 1$. Stability region for the RK5 scheme is shown in figure 3.11 in the ($z = x + i\,y$) plane ($x=\mathrm{Re}(z)$ and $y = \mathrm{Im}(z)$). It can be seen that for an (x) value of about -0.01 (i.e. ~ $-4\,\lambda\,\mu = -0.01$) which corresponds to ($\mu \approx 0.005$), which is typical of fluid discretization techniques, the corresponding (y) value , i.e. λ, is 4.0. Therefore the maximum allowable CFL number is about 4 for the model problem of (3-38). The non-linearity of the Euler equations means that the above analysis is only an estimate. A typical CFL value of 3.2 is what has been generally agreed upon in the literature.

For the structural part of the aeroelastic model, there is usually no damping present, i.e. ($\mu = 0$). For an undamped system the stability limit (where y-axis cuts the $| f(z) | = 1$ contour) is considerably less (~ 3).

Figure 3.12 shows a graph of the amplification factor against the wave number (p), for different values of damping represented by μ. It can be seen that, for a system with a small amount of damping, the time-marching scheme is always stable. Furthermore, lower wave numbers are not damped at all ($| A(z) | = 1$) while higher wave numbers which are artifacts of the discretization process and not representative of the behaviour of the differential equations are damped out strongly.

However, for an undamped system, although the RK5 scheme is stable at the CFL number of 3.2, it has the disadvantage of retaining the large wave numbers undamped. This does not matter if a modal representation of the structure is used, as it is in this work, however, for a full non-linear structural model this difficulty is significant. In the latter case, some form of damping needs to be incorporated in the structural model, if only to make the solution stable.

3.4.1b Time Step Limit

The allowable time step δt is determined from the minimum amount of time required for flow information pass across one computational cell (CFL condition), i.e. for a one-dimensional flow:

$$\delta t \leq \mathrm{CFL} \cdot \min \left(\frac{S}{c.L + |U|} \right) \tag{3-41}$$

where U is the local contra-variant velocity, S is the control volume area , L is the length of the control volume side perpendicular to U and c is the local speed of sound. Furthermore, δt is also limited by the largest natural frequency (ω_{max}) retained in the structural modal representation. i.e.

$$\delta t \leq 0.03 \cdot CFL \cdot \frac{2\pi}{\omega_{max}} \tag{3-42}$$

In most computations, however, the value for δt is determined from equation (3-41) which is in fact very restrictive. Obviously, it is advantageous if the allowable time step could be determined from purely accuracy considerations. There are several strategies for relaxing the above constraints by adding a degree of implicitness to the solution procedure. Two of the more recognised strategies, known as "residual averaging" and "muti-grid" [45-47], have been incorporated in this work and will be discussed in chapter 6.

3.4.2 Boundary Conditions

There are two types of boundary conditions to be imposed; the first is the purely fluid or structural boundary conditions and the other is the compatibility conditions At the fluid/structure interface.

In terms of the fluid boundary conditions, at solid boundaries, the no-flow through condition is imposed. The no-flow through condition is imposed simply by setting the contra-variant velocity in the direction normal to the wall to zero.

In the far-field boundaries, non-reflective boundary conditions, based on the assumption of one-dimensional flow, are assumed [47,48]. This treatment is adequate as long as shocks do not cross the boundary a phenomenon which causes a weak reflection. The full details of the non-reflective boundary conditions are given in the addendum at the end of this chapter.

The final form of the non-reflective boundary conditions is somewhat different from the rest of the fluid domain, as they are deduced in terms of the primitive variables unlike the interior of the flow domain. Hence, originally, the updating of the farfield boundary values were performed separately by a simple explicit Euler scheme at the end of each time step [45]. This approach, although convenient, tends to cause considerable difficulties, especially during steady flow calculations. The effect of this two type integration is that convergence rate on the farfield boundary is much slower than that in the interior domain. Therefore, it is necessary to implement the non-reflective boundary conditions at the end of **each stage** of the RK scheme and using the same time integration for the entire domain.

The other set of boundary conditions is that of fluid/structural coupling through pressure forces. As there is a one-to-one correspondence between the structural and fluid nodes, it is tempting to define the pressure load on the structure at any node by multiplying the pressure at that node by the fluid control volume surface at that node. Using such an approach, the force at node (i) in figure 3.13 becomes:

$$F_i = P_i \cdot \delta S_{cv} \tag{3-43}$$

However, such an integration process is very inaccurate since the force at node (i) does not see the effect of pressures at the neighbouring nodes and, conversely, the pressure force at node (i+1) is not converted to a corresponding force at node (i).

The force acting on the structure should be determined from multiplying the pressure acting on each surface by the area of that surface. (for two-dimensional models the surface being a length) This force is then distributed among the relevant structural nodes, using the shape function of the structural element concerned, i.e.

$$F_S = \int H_S^T \, P \, dS \tag{3-44}$$

where H_S^T is the transpose of the surface shape function.

3.4.3 Fluid Mesh Kinematics

In order to conform to the instantaneous shape of the deforming structure and at the same time retain the quality of the fluid mesh, it is necessary to deform the fluid mesh as the time-marching solution proceeds. Of course, if the structure is rigid, or has a very small motion, such a process can be avoided. However, in the general case, blades are not rigid and the amplitude of structural vibrations is not known prior to the analysis.

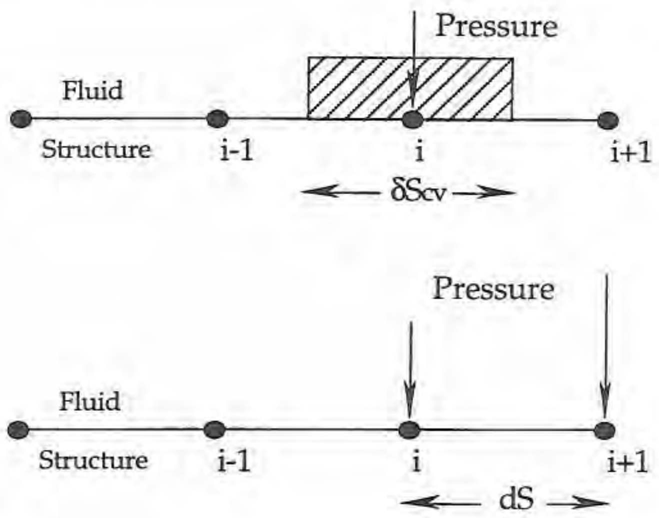

δScv = Fluid Control Volume Surface
dS = Structural Surface Area

Figure 3.14 - Fluid pressure force on structure

It is of utmost importance that the mesh kinematics retains the quality of the fluid mesh and that the deforming mesh movement algorithm is computationally efficient. In this work a deforming mesh algorithm developed by Robinson et. al. [49] has been employed. This algorithm is of high quality, and robust, however, its main drawback is its somewhat high storage requirement.

The basic idea behind the algorithm is to model the fluid mesh as a spring network where each cell side is represented by a linear spring. The stiffness of each spring is inversely proportional to a specified power of the length of that edge. For an edge between two nodes i and i+1 The stiffness $k_{i,i+1}$ is given by:

$$k_{i,i+1} = [\,(x_{i+1} - x_i)^2 + (y_{i+1} - y_i)^2\,]^{-p} \tag{3-45}$$

Value of p is usually between 1 and 1.5.

The process for moving the mesh is as follows. At each time step, the instantaneous position and velocity of the boundary points are known. Points on the outer boundaries are usually held fixed, while those on the surface of the structure have the same kinematic conditions as the structural nodes to which they are attached. The object is to move the inner nodes according to these boundary constraints. The displacements on the interior fluid nodes are determined by solving the static equilibrium equations resulting from a "force" summation at each node. To accelerate the convergence of this process, the solution is first approximated by using an initial guess, such as:

$$\delta \overset{*}{x}_{t+\delta t} = \dot{x}_t \, \delta t$$
$$\delta \overset{*}{y}_{t+\delta t} = \dot{y}_t \, \delta t \tag{3-46}$$

These displacements are then corrected using several Jacobi iterations of the static equlibrium equations written as:

$$\delta x_{i,j} = \frac{\sum_{j=1}^{4} \sum_{i=1}^{4} k.\delta x}{\sum_{j=1}^{4} \sum_{i=1}^{4} k}$$
$$\delta y_{i,j} = \frac{\sum_{j=1}^{4} \sum_{i=1}^{4} k.\delta y}{\sum_{j=1}^{4} \sum_{i=1}^{4} k} \tag{3-47}$$

summation is carried out over all the adjoining nodes.

The new position of the fluid mesh can usually be obtained within two to five Jacobi iterations. Mesh velocity is also estimated as

$$\dot{x}_{t+\delta t} = \frac{\delta x_{t+\delta t}}{\delta t} \qquad \text{and} \qquad \dot{y}_{t+\delta t} = \frac{\delta y_{t+\delta t}}{\delta t} \tag{3-48}$$

The grid position is adjusted at the end of each time step.

With grid kinematics, the solution procedure for one time step is completed.

Addendum - Non-Reflective Boundary Conditions for Far-field Flow Boundaries

A.1 Theory

The whole concept of the non-reflective boundary conditions is to impose physical boundary conditions such as to prevent the outgoing waves producing unwanted reflections at the boundaries.

In treating the boundary conditions it is appropriate to work with characteristic variables. The system of hyperbolic Euler equations for the flow are first written along the characteristic lines. These characteristics are the directions along which flow information propagate and, therefore, are the eigenvalues of the system of hyperbolic Euler equations. In two-dimensional flow these eigenvalues are:

$$\lambda_1 = u_\perp \, , \lambda_2 = u_\perp \, , \lambda_3 = u_\perp + c \, , \lambda_4 = u_\perp - c \qquad \text{(A-1)}$$

where c is the local speed of sound and $u_\perp$ is the outgoing flow velocity normal to the boundary.

The system of Euler equations governing the fluid flow along these characteristics are as follows:

$$\lambda_1: \qquad \frac{\partial \rho}{\partial t} - \frac{1}{c^2}\frac{\partial P}{\partial t} + \lambda_1 g_1 = 0$$

$$\lambda_2: \qquad n_y \frac{\partial u}{\partial t} - n_x \frac{\partial v}{\partial t} + \lambda_2 g_2 = 0$$

$$\text{(A-2a)}$$

$$\lambda_3: \qquad n_x \frac{\partial u}{\partial t} + n_y \frac{\partial v}{\partial t} + \frac{1}{\rho c}\frac{\partial \rho}{\partial t} + \lambda_3 g_3 = 0$$

$$\lambda_4: \qquad n_x \frac{\partial u}{\partial t} + n_y \frac{\partial v}{\partial t} - \frac{1}{\rho c}\frac{\partial \rho}{\partial t} + \lambda_4 g_4 = 0$$

where

$$g_1 = \frac{\partial \rho}{\partial n} - \frac{1}{c^2}\frac{\partial P}{\partial n}$$

$$g_2 = n_y \frac{\partial u}{\partial n} - n_x \frac{\partial v}{\partial n}$$

$$g_3 = n_x \frac{\partial u}{\partial n} + n_y \frac{\partial v}{\partial n} + \frac{1}{\rho c}\frac{\partial \rho}{\partial n} \qquad \text{(A-2b)}$$

$$g_4 = n_x \frac{\partial u}{\partial n} + n_y \frac{\partial v}{\partial n} - \frac{1}{\rho c}\frac{\partial \rho}{\partial n}$$

and n is the direction normal to the boundary (outgoing) with the unit vector of $\vec{n} = (n_x, n_y)$.

The first characteristic equation describes entropy perturbations, The second characteristic corresponds to vorticity waves, while the last two characteristics correspond to acoustic pressure waves.

The non-reflective boundary condition means that for each outgoing characteristic, in this formulation $\lambda_i \leq 0$, the corresponding characteristic equation should be solved, while for each incoming wave, the local perturbations are made to vanish, i.e. $g_i = 0$.

Depending on the value of $u_\perp$, four types of boundary conditions are possible. These are:

i. Supersonic inflow ($u_\perp < -c$)

All the four eigenvalues are positive, i.e. the equations describe incoming waves. There are four incoming characteristics and therefore, non-reflective boundary conditions along all the characteristics should be imposed. This leads to $g_1 = g_2 = g_3 = g_4 = 0$. Therefore, solving equations (A-2) yields

$$\frac{\partial \rho}{\partial t} = 0 \ , \ \frac{\partial u}{\partial t} = 0 \ , \ \frac{\partial v}{\partial t} = 0 \ , \ \frac{\partial P}{\partial t} = 0 \qquad \text{(A-3)}$$

ii. Subsonic inflow ($-c < u_\perp < 0$)

Only one eigen-value, λ_3, is positive. There are three incoming characteristics and one out-going characteristic. Three non-reflective boundary conditions are imposed, i.e. $g_1 = g_2 = g_3$ 0. Solving the set of equations (A-2) subject to these conditions results

$$\frac{\partial \rho}{\partial t} = -\frac{\rho}{2c}\lambda_3 g_3$$

$$\frac{\partial u}{\partial t} = -\frac{n_x}{2}\lambda_3 g_3$$

$$\frac{\partial v}{\partial t} = -\frac{n_y}{2}\lambda_3 g_3 \qquad \text{(A-4)}$$

$$\frac{\partial P}{\partial t} = -\frac{\rho c}{2}\lambda_3 g_3$$

iii. Subsonic outflow ($c > u_{\perp} > 0$)

Three of the four eigenvalues are positive, i.e. there are incoming waves. One non-reflective boundary condition need to be imposed along λ_4. This leads to $g_4 = 0$. Therefore, The boundary condition equations become:

$$\frac{\partial \rho}{\partial t} = -\frac{\rho}{2c}\lambda_3 g_3 - \lambda_1 g_1$$

$$\frac{\partial u}{\partial t} = -\frac{n_x}{2}\lambda_3 g_3 - n_y \lambda_2 g_2$$

$$\frac{\partial v}{\partial t} = -\frac{n_y}{2}\lambda_3 g_3 - n_x \lambda_2 g_2 \qquad \text{(A-5)}$$

$$\frac{\partial P}{\partial t} = -\frac{\rho c}{2}\lambda_3 g_3$$

iv. Supersonic outflow ($u_{\perp} > c$)

All the eigenvalues are positive, i.e. no incoming waves. No non-reflective boundary conditions are necessary and bounday values can be extrapolated from immediate upstream values. Alternatively, and this is more accurate, the system of equations (A-2) should be solved.

$$\frac{\partial \rho}{\partial t} = -\frac{\rho}{2c}(\lambda_3 g_3 + \lambda_4 g_4) - \lambda_1 g_1$$

$$\frac{\partial u}{\partial t} = -\frac{n_x}{2}(\lambda_3 g_3 - \lambda_4 g_4) - n_y \lambda_2 g_2$$

$$\frac{\partial v}{\partial t} = -\frac{n_y}{2}(\lambda_3 g_3 - \lambda_4 g_4) + n_x \lambda_2 g_2 \qquad \text{(A-6)}$$

$$\frac{\partial P}{\partial t} = -\frac{\rho c}{2}(\lambda_3 g_3 + \lambda_4 g_4)$$

A.2 Implementation

In implementing the model outlined in A.1, there are three issues of importance, namely, i) defining the normal direction to the boundary, ii) defining $u_\perp$, and iii) defining the differential of the dependent variables normal to the boundary.

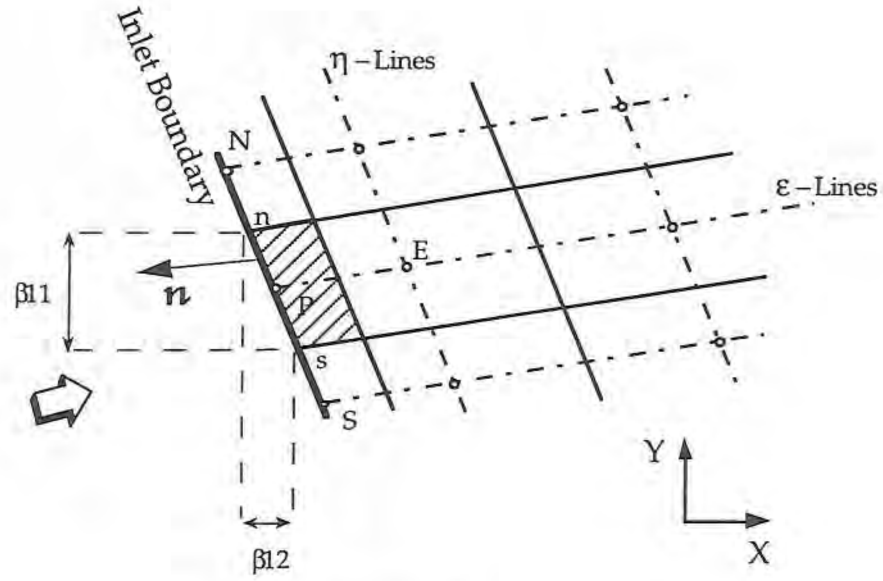

Figure a.1

Referring to figure a.1, the normal to the boundary at node (P) is defined using the Jacobians for the control volume at face (s). β_{xx}, β_{xy} define the components of the length of the control volume edge at face (s), therefore:

$$\delta l = \sqrt{\beta_{11}^2 + \beta_{12}^2}, \quad n_x = -\frac{\beta_{11}}{\delta l}, \qquad n_y = -\frac{\beta_{12}}{\delta l} \qquad \text{(A-7)}$$

and

$$\vec{n} = (n_x, n_y) \qquad \text{(A-8)}$$

Normal flow velocity to the boundary becomes is defined as

$$u_{\perp} = \vec{n} \cdot \vec{U} = n_x u + n_y v \tag{A-9}$$

The differential normal to the boundary for a variable Φ can be defined in the strandard form as follows:

$$\frac{\partial \Phi}{\partial n} = (n_x d_x + n_y d_y) \frac{\Phi_E - \Phi_P}{\delta d} + (n_x h_x + n_y h_y) \frac{\Phi_N - \Phi_S}{\delta h} \tag{A-10}$$

where

$$\delta d = \sqrt{(x_E - x_P)^2 + (y_E - y_P)^2}, \qquad \delta h = \sqrt{(x_N - x_S)^2 + (y_N - y_S)^2}$$

$$d_x = \frac{x_E - x_P}{\delta d} \qquad h_x = \frac{x_N - x_S}{\delta h} \tag{A-11}$$

$$d_y = \frac{y_E - y_P}{\delta d} \qquad h_y = \frac{y_N - y_S}{\delta h}$$

Chapter 4

Validation of Aerodynamic Model

Here they are - A few words, where a book is needed.
Louis Althusser - Freud and Lacan

4.0 About this Chapter

A series of one dimensional analytical test cases for the validation of the aerodynamic model is given in part (4.1). This is followed by a number of two-dimensional test cases for the evaluation of the steady flow modelling in part (4.2). Finally, in part (4.3), the unsteady flow modelling is evaluated against the experimental data available.

4.1 Shock Tube Flow

The shock tube problem, also known as the Riemann problem, is a difficult one dimensional test case which represents an exact solution to the one-dimensional system of the Euler equations [50].

The shock tube problem is defined by the sudden breakdown of a diaphragm in a long one-dimensional tube which separates two initial gas states at different pressures and densities. After the diaphragm is removed, the pressure discontinuity, i.e. the shock wave, propagates into the low pressure region and at the same time an expansion fan propagates into the high pressure region. A contact discontinuity which separates the two regions of the high and the low pressures also advances in the direction of the shock wave.

Two flow conditions are used for this investigation. In the first case, a pressure ratio of 10 and a density ratio of 8 are chosen. Figures (4.1a-4.1e) show the results of the calculation 6.1 ms after the diaphragm is removed. It can be seen that the agreement between the numerical results and the analytical solution is excellent. Position of the shock wave, contact discontinuity and expansion fan are accurately predicted and their strength is satisfactorily obtained.

In the above calculations the pressure switch of equation (3-24) is not used. The pressure switch option is designed for a better definition of shock waves by blending more second-order spatial accuracy into the flow discretization in the region of shock waves, or indeed, any other region with large flow gradients present. The above test case is repeated using the pressure switch and the results are shown in figures (4.2a-4.2e). It can be seen that while the shock wave is resolved much better, spurious oscillations ahead of the shock wave do occur, even for this moderate initial pressure ratio.

The influence of the pressure switch on the solution is well known [51]. In a one-dimensional flow, the turning-off of the pressure switch results in a model which is equivalent to first-order upwind differencing which is the proper representation of the flow. The pressure switch introduces the effect of the downstream disturbances which is physically unrealistic. Therefore, in a one-dimensional flow, the first-order upwind differencing models the flow accurately and reducing the amount of numerical dissipation via the pressure switch leads to spurious oscillations in the vicinity of the shock wave.

In the second test case, both the pressure and density ratios are increased to 100. This higher pressure ratio between the two regions of the tube results in the formation of a very strong shock wave which propagates very rapidly in the low pressure region. The results for this case are shown in figures (4.3a-4.3e). Again, it can be seen, that the agreement between the numerical results and the analytical solution is very good.

The outcome of these two test cases is that the basic discretization of the Euler equations, outlined in chapter 3, have been implementated correctly.

4.2 Steady Flow

4.2.1 Channel Flow

The first two-dimensional steady flow test case considered is that of a channel with an arc obstacle on the lower wall. The width of the channel is equal to the length of the arc and the width to length ratio for the circular arc is 10%. This geometry has been used by many researchers and ther are a large number of numerical results available for comparison. The results here have been compared with those given by Ni [52].

Figure 4.4 shows the computational mesh which is composed of 65x17 points. The mesh is identical to that used in reference [52]. The first set of calculations is for an incoming flow at a Mach number of 0.5. In this case, the flow remains entirely subsonic. Figure 4.5 shows the surface Mach number distribution along the lower wall. It can be seen that the solution is almost symmetrical about the mid-chord which is expected for subsonic flows. Figure 4.6 shows the Mach number distribution throughout the channel. It can be seen that the results are in very good agreement with those from reference [52].

For the next case, the inlet Mach number is increased to 0.675. At this Mach number a supersonic region is formed on the lower wall which is terminated by a shock wave at about 75% of the arc chord, as shown in figures 4.7 and 4.8. The shock wave is captured across three grid points. The agreement between the results of the present study and those from reference [52] is again very good. This is particularly encouraging as the solution technique used by Ni is quite different from that used here.

Figure 4.9 shows the percentage of the mass flow error which is an indication of the accuracy (or inaccuracy) of the numerical model. This figure shows that the mass is conserved. However, due to the way the model treats discontinuities, high frequency oscillations occur at the shock wave location. There can also seen a slight jump in the mass error at the "leading" and "trailing" edges of the circular arc. However, this error can be reduced with a higher grid resolution in these regions.

The entropy contours are plotted in figure 4.10 which shows the increase in entropy due to the shock wave. The maximum increase in entropy is observed to be less 2%.

Foe the sake of completeness, a plot of convergence history for the transonic channel flow is given in figure 4.11 in the form of a residual vs number of time steps. The convergence rate levels off when the density residuals are of the order of the machine accuracy, of course, there is no need to continue the computation till this level of convergence has been reached.

The final channel flow test case considered is for an inlet Mach number of 1.4 past a circular arc with a width to length ratio of 0.04. Figure 4.12 shows the formation of shock waves at the corners of the arc. The shock formed at the "leading" edge is reflected from the top wall and mixes with the shock wave formed at the "trailing" edge, hence, diffusing the latter. Figure 4.13 shows the iso-mach contours and the entropy gain throughout the channel. Again, the agreement with the results given in reference [52] is excellent.

The above calculations indicate that the numerical modelling of the fluid flow, detailed in chapter 3, is correct. Furthermore, the non-reflective boundary conditions seem to behave satisfactorily. In terms of the efficiency of the solution procedure, the main conclusion is that the convergence rate is fastest for the supersonic and transonic cases. In all cases considered, 1,000 time steps were required for a fully-converged solution.for supersonic flows, this number increases to 15,000 for the transonic case and to 50,000 for the subsonic case. The reason behind this disparity is the weakening of the coupling between the momentum and continuity equations as the inlet Mach number is reduced.

4.2.2 Single Airfoil

The standard test case for the steady flow calculations about an airfoil is that of NACA-0012 airfoil operating at a Mach number of 0.8. There are plenty of numerical results available for both non-lifting, i.e. zero incidence, and lifting cases. The latter is usually performed at an incidence of 1.25 degrees. These two test cases have been chosen for the current validation exercise.

Calculations are performed on a C-type computational mesh which is shown in figure 4.14. The far-field boundary is situated at 10 chords away from the airfoil. Three sets of mesh densities are employed; a 'coarse' mesh of 96x16 points, a 'medium' mesh of 131x16 points and, a 'fine' mesh of 192x32 grid points.

4.2.2.1 NACA-0012 Airfoil, Non-lifting Case

Figure 4.15 shows the surface pressure distribution for the case of an incoming flow with a Mach number of 0.8 and at zero incidence. As expected, the results show the formation of a supersonic region on both airfoil surfaces which is terminated by a shock wave at mid-chord. The solution is symmetric and the resultant lift and drag coefficients for the fine mesh are as follows:

$$C_L = 0.73\text{x}10^{-8}, \qquad C_D = 0.0086$$

Mavripolis [43] gives a value of 0.0088 for the coefficient of drag from an Euler solver on an unstructured mesh with the same number of grid nodes.

Figure 4.16 shows the variation of the entropy on the surface of the airfoil. Ahead of the shock wave there should be no entropy gain, while in fact there is an increase in entropy at the trailing edge which remains constant up to the shock wave location There is a further increase in the entropy due to the shock wave. At the trailing edge point, a further small increase in the value of entropy occurs. The oscillatory behaviour of the entropy near the shock wave is due to the fact that the numerical dissipation is scaled by pressure which does not necessarily damp out entropy fluctuations in the shock wave region. Figure 4.17 shows the pressure contours in the flow field. Figure 4.18 shows the entropy variation throughout the flow domain.

4.2.2.2 NACA-0012 Airfoil, Lifting Case

This test case considers a flow past a NACA-0012 airfoil at an incoming Mach number of 0.8 with an incidence of 1.25 degrees. Calculations are performed on three different mesh densities and the results are given in figure 4.19. The solution is identified by a large supersonic region on the top surface which is terminated by a strong shock wave located at 67% of the chord, downstream of the leading edge. There is also a very weak shock wave formed on the lower surface which is discernible only on the finest grid, as shown in figure 4.20. Table 4.1 gives the values of lift and drag coefficients for the three mesh densities considered. For comparison purposes, the corresponding values from reference [43] have also been included.

Mesh	C_L	C_D
109x16	0.3410	0.0234
131x16	0.3500	0.0232
192x32	0.3650	0.0228
128x32 Triangular O-mesh [43]	0.3440	0.0227
560x65 Quadrilateral C-mesh [43]	0.3620	0.0236

Table 4.1 - Comparison of Lift and Drag coefficients for NACA-0012 Airfoil
Mach number = 0.80, Incidence = 1.25 degrees

Figure 4.21 shows the entropy gain along the airfoil surface and figure 4.22 shows the entropy variation in the computational domain. The variation of the entropy compares very closely with the corresponding results given in reference [43].

4.3 Unsteady Flow

Three AGARD test cases have been used to validate the modelling of the unsteady flow. The experimental data for these test cases were obtained from [53 and 54]. All computations were performed on a 131x32 C-mesh with far-field boundaryies being located at 10 chords away from the airfoil.

4.3.1 Case 1

The first case considered is a NACA-0012 airfoil pitching about its mid-chord. The incoming Mach number is 0.6 and the initial incidence is 2.89 degrees. The airfoil goes through its pitching motion at a reduced frequency of 0.0808 and the pitching amplitude is 2.41 degrees. Figure 4.23 shows the steady surface pressure distribution along the airfoil surface. Figure 4.24 shows the corresponding steady pressure distribution in the flow domain.

Figures 4.25 and 4.26 show the variation of the lift and moment coefficients. It can be seen that the transient behaviour dies down after three periods. The comparison of the experimental data and the computations is performed on the fourth period of the computations.

Figure 4.27 shows a plot of the lift coefficient against the instantaneous incidence and includes experimental data from reference [53]. It can be seen that the agreement is very good. Figure 4.28 shows the comparison for the moment coefficient for which the agreement is not as good as that for the lift. This discrepancy can be due to the higher sensitivity of the moment to the distribution of the pressure along the airfoil surface.

Figures 40.28a-4.29j show how the computed unsteady pressures compare with the experimental data. It is immediately seen that the overall agreement is very good, apart from the discrepancy observed near the trailing edge point which is due to the viscous effects which are not modelled.

It is also interesting to point out that the level of agreement between the experimental data and the computed results is better at those instances when the airfoil is stationary. For example, in figure 4.29a, the airfoil is moving through the steady state position at its maximum speed and the agreement between the results is not very good. However, when the airfoil reaches its maximum pitch angle and is momentarily stationary, figure 4.29d, the agreement is excellent and the shock position and strength is accurately predicted.

4.3.2 Case 2

The second test case considered is again a NACA-0012 airfoil in pitching motion about its mid-chord. The incoming Mach number is 0.755 and the initial incidence is 0.016 degrees. The airfoil goes through its pitching motion at a reduced frequency of 0.0814 and the pitching amplitude is 2.51 degrees.

Figures 4.30a-4.30d show the instantaneous unsteady surface pressure distributions during the fifth cycle of airfoil oscillations The comparison between the computed results and the experimental data of reference [53] is shown to be very good.

Figures 4.31 and 4.32 show the variation of the lift and moment coefficients against the airfoil incidence. Again the agreement is very good. The moment time history is given in figure 4.33. This graph is of particular interest as is shows the effect of the shock formation and disappearance during each cycle.

Finally, this case is also used for a comparative study of the cell-vertex and cell-centred schemes. Figures 4.34 and 4.35 show the variation of the lift and moment coefficients against incidence. It can be seen that while the lift distribution is not effected by the choice of discretization scheme, the cell-vertex scheme gives a marginally better solution of the coefficient of moment.

4.3.2 Case 3

The final case to be considered is a NACA-64A010 airfoil in pitching motion about its mid-chord. The incoming Mach number is 0.796 and the initial incidence is -0.21 degrees. The airfoil goes through its pitching motion at a reduced frequency of 0.202 and a pitching amplitude of 1.021degrees.

Figures 4.36a-4.36d show the instantaneous unsteady surface pressures during the fourth cycle of airfoil oscillations The comparison between the computed results and the experimental data of reference [54] is seen to be very good.

Figures 4.37 and 4.38 show the variationof the coefficients of lift and moment against the airfoil incidence. The agreement for the lift coefficient is excellent, however, the correlation between the results for the moment coefficient is poor. This pattern has also been observed in reference [45], in which the discrepancy has been explained by the probable error in the integration of the experimental data when calculating the moment coefficient. This argument can certainly be justified by the good correspondence between the surface pressure distributions shown in figure 4.36. Another argument is the poor integration of the experimental data due to the low number of points available.

4.4 Conclusions

There is a good overall agreement between the experimental data and the model proposed in chapter 3 for both steady and unsteady flows. This is particularly encouraging in view of the whole host of experimental features that are present in the test and are not modelled numerically.

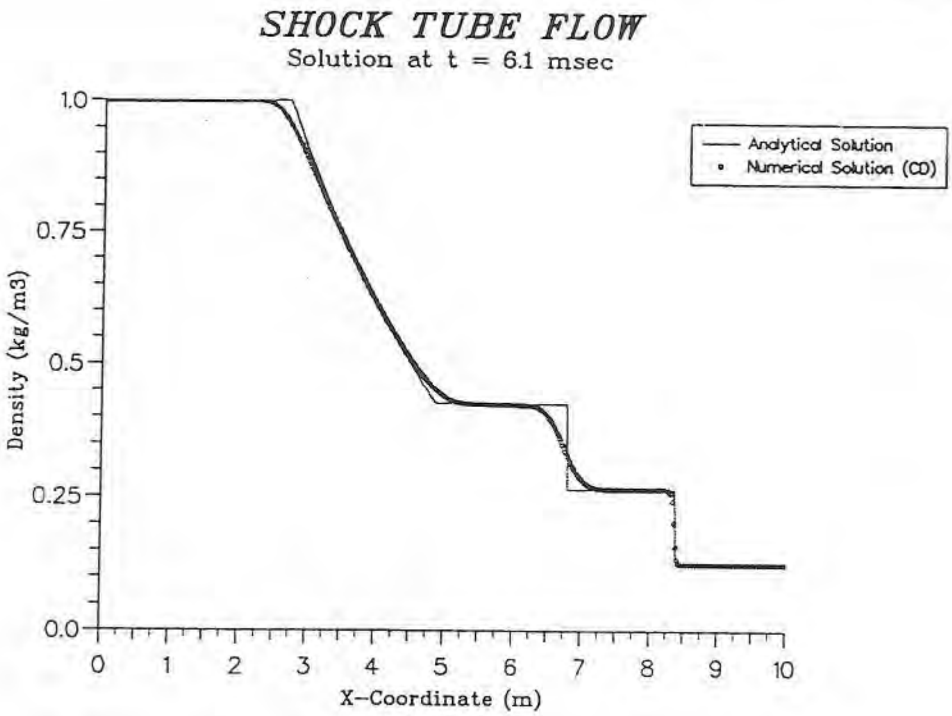

Figure 4.1a

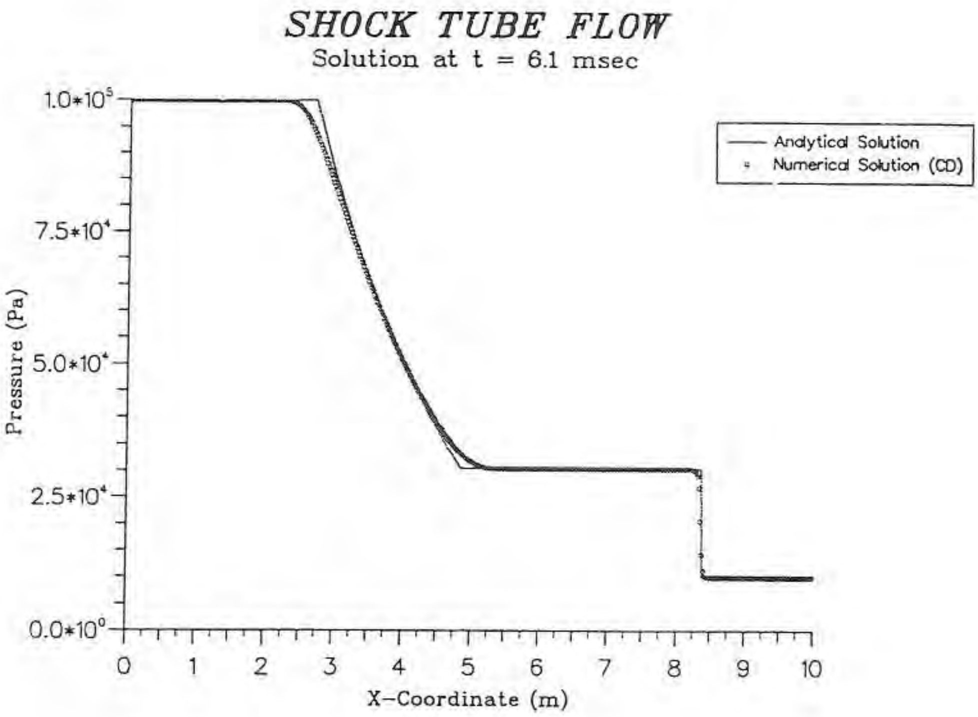

Figure 4.1b

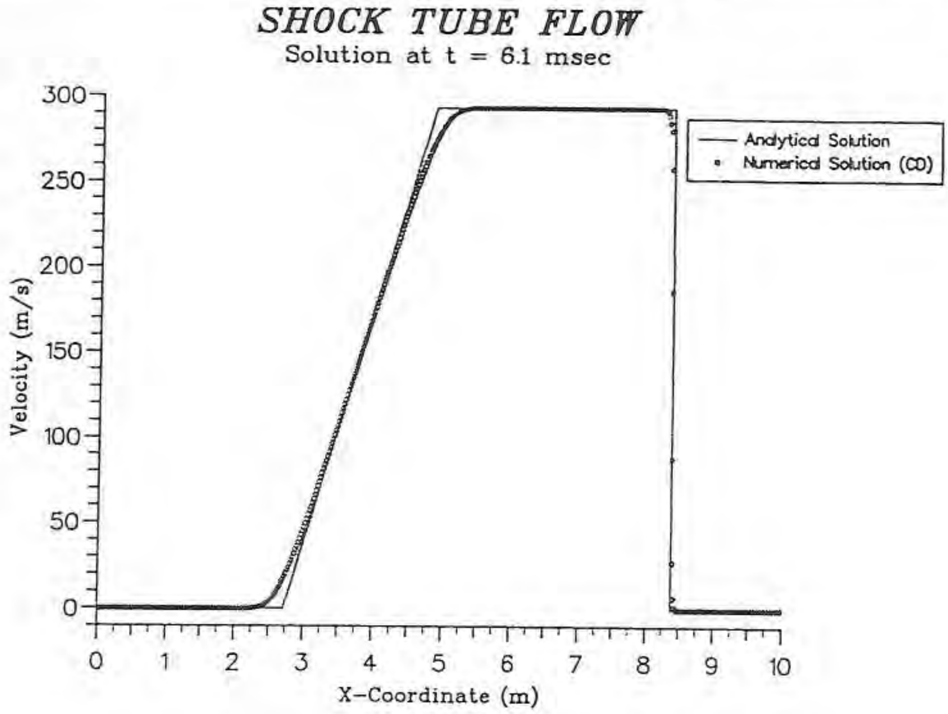

Figure 4.1c

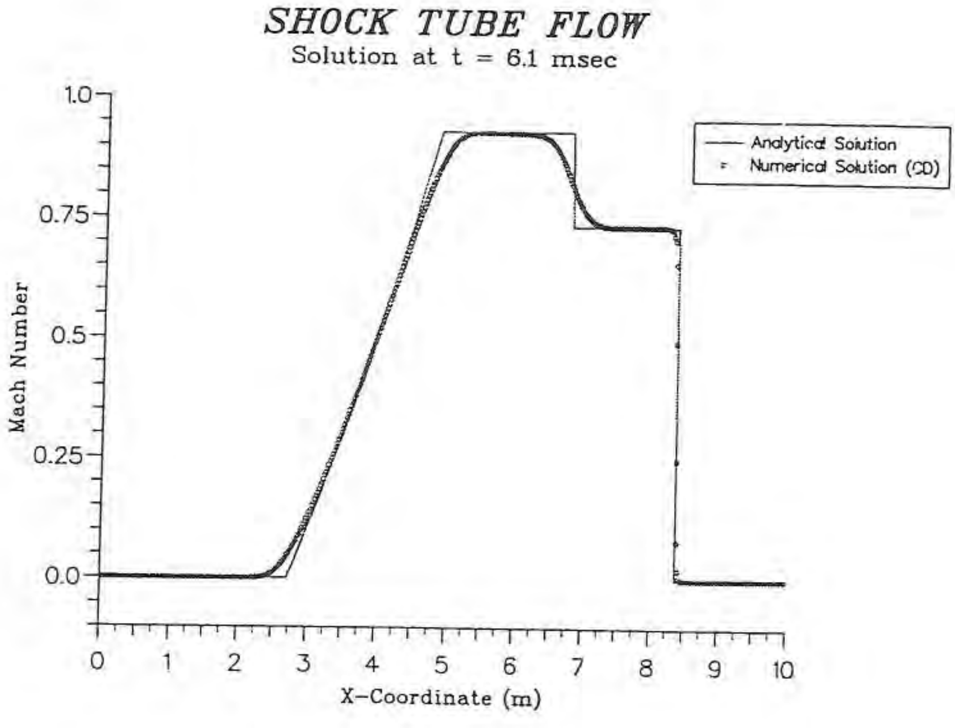

Figure 4.1d

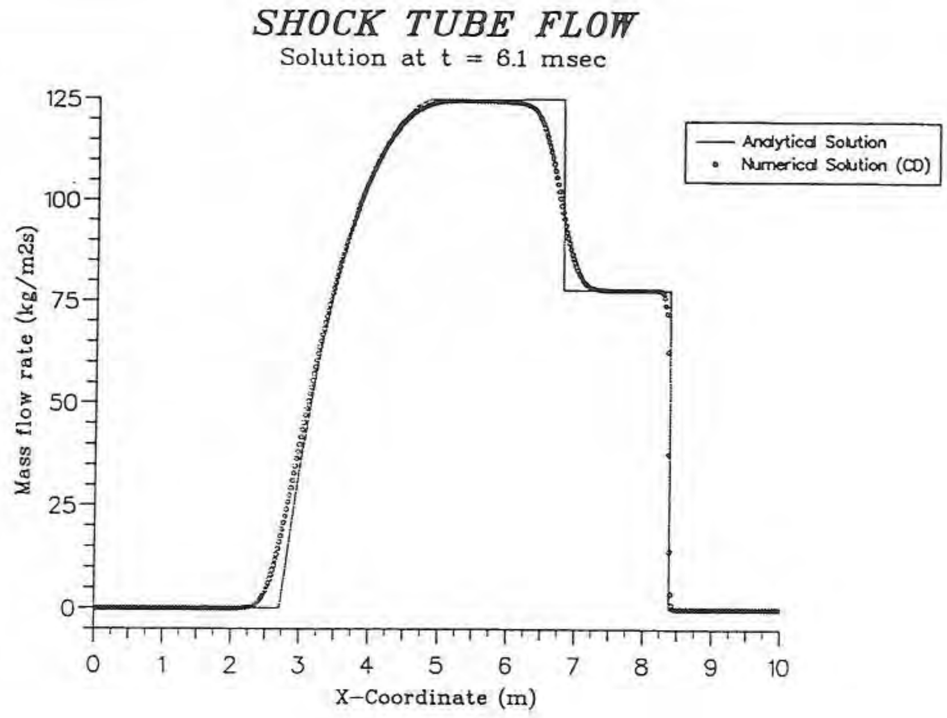
SHOCK TUBE FLOW
Solution at t = 6.1 msec
Analytical Solution
Numerical Solution (CD)
Mass flow rate (kg/m2s)
X–Coordinate (m)
125
100
75
50
25
0
0 1 2 3 4 5 6 7 8 9 10

Figure 4.1e

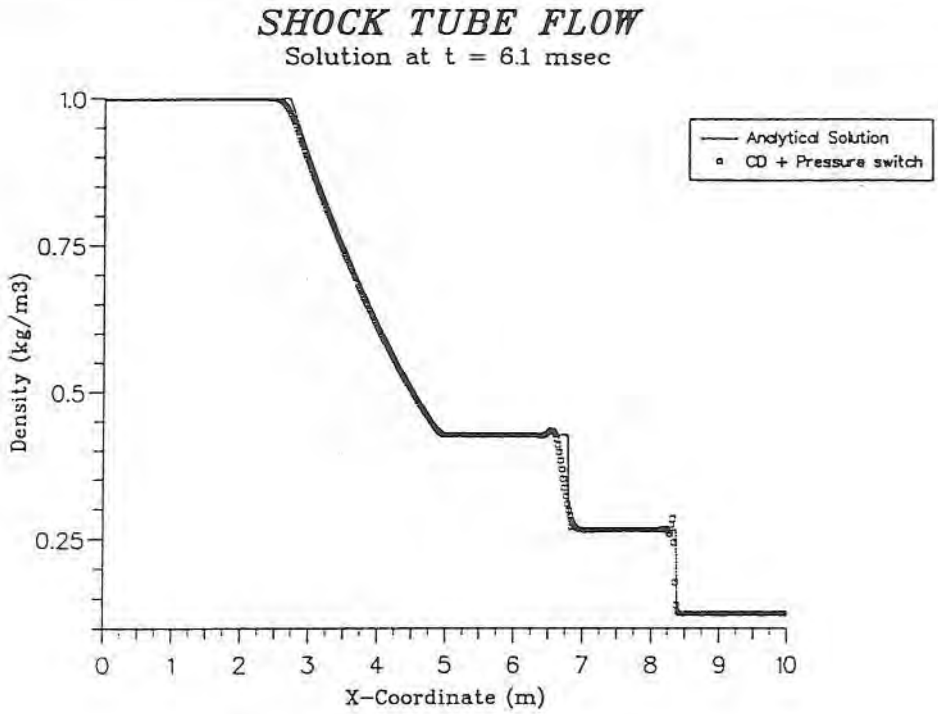

Figure 4.2a

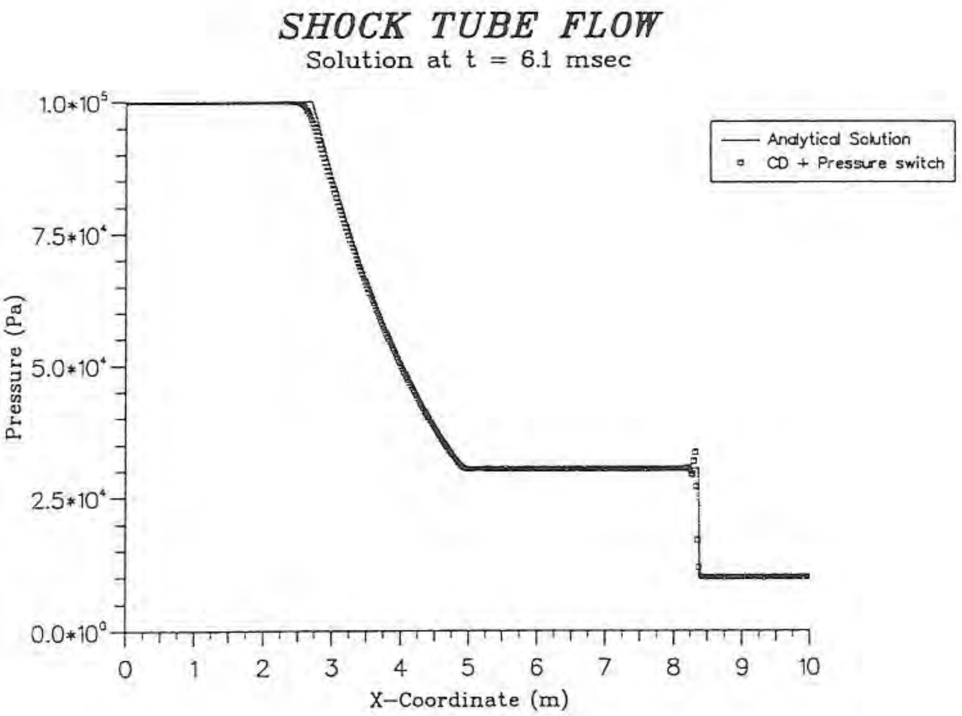

Figure4.2b

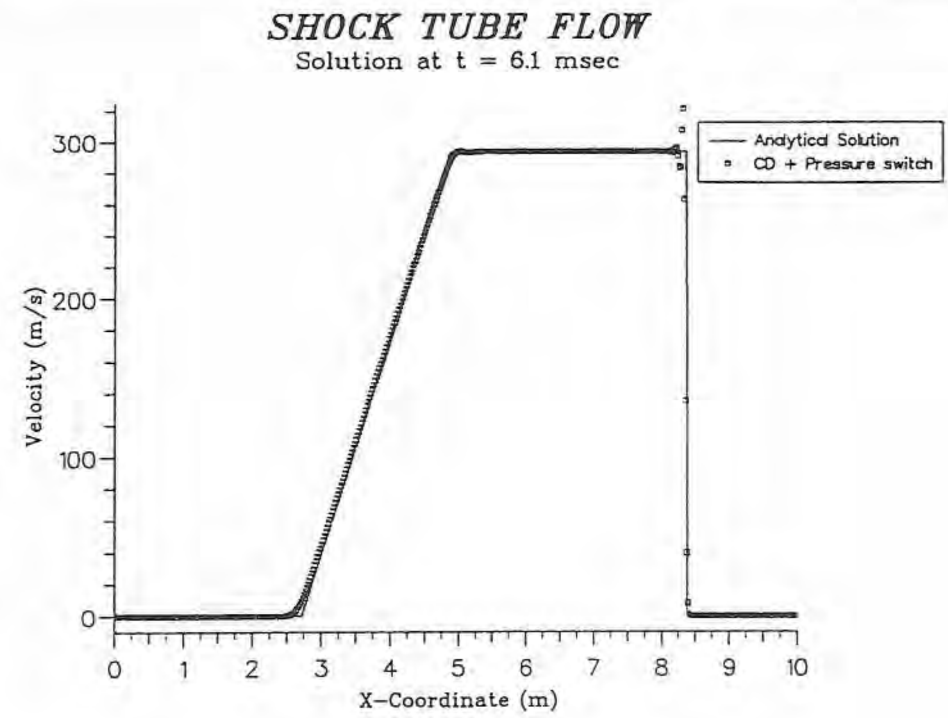

Figure 4.2c

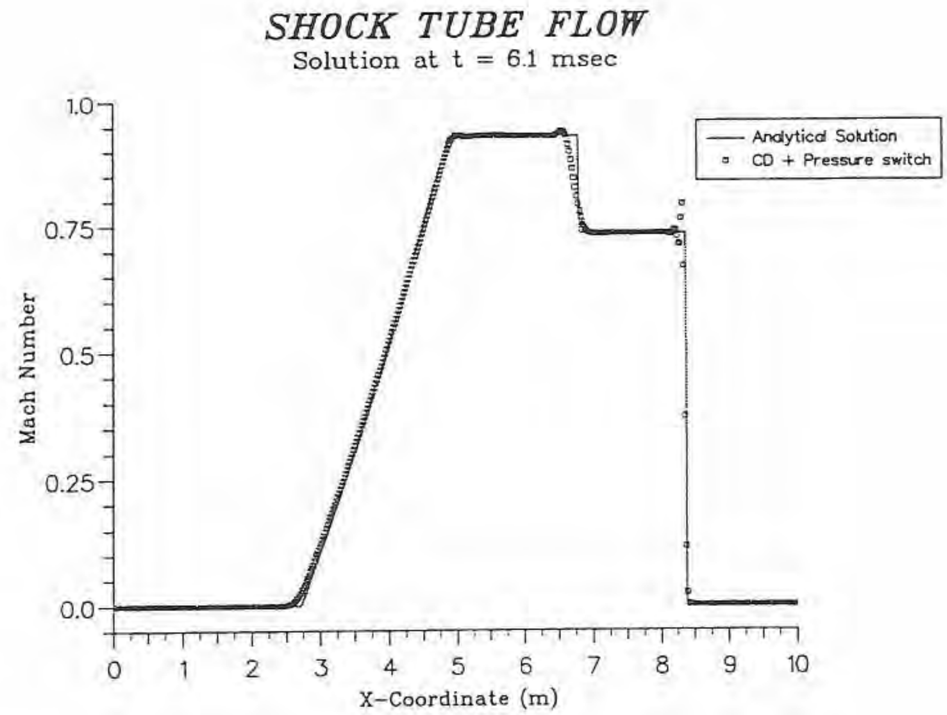

Figure 4.2d

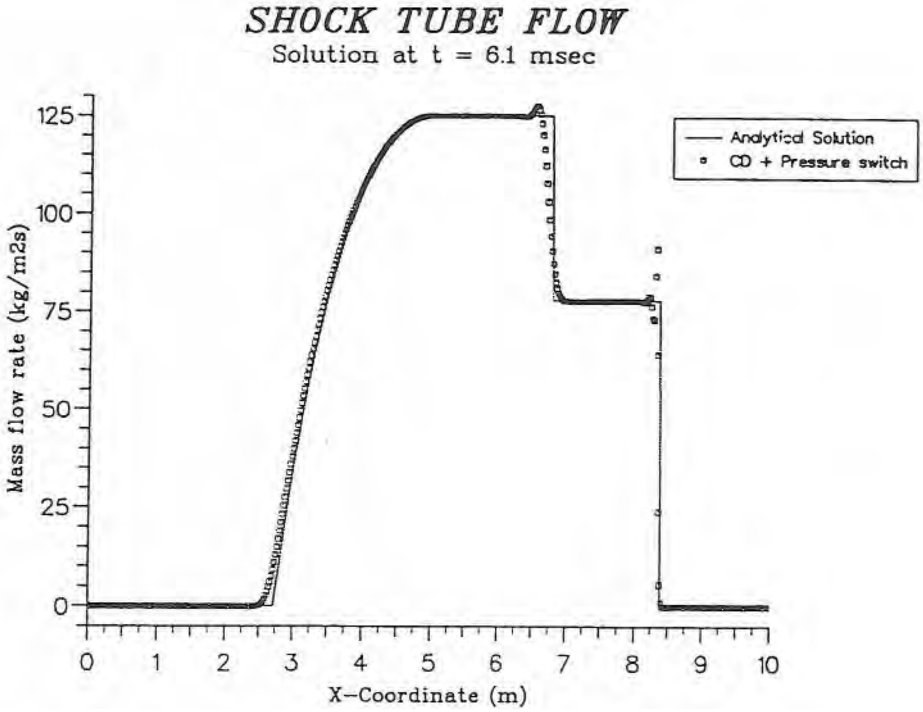
SHOCK TUBE FLOW
Solution at t = 6.1 msec
Analytical Solution
CD + Pressure switch
Mass flow rate (kg/m2s)
X-Coordinate (m)
125
100
75
50
25
0
0
1
2
3
4
5
6
7
8
9
10

Figure 4.2e

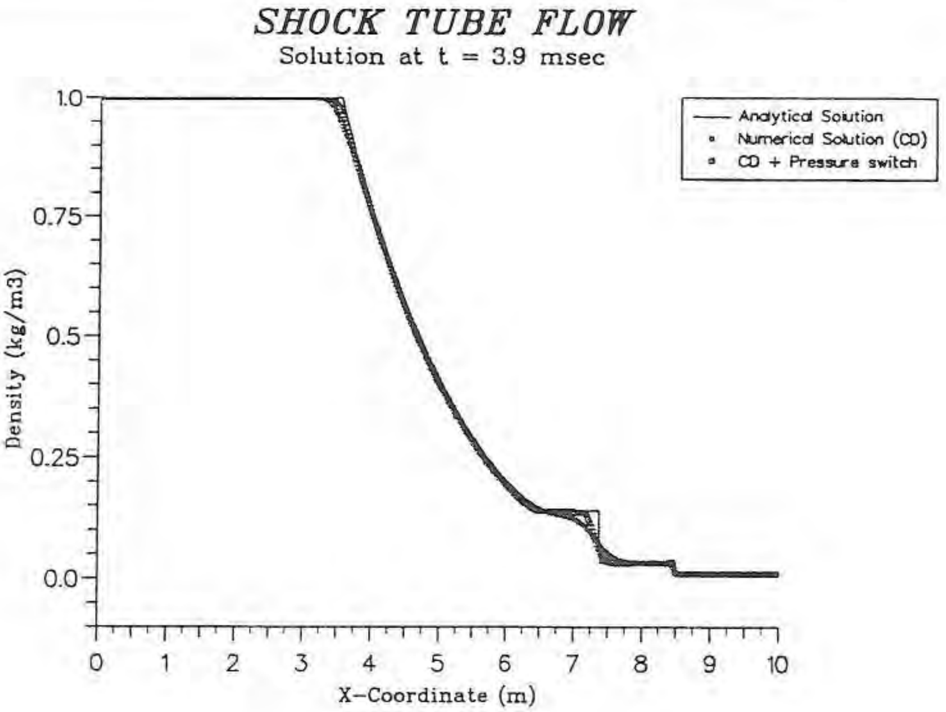

Figure 4.3a

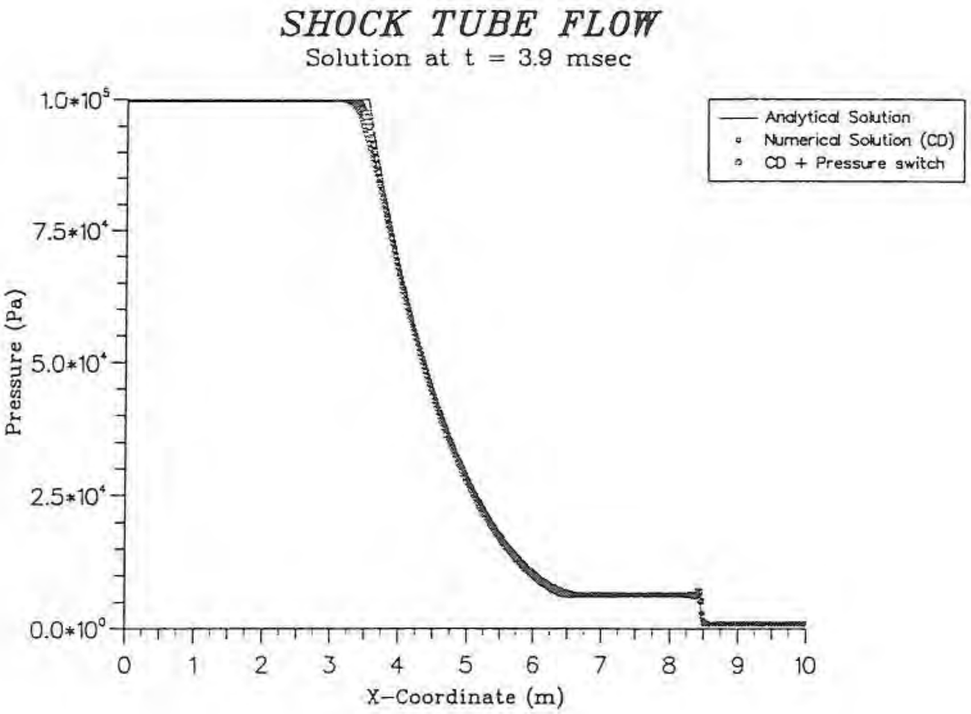

Figure 4.3b

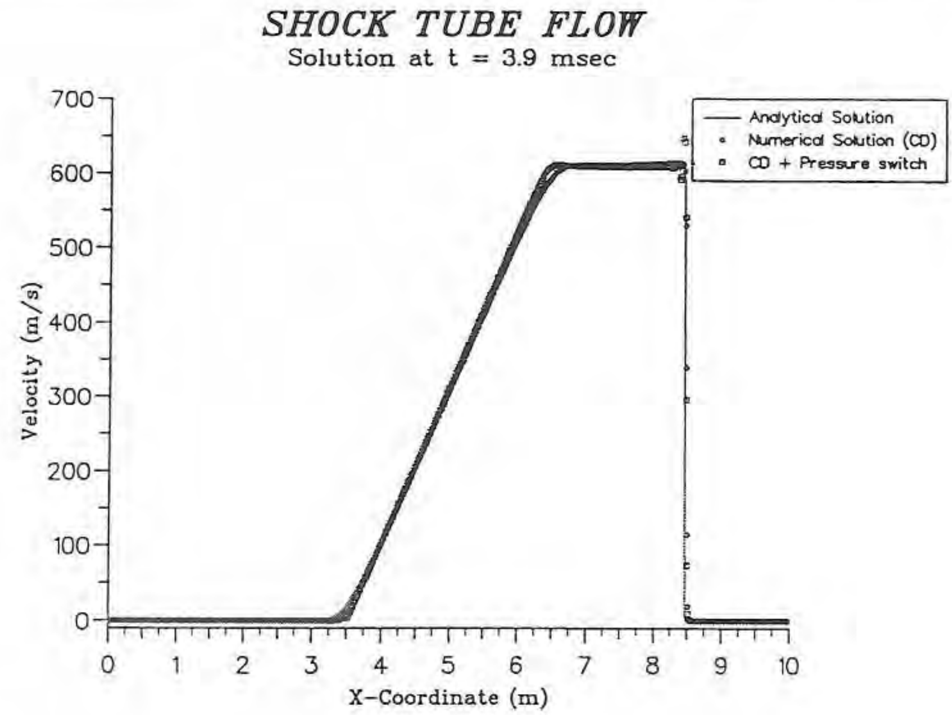

Figure 4.3c

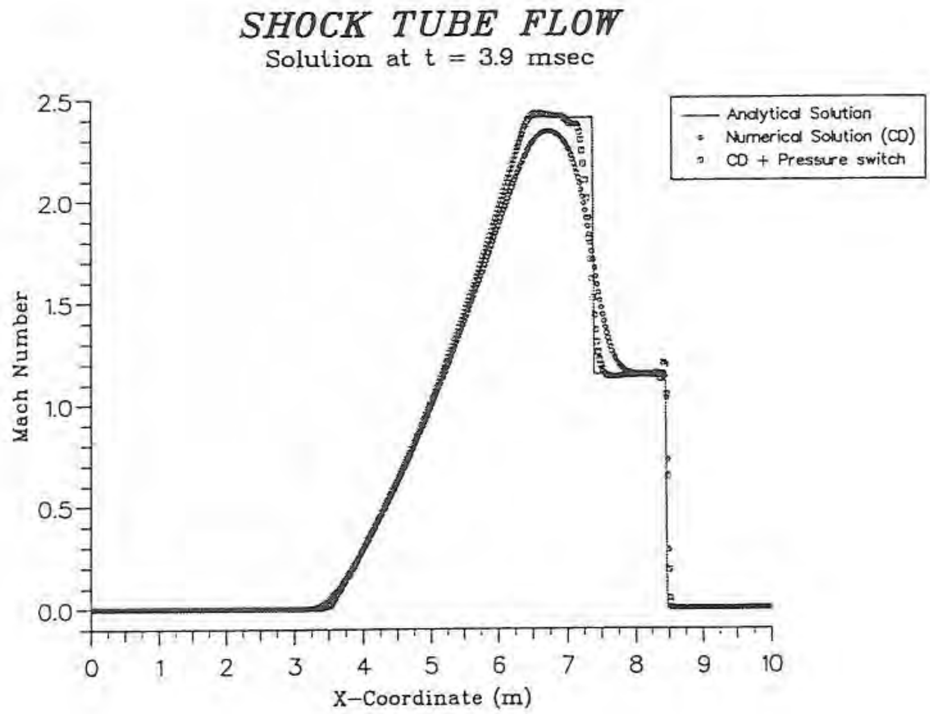

Figure 4.3d

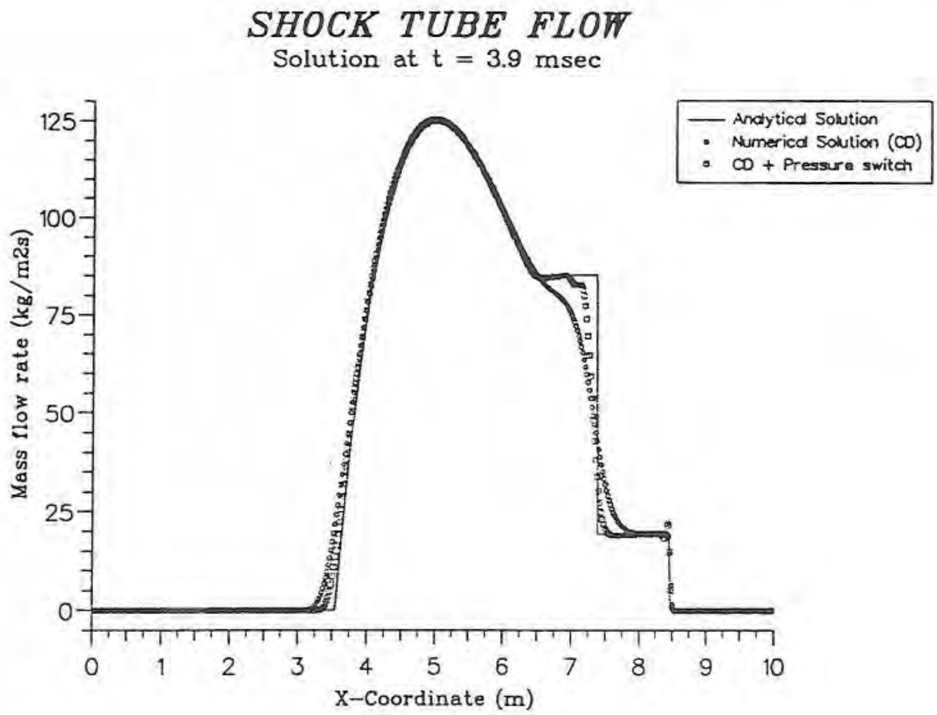

Figure 4.3e

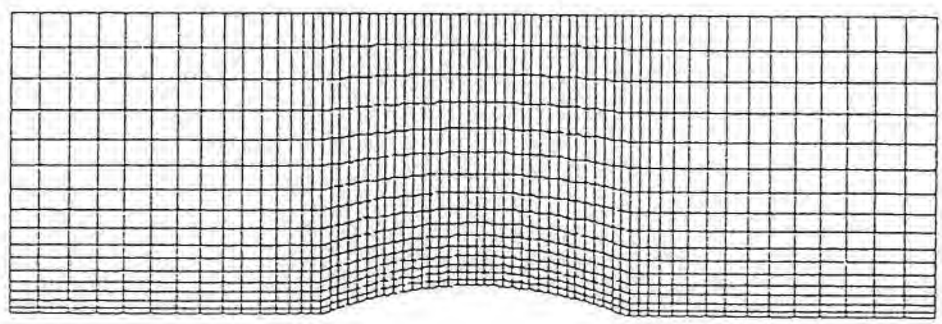

figure 4.4

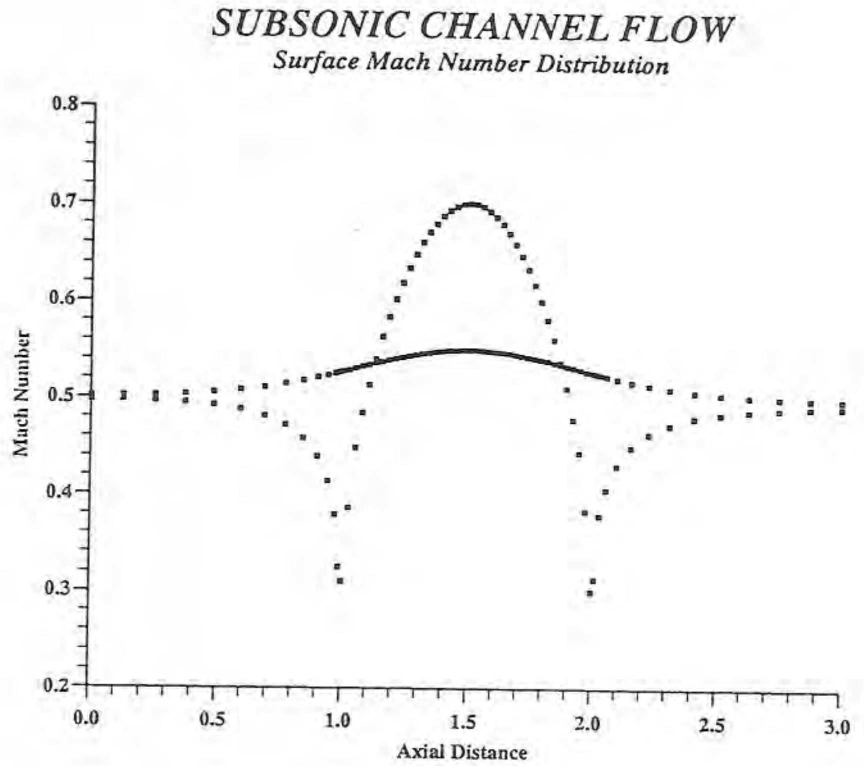

Figure 4.5

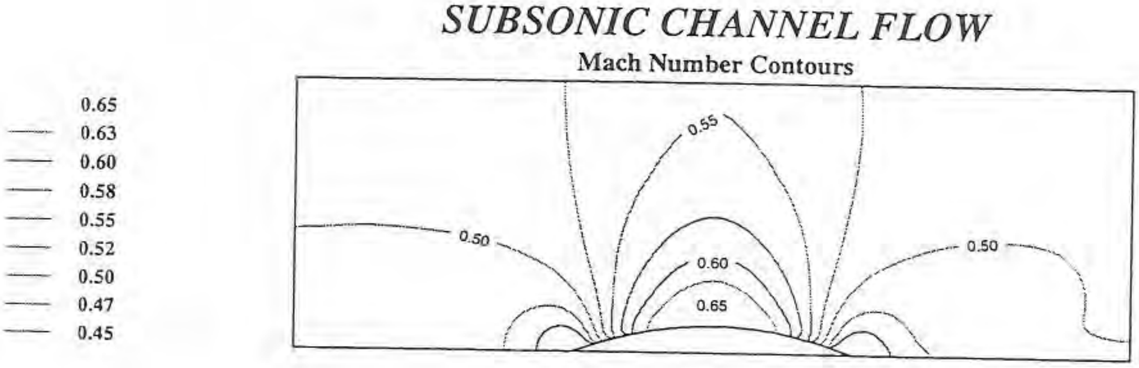

Figure 4.6

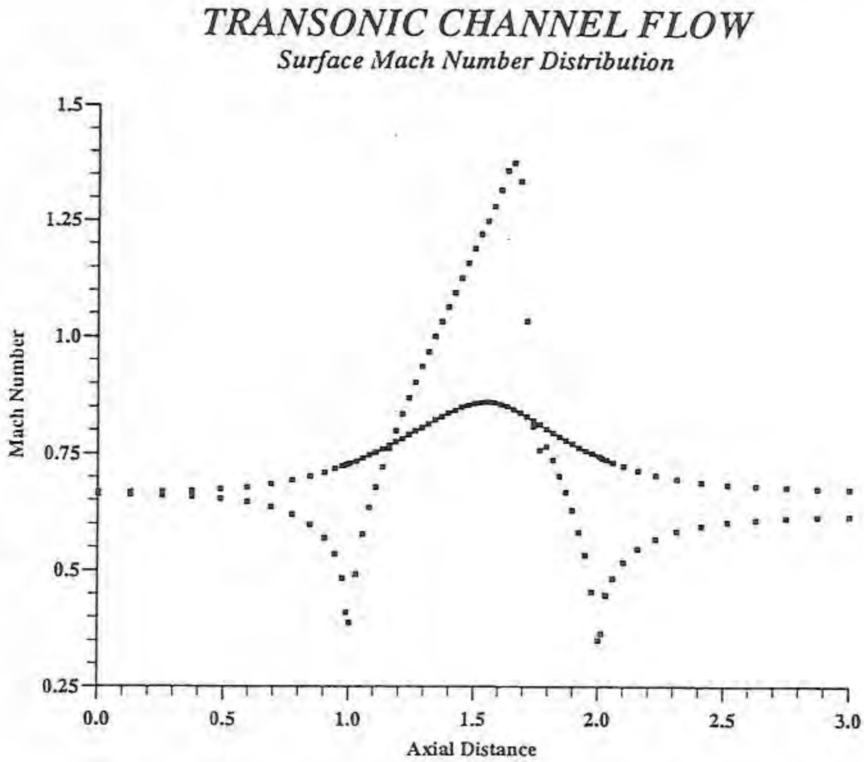

Figure 4.7

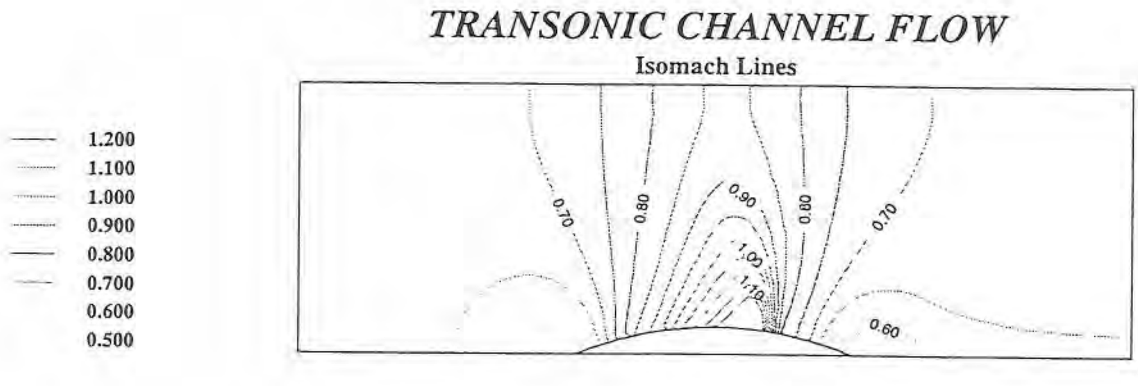

Figure 4.8

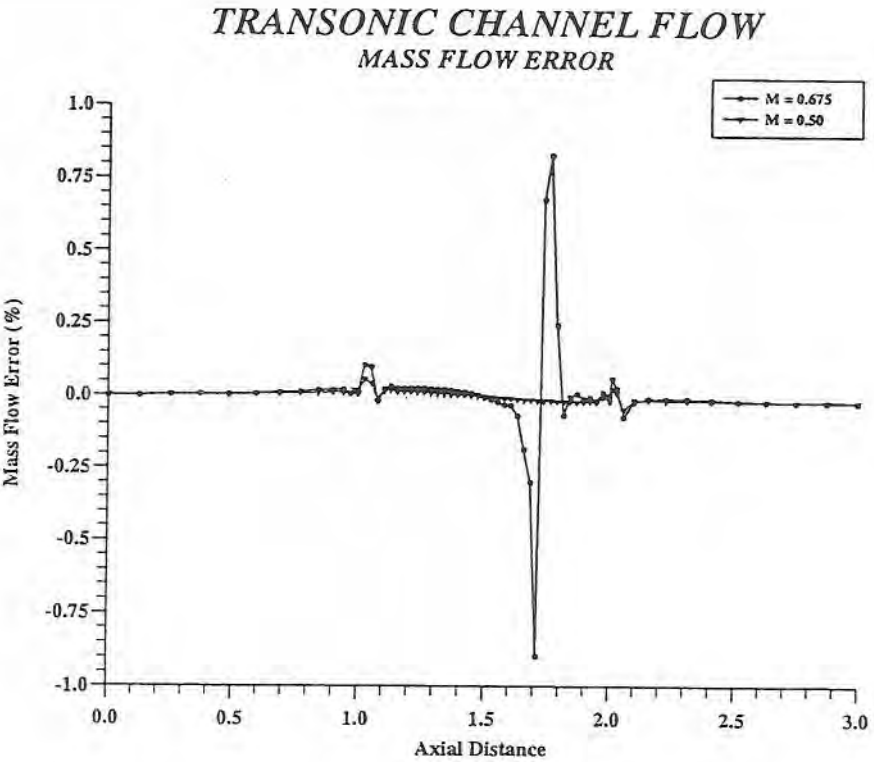
TRANSONIC CHANNEL FLOW
MASS FLOW ERROR
M = 0.675
M = 0.50
Mass Flow Error (%)
1.0
0.75
0.5
0.25
0.0
-0.25
-0.5
-0.75
-1.0
0.0
0.5
1.0
1.5
2.0
2.5
3.0
Axial Distance

Figure 4.9

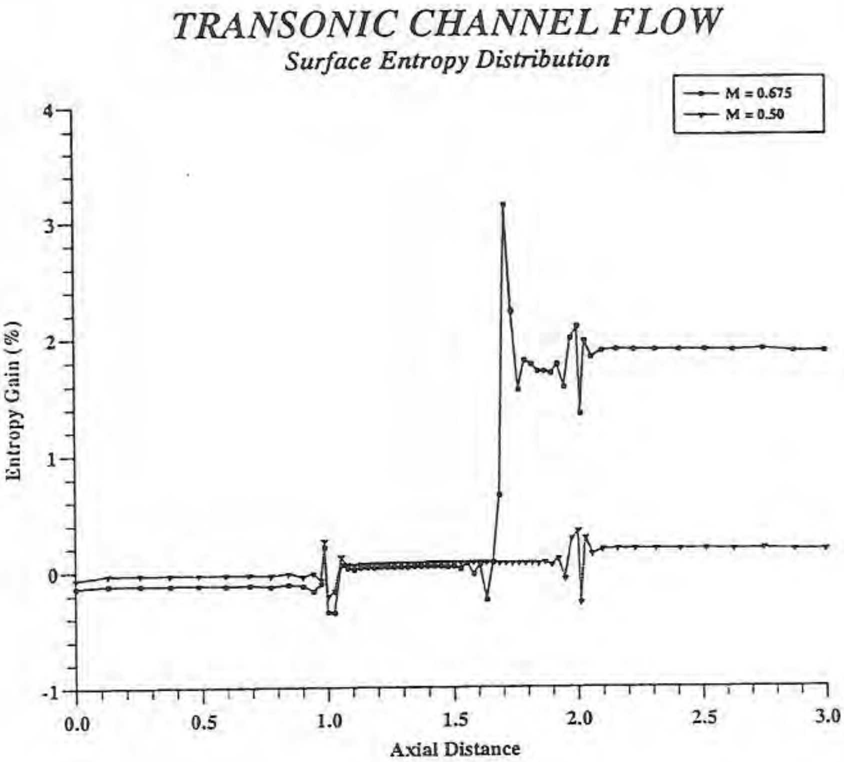

Figure 4.10a

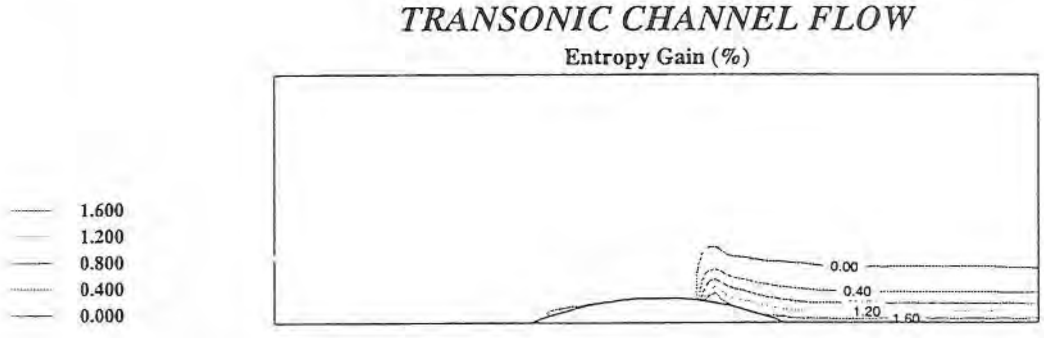

Figure 4.10b

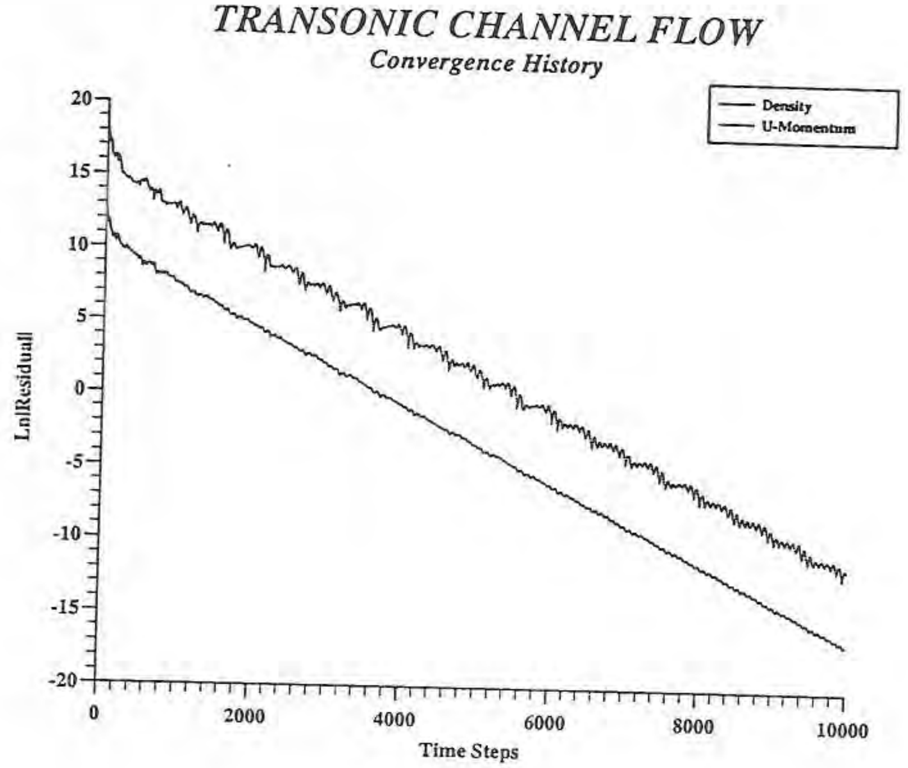

Figure 4.11

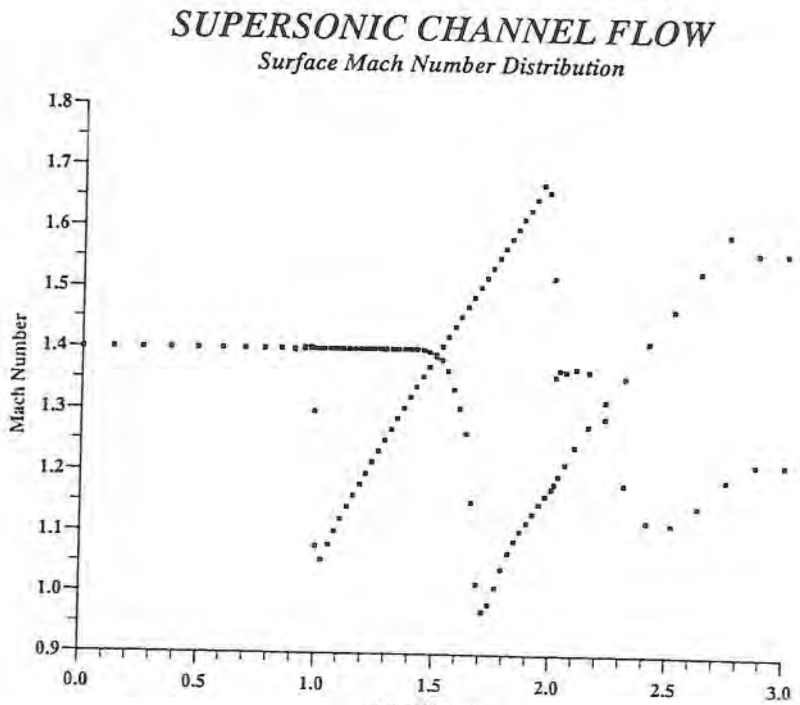

figure 4.12

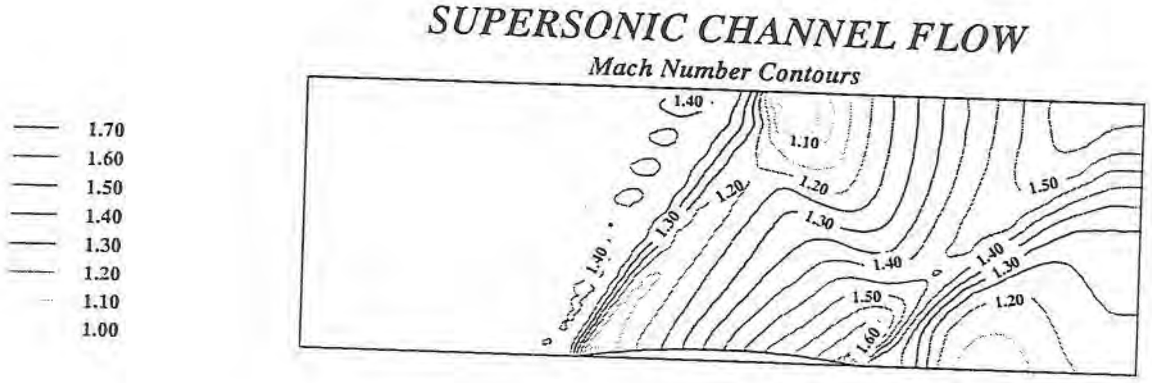

Figure 4.13a

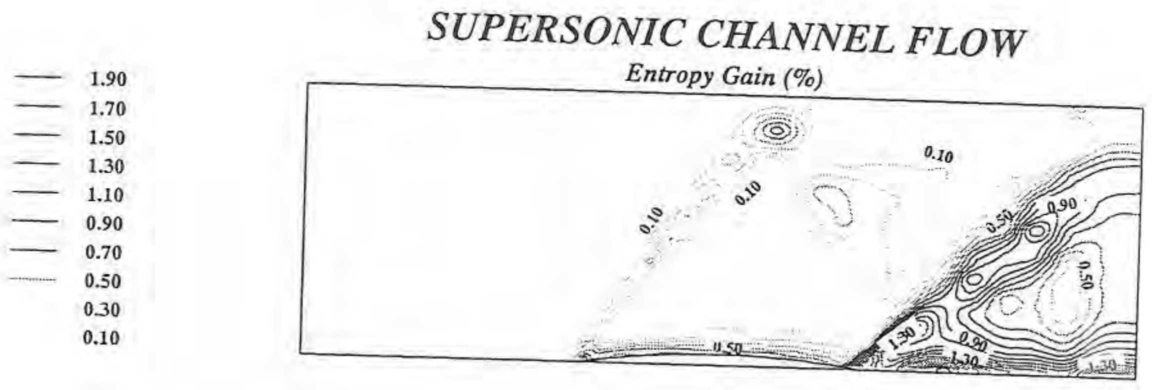

Figure 4.13b

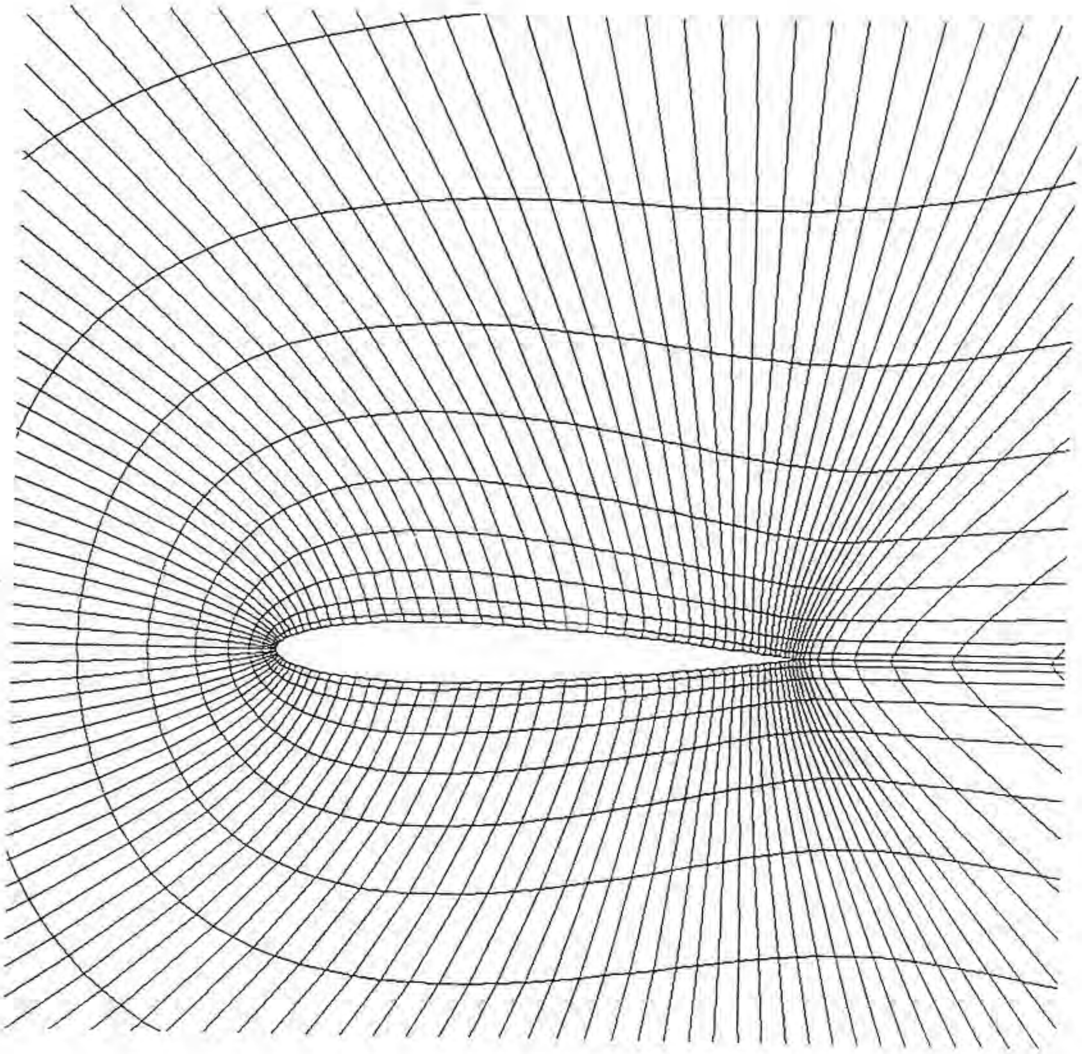

Figure 4.14 - Fluid mesh

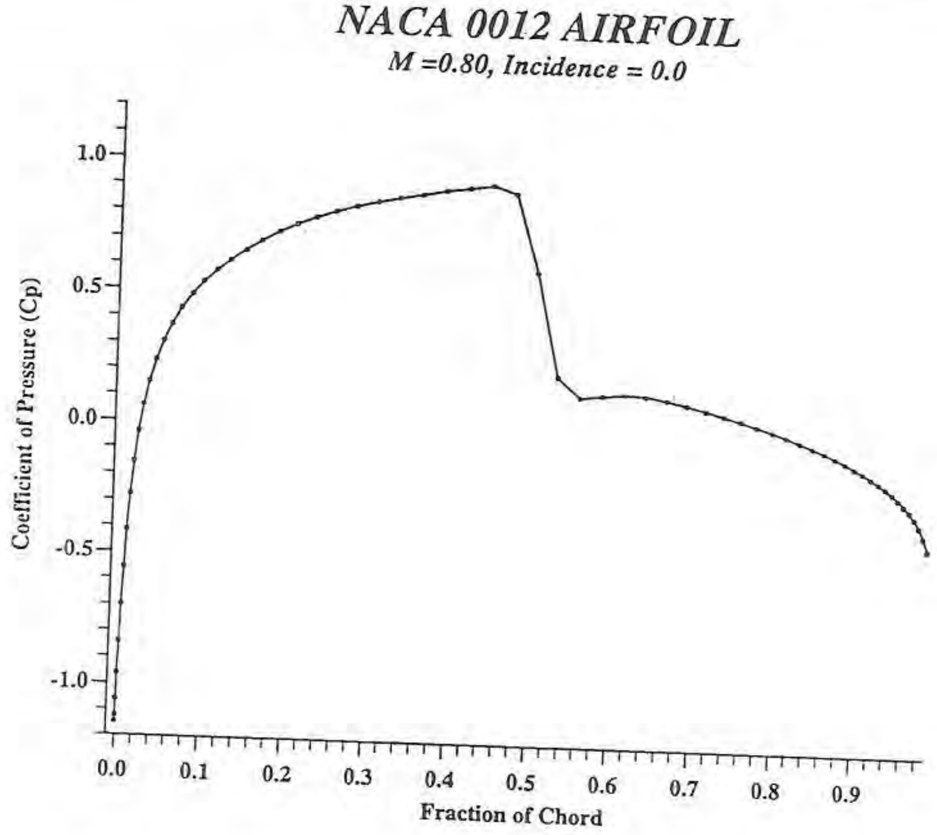

Figure 4.15

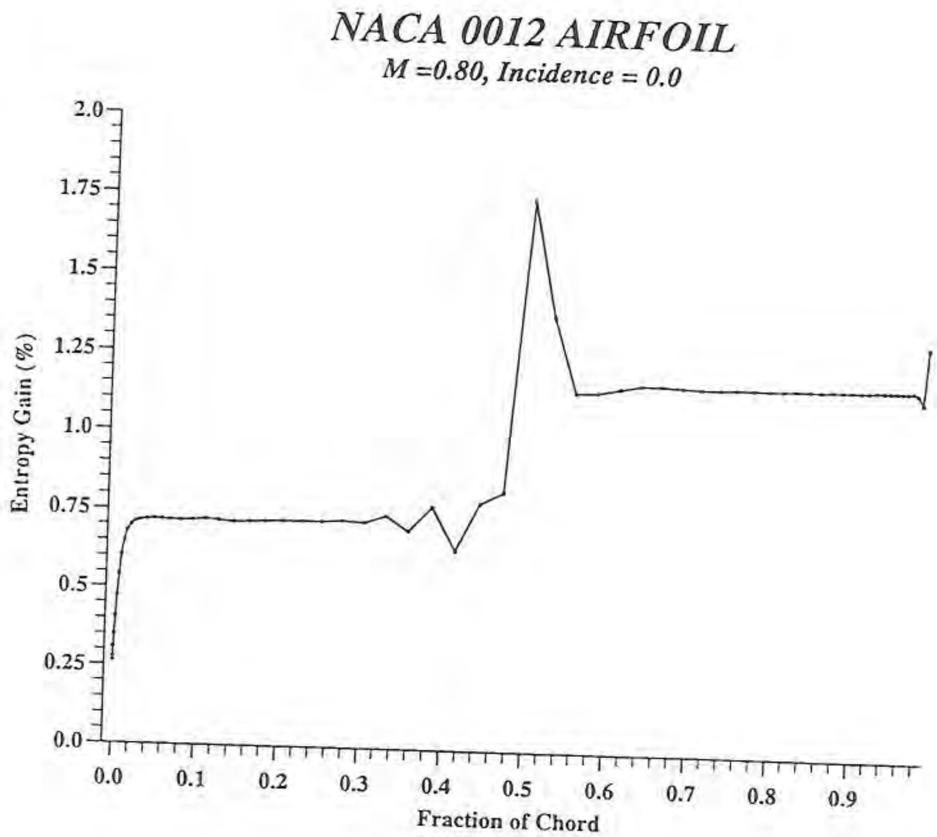

Figure 4.16

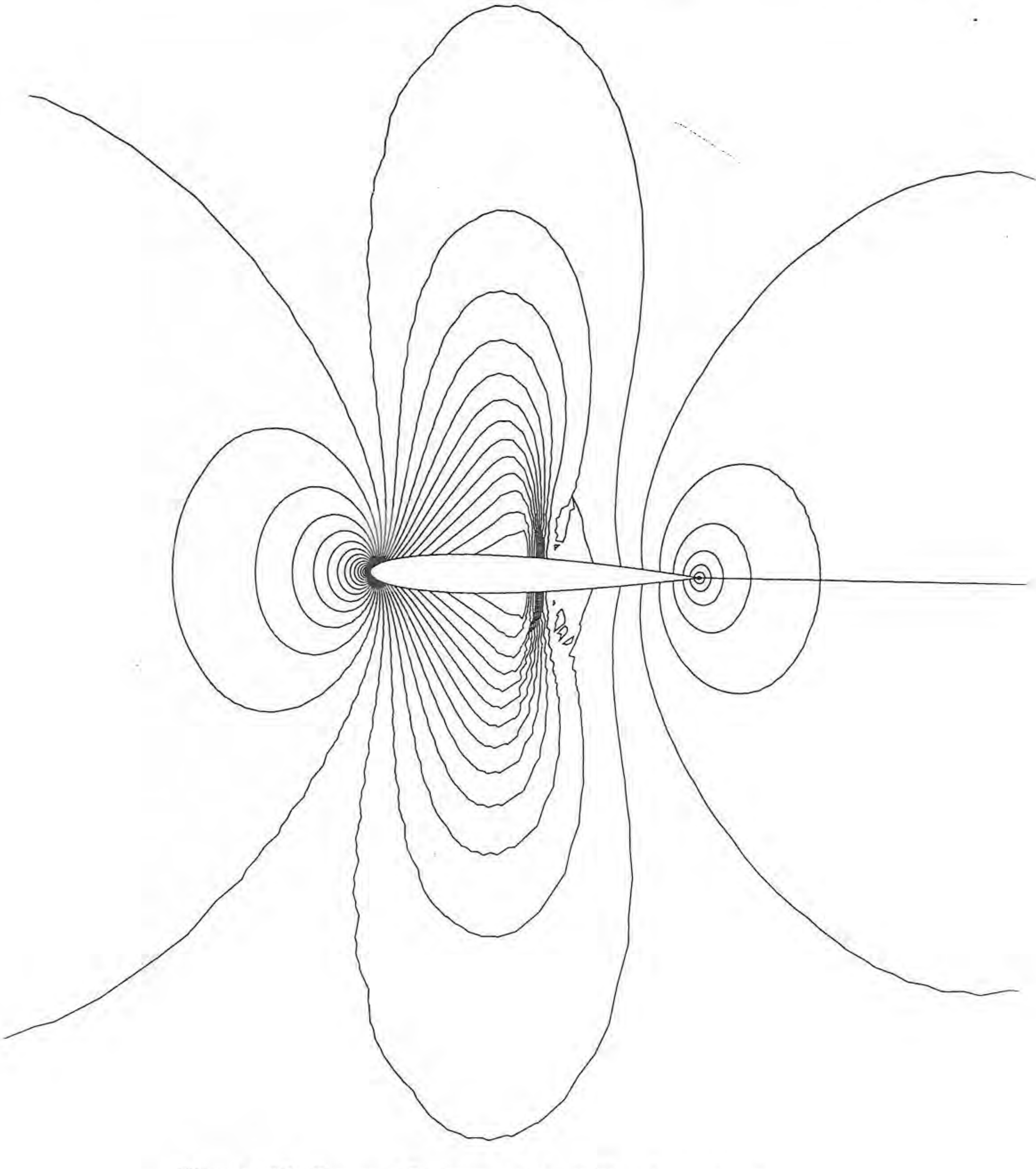

Figure 4.17 - Pressure Contours at M = 0.80 and zero incidence

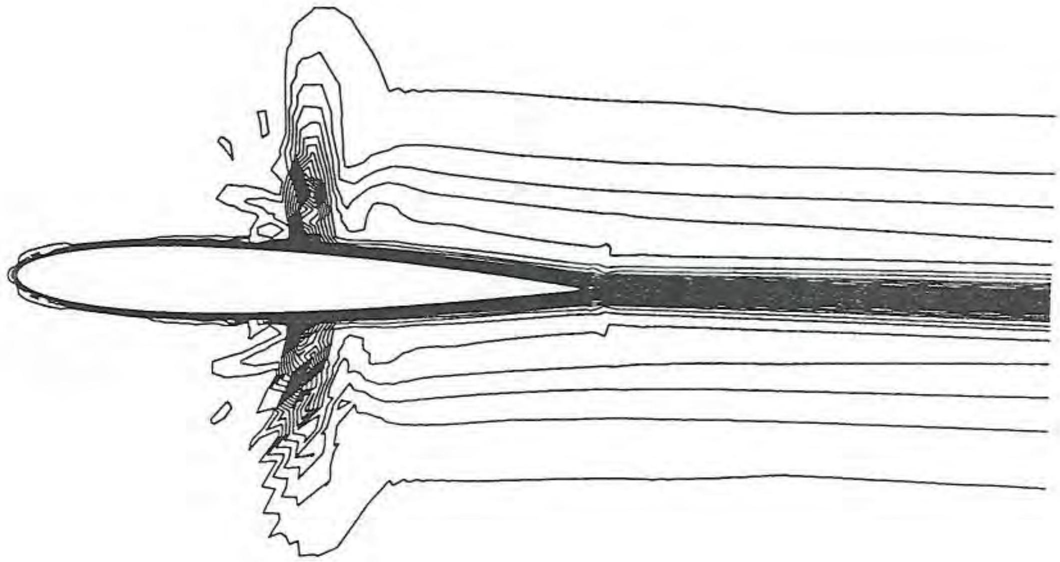

Figure 4.18 - Entropy contours

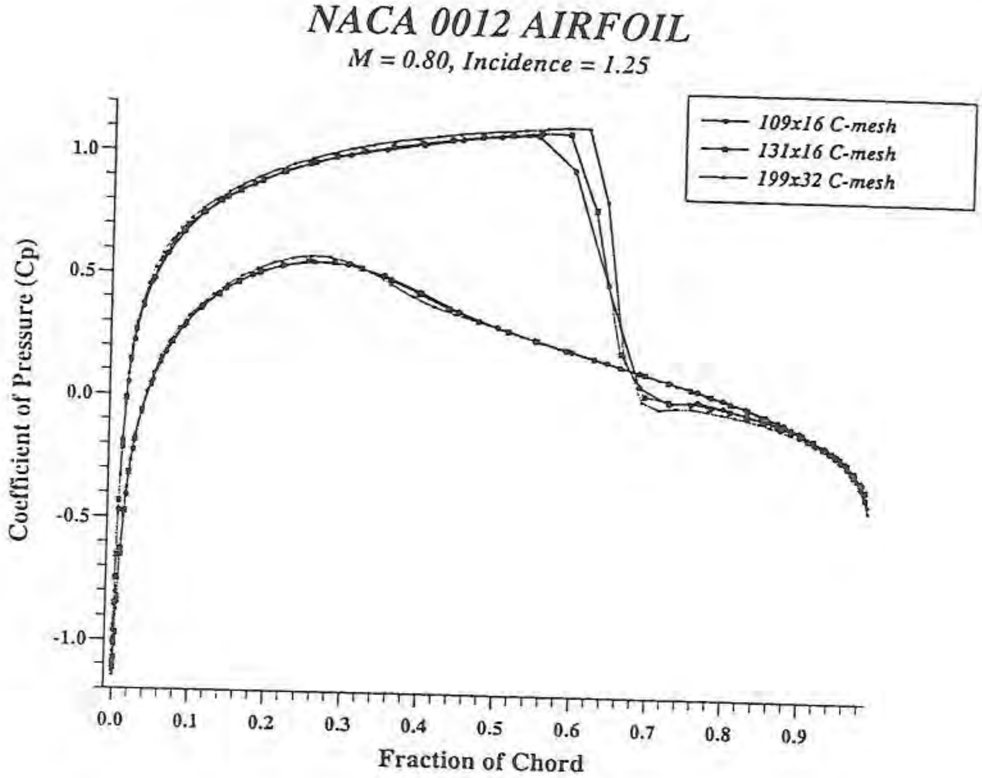

Figure 4.19

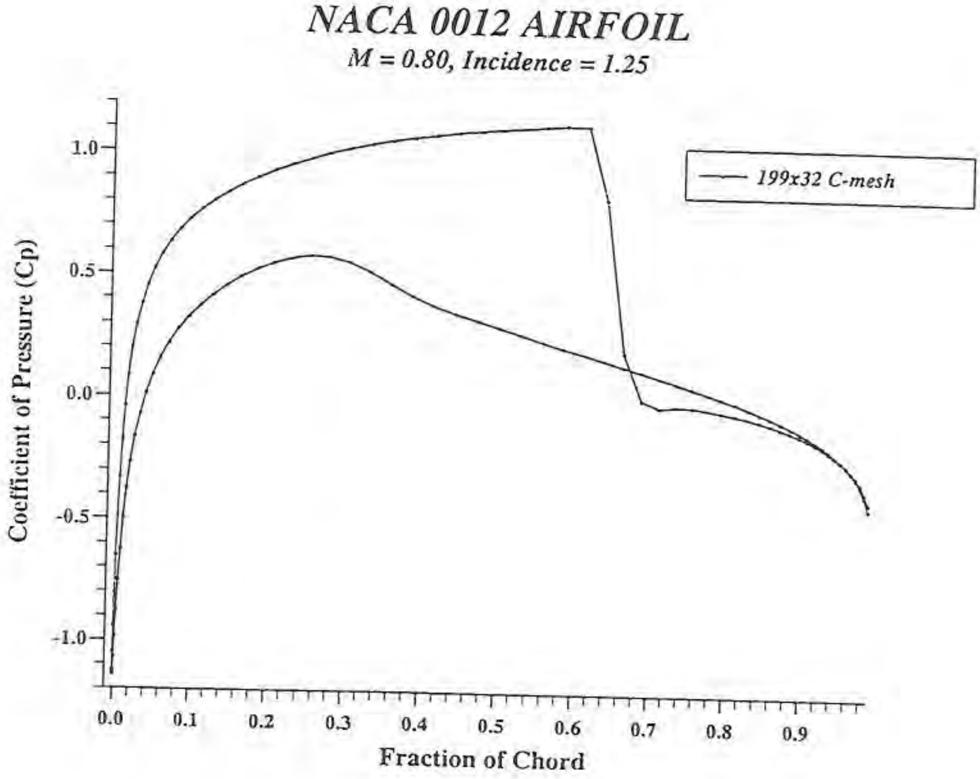

Figure 4.20

NACA 0012 AIRFOIL

M = 0.80, Incidence = 1.25

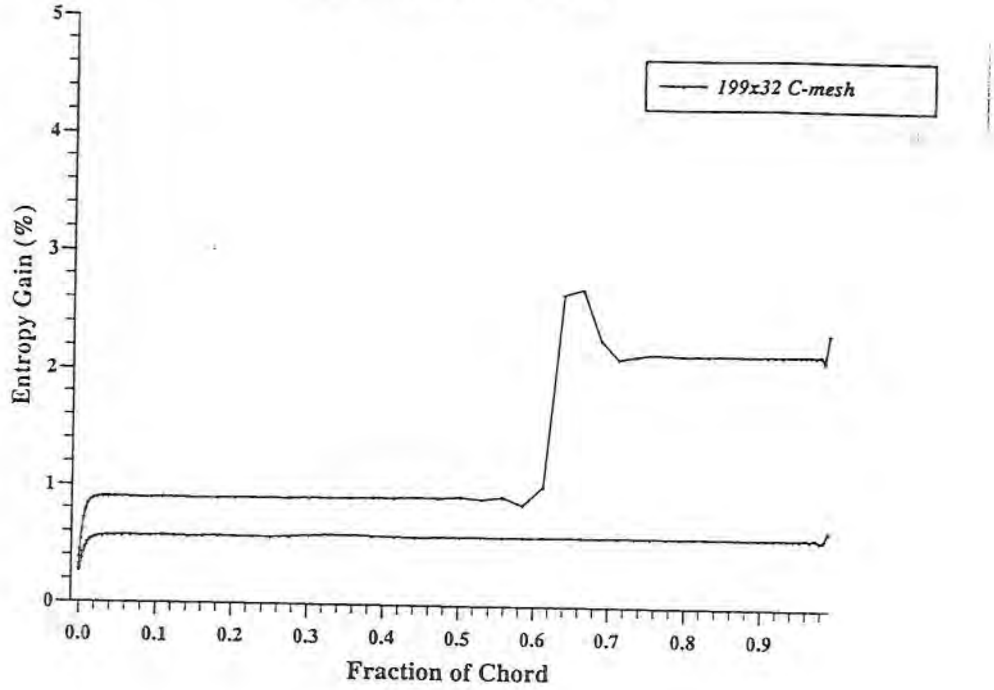

Figure 4.21

NACA 0012 AIRFOIL

Entropy Gain (%)

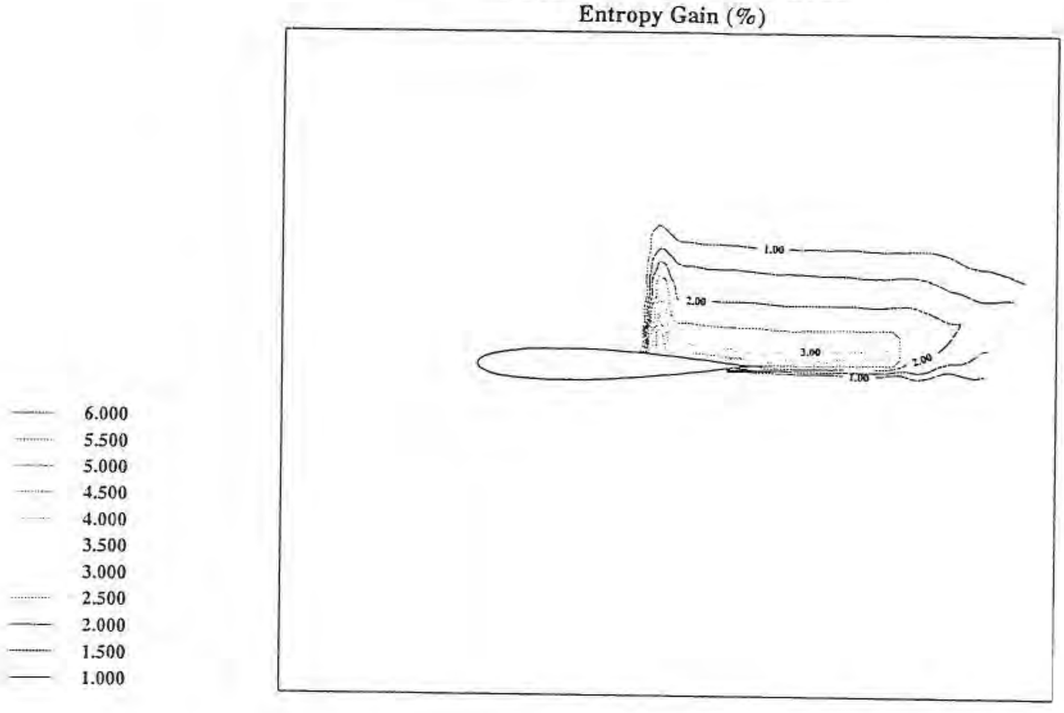

Figure 4.22

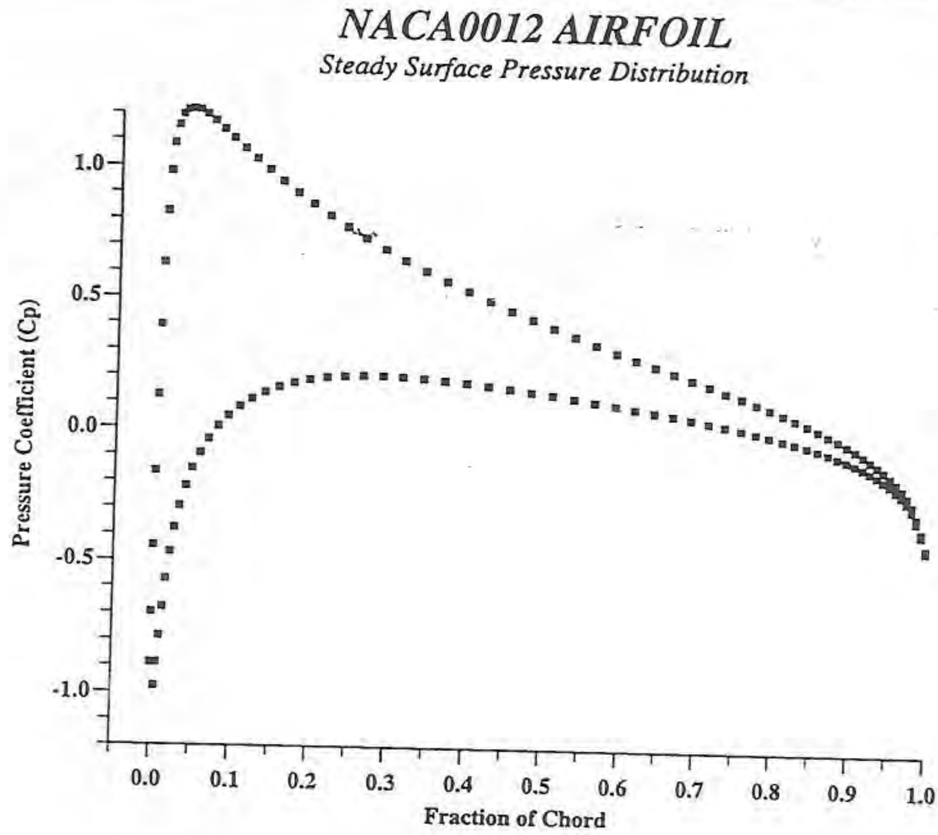

Figure 4.23

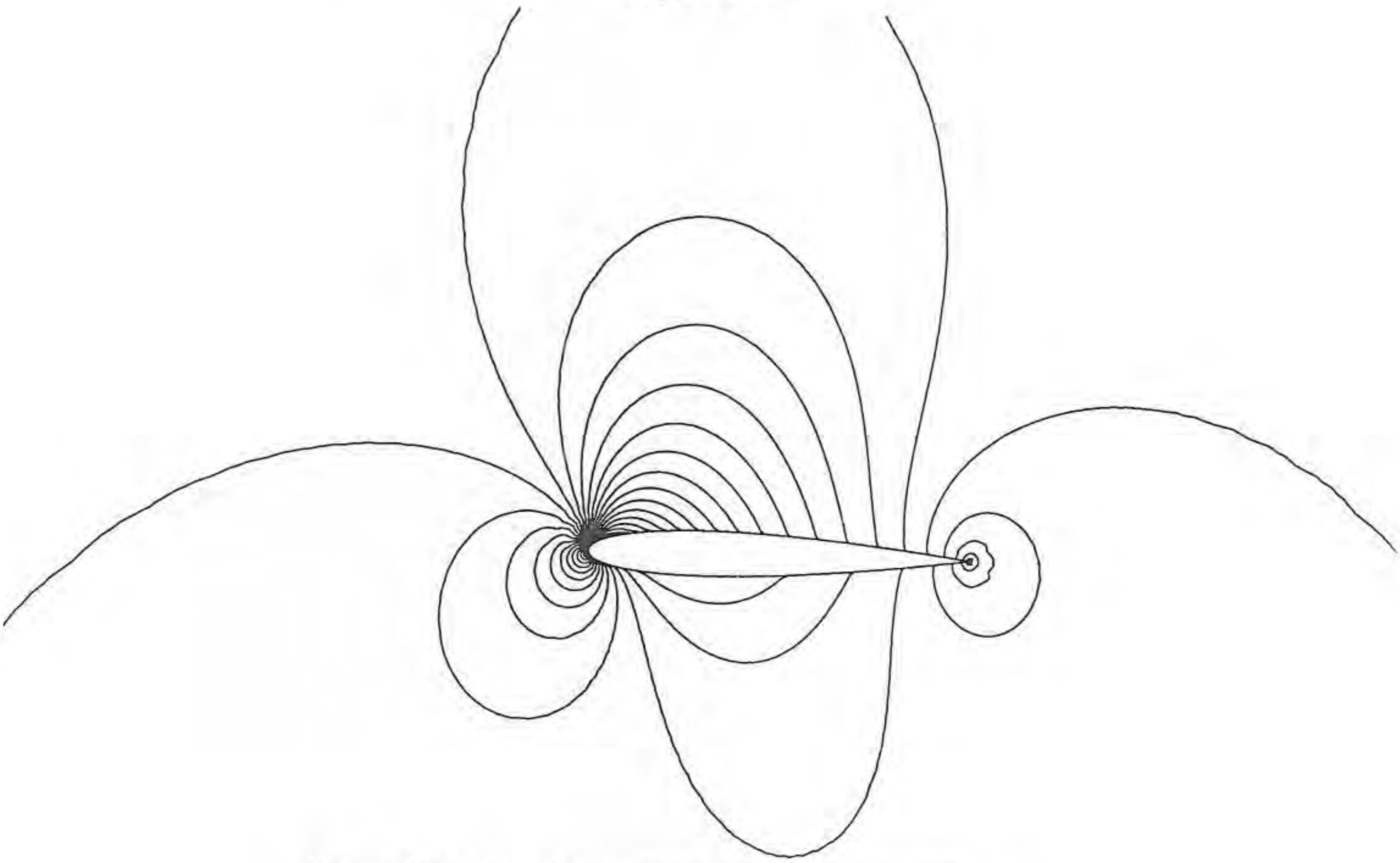

Figure 4.24 - Steady pressure contours, AGARD case 1

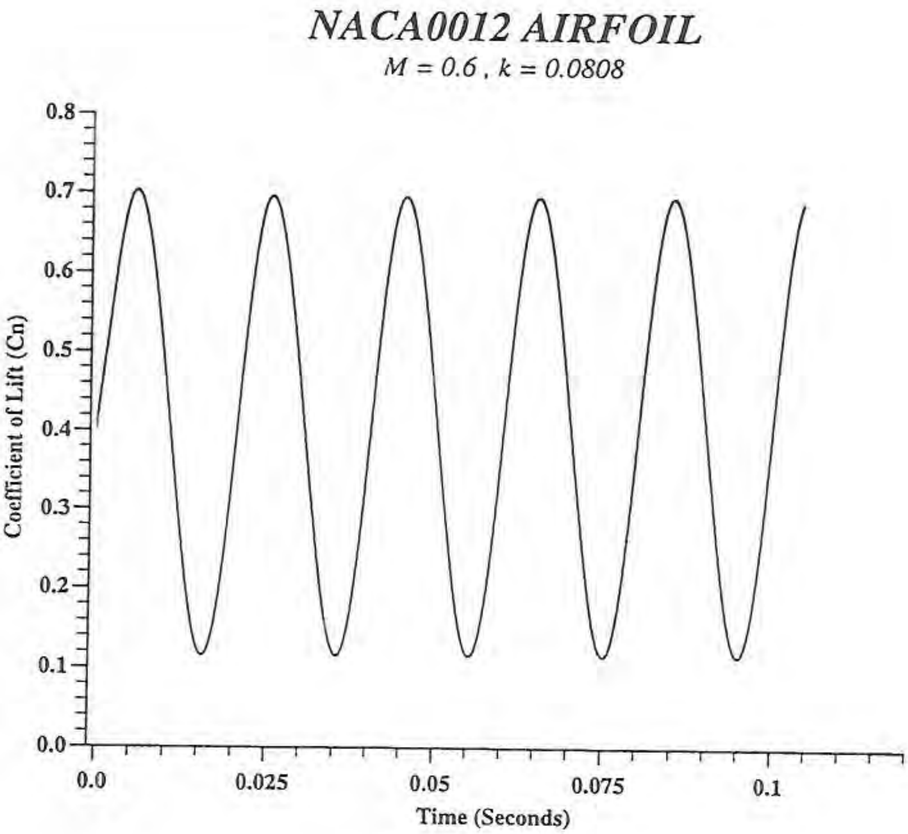

Figure 4.25

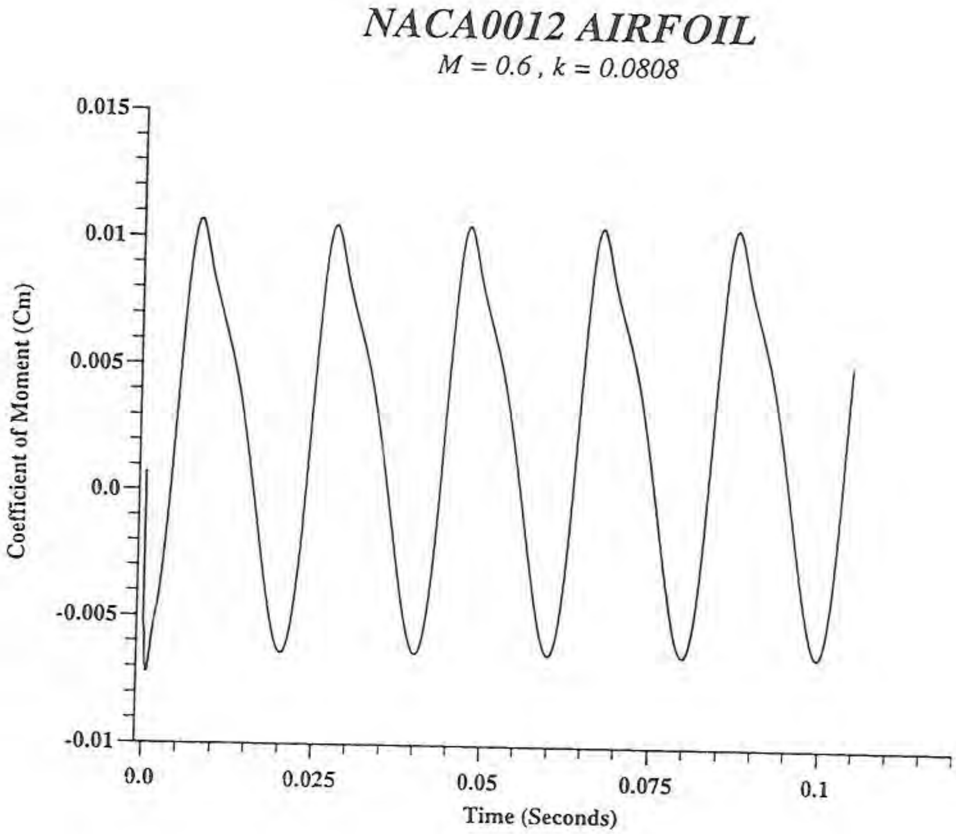

Figure 4.26

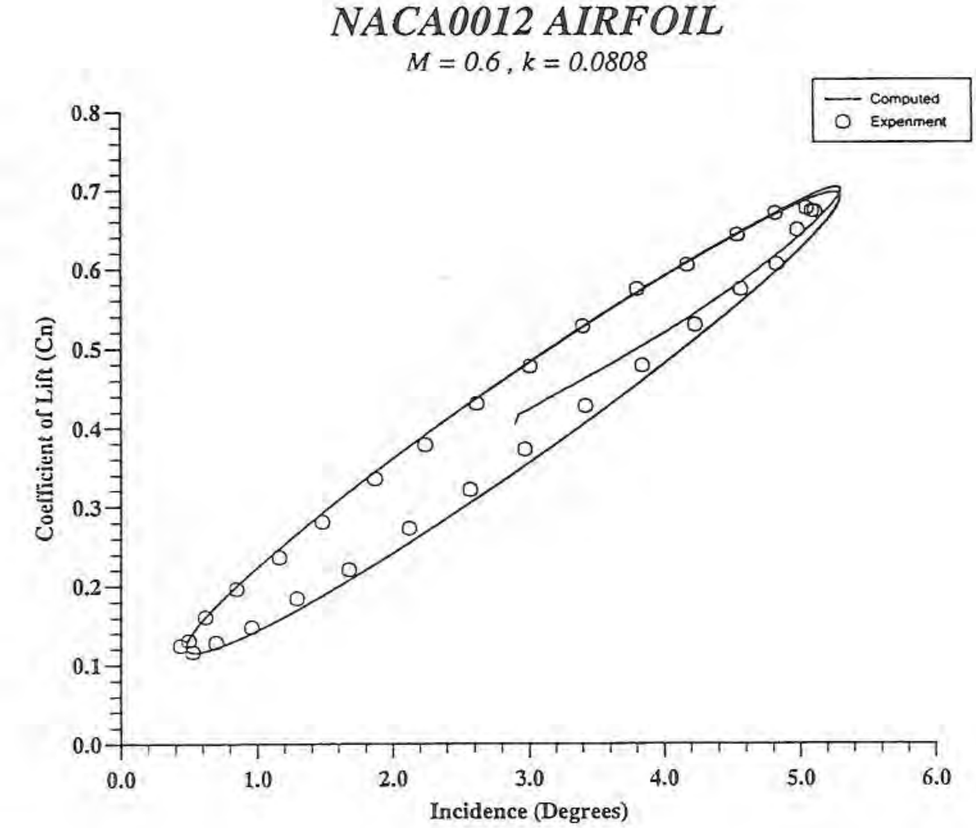

Figure 4.27

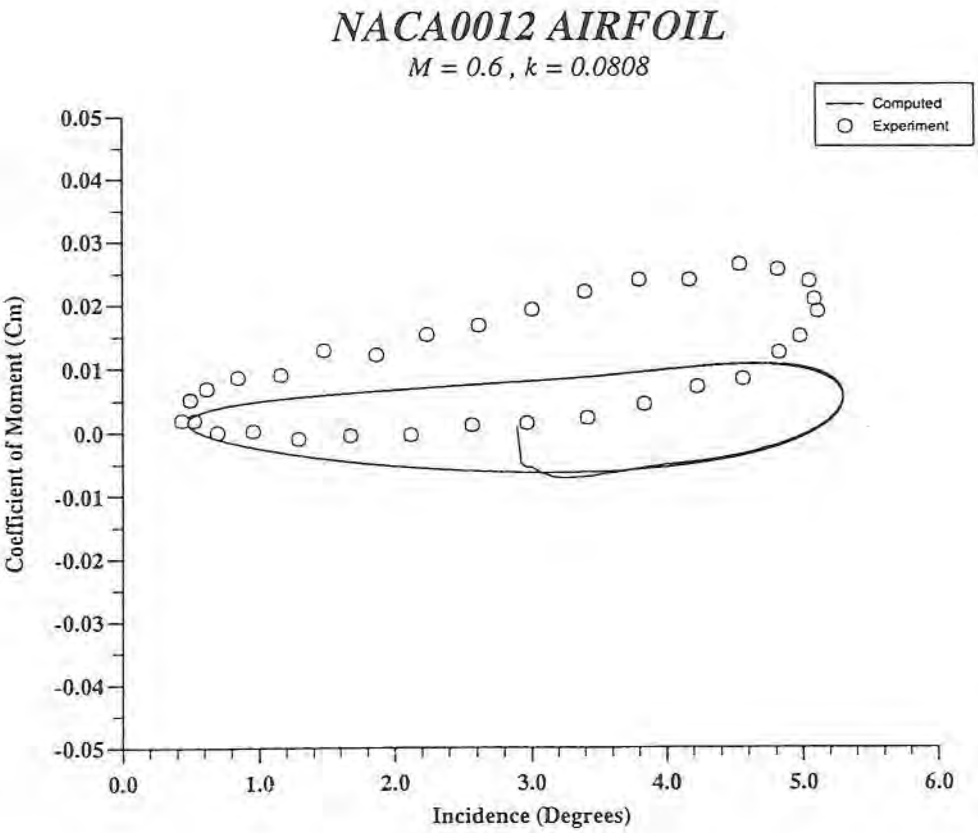

Figure 4.28

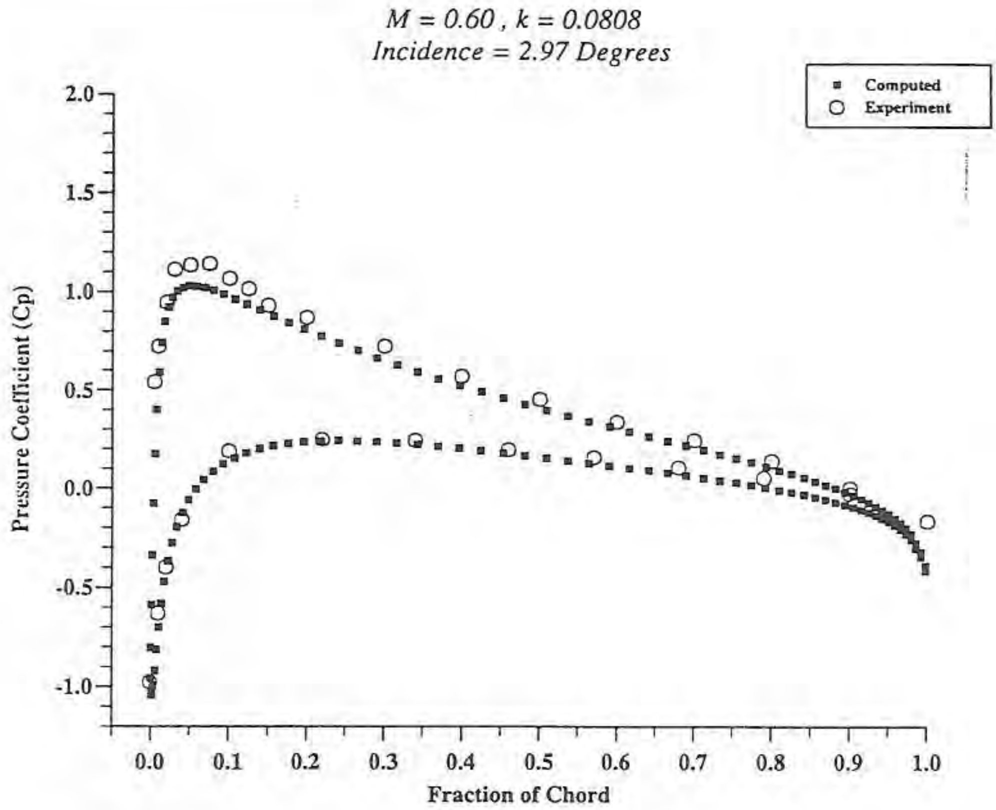

Figure 4.29a

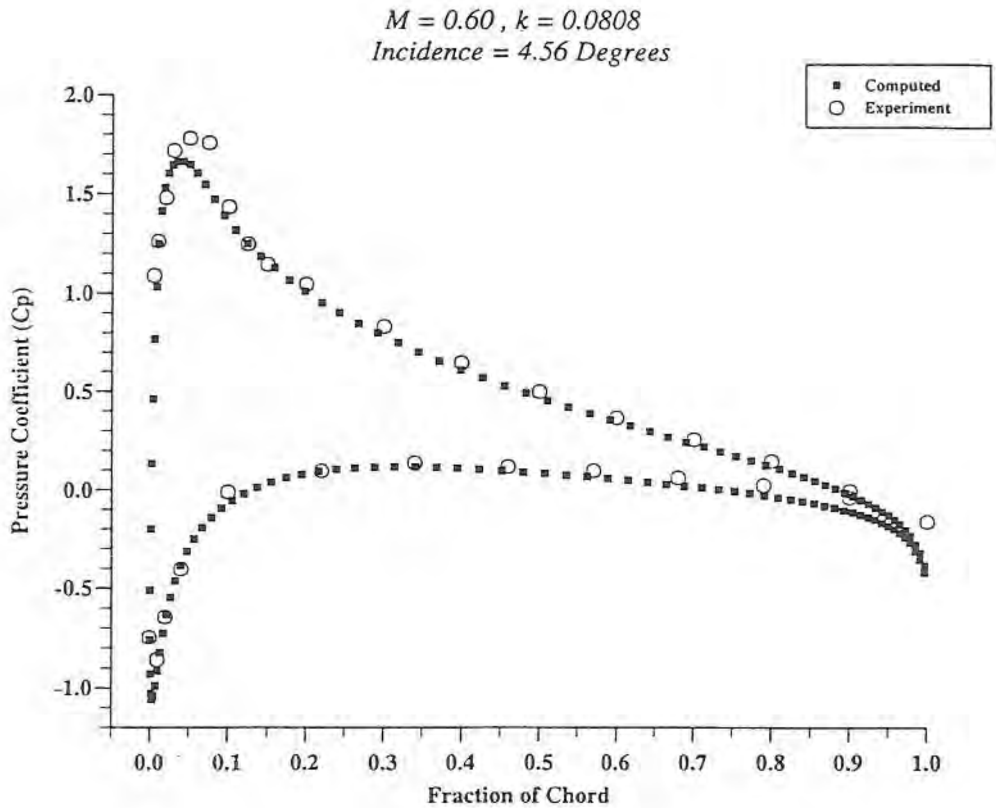

Figure 4.29b

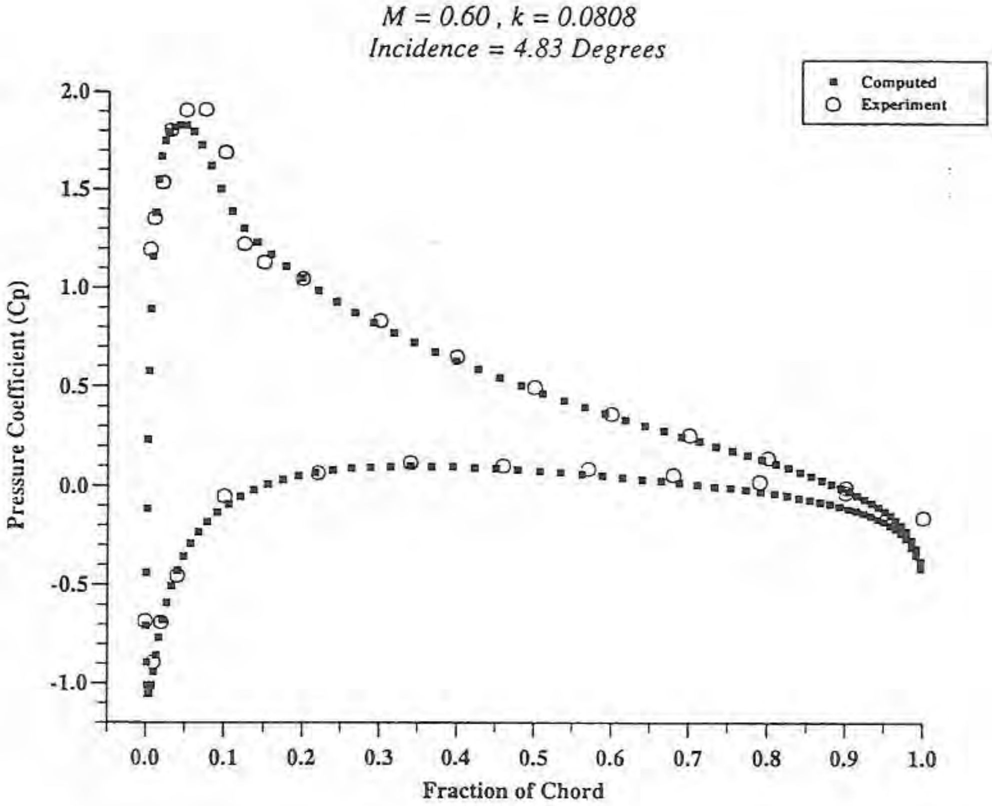

Figure 4.29c

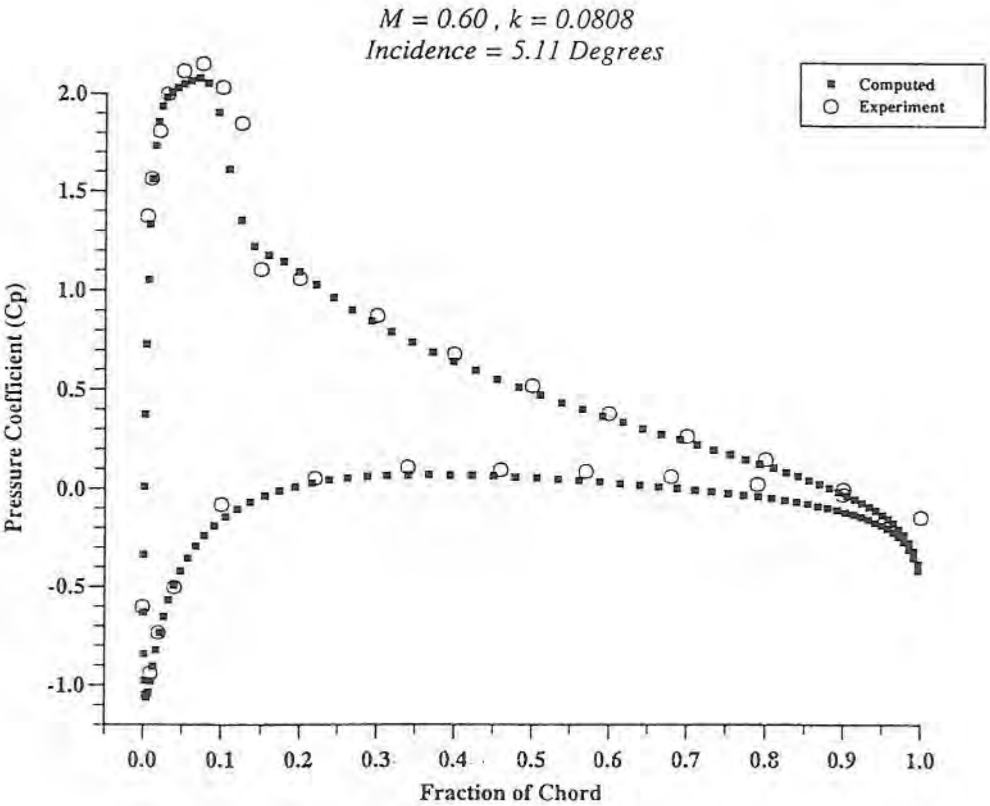

Figure 4.29d

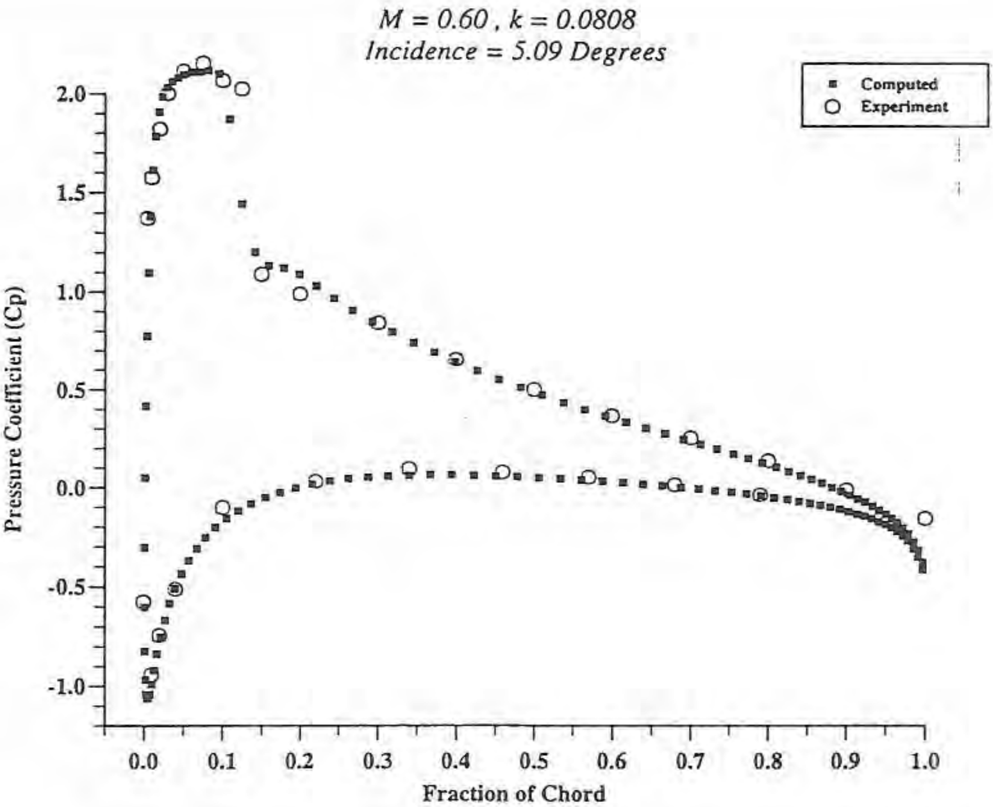

Figure 4.29e

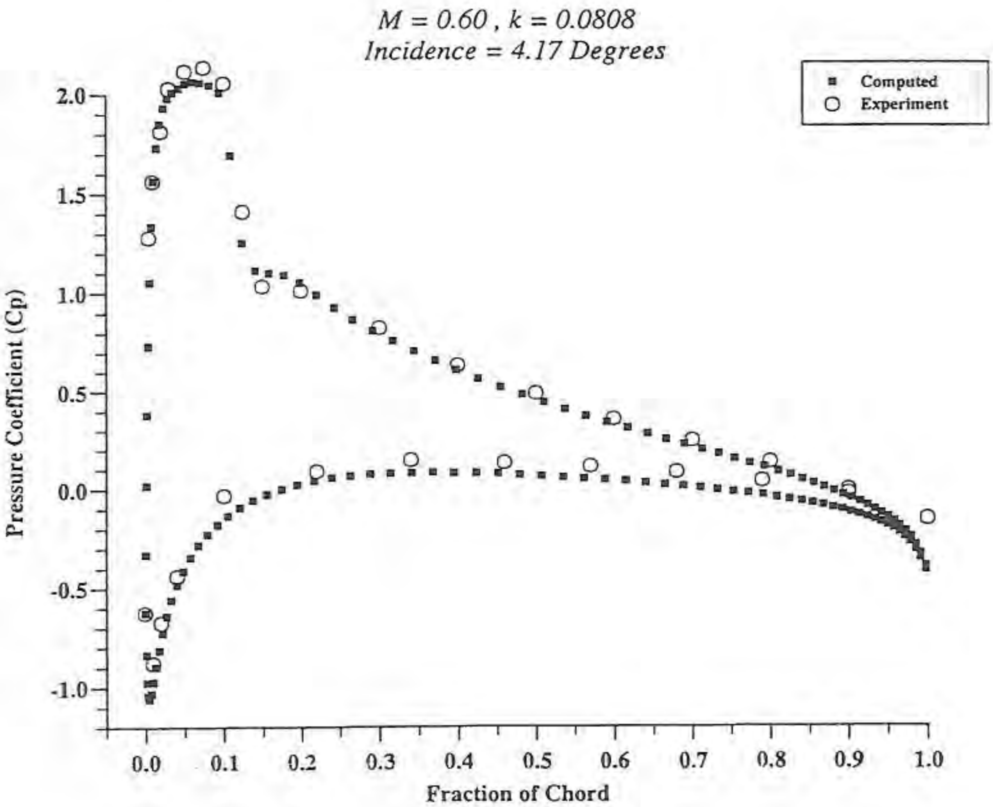

Figure 4.29f

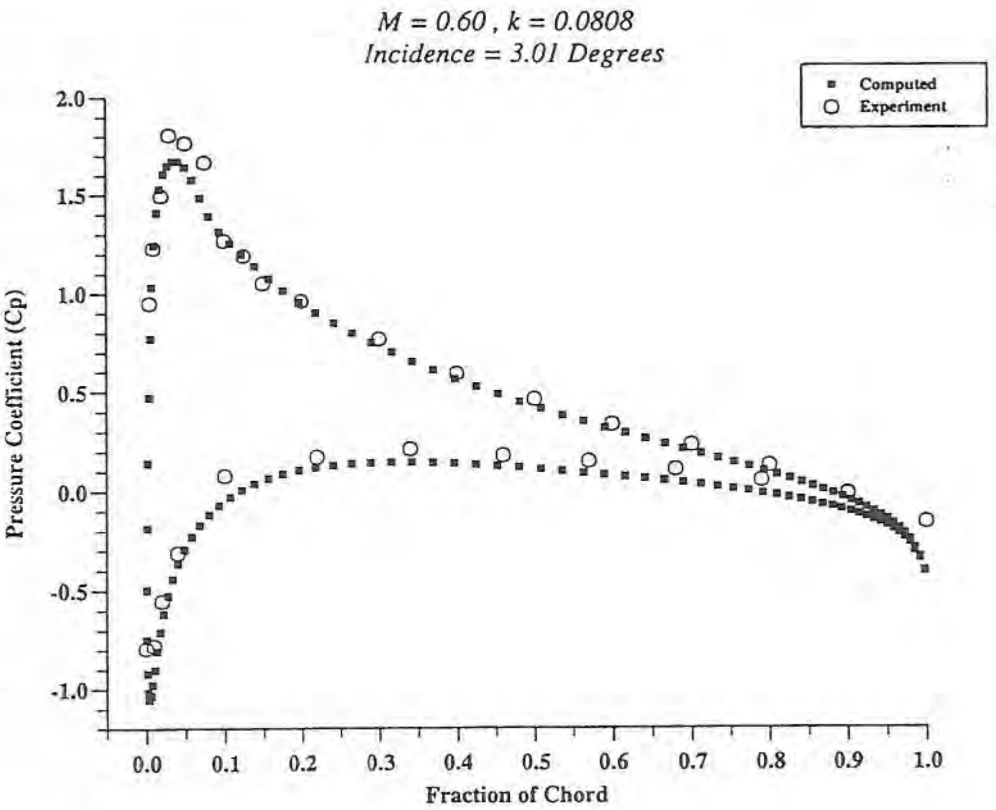

Figure 4.29g

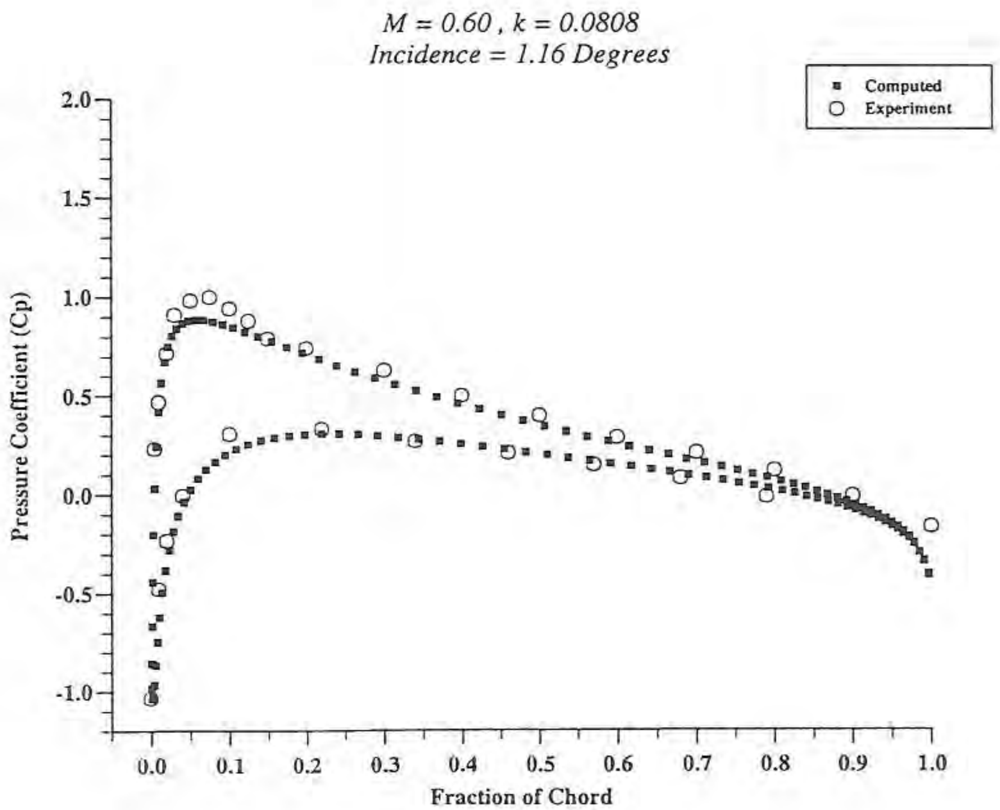

Figure 4.29h

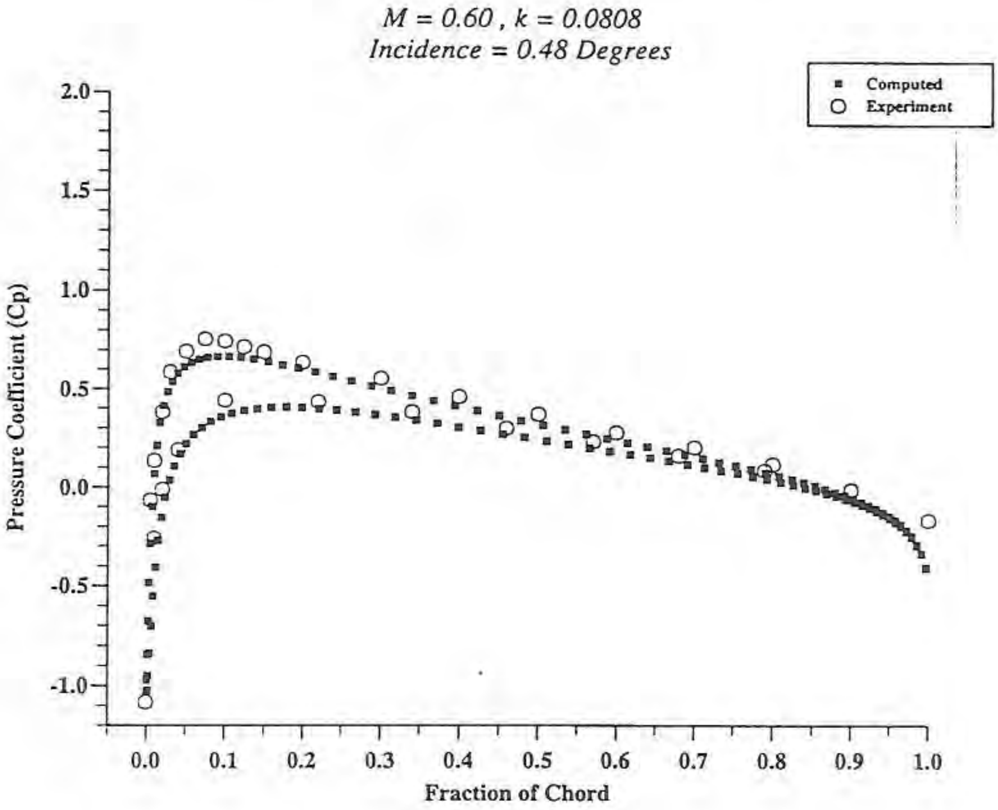

Figure 4.29i

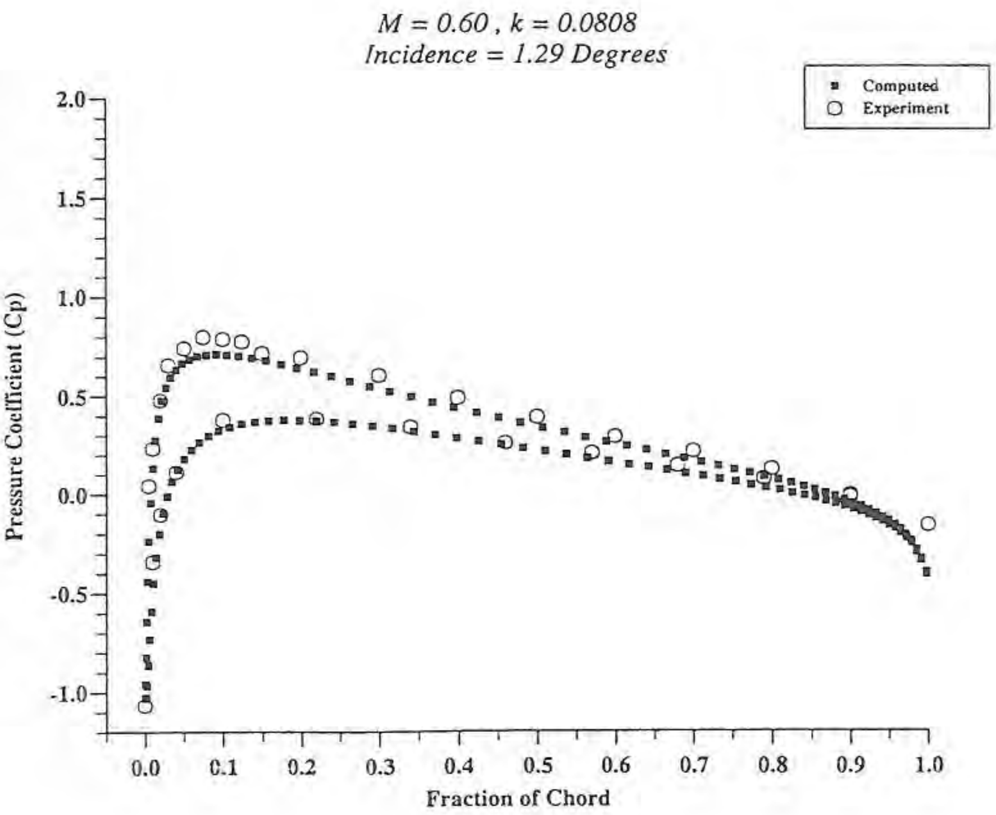

Figure 4.29j

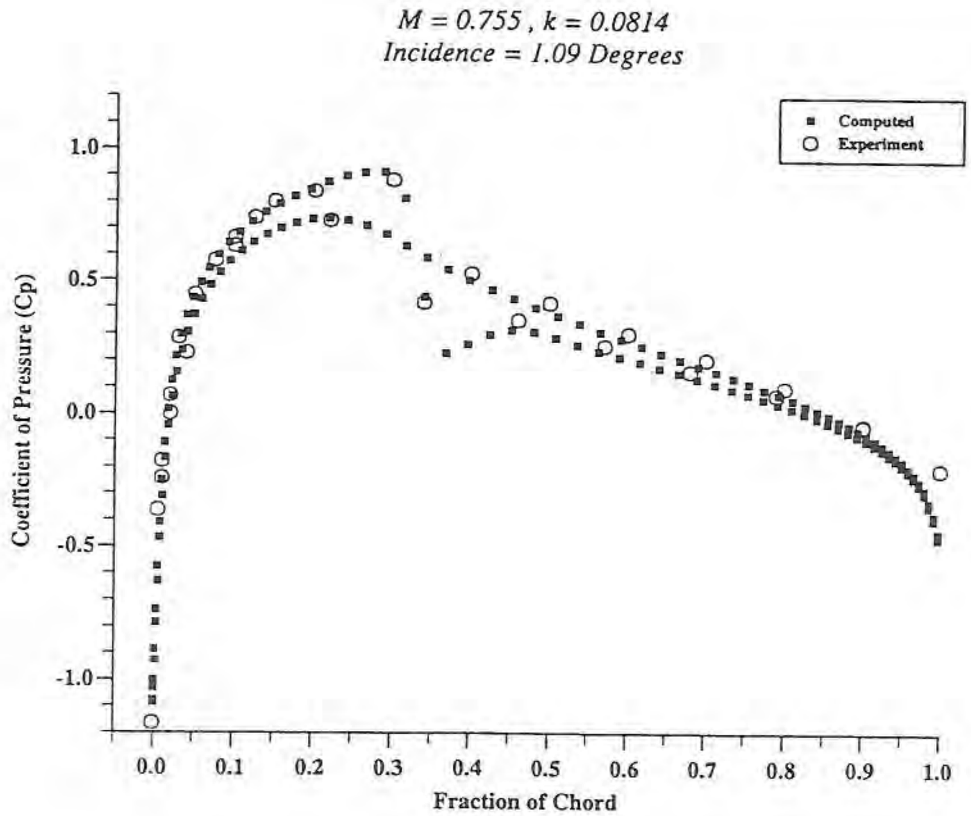

Figure 4.30a

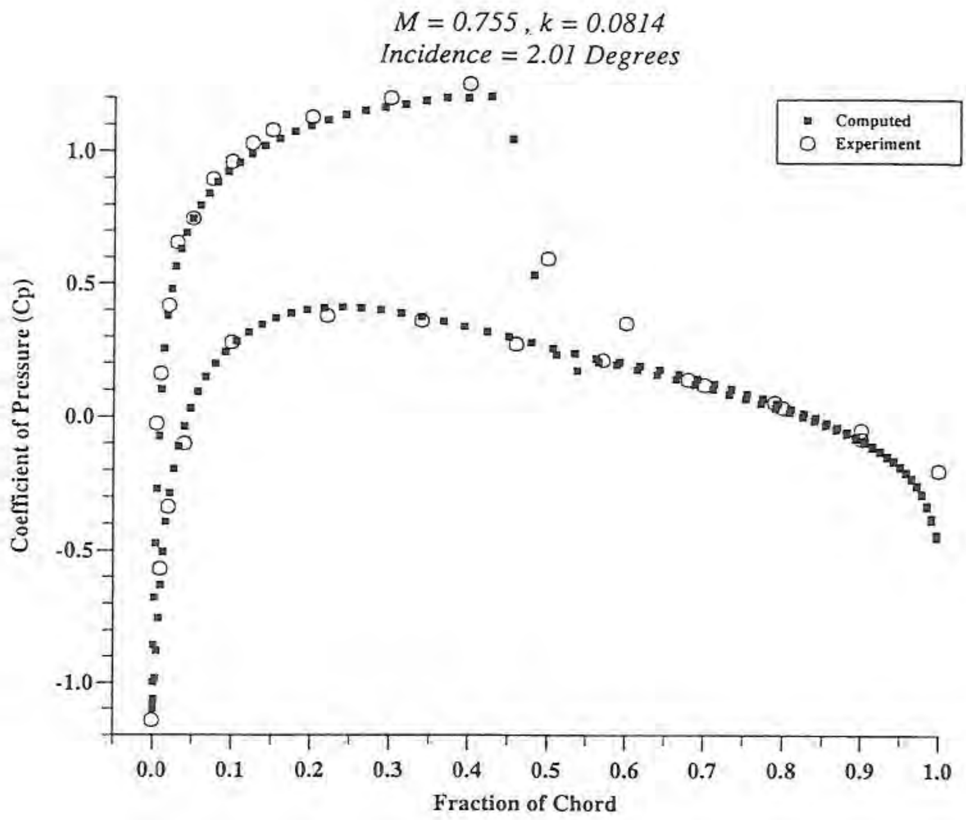

Figure 4.30b

M = 0.755 , k = 0.0814
Incidence = -2.41 Degrees

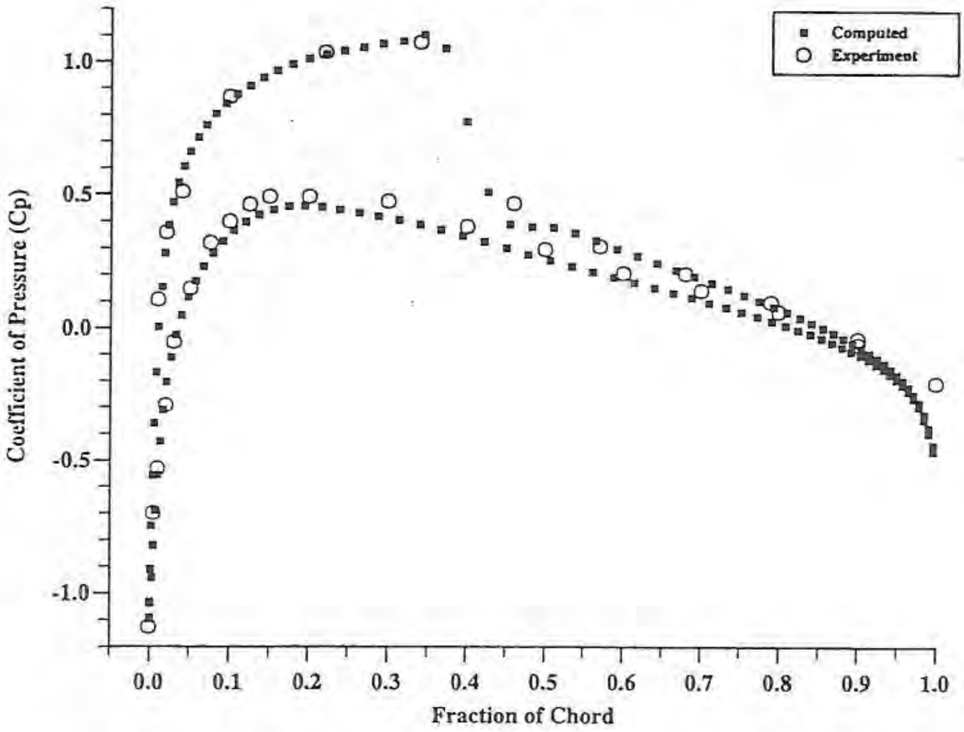

Figure 4.30c

M = 0.755 , k = 0.0814
Incidence = -2.00 Degrees

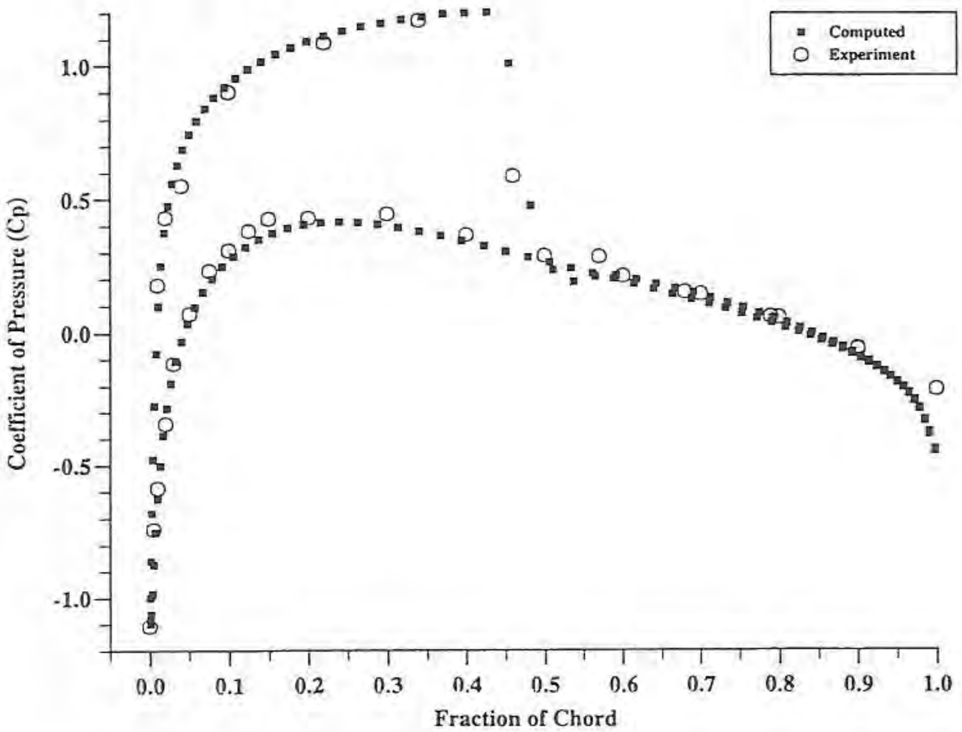

Figure 4.30d

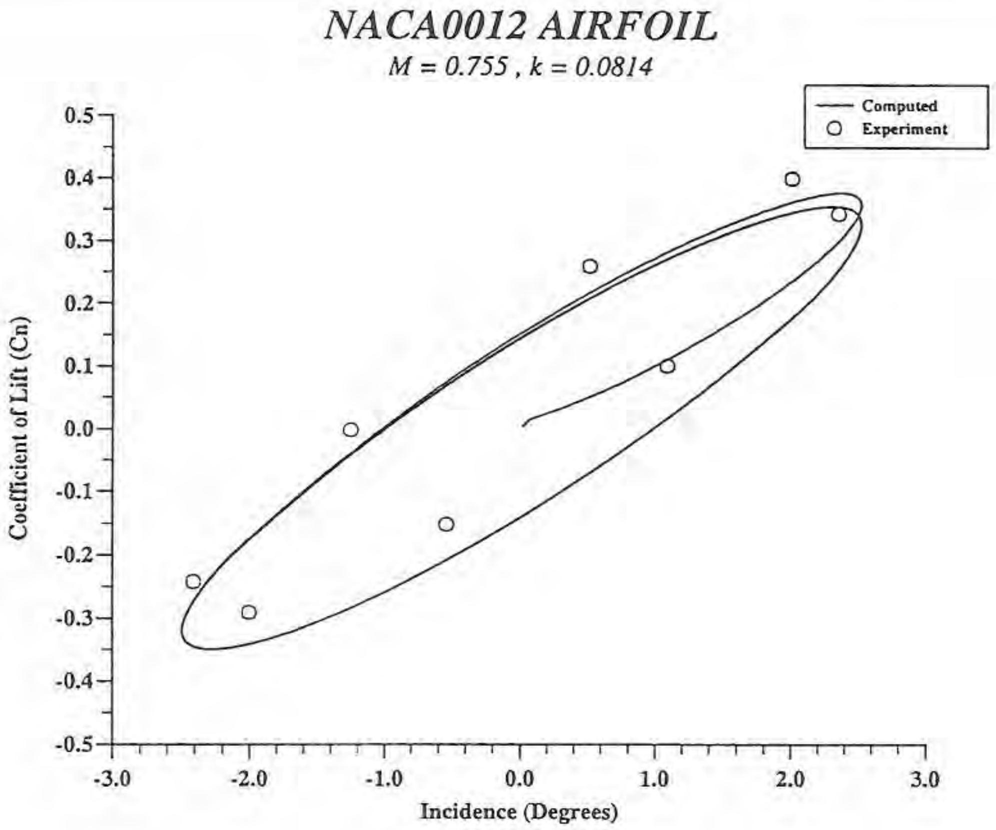

Figure 4.31

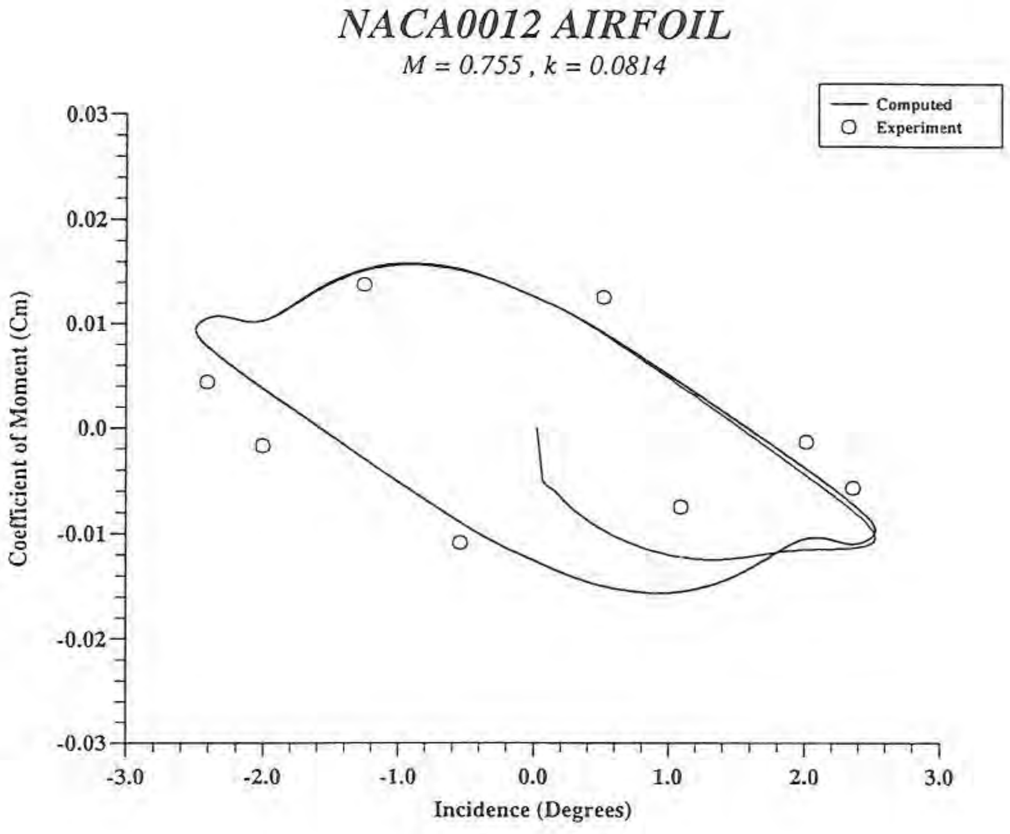

Figure 4.32

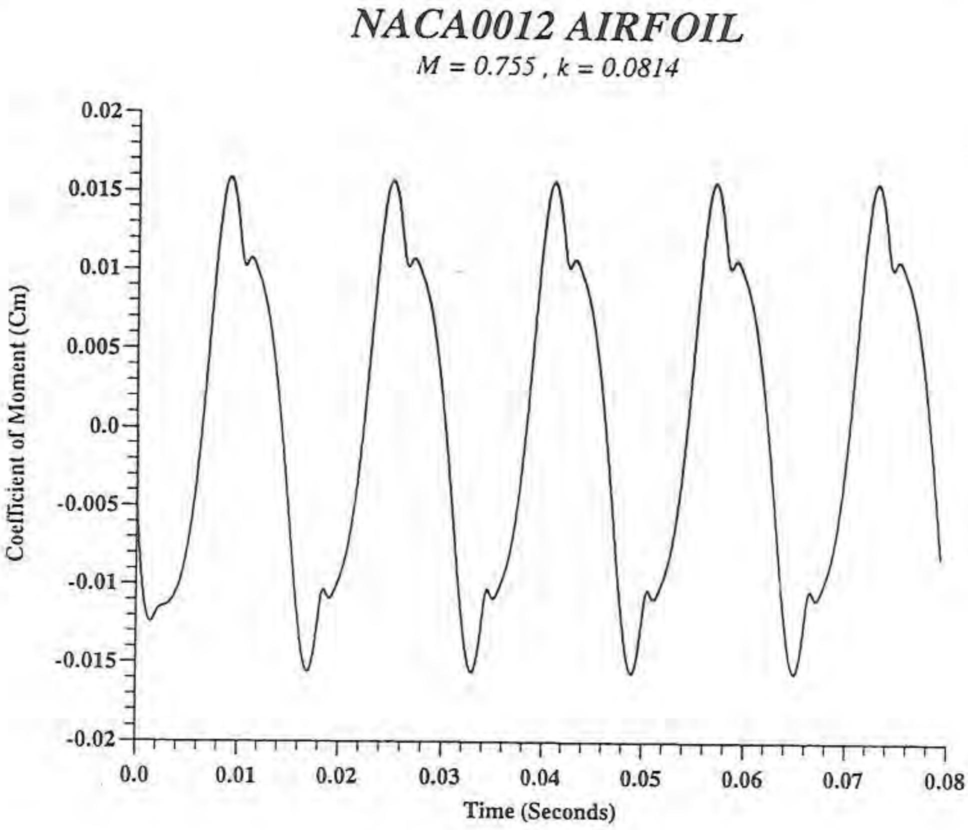

Figure 4.33

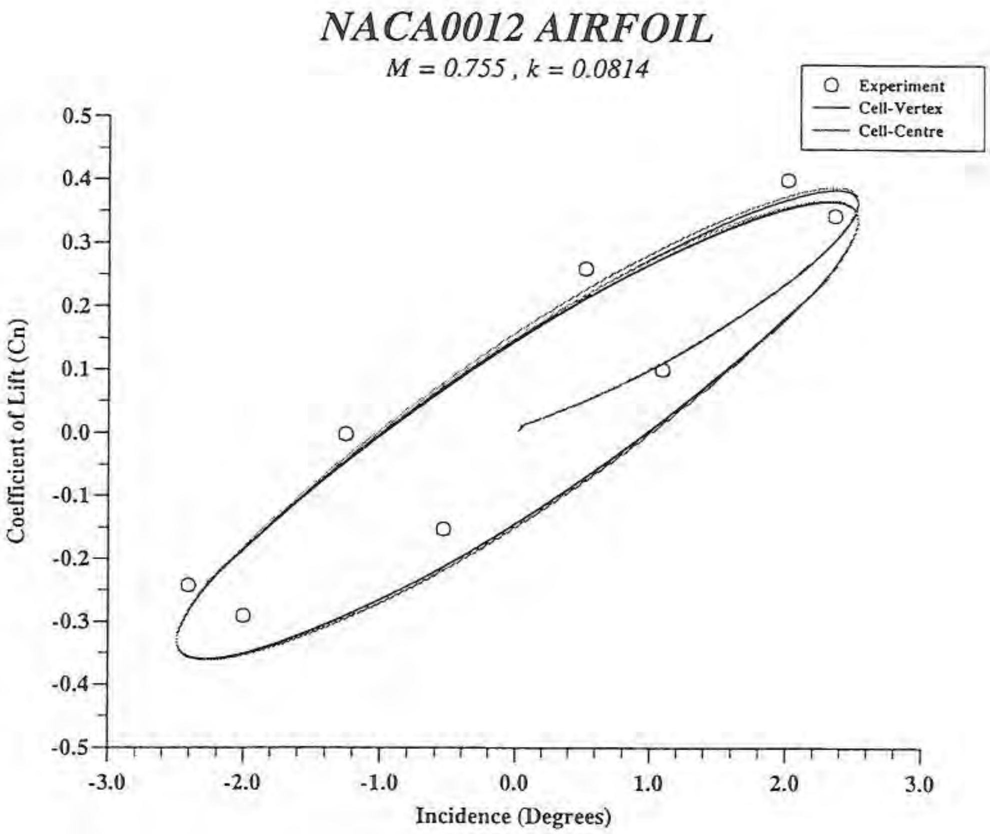

Figure 4.34

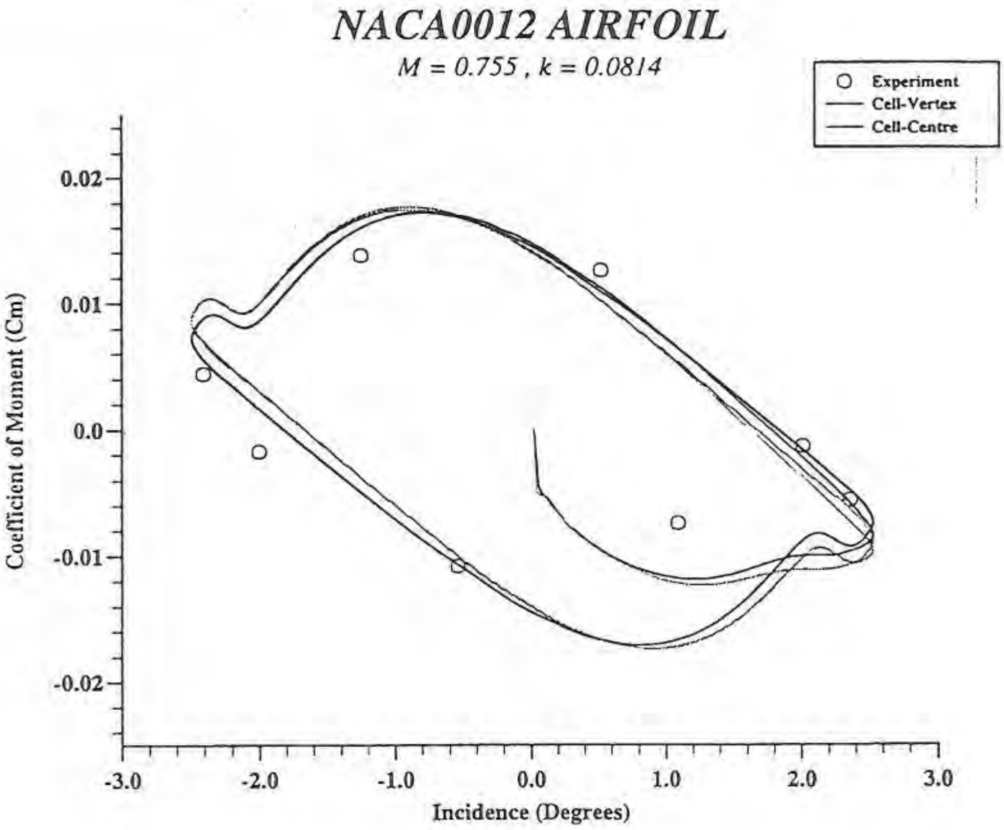
NACA0012 AIRFOIL
M = 0.755 , k = 0.0814
Experiment
Cell-Vertex
Cell-Centre
0.02
0.01
0.0
-0.01
-0.02
Coefficient of Moment (Cm)
-3.0
-2.0
-1.0
0.0
1.0
2.0
3.0
Incidence (Degrees)

Figure 4.35

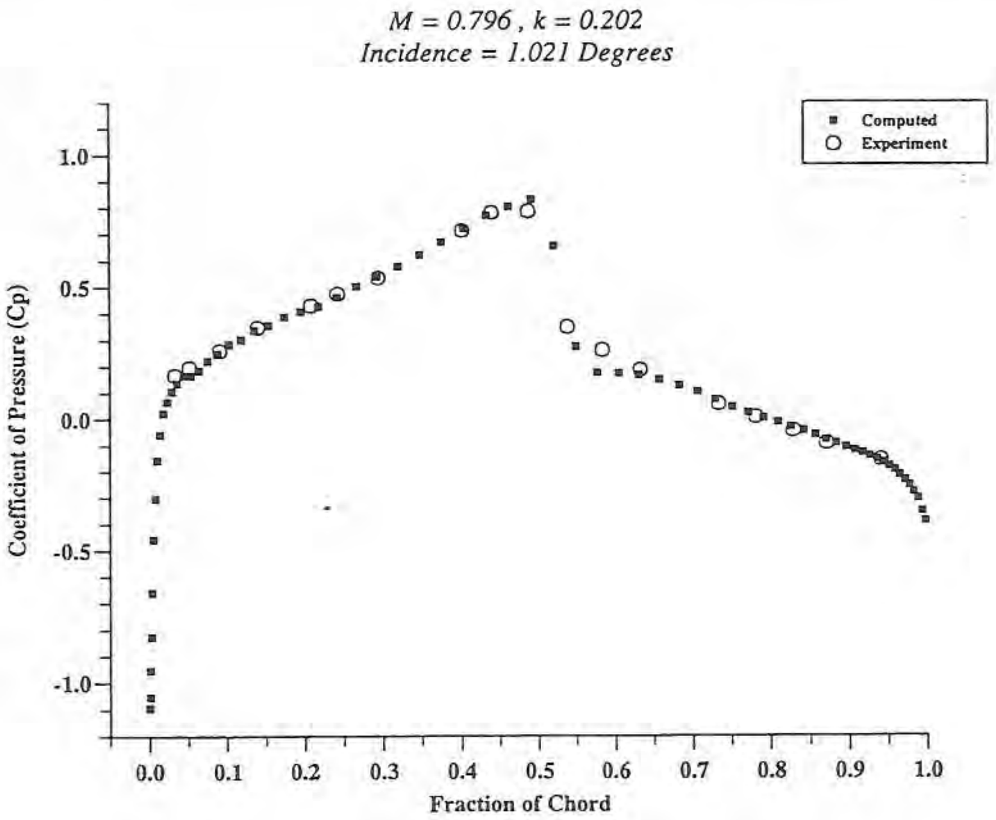

Figure 4.36a

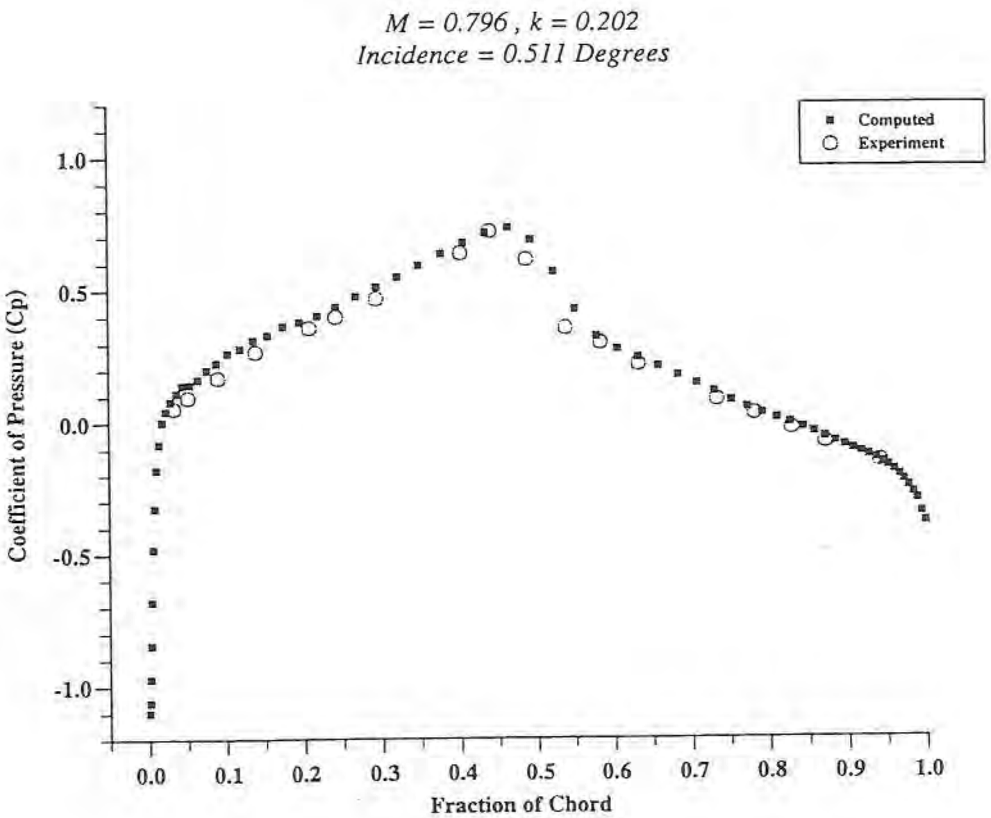

Figure 4.36b

M = 0.796 , k = 0.202
Incidence = 0.007 Degrees

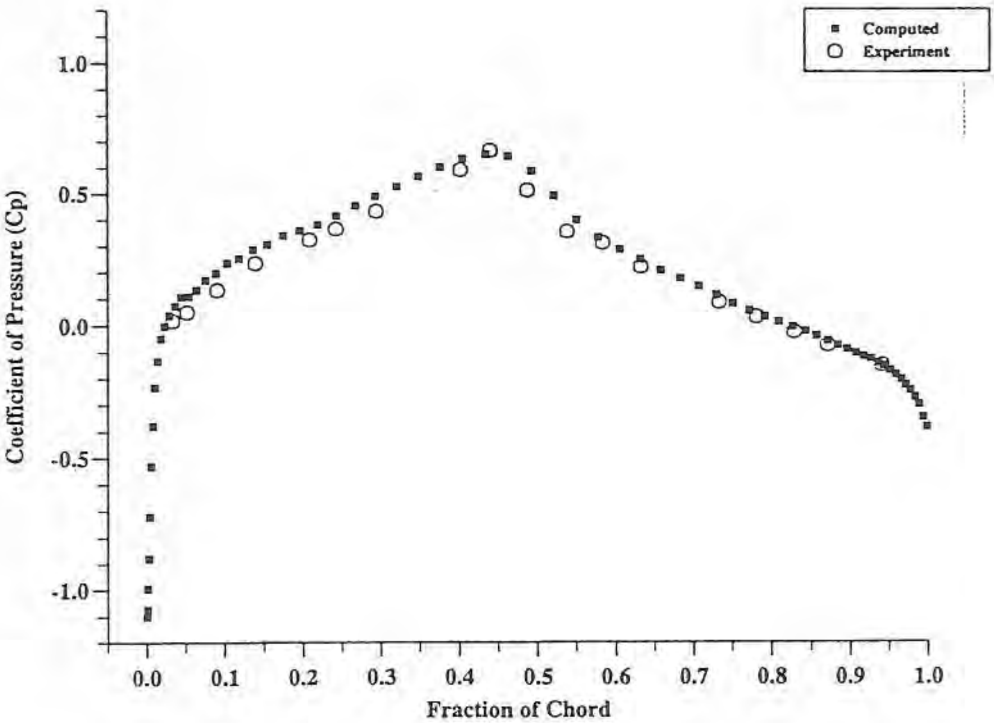

Figure 4.36c

M = 0.796 , k = 0.202
Incidence = -0.496 Degrees

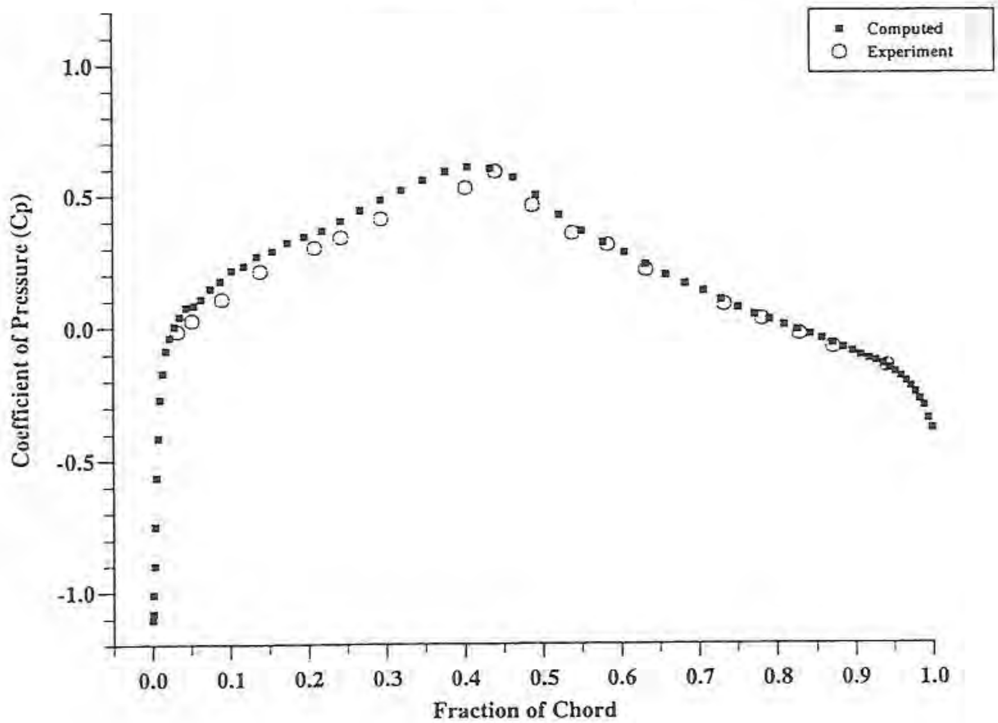

Figure 4.36d

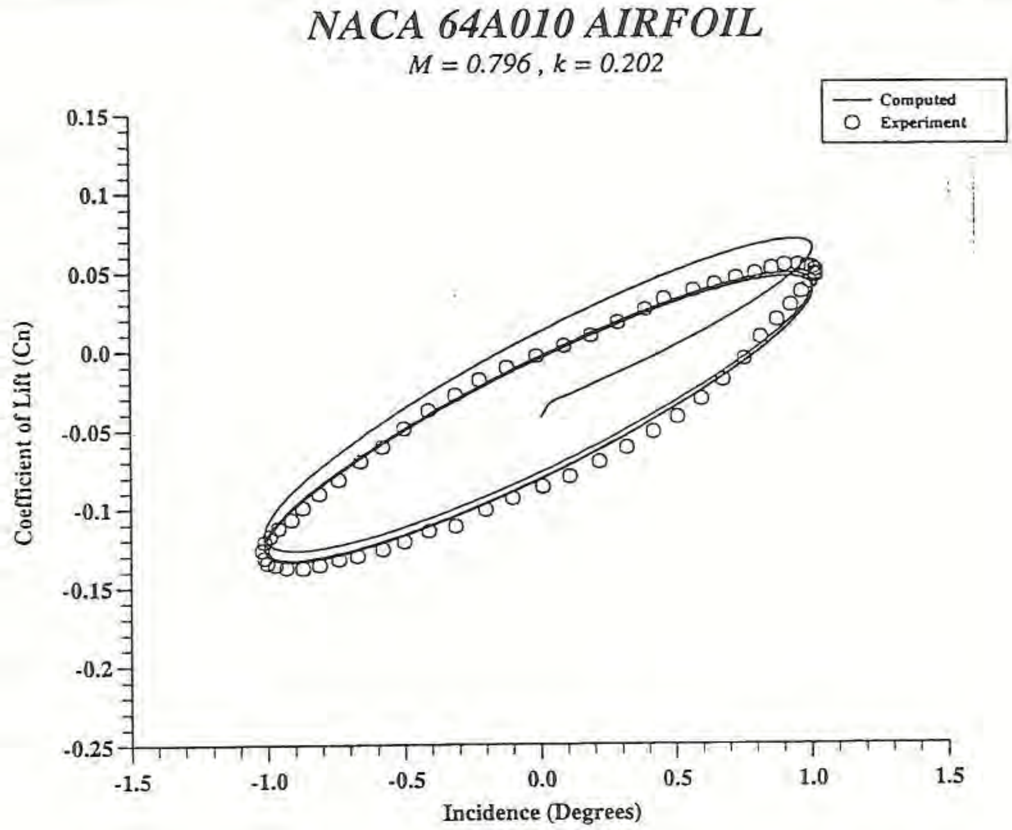

Figure 4.37

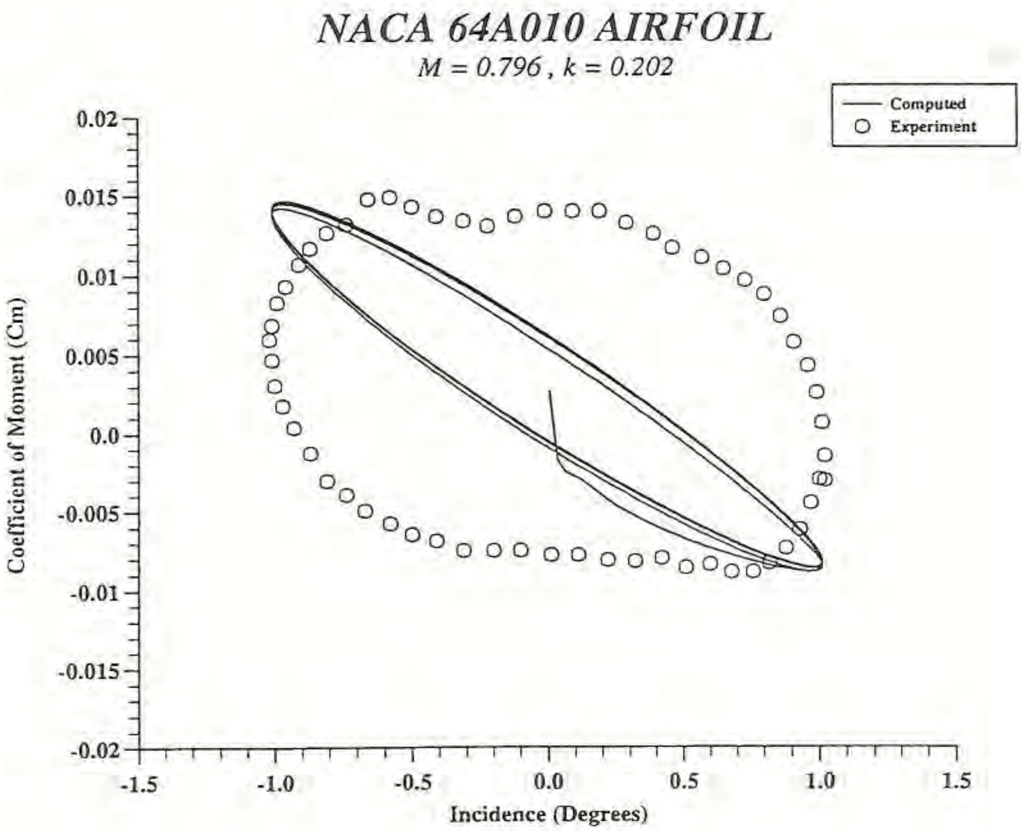

Figure 4.38

Chapter 5

Validation of Aeroelasticity Model

It will take you a lifetime, and you will regret it.
Hermann Hesse - The Glass Bead Game

5.0 About this Chapter

The aeroelasticity test case has been described in part 5.1. Part 5.2 details the steady flow modelling issues of interest. Part 5.3 describes the structural model used in this validation study. Part 5.4 presents the results of the numerical calculations performed. In part 5.5, the aeroelasticity flutter boundaries predicted numerically are compared to those available in the literature. Finally, in part 5.6, the main conclusions of this validation study have been enumerated.

5.1 Problem Definition

The experimental data for the validation of aeroelasticity results are very rare. This has meant that most attempts at validation exercises have tended to rely on the numerical work, an approach which is also adopted in this work. In this sense, the following study is more of a demonstration of the aeroelasticity model developed and outlined in chapter 3.

One of the main study cases for aeroelasticity investigation is that of the NACA-64a006 airfoil in free-stream air flow. There are many examples of the results for this case available in the literature. In this study, comparisons are made against results from references [17-18]. This choice is appropriate as the results from the above references are based on non-linear time-domain analyses which are directly comparable with the results produced here.

The geometry of the NACA-64a006 airfoil has been taken from reference [55] which provides a tabulated data of the airfoil profile.

5.2 Steady Flow Model

The first step in an aeroelasticity analysis is the determination of the steady flow. For the airfoil calculations outlined below, the steady flow calculation consists of introducing the uniform incoming flow over the entire computational domain and imposing the airfoil boundary conditions. The resultant residuals are then eliminated by the time-marching procedure. The steady solution is reached when the residuals become small enough to be considered as insignificant. Since time-accuracy is not required for steady flow calculations, local time stepping may be employed.

Steady flow calculations are performed on a typical C-mesh, as shown in figure 5.1. A 96x16 mesh is used with 66 points on the airfoil surface. The far-field boundary is set at 15 chords away from the airfoil.

A point of interest is the treatment of the trailing edge point and the grid nodes on the wake-line. The wake-line is, in fact, defined by two sets of coincident points. The residuals for each of these points is defined from their corresponding control volumes (T) and (B) as shown in figure 5.2a. The residuals from control volumes (T) and (B) are then added together to form the total residual for the corresponding grid nodes. So the pair of coincident nodes on the wake-line will return the same flow values.

The same treatment at the trailing edge node, however, leads to a loss of geometry as shown for the control volume (t) in figure 5.2a. A proper control volume definition is derived from a six point arrangement as shown for the control volume (b) at the trailing edge node (the five points marked plus the trailing edge node itself). This is the treatment adopted here. The total residual for the pair of trailing edge nodes is then obtained by adding the residuals from control volumes (b) and (t).

Of course, the special treatment of the wake-line, is not required in a Cell-Centre model. In the latter case, the flow variables are not being solved for on the wake-line itself, as shown in figure 5.2b and hence no special treatment is required.

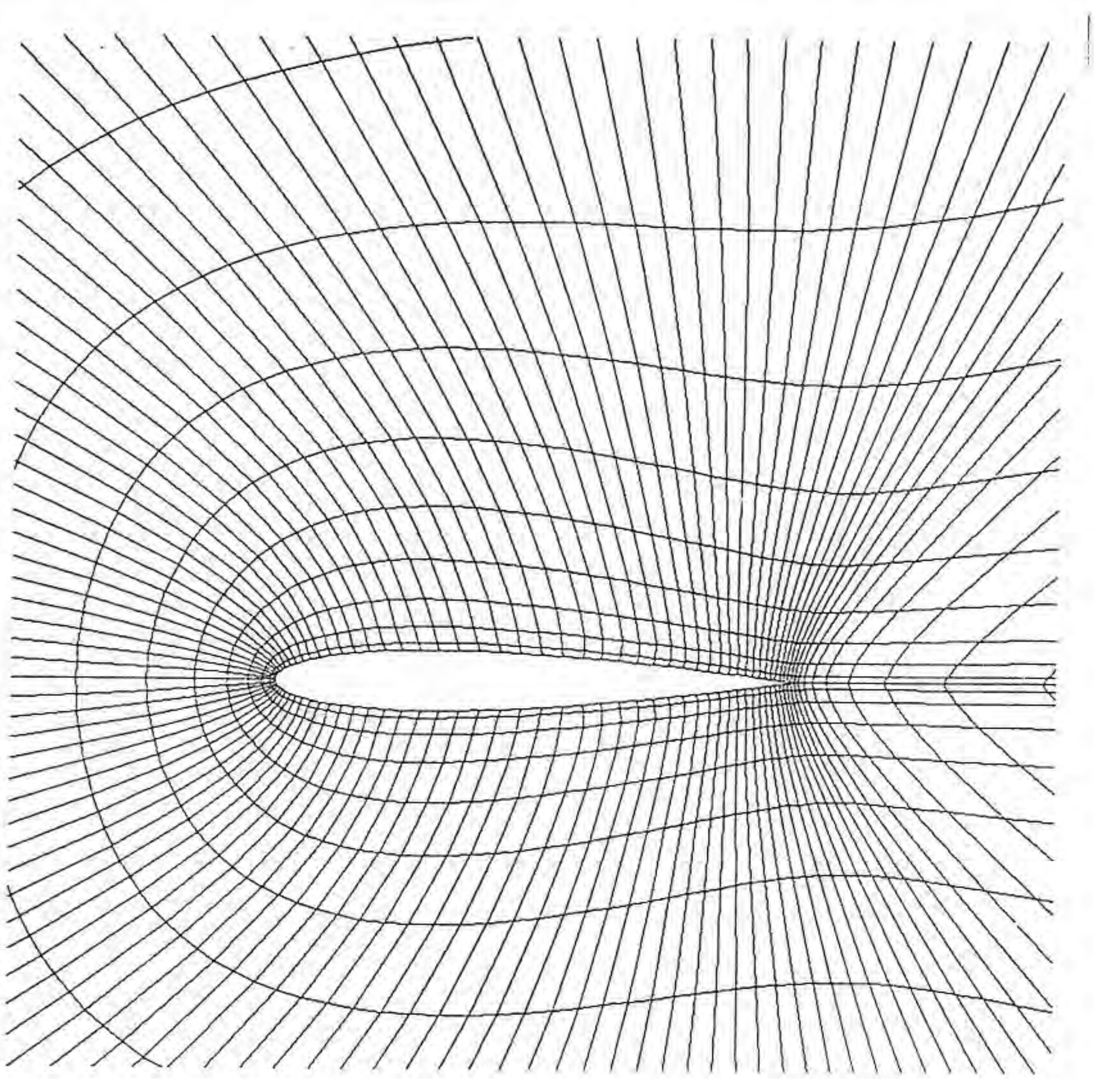

Figure 5.1 - A typical mesh for aeroelastic calculations

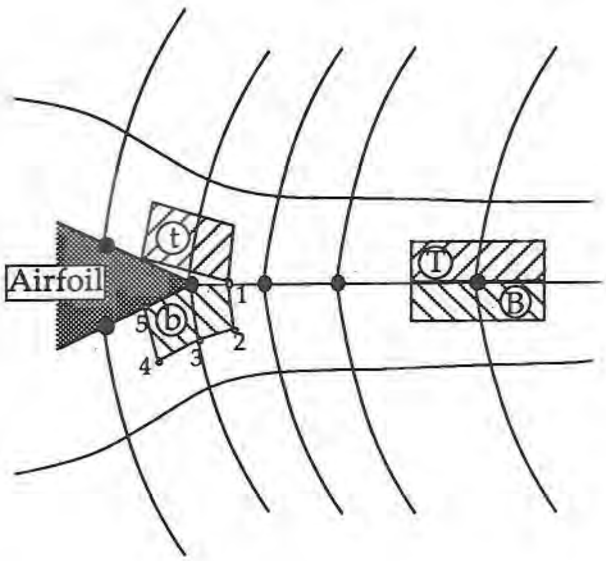

Figure 5.2a - Cell-Vertex Modelling Along the Wake Line

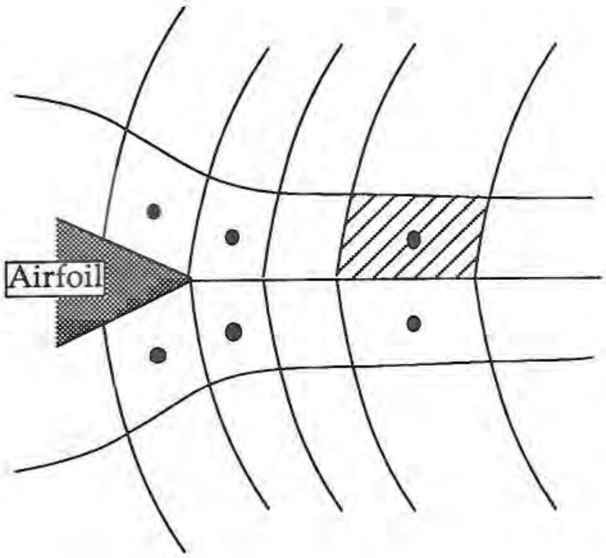

Figure 5.2b - Cell-Centre Modelling Along the Wake Line

5.3 Structural Model

The usual structural model used for airfoil, representing an isolated blade or wing, flutter calculations is that of the typical section model shown in figure 5.3. This representation which was first proposed by Theodorsen and Garrick [56] is an attempt to model wing flutter while neglecting three-dimensional effects. This model also neglects the flexibility of the wing by considering the typical section to be rigid.

The typical section has two degrees of freedom; a translational motion along the y-direction (plunging) and a rotational degree of freedom (pitching). The corresponding plunging and pitching stiffnesses are modelled by a translational spring K_h and a torsional spring K_t which are located at the elastic axis. The latter being defined as the point where a translational load does not produce any torsional effects.

The relevant structural parameters that define the typical section are: the chord, c, the location of the centre of gravity aft of the leading edge, b, the offset between the centre of gravity and the elastic axis, a, mass per unit span, m, radius of gyration about the elastic axis, r_{EA}. Finally, the dynamic properties of the section are defined by the uncoupled natural frequencies in plunge and pitching motion, ω_y and ω_θ respectively. In this study the above parameters have the following values:

$$c = 0.25\text{m}$$

$$b = 0.5\ c$$

$$a = 0.1\ c$$

$$r_{EA} = \sqrt{0.29}$$

$$R = \frac{\omega_y}{\omega_\theta} = 0.34335$$

The actual values for the uncoupled natural frequencies of the section, of course, change depending on the flutter case being considered, i.e. according to value of the reduced velocity. However, their ratio remains the same as that given above.

In this study, the limitation of the rigid-section dynamics is removed by a finite element model of the typical section that while retaining all the properties of the typical section also allows for its flexibility. The finite element of the section is obtained via a three-dimensional structural model, as shown in figure 5.4. The 3D structural model has a uniform profile of a NACA-64a006 airfoil. The two ends of the 3D structure are clamped and the in-plane modal properties of the mid-section are taken as being representative of the typical section dynamics. The chord length for the 3D structure, i.e. c, is 0.25m and its span-wise length is 1.5m. The dimensions of the 3D structure, specifically its span-wise length, is chosen from the simple beam theory so as to make the uncoupled plunging frequency close to the order of values required for ω_h. The 3D structure is modelled as hollow and its skin thickness is taken to be 5% of the airfoil thickness at each point.

Each section of the 3D structural model is defined with 44 grid points which are coincident with the grid nodes defining the airfoil for fluid flow mesh, shown previously in figure 5.1. However, some of the fluid grid nodes, both at the leading edge and the trailing edge, have been removed for the structural eigen-solution. The grid cluster required for the flow calculations are not only unnecessary but, indeed, undesirable for free-vibration analysis of the 3D structural model. The modal values at these missing nodes are, subsequently, estimated using cubic-spline interpolation.

There are, in total, seventeen airfoil sections which define the 3D structure. The 3D structure is modelled using three-dimensional shell elements with five degrees of freedom at each node. The modal properties extracted are only the degrees of freedom relevant to the typical section, i.e. (y , θ_z). The modelling and the eigen-solution are performed on the finite element package ANSYS.

The above model gives the centre of mass at the right position, i.e. at the mid-chord, however, the elastic axis ends up being coincident with the centre of mass. To position the elastic axis at the required location, a series of uniform translational springs are introduced at the leading edge line of the 3D structural model. Furthermore, a series of torsional springs are added at the leading andtailing edges of the 3D structure to ensure the correct ratio between the uncoupled plunging and pitching natural frequencies. The values of these translational and torsional springs are first estimated from the simple beam theory, i.e. a two-dimensional beam along the chord direction, and further adjusted by trial and error.

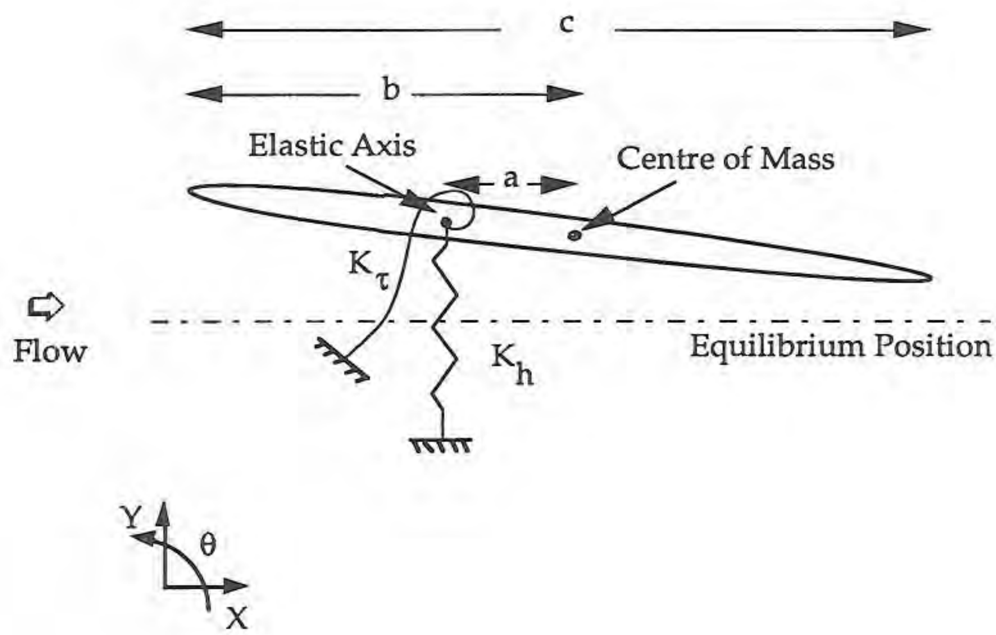

Figure 5.3 - Typical Section Model

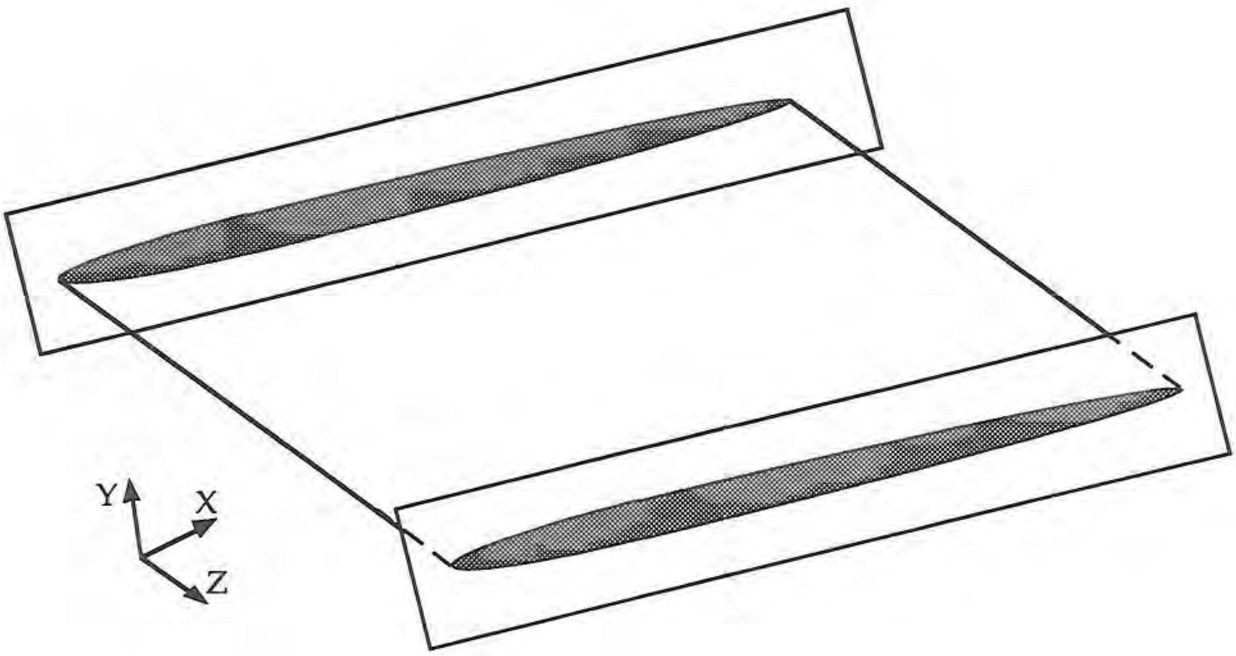

Figure 5.4 Three-Dimensional Model of NACA-64a006 Airfoil

Figure 5.5a shows the modeshapes obtained from the eigensolution analysis. Only those modes that give in-plane motions, i.e. Y-plane, for the mid-section of the wing have been retained and those with three-dimensional effects have been discarded. Figure 5.5b shows the corresponding modeshapes for the mid-section of the 3D structural model at each frequency. It can be seen that the first mode is that of a plunging motion with a small rotational component, the trailing edge has a more marked Y-displacement than the leading edge, a feature due to the offset between the elastic axis and the centre of mass. The second mode, which is the third mode of the 3D structure, is, mainly, in torsion with some translational motion superimposed on it, i.e. the elastic axis is displaced in the Y-direction. These two modes define the typical section, the higher modes representing the section flexibility of the airfoil section. Of course, it should be pointed out the the plunging and pitching modes obtained are not rigid section modes either and include some flexibility. The first five of the mid-section modes, corresponding to modes 1, 3, 4, 7 and 9 of the 3D structural model, have been retained for aeroelasticity analysis. The corresponding frequencies of these modes and their nature are given in Table 5.1.

Airfoil Section Mode	Frequency (Hz)
First Flap (Plunging)	36.12
First Torsion (Pitching)	143.50
Second Flap	164.60
Second Torsion	324.20
Combined Flap & Torsion	453.30

Table 5.1 - Modeshapes Natural Frequencies for NACA-64a006 Airfoil

One of the important aspects of aeroelasticity analysis in time domain is the effect of stability and accuracy of the time-marching algorithm. The stability and accuracy of the five-stage Runge-Kutta scheme, used here, was described in some detail in relation to fluid flow modelling in chapter 3. A similar investigation for the structural model would seem to be appropriate. An "empirical" study of time-marching for the structural modal model has been performed using the above typical section model as a test case. The airfoil is set to vibrate freely in a vacuum. Figure 5.6 shows the time-history of the trailing edge motion due to an initial impulse at the leading edge point in the Y-direction. The main observation to be

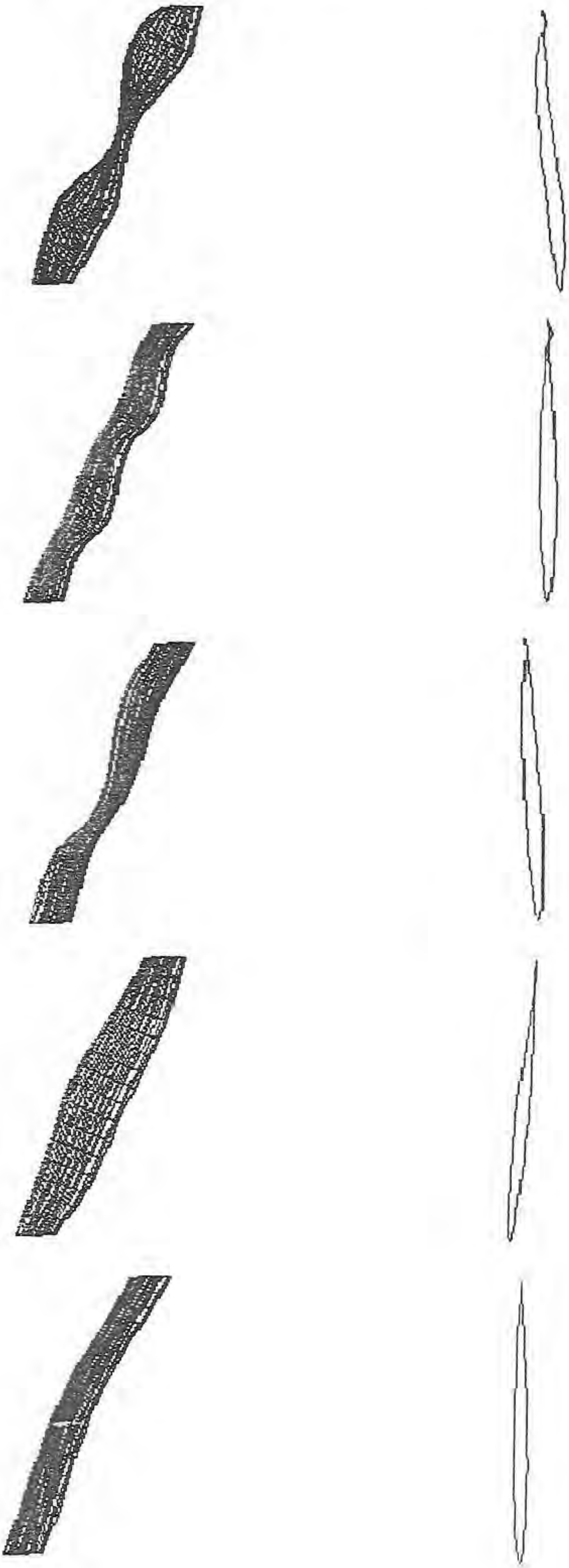

Figure 5.5(a&b) - Modeshapes

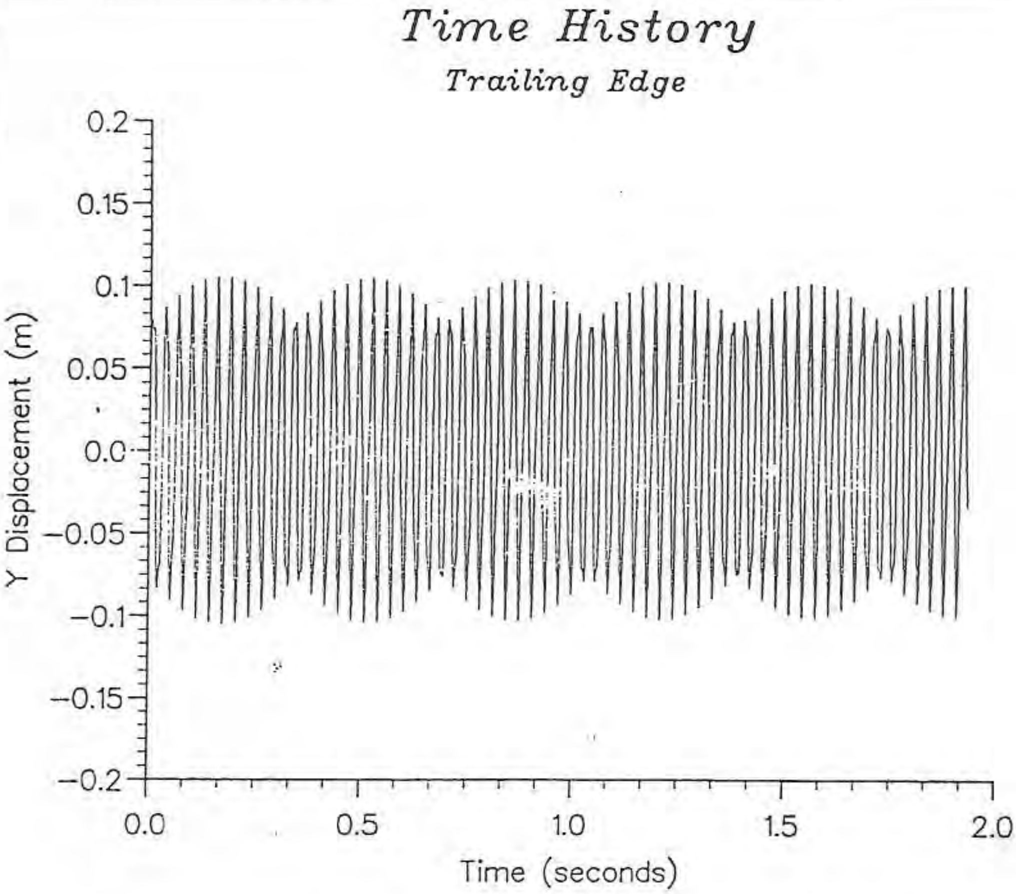

Figure 5.6

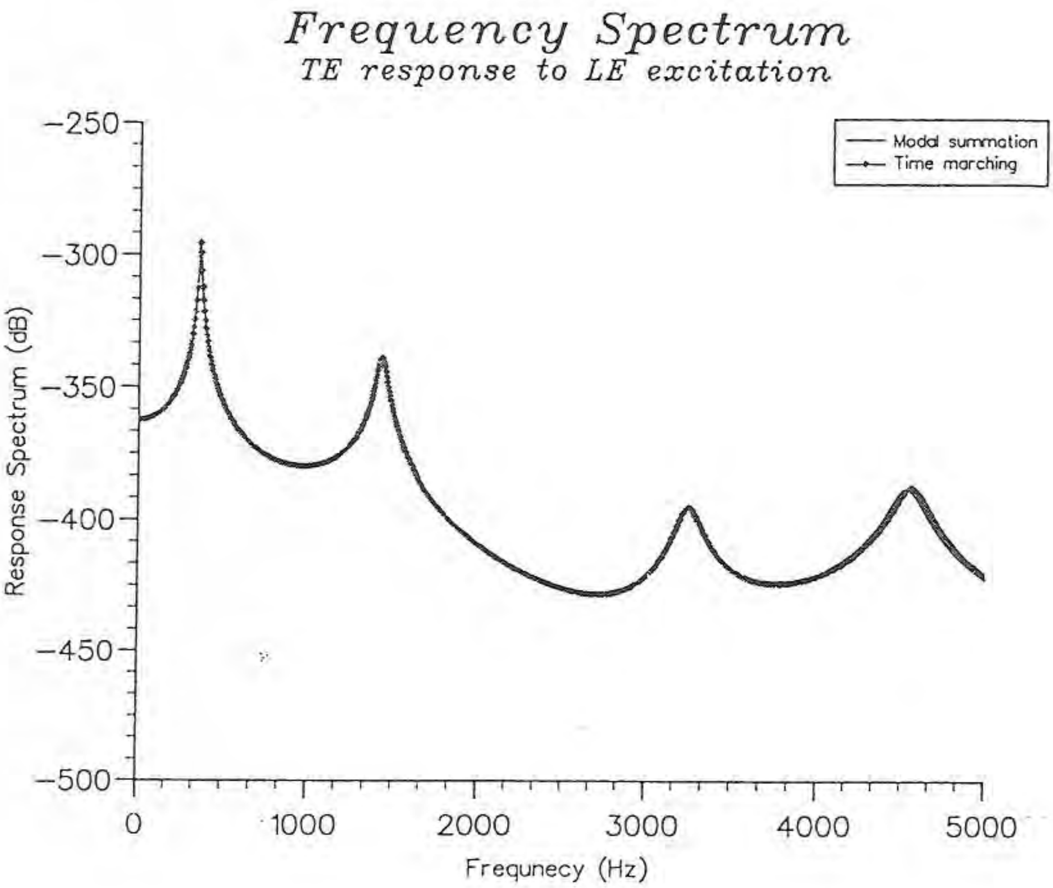

Figure 5.7

Grounded No wg!

made from this time-history is that the amplitude of vibrations remains constant, i.e. the time-marching algorithm is stable and does not dampen the airfoil oscillations. A frequency spectrum of the time-history is obtained by Fourier transform which is shown in figure 5.7. Also included in figure 5.7, is the frequency spectrum for the airfoil obtained from a modal summation calculation which represents the "exact" solution of the response spectrum. It can be seen that the modal summation result and the time-marching solution are almost identical apart from a small deviation at the fourth mode at which a frequency shift of 6% occurs. This minor discrepancy is due to the large time steps taken for the time-marching analysis leading to poor resolution of higher mode components. A smaller time step which resolves the higher modes more accurately would eliminate the above frequency shift. This, of course, is of no concern since for flutter calculations the allowable time step is determined by fluid flow stability requirements and the resultant time step resolves all structural modes very finely.

5.4 Aeroelasticity Analysis

The aim of the aeroelasticity analysis detailed here is to determine the flutter boundary of the NACA-64a006 airfoil in fluid flow air-stream at transonic flow regimes. A series of flow speeds and structural dynamics properties have been chosen for this investigation. The three parameters identifying each case is the flow Mach number (M), the structure to fluid mass ratio (μ) and, the reduced velocity ($\bar{U}$). Mach number is a well known non-dimensionalised flow parameter and needs no explanation. Mass ratio is the measure of the relative inertial effects of the structure and the fluid surrounding it. Reduced velocity is a measure of the relative dynamic influence of the flow and the structure. These parameters, in their non-dimensionalised forms, are determined as follows:

$$\text{Mass Ratio}: \ \mu = \frac{\text{structural mass per unit length}}{\frac{1}{4}\pi\,\rho_\infty\,c^2}$$

$$\text{Reduced Velocity}: \ \bar{U} = \frac{U_\infty}{\frac{1}{2}c\,\omega_\theta}$$

where U_∞ is the uniform free stream velocity and ρ_∞ is the density of the incoming flow.

It is important to note that specifying the mass ratio determines the mass of the airfoil section. This mass should then be used to mass-normalise the modeshapes obtained from the eigen-solution outlined in the previous section. Furthermore, specifying the reduced velocity determines the uncoupled rotational (pitching) frequency of the airfoil which is then used to scale the natural frequencies of the airfoil to their proper values.

The cases considered in this study are summarised in Table 5.2. In all cases the mass ratio is taken to be 10.

The solution procedure is initiated from the steady flow condition and by disturbing the airfoil from its equilibrium position by an impulse at time t=0. Calculations then proceed in a time accurate fashion. The reasoning behind the initial impulse is to speed up the flutter calculations, since, although the steady flow loading on the airfoil can initiate vibrations, the computation to the final solution, e.g. a limit cycle behaviour, takes considerably longer. Such short cuts in non-linear problems should always be treated with caution. The effect of the magnitude of the initial impulse on the final solution, i.e. stability/unstability of the airfoil or its limit cycle amplitude, must be investigated duly. The conclusion (from studies not presented here) is that the final solution is unaffected by the magnitude of the initial impulse. Of course, the ensuing time history itself is bound to be dependent on the initial impulse. Some researchers working on non-linear flutter have reported the dependency of the final limit cycle amplitude on the initial conditions [17]. However, in these cases, calculation is started by an initial physical displacement. Regardless of the justification for an initial displacement to start flutter calculations, it remains a fact that this leads to a different dynamics problem. Flutter of an airfoil in free stream at zero incidence is dynamically different from flutter of the same airfoil at a non-zero incidence. So applying an initial displacement changes the problem to be investigated; a case of comparing apples with oranges.

The other point regarding flutter calculations is the question of how to treat the wake-line in fluid mesh motion. Some researchers have considered the option of moving the wake-line with the trailing edge point velocities.[57]. This, however, leads to large a deformation of the mesh and is unacceptable for large airfoil motions. The alternative adopted here is that of reference [58]. The grid nodes on the wake-line are allowed to move on a parabolic arc tangent to the airfoil at its trailing edge point which returns to the centreline at the rear of the computational mesh. This is shown in figure 5.8. The resulting mesh motion allows a much larger airfoil motions to be handled with little loss of mesh quality.

Figure 5.9 shows the pitch and plunge results, defined at the elastic axis, at a Mach number of 0.8 and a reduced velocity of 1.60. Airfoil is stable and $\bar{U} = 1.60$ is below the flutter boundary. Increasing $\bar{U}$ to 1.90 results in an unstable solution as shown in figure 5.10. The amplitude of airfoil vibrations grow until a limit cycle is reached in 15 cycles. Limit cycle is reached when the shock moves to the trailing edge point and dynamic pressure loads acting on the blade level off. This can be seen from the lift and moment variation against the instantaneous angle of incidence shown in figure 5.11. Incidence is defined as the deviation of the line joining the leading edge to the trailing edge from its original position.

Further increase of the reduced velocity to 2.25 leads to a larger limit cycle amplitude as shown in figure 5.12. Furthermore, airfoil reaches its limit cycle only after 5 cycles. The other important feature is that there is an overshoot in airfoil vibrations before it settles down to its limit cycle behaviour. This is a common feature of limit cycles observed in this study as the airfoil moves further into the flutter region, characterised by an increase in the value of reduced velocity.

The cause of non-linear response is, of course, shock wave motion. In this case, i.e. M = 0.80,, the type of shock motion is that of Tijdeman's type A [59]. The shock wave remains distinct while its location and strength changes during a cycle of blade oscillations. This can be seen in figure 5.13 which gives the time history of the aerodynamics moment. It can be seen that the moment varies sinusoidally with the airfoil oscillations.

The next case considered is at a Mach number of 0.87. At a reduced velocity of 1.90 the airfoil is stable as shown in figure 5.14. So $\bar{U} = 1.90$ is below the flutter boundary. Increasing the reduced velocity to 2.0 results in a limit cycle behaviour with a pitch amplitude of 0.14 radians as shown in figure 5.15. Therefore, the flutter boundary at this Mach number is between reduced velocities of 1.90 and 2.0. Further increases in the reduced velocity results in limit cycle behaviours which are qualitatively similar to that described above. However, at higher reduced velocities at this flow speed the nature of the shock motion is different. For example, at $\bar{U} = 2.25$ the shock motion is similar to the Tijdeman's type B, i.e. the shock wave weakens and disappears during a portion of the airfoil oscillations. This can be seen from the time history of the aerodynamics moment, shown in figure 5.16. A sharp dip appears in the time history corresponding to disappearance and re-formation of the shock, Lift variation, however, remains sinusoidal as can be seen from the time history shown in figure 5.17.

A further increase of the reduced velocity to 5.0 results in a strong divergence as seen in figure 5.18. Some researchers have described this behaviour as explosive flutter. However, it can be seen that there is no periodic behaviour in the time history and, in fact, at this reduced speed the divergence boundary has been crossed.

The next case considered is at a Mach number of 0.92. At a reduced speed of 2.0 the airfoil is stable as seen in figure 5.19. A 2% increase in the reduced velocity (from 2.0 to 2.02) results in a limit cycle behaviour, as shown in figure 5.20. At a reduced velocity of 2.20 another type of limit cycle behaviour occurs, as can be seen in figure 5.21. Here the type B motion of the shock wave, described earlier, is combined with a phase-lag between the shock motion and the airfoil oscillations, resulting in a double dip in the moment time history. Due to the phase-lag developed, the shock wave disappears twice in each period and is re-formed again.

Increasing the reduced velocity to 2.50 results in a "beating" effect superimposed on the limit cycle pattern, as shown in figure 5.22. This is the result of the presence of higher modes in the solution. This effect is also discernible at lower reduced speeds albeit much less markedly.

The final flow speed investigated is M = 0.85. The airfoil is stable at a reduced speed of 1.80 and its oscillations die away quickly, as shown in figure 5.23. Therefore, at this reduced speed the airfoil is below the flutter boundary point. However, if the reduced speed is lowered to 1.75, an unexpected form of instability occurs, as shown in figure 5.24. Airfoil oscillations first die away quickly but then the airfoil undergoes a weak divergence and settles in a new equilibrium position. The conclusion is that the original airfoil position represents an unstable equilibrium point. Because of airfoil symmetry and initial zero incidence, there are, in fact, two stable equilibrium positions on either side of the original position and the airfoil arrives at one of them depending on the direction of the initial impulse. The weak divergence below the flutter boundary is a non-linear phenomenon that cannot be predicted by traditional models. Furthermore, it is interesting to point out that weak divergence is a dynamic problem and requires a time accurate solution. Kousen[60] has attempted to predict this type of divergence by a static, i.e. time-path independent method and the results are inaccurate. Weak divergence is a non-linear dynamic phenomenon which can only be predicted by integrated and non-linear solution techniques.

Figure 5.25 shows a comparison of the surface pressure distribution on the airfoil before and after divergence.

Figure 5.26 shows the resulting time histories for pitch and plunge motions for a reduced speed of 2.0. It can be seen that the limit cycle behaviour prevents the divergence tendency of the airfoil. The airfoil starts to undergo weak divergence but then the limit cycle sets in. Furthermore, the mean position of the airfoil starts to return to the original position. The ability to predict this form of interaction between divergence and flutter, or static aeroelasticity and dynamic aeroelasticity, is a unique feature of integrated models. Figure 5.27 shows the variation of lift and moment against incidence for this case.

A further increase in the reduced speed to 2.25 results in a return to the usual limit cycle behaviour at this flow speed. Figure 5.28 shows the time histories and phase plane plots for the airfoil vibrations at $M = 0.85$ and $\bar{U} = 2.25$. Again the type B of shock motion can be observed from the moment time history given in figure 5.29.

One final case that is worth reporting here, is that of the chaotic flutter behaviour, observed at $M = 0.92$ and $\bar{U} = 5.0$. Figure 5.30 shows the airfoil pitch and plunge oscillations at this condition. It can be seen that the airfoil undergoes a kind of limit cycle but there is no periodicity in the time history. This is an unexpected result and its physical meaning is not understood. This numerical result has also been reported by other researchers in the literature [61]. One possible explanation for the chaotic flutter is that the time-lag between the shock oscillations and the airfoil motion is not allowed to settle to a constant due to flow non-linearities.

In this study, the limitation of the rigid-section dynamics is removed by a finite element model of the typical section that while retaining all the properties of the typical section also allows for its flexibility. The finite element of the section is obtained via a three-dimensional structural model, as shown in figure 5.4. The 3D structural model has a uniform profile of a NACA-64a006 airfoil. The two ends of the 3D structure are clamped and the in-plane modal properties of the mid-section are taken as being representative of the typical section dynamics. The chord length for the 3D structure, i.e. c, is 0.25m and its span-wise length is 1.5m. The dimensions of the 3D structure, specifically its span-wise length, is chosen from the simple beam theory so as to make the uncoupled plunging frequency close to the order of values required for ω_h. The 3D structure is modelled as hollow and its skin thickness is taken to be 5% of the airfoil thickness at each point.

Each section of the 3D structural model is defined with 44 grid points which are coincident with the grid nodes defining the airfoil for fluid flow mesh, shown previously in figure 5.1. However, some of the fluid grid nodes, both at the leading edge and the trailing edge, have been removed for the structural eigen-solution. The grid cluster required for the flow calculations are not only unnecessary but, indeed, undesirable for free-vibration analysis of the 3D structural model. The modal values at these missing nodes are, subsequently, estimated using cubic-spline interpolation.

There are, in total, seventeen airfoil sections which define the 3D structure. The 3D structure is modelled using three-dimensional shell elements with five degrees of freedom at each node. The modal properties extracted are only the degrees of freedom relevant to the typical section, i.e. (y , θ_z). The modelling and the eigen-solution are performed on the finite element package ANSYS.

The above model gives the centre of mass at the right position, i.e. at the mid-chord, however, the elastic axis ends up being coincident with the centre of mass. To position the elastic axis at the required location, a series of uniform translational springs are introduced at the leading edge line of the 3D structural model. Furthermore, a series of torsional springs are added at the leading andtailing edges of the 3D structure to ensure the correct ratio between the uncoupled plunging and pitching natural frequencies. The values of these translational and torsional springs are first estimated from the simple beam theory, i.e. a two-dimensional beam along the chord direction, and further adjusted by trial and error.

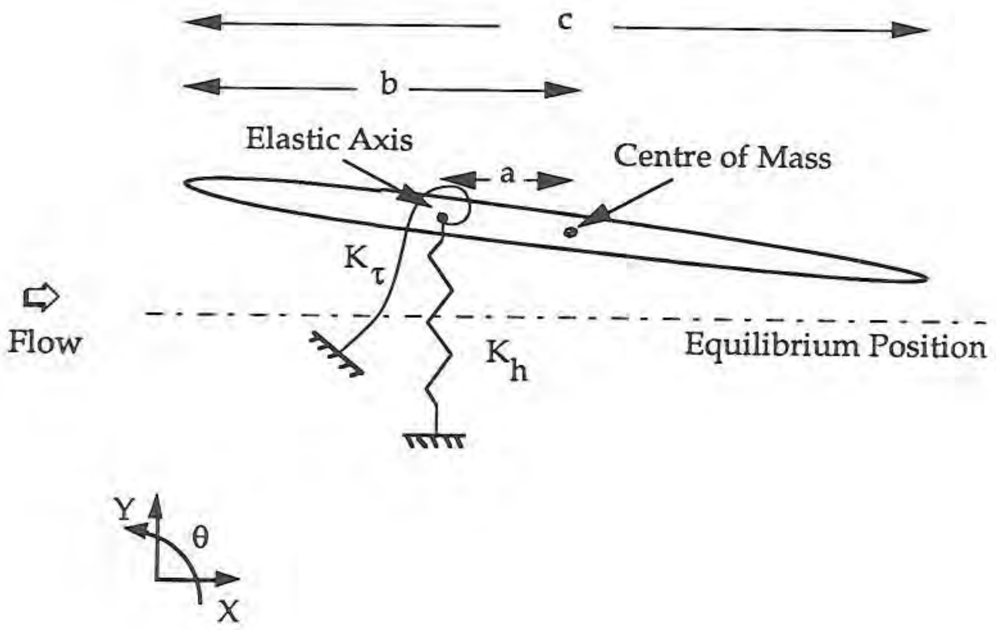

Figure 5.3 - Typical Section Model

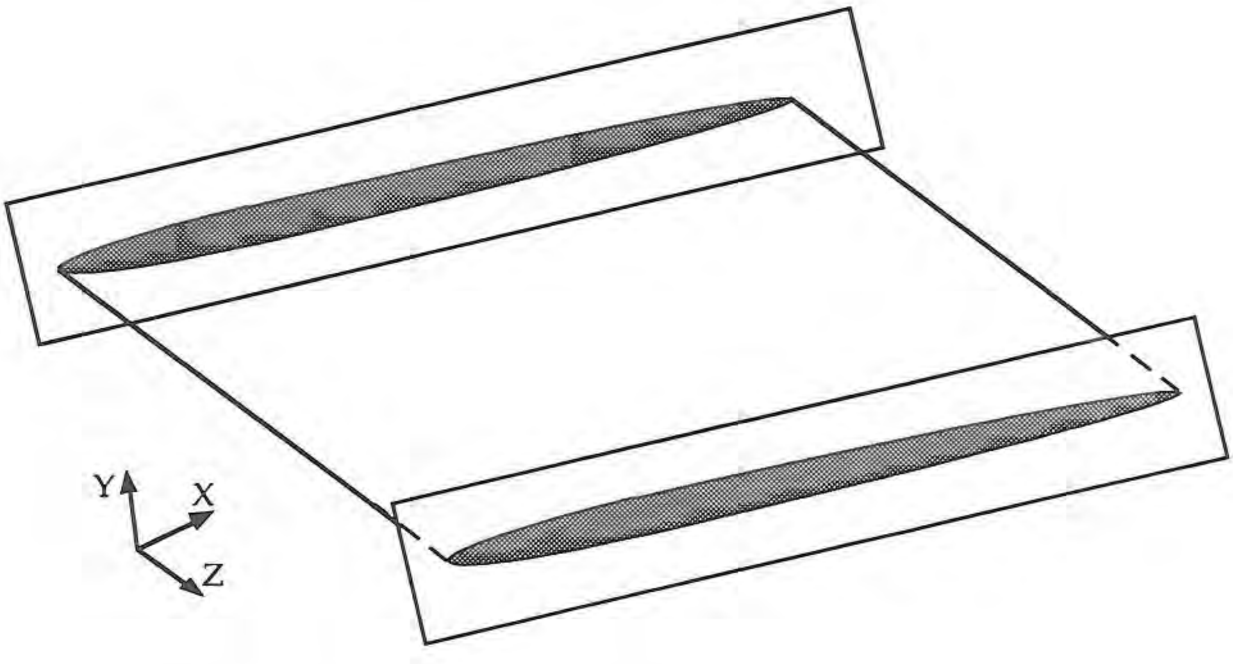

Figure 5.4 Three-Dimensional Model of NACA-64a006 Airfoil

Figure 5.5a shows the modeshapes obtained from the eigensolution analysis. Only those modes that give in-plane motions, i.e. Y-plane, for the mid-section of the wing have been retained and those with three-dimensional effects have been discarded. Figure 5.5b shows the corresponding modeshapes for the mid-section of the 3D structural model at each frequency. It can be seen that the first mode is that of a plunging motion with a small rotational component, the trailing edge has a more marked Y-displacement than the leading edge, a feature due to the offset between the elastic axis and the centre of mass. The second mode, which is the third mode of the 3D structure, is, mainly, in torsion with some translational motion superimposed on it, i.e. the elastic axis is displaced in the Y-direction. These two modes define the typical section, the higher modes representing the section flexibility of the airfoil section. Of course, it should be pointed out the the plunging and pitching modes obtained are not rigid section modes either and include some flexibility. The first five of the mid-section modes, corresponding to modes 1, 3, 4, 7 and 9 of the 3D structural model, have been retained for aeroelasticity analysis. The corresponding frequencies of these modes and their nature are given in Table 5.1.

Airfoil Section Mode	Frequency (Hz)
First Flap (Plunging)	36.12
First Torsion (Pitching)	143.50
Second Flap	164.60
Second Torsion	324.20
Combined Flap & Torsion	453.30

Table 5.1 - Modeshapes Natural Frequencies for NACA-64a006 Airfoil

One of the important aspects of aeroelasticity analysis in time domain is the effect of stability and accuracy of the time-marching algorithm. The stability and accuracy of the five-stage Runge-Kutta scheme, used here, was described in some detail in relation to fluid flow modelling in chapter 3. A similar investigation for the structural model would seem to be appropriate. An "empirical" study of time-marching for the structural modal model has been performed using the above typical section model as a test case. The airfoil is set to vibrate freely in a vacuum. Figure 5.6 shows the time-history of the trailing edge motion due to an initial impulse at the leading edge point in the Y-direction. The main observation to be

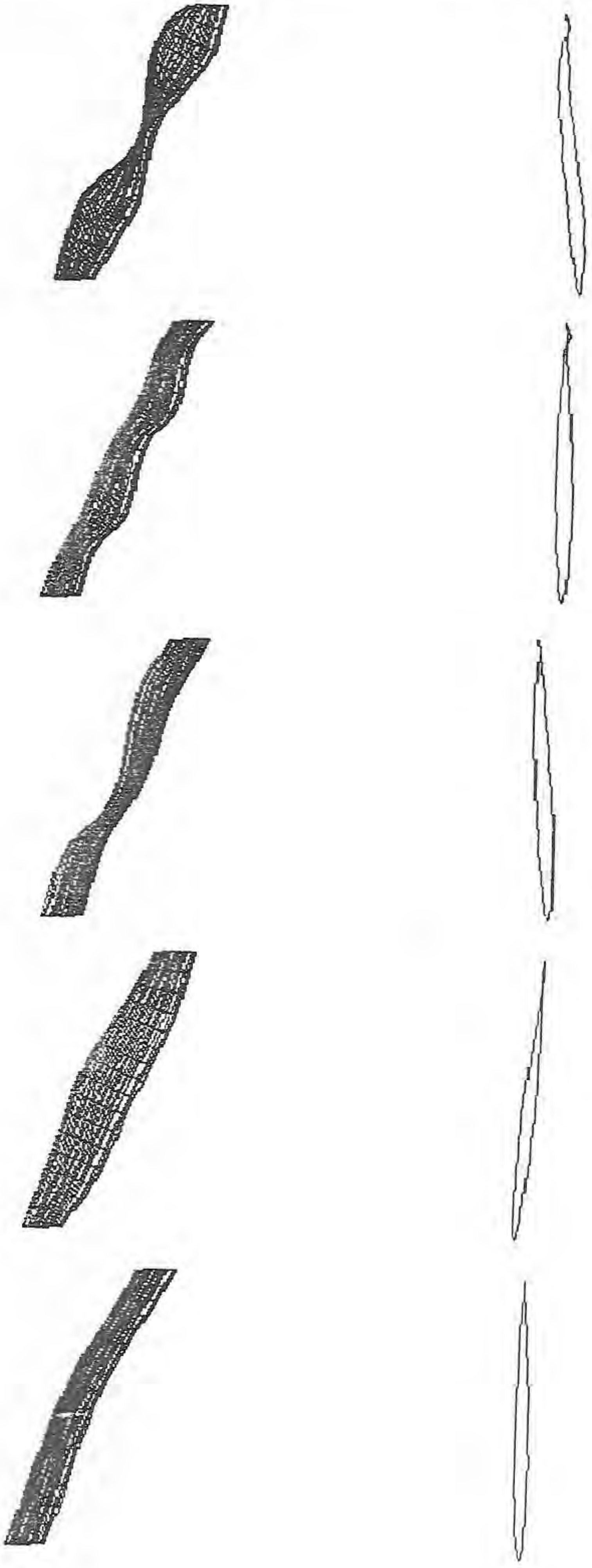

Figure 5.5(a&b) - Modeshapes

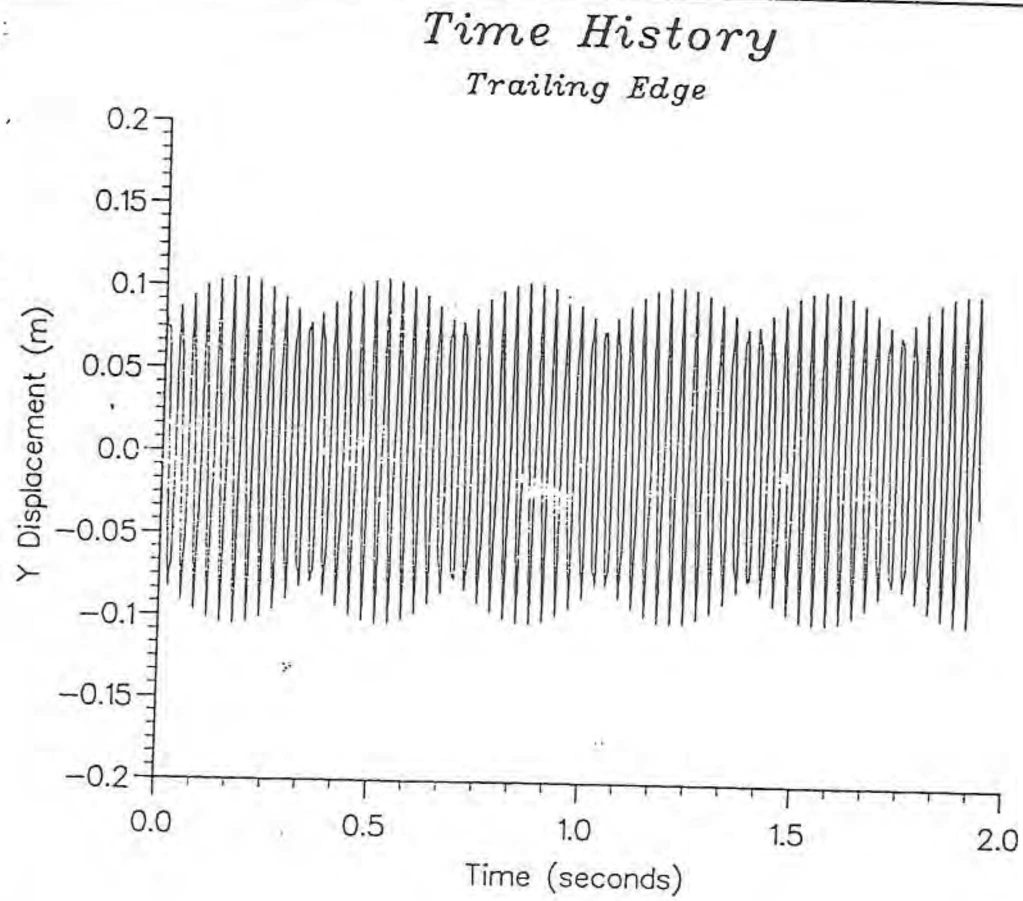

Figure 5.6

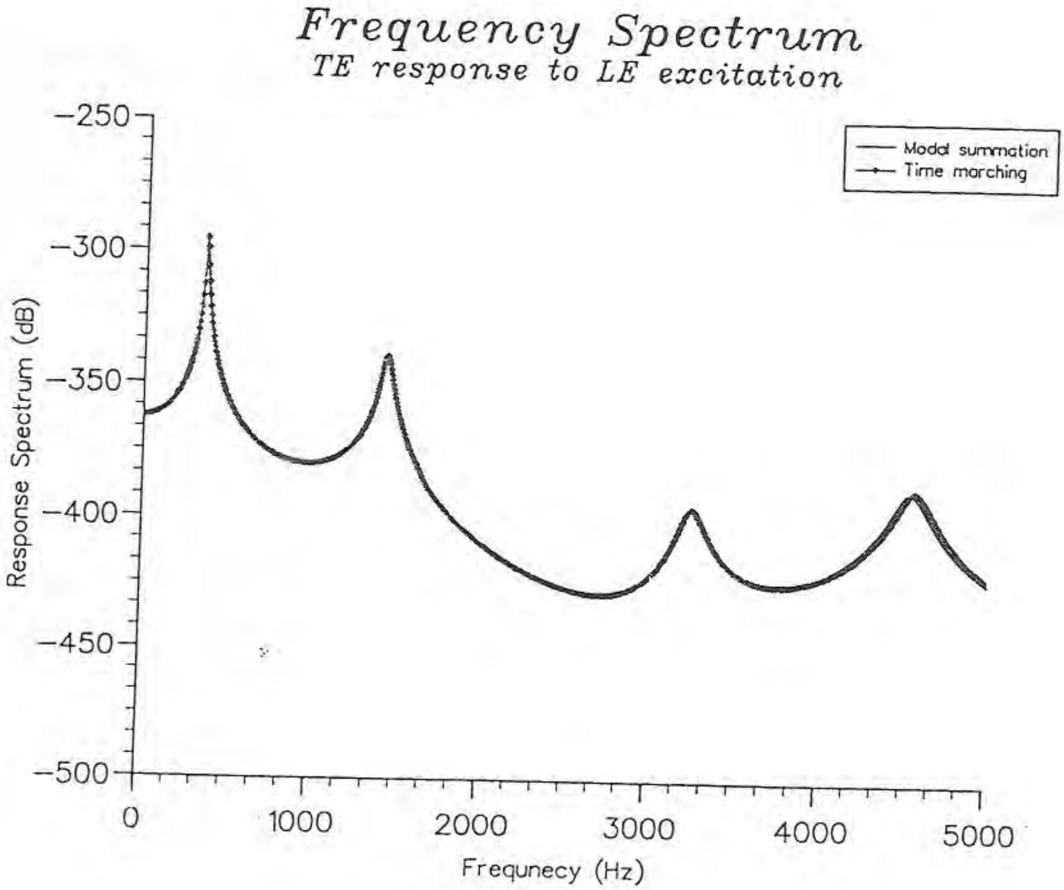

Figure 5.7

bounded No wg!

made from this time-history is that the amplitude of vibrations remains constant, i.e. the time-marching algorithm is stable and does not dampen the airfoil oscillations. A frequency spectrum of the time-history is obtained by Fourier transform which is shown in figure 5.7. Also included in figure 5.7, is the frequency spectrum for the airfoil obtained from a modal summation calculation which represents the "exact" solution of the response spectrum. It can be seen that the modal summation result and the time-marching solution are almost identical apart from a small deviation at the fourth mode at which a frequency shift of 6% occurs. This minor discrepancy is due to the large time steps taken for the time-marching analysis leading to poor resolution of higher mode components. A smaller time step which resolves the higher modes more accurately would eliminate the above frequency shift. This, of course, is of no concern since for flutter calculations the allowable time step is determined by fluid flow stability requirements and the resultant time step resolves all structural modes very finely.

5.4 Aeroelasticity Analysis

The aim of the aeroelasticity analysis detailed here is to determine the flutter boundary of the NACA-64a006 airfoil in fluid flow air-stream at transonic flow regimes. A series of flow speeds and structural dynamics properties have been chosen for this investigation. The three parameters identifying each case is the flow Mach number (M), the structure to fluid mass ratio (μ) and, the reduced velocity ($\bar{U}$). Mach number is a well known non-dimensionalised flow parameter and needs no explanation. Mass ratio is the measure of the relative inertial effects of the structure and the fluid surrounding it. Reduced velocity is a measure of the relative dynamic influence of the flow and the structure. These parameters, in their non-dimensionalised forms, are determined as follows:

$$\text{Mass Ratio}: \ \mu = \frac{\text{structural mass per unit length}}{\frac{1}{4}\pi\,\rho_\infty\,c^2}$$

$$\text{Reduced Velocity}: \ \bar{U} = \frac{U_\infty}{\frac{1}{2}c\,\omega_\theta}$$

where U_∞ is the uniform free stream velocity and ρ_∞ is the density of the incoming flow.

It is important to note that specifying the mass ratio determines the mass of the airfoil section. This mass should then be used to mass-normalise the modeshapes obtained from the eigen-solution outlined in the previous section. Furthermore, specifying the reduced velocity determines the uncoupled rotational (pitching) frequency of the airfoil which is then used to scale the natural frequencies of the airfoil to their proper values.

The cases considered in this study are summarised in Table 5.2. In all cases the mass ratio is taken to be 10.

The solution procedure is initiated from the steady flow condition and by disturbing the airfoil from its equilibrium position by an impulse at time t=0. Calculations then proceed in a time accurate fashion. The reasoning behind the initial impulse is to speed up the flutter calculations, since, although the steady flow loading on the airfoil can initiate vibrations, the computation to the final solution, e.g. a limit cycle behaviour, takes considerably longer. Such short cuts in non-linear problems should always be treated with caution. The effect of the magnitude of the initial impulse on the final solution, i.e. stability/unstability of the airfoil or its limit cycle amplitude, must be investigated duly. The conclusion (from studies not presented here) is that the final solution is unaffected by the magnitude of the initial impulse. Of course, the ensuing time history itself is bound to be dependent on the initial impulse. Some researchers working on non-linear flutter have reported the dependency of the final limit cycle amplitude on the initial conditions [17]. However, in these cases, calculation is started by an initial physical displacement. Regardless of the justification for an initial displacement to start flutter calculations, it remains a fact that this leads to a different dynamics problem. Flutter of an airfoil in free stream at zero incidence is dynamically different from flutter of the same airfoil at a non-zero incidence. So applying an initial displacement changes the problem to be investigated; a case of comparing apples with oranges.

The other point regarding flutter calculations is the question of how to treat the wake-line in fluid mesh motion. Some researchers have considered the option of moving the wake-line with the trailing edge point velocities.[57]. This, however, leads to large a deformation of the mesh and is unacceptable for large airfoil motions. The alternative adopted here is that of reference [58]. The grid nodes on the wake-line are allowed to move on a parabolic arc tangent to the airfoil at its trailing edge point which returns to the centreline at the rear of the computational mesh. This is shown in figure 5.8. The resulting mesh motion allows a much larger airfoil motions to be handled with little loss of mesh quality.

Figure 5.9 shows the pitch and plunge results, defined at the elastic axis, at a Mach number of 0.8 and a reduced velocity of 1.60. Airfoil is stable and $\bar{U} = 1.60$ is below the flutter boundary. Increasing $\bar{U}$ to 1.90 results in an unstable solution as shown in figure 5.10. The amplitude of airfoil vibrations grow until a limit cycle is reached in 15 cycles. Limit cycle is reached when the shock moves to the trailing edge point and dynamic pressure loads acting on the blade level off. This can be seen from the lift and moment variation against the instantaneous angle of incidence shown in figure 5.11. Incidence is defined as the deviation of the line joining the leading edge to the trailing edge from its original position.

Further increase of the reduced velocity to 2.25 leads to a larger limit cycle amplitude as shown in figure 5.12. Furthermore, airfoil reaches its limit cycle only after 5 cycles. The other important feature is that there is an overshoot in airfoil vibrations before it settles down to its limit cycle behaviour. This is a common feature of limit cycles observed in this study as the airfoil moves further into the flutter region, characterised by an increase in the value of reduced velocity.

The cause of non-linear response is, of course, shock wave motion. In this case, i.e. M = 0.80,, the type of shock motion is that of Tijdeman's type A [59]. The shock wave remains distinct while its location and strength changes during a cycle of blade oscillations. This can be seen in figure 5.13 which gives the time history of the aerodynamics moment. It can be seen that the moment varies sinusoidally with the airfoil oscillations.

The next case considered is at a Mach number of 0.87. At a reduced velocity of 1.90 the airfoil is stable as shown in figure 5.14. So $\bar{U} = 1.90$ is below the flutter boundary. Increasing the reduced velocity to 2.0 results in a limit cycle behaviour with a pitch amplitude of 0.14 radians as shown in figure 5.15. Therefore, the flutter boundary at this Mach number is between reduced velocities of 1.90 and 2.0. Further increases in the reduced velocity results in limit cycle behaviours which are qualitatively similar to that described above. However, at higher reduced velocities at this flow speed the nature of the shock motion is different. For example, at $\bar{U} = 2.25$ the shock motion is similar to the Tijdeman's type B, i.e. the shock wave weakens and disappears during a portion of the airfoil oscillations. This can be seen from the time history of the aerodynamics moment, shown in figure 5.16. A sharp dip appears in the time history corresponding to disappearance and re-formation of the shock, Lift variation, however, remains sinusoidal as can be seen from the time history shown in figure 5.17.

A further increase of the reduced velocity to 5.0 results in a strong divergence as seen in figure 5.18. Some researchers have described this behaviour as explosive flutter. However, it can be seen that there is no periodic behaviour in the time history and, in fact, at this reduced speed the divergence boundary has been crossed.

The next case considered is at a Mach number of 0.92. At a reduced speed of 2.0 the airfoil is stable as seen in figure 5.19. A 2% increase in the reduced velocity (from 2.0 to 2.02) results in a limit cycle behaviour, as shown in figure 5.20. At a reduced velocity of 2.20 another type of limit cycle behaviour occurs, as can be seen in figure 5.21. Here the type B motion of the shock wave, described earlier, is combined with a phase-lag between the shock motion and the airfoil oscillations, resulting in a double dip in the moment time history. Due to the phase-lag developed, the shock wave disappears twice in each period and is re-formed again.

Increasing the reduced velocity to 2.50 results in a "beating" effect superimposed on the limit cycle pattern, as shown in figure 5.22. This is the result of the presence of higher modes in the solution. This effect is also discernible at lower reduced speeds albeit much less markedly.

The final flow speed investigated is M = 0.85. The airfoil is stable at a reduced speed of 1.80 and its oscillations die away quickly, as shown in figure 5.23. Therefore, at this reduced speed the airfoil is below the flutter boundary point. However, if the reduced speed is lowered to 1.75, an unexpected form of instability occurs, as shown in figure 5.24. Airfoil oscillations first die away quickly but then the airfoil undergoes a weak divergence and settles in a new equilibrium position. The conclusion is that the original airfoil position represents an unstable equilibrium point. Because of airfoil symmetry and initial zero incidence, there are, in fact, two stable equilibrium positions on either side of the original position and the airfoil arrives at one of them depending on the direction of the initial impulse. The weak divergence below the flutter boundary is a non-linear phenomenon that cannot be predicted by traditional models. Furthermore, it is interesting to point out that weak divergence is a dynamic problem and requires a time accurate solution. Kousen[60] has attempted to predict this type of divergence by a static, i.e. time-path independent method and the results are inaccurate. Weak divergence is a non-linear dynamic phenomenon which can only be predicted by integrated and non-linear solution techniques.

Figure 5.25 shows a comparison of the surface pressure distribution on the airfoil before and after divergence.

Figure 5.26 shows the resulting time histories for pitch and plunge motions for a reduced speed of 2.0. It can be seen that the limit cycle behaviour prevents the divergence tendency of the airfoil. The airfoil starts to undergo weak divergence but then the limit cycle sets in. Furthermore, the mean position of the airfoil starts to return to the original position. The ability to predict this form of interaction between divergence and flutter, or static aeroelasticity and dynamic aeroelasticity, is a unique feature of integrated models. Figure 5.27 shows the variation of lift and moment against incidence for this case.

A further increase in the reduced speed to 2.25 results in a return to the usual limit cycle behaviour at this flow speed. Figure 5.28 shows the time histories and phase plane plots for the airfoil vibrations at $M = 0.85$ and $\bar{U} = 2.25$. Again the type B of shock motion can be observed from the moment time history given in figure 5.29.

One final case that is worth reporting here, is that of the chaotic flutter behaviour, observed at $M = 0.92$ and $\bar{U} = 5.0$. Figure 5.30 shows the airfoil pitch and plunge oscillations at this condition. It can be seen that the airfoil undergoes a kind of limit cycle but there is no periodicity in the time history. This is an unexpected result and its physical meaning is not understood. This numerical result has also been reported by other researchers in the literature [61]. One possible explanation for the chaotic flutter is that the time-lag between the shock oscillations and the airfoil motion is not allowed to settle to a constant due to flow non-linearities.

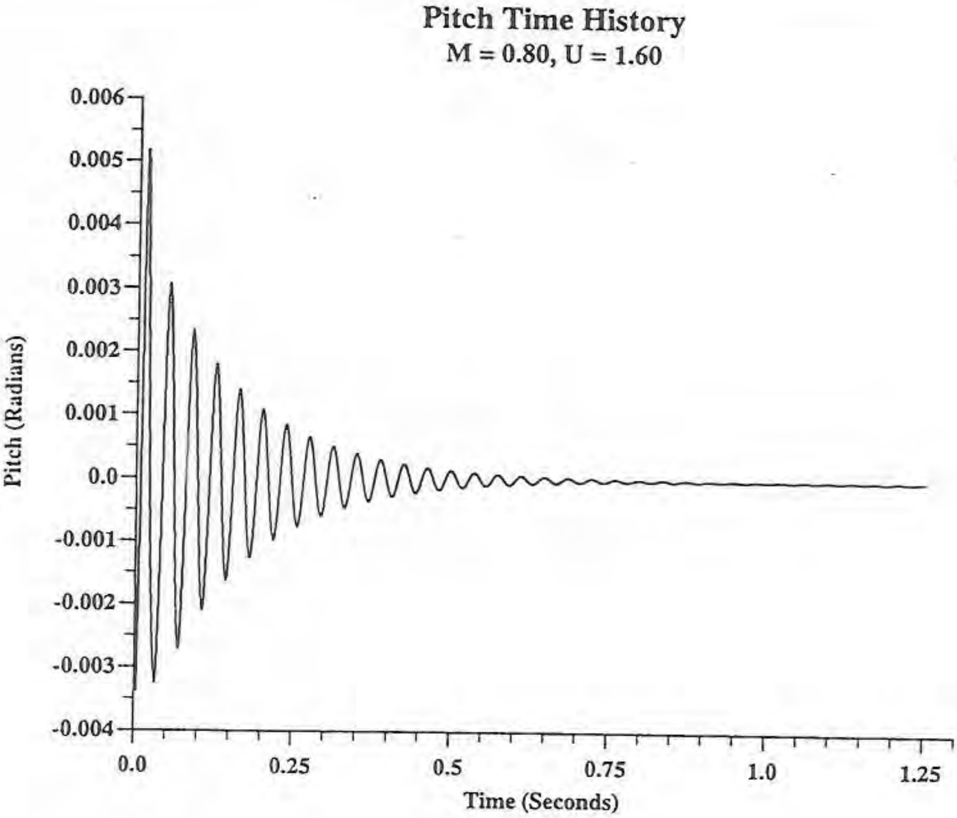

Figure 5.9a

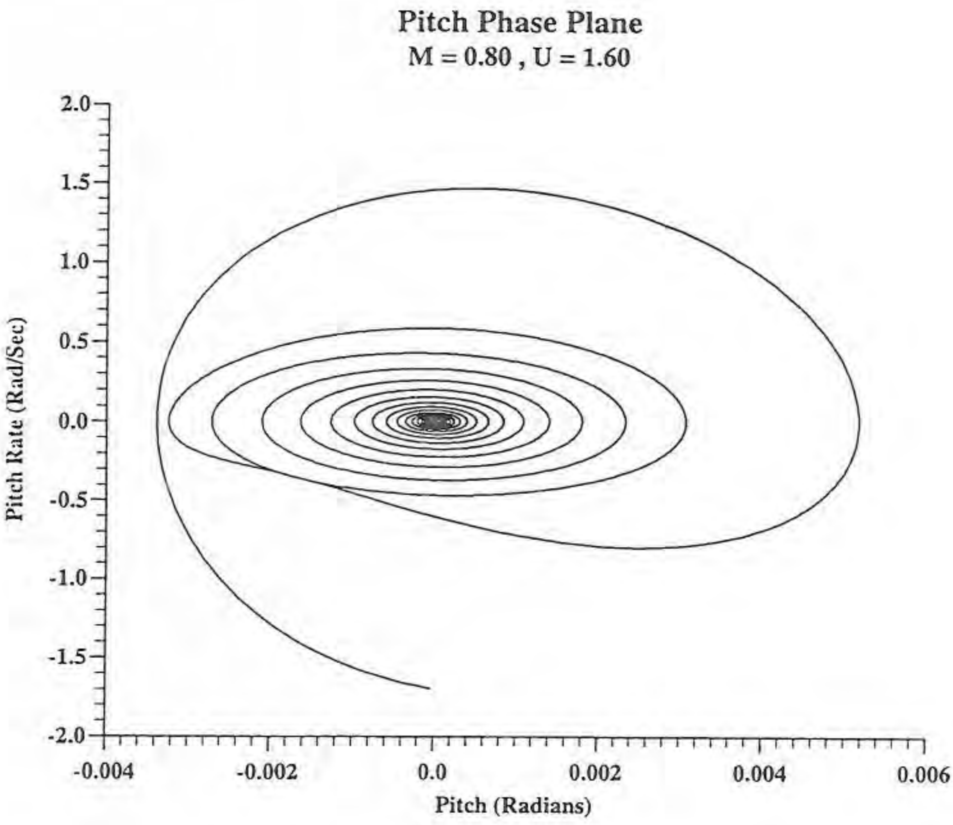

Figure 5.9b

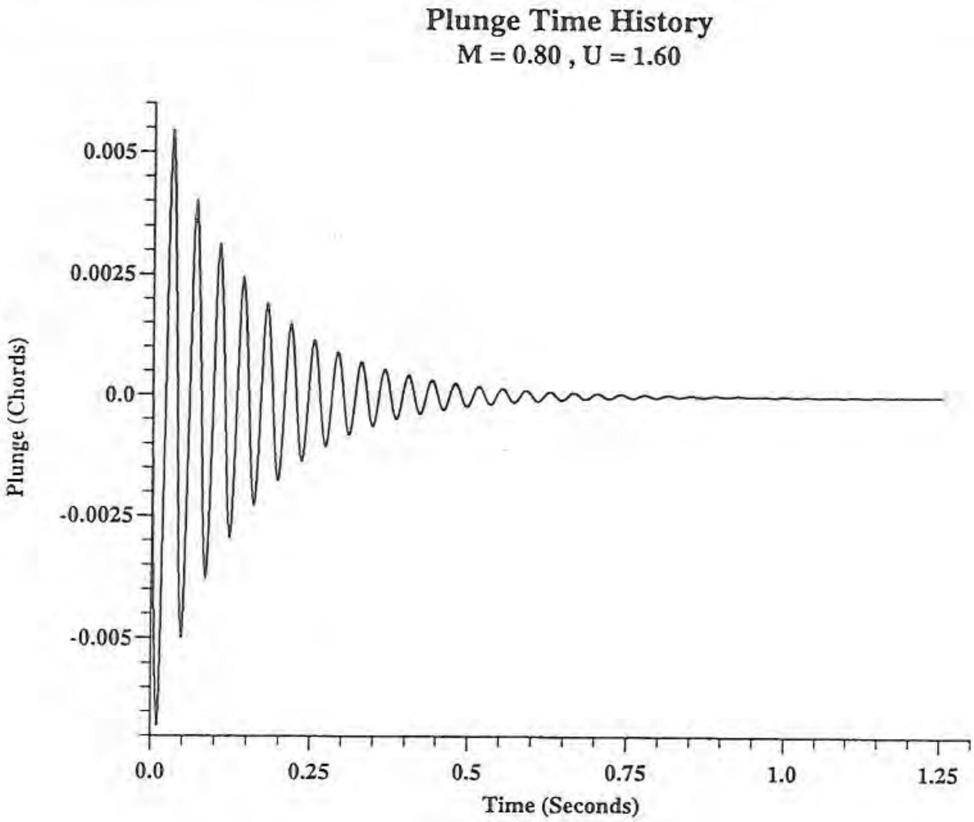

Figure 5.9c

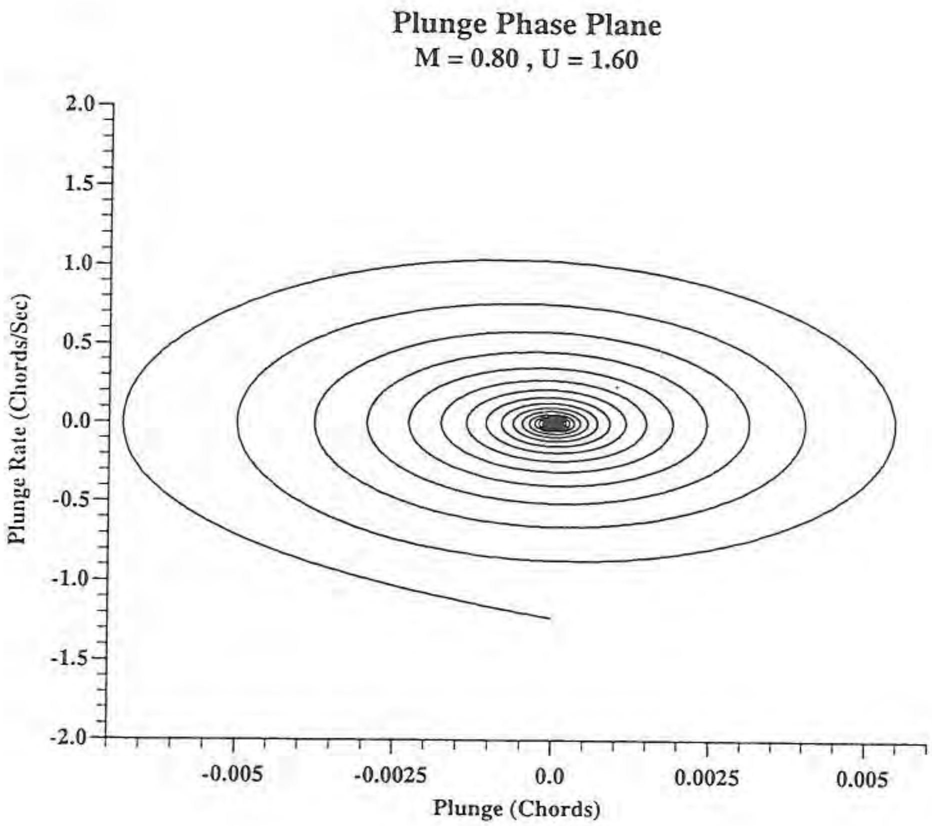

Figure 5.9d

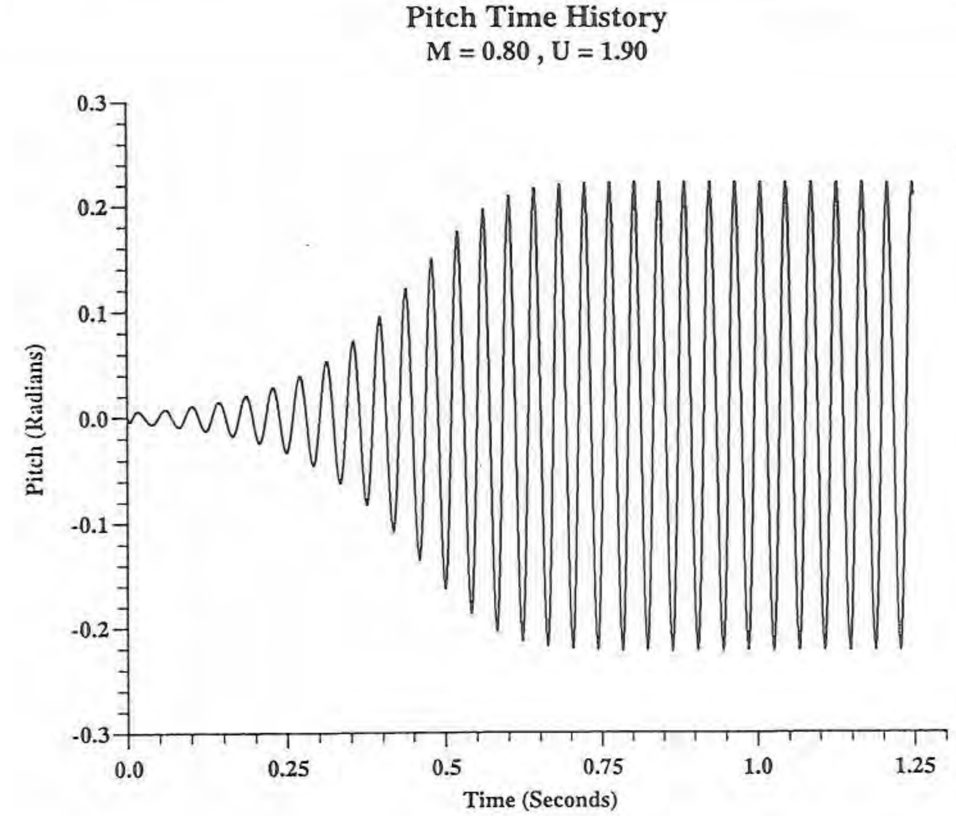

Figure 5.10a

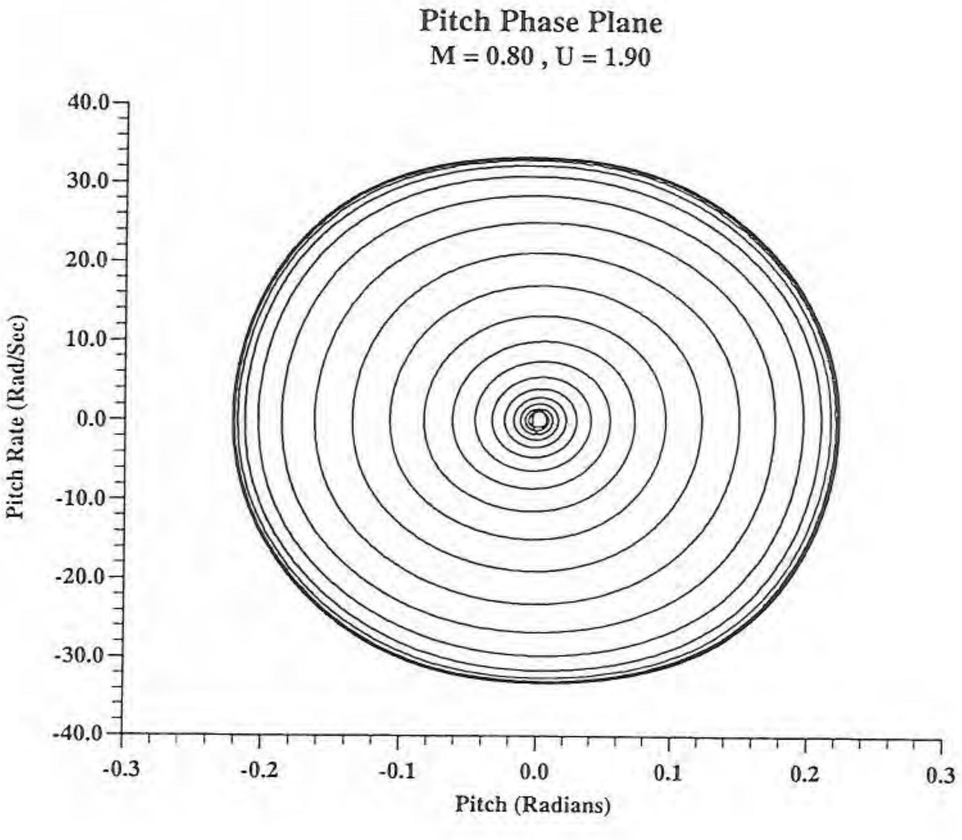

Figure 5.10b

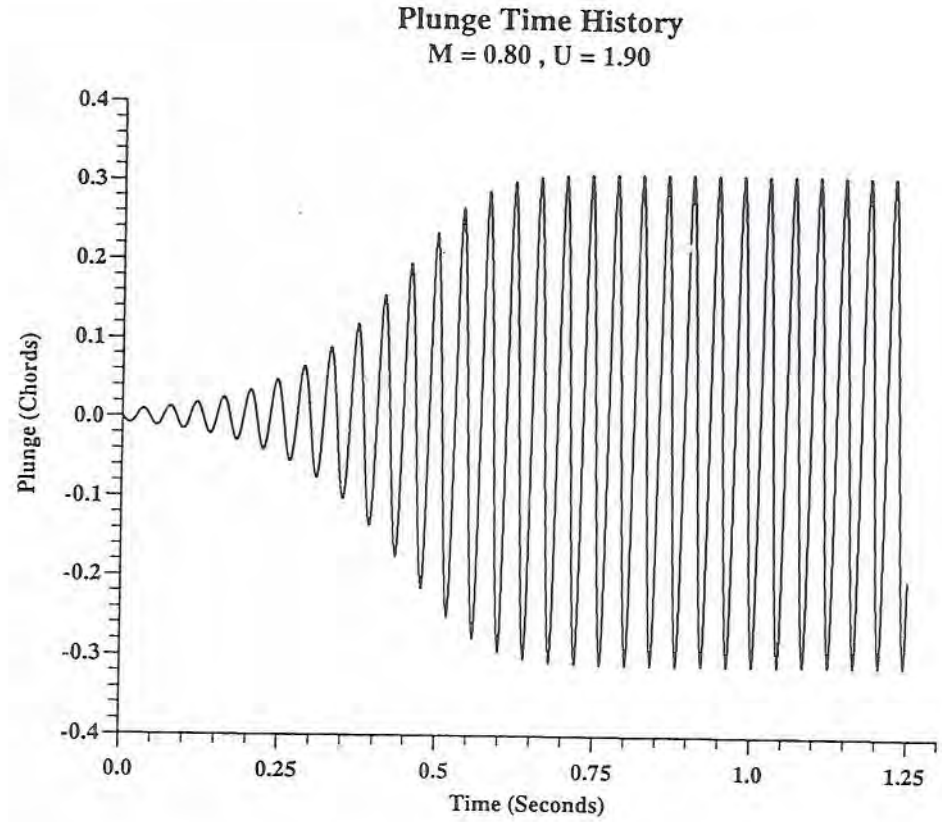

Figure 5.10c

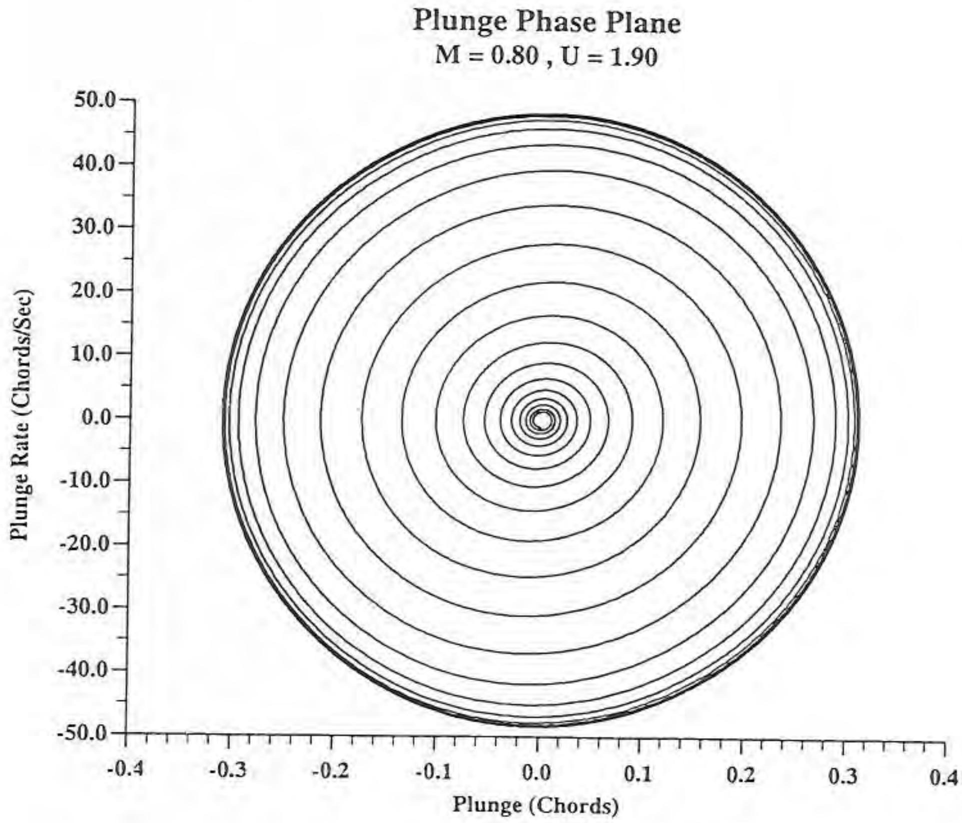

Figure 5.10d

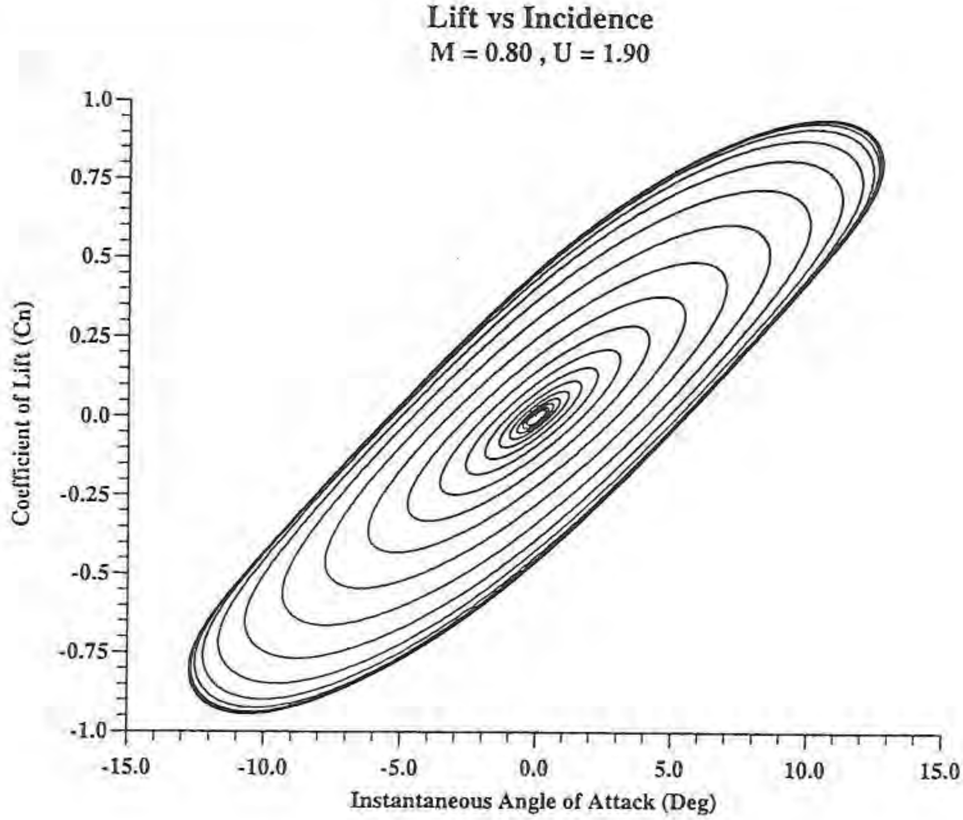

Figure 5.11a

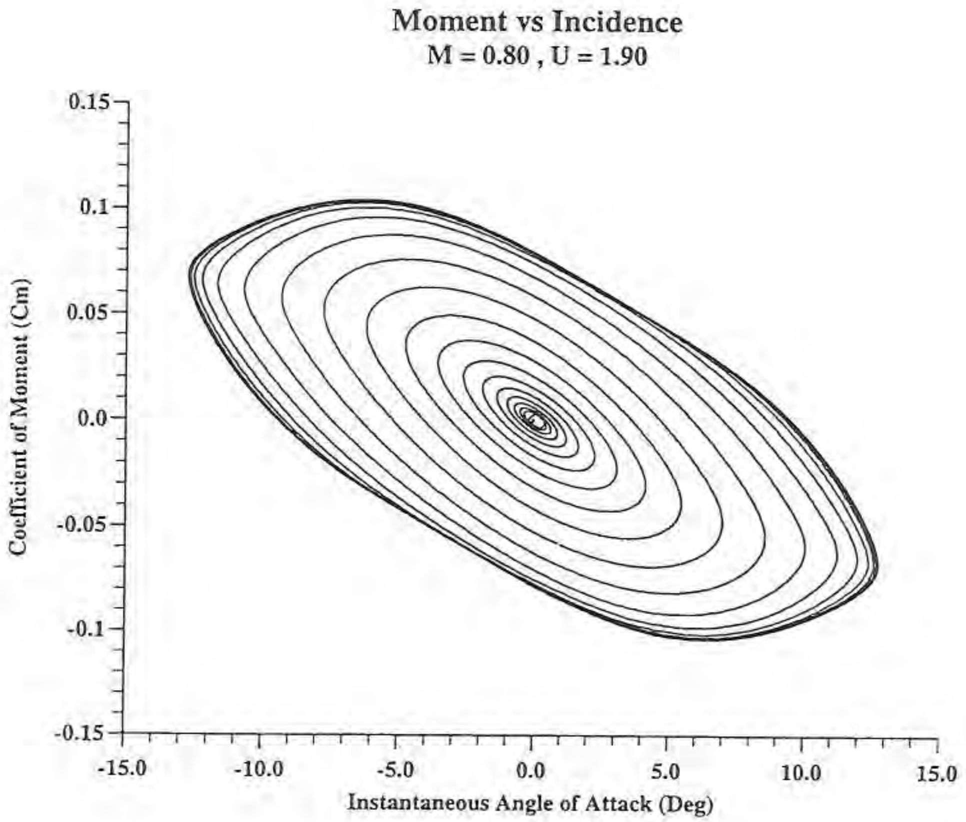

Figure 5.11b

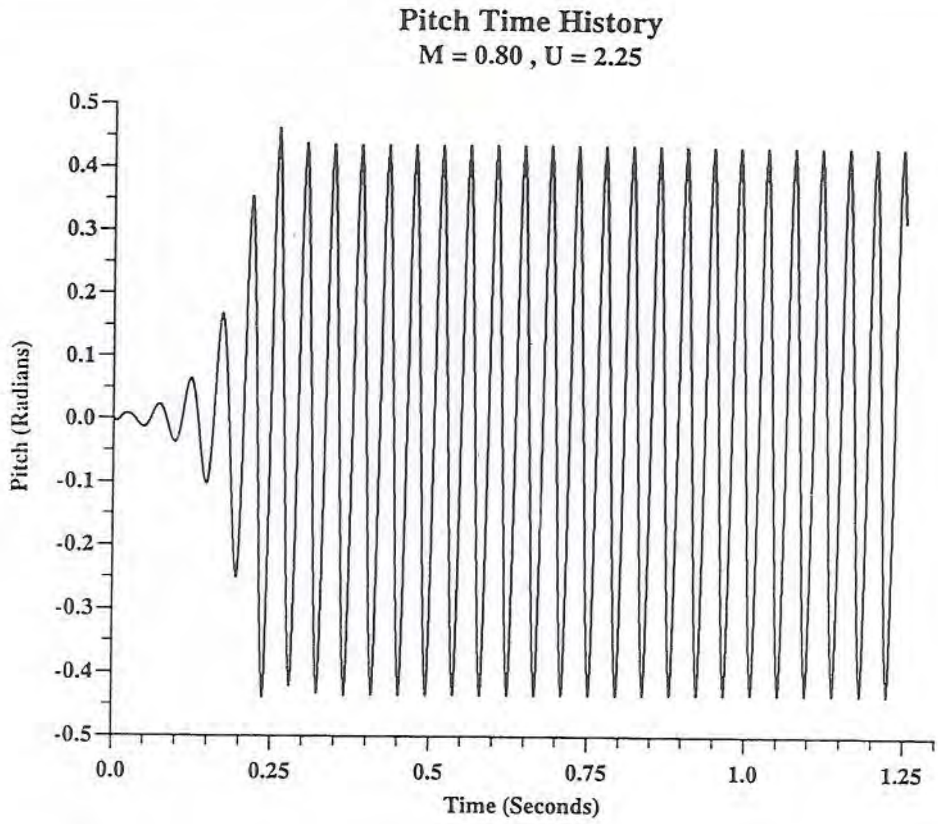

Figure 5.12a

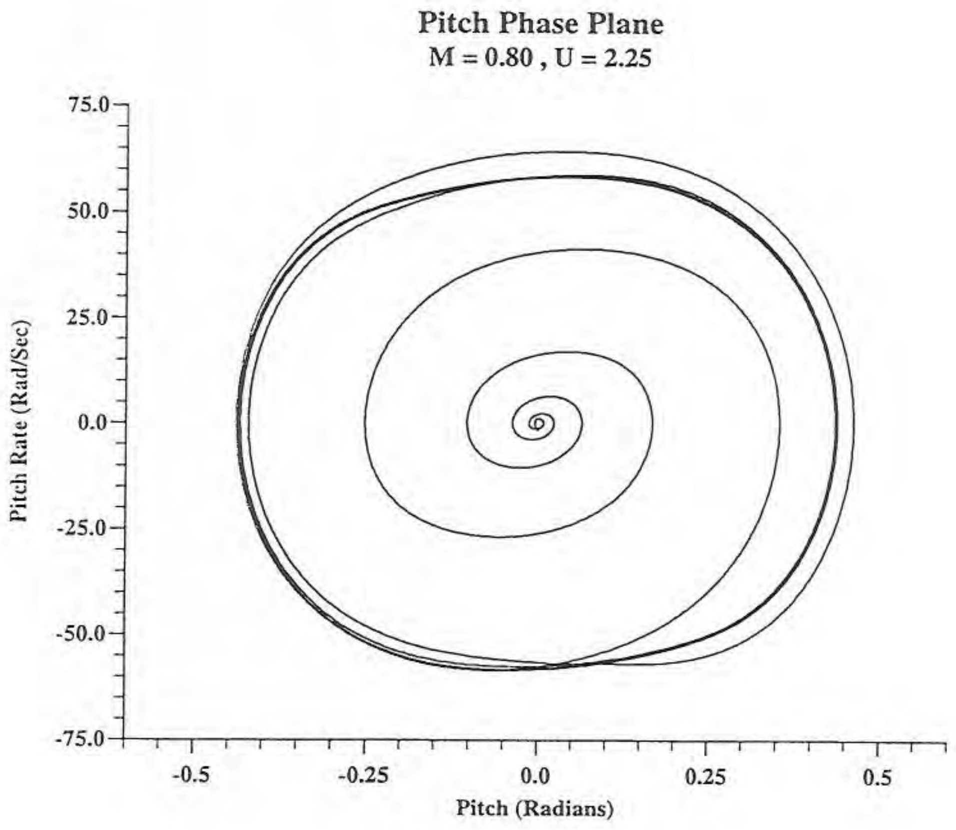

Figure 5.12b

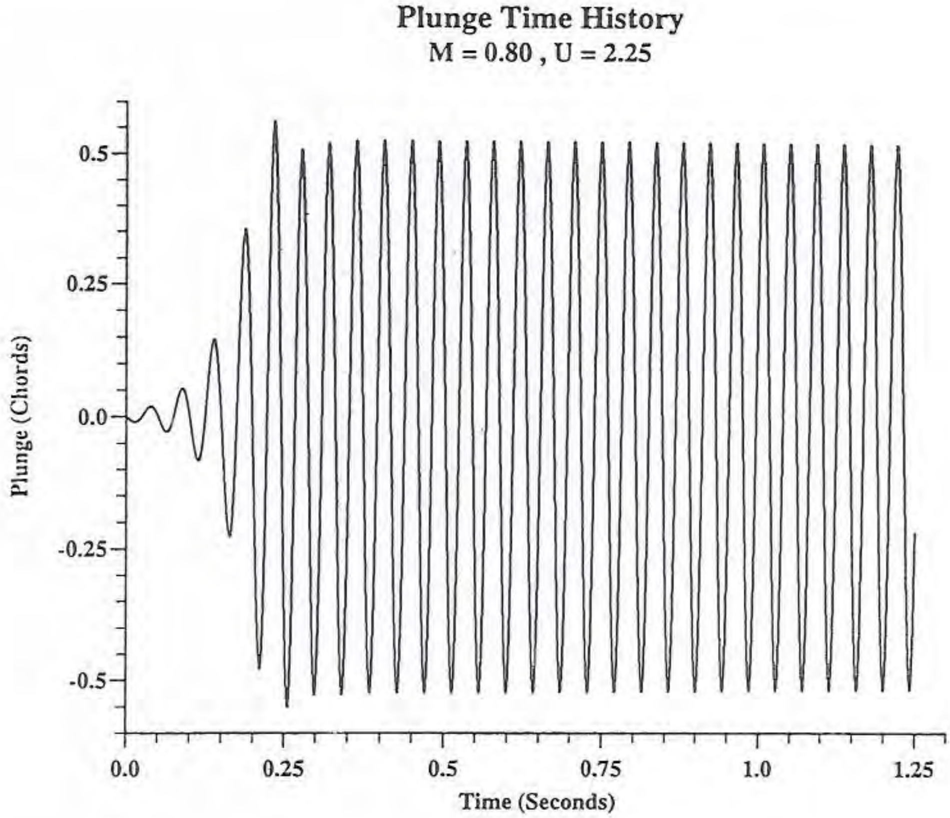

Figure 5.12c

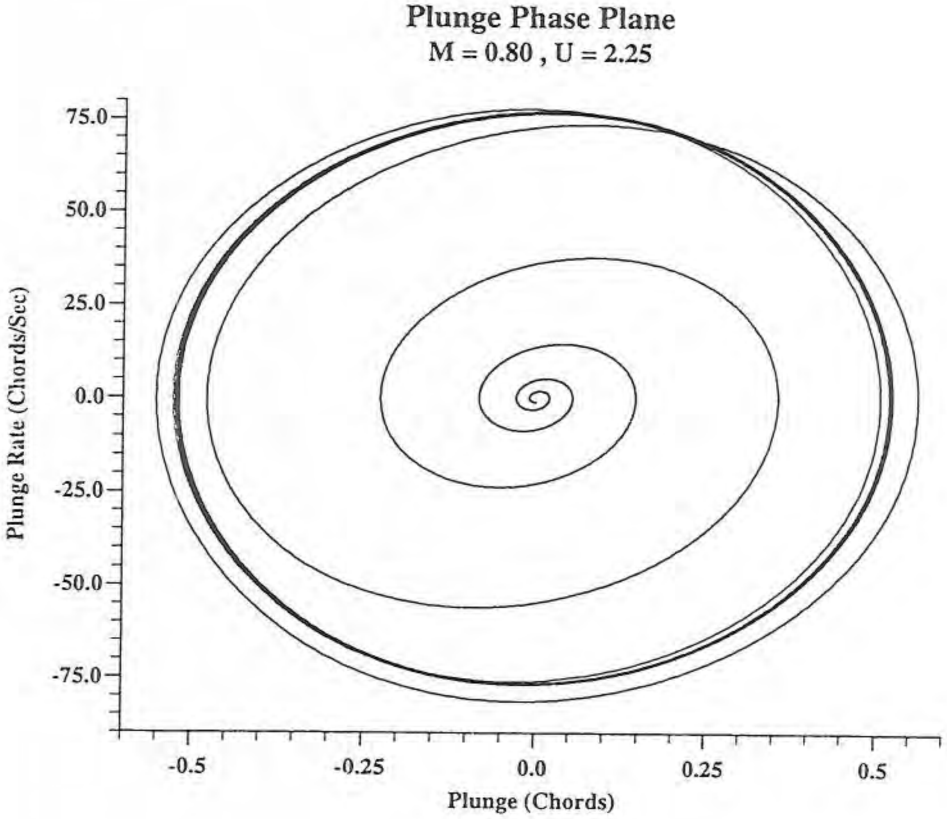

Figure 5.12d

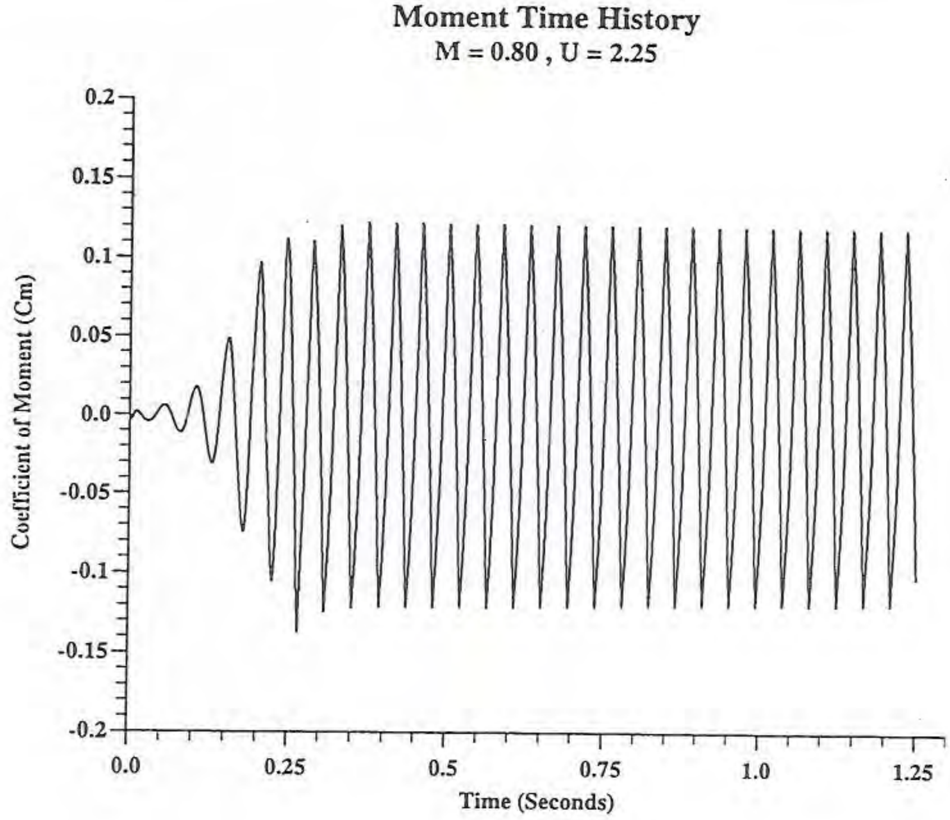

Figure 5.13a

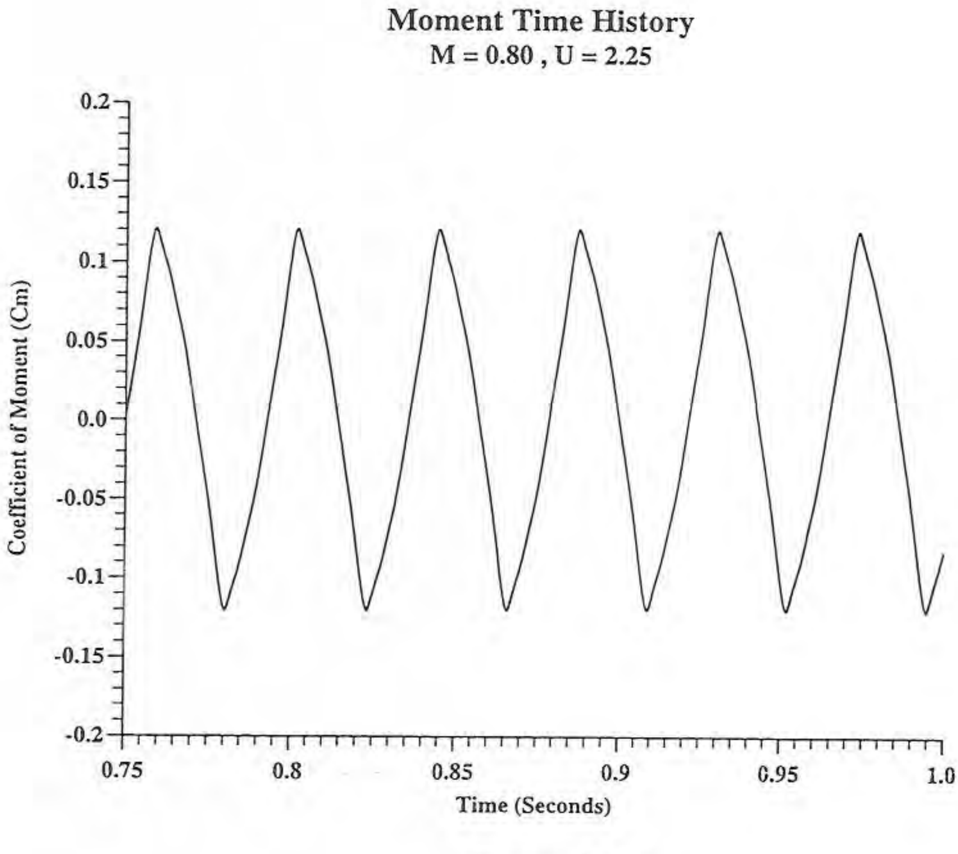

Figure 5.13b

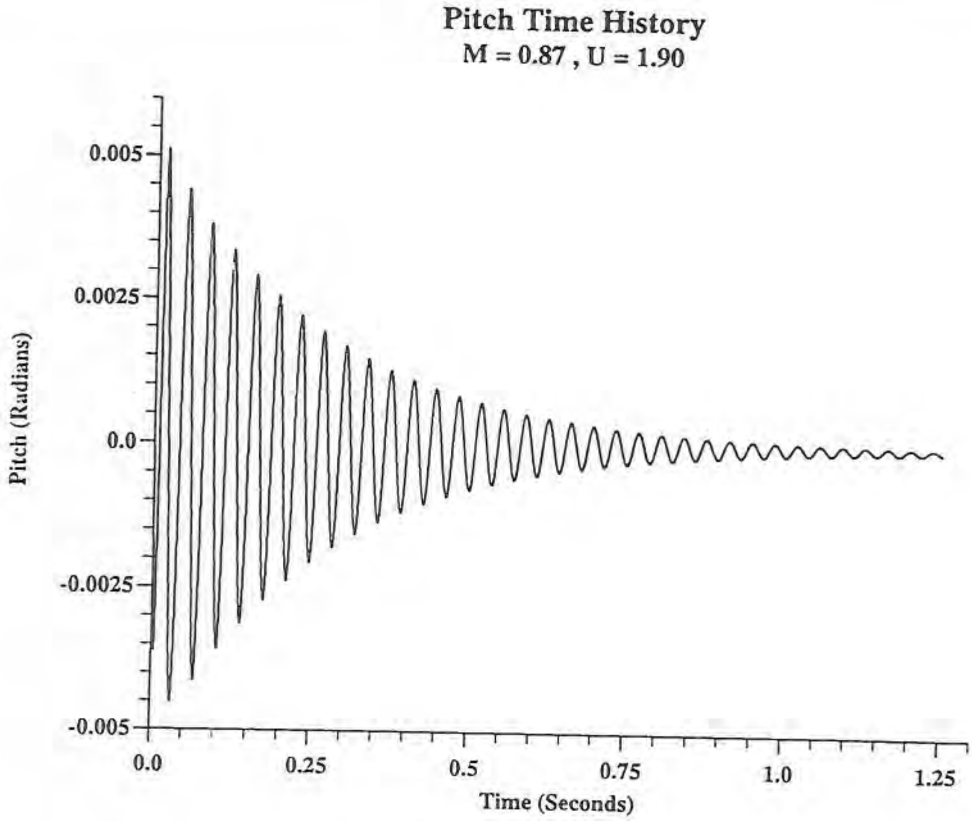

Figure 5.14a

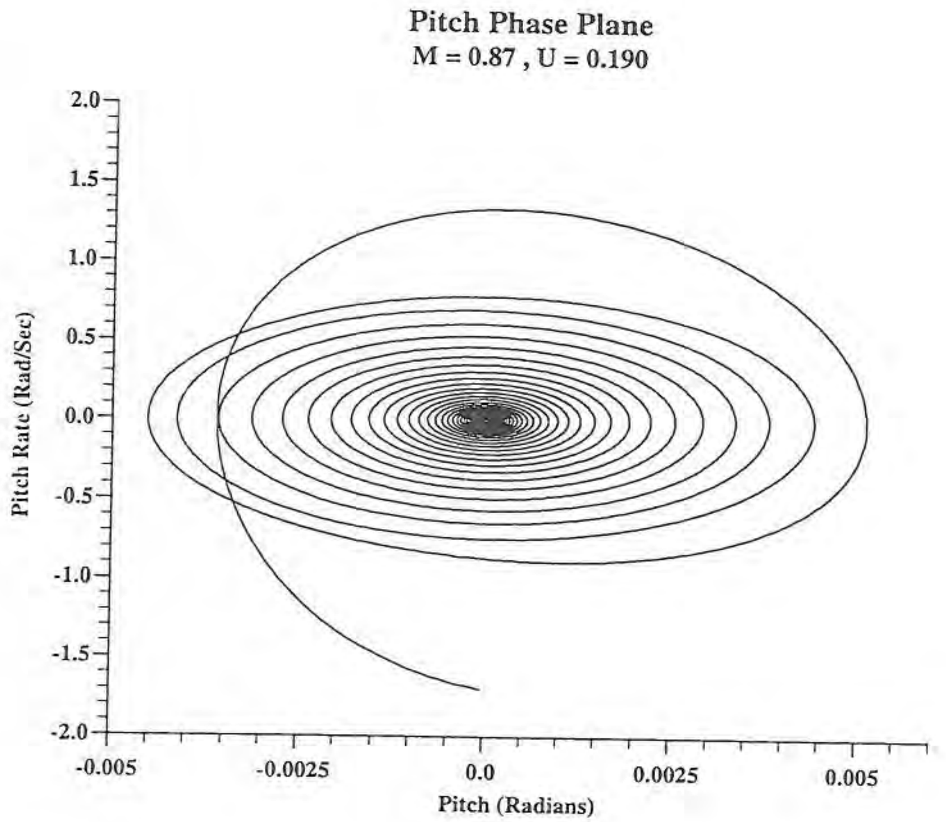

Figure 5.14b

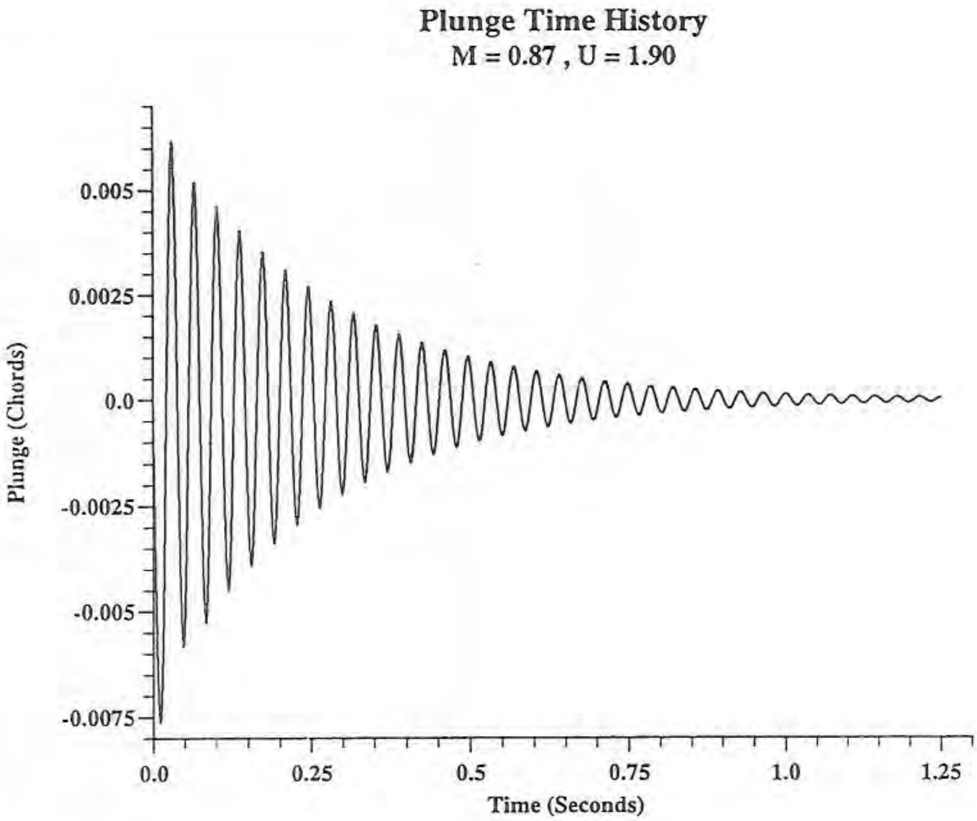

Figure 5.14c

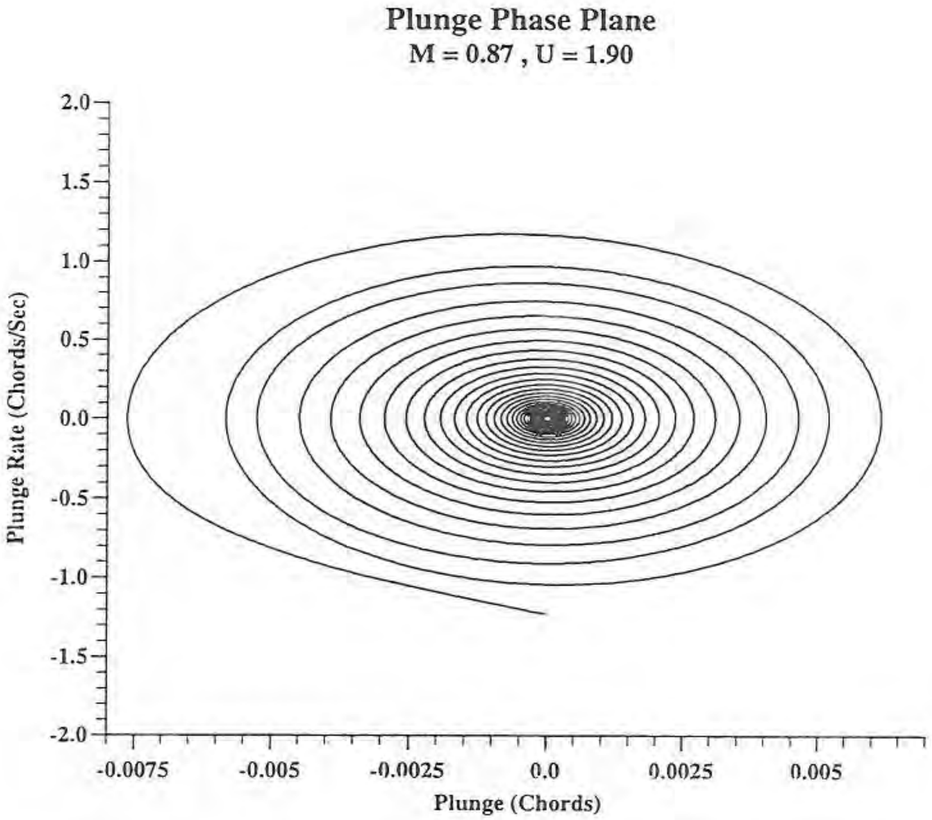

Figure 5.14d

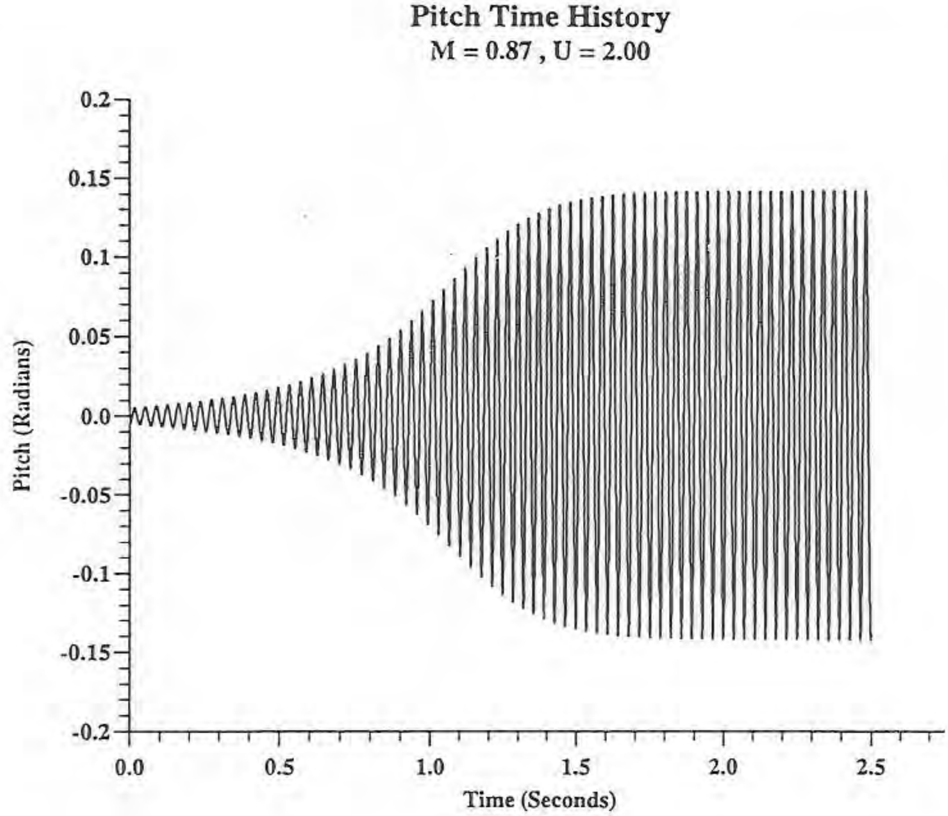

Figure 5.15a

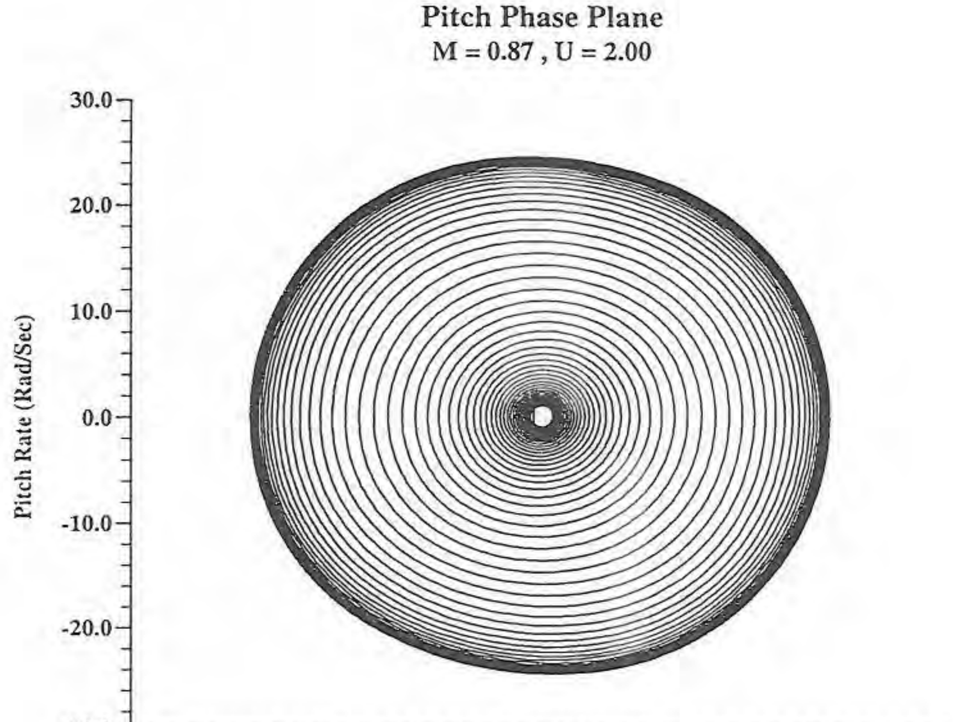

Figure 5.15b

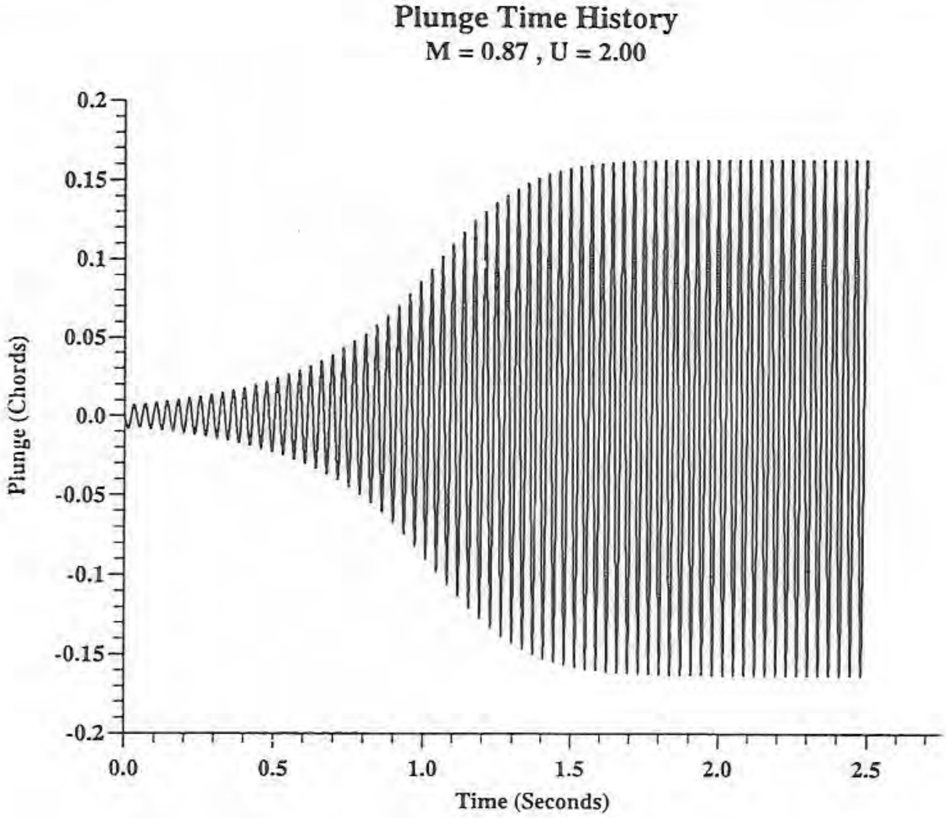

Figure 5.15c

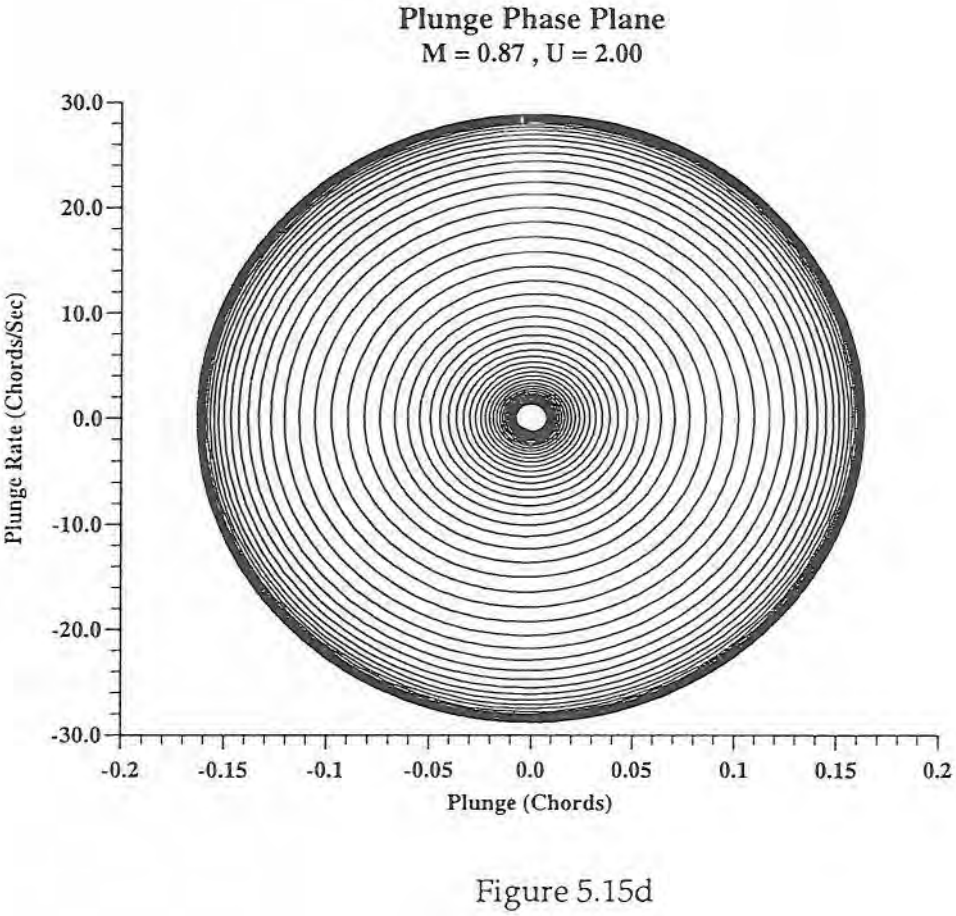

Figure 5.15d

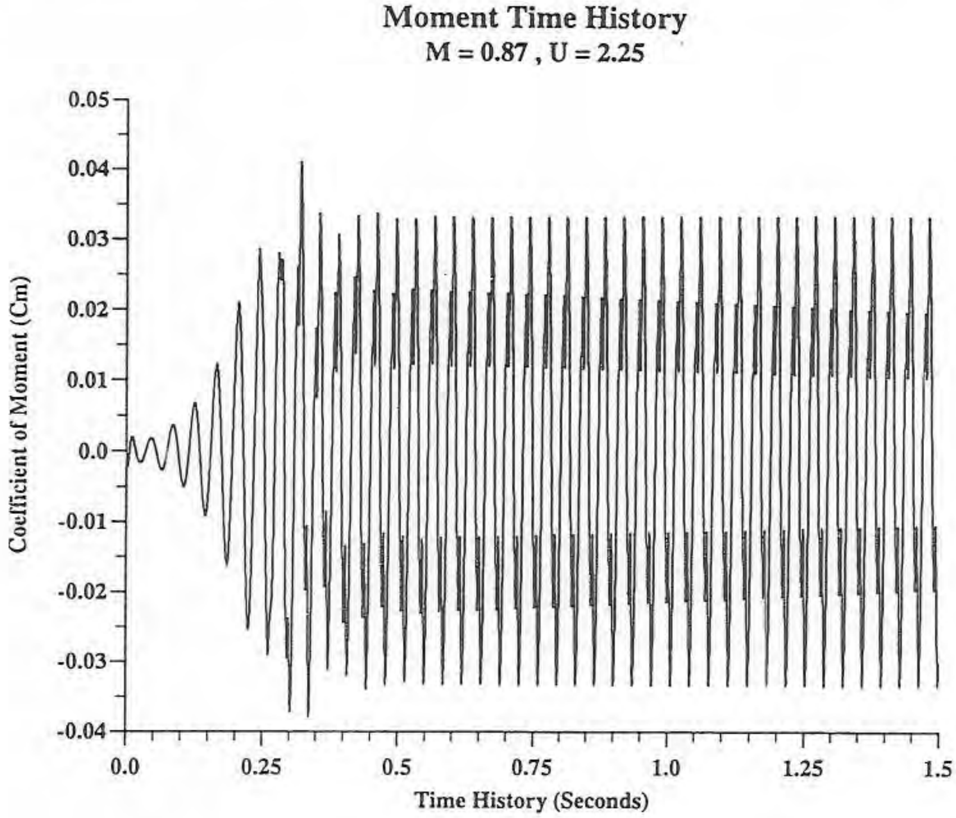

Figure 5.16a

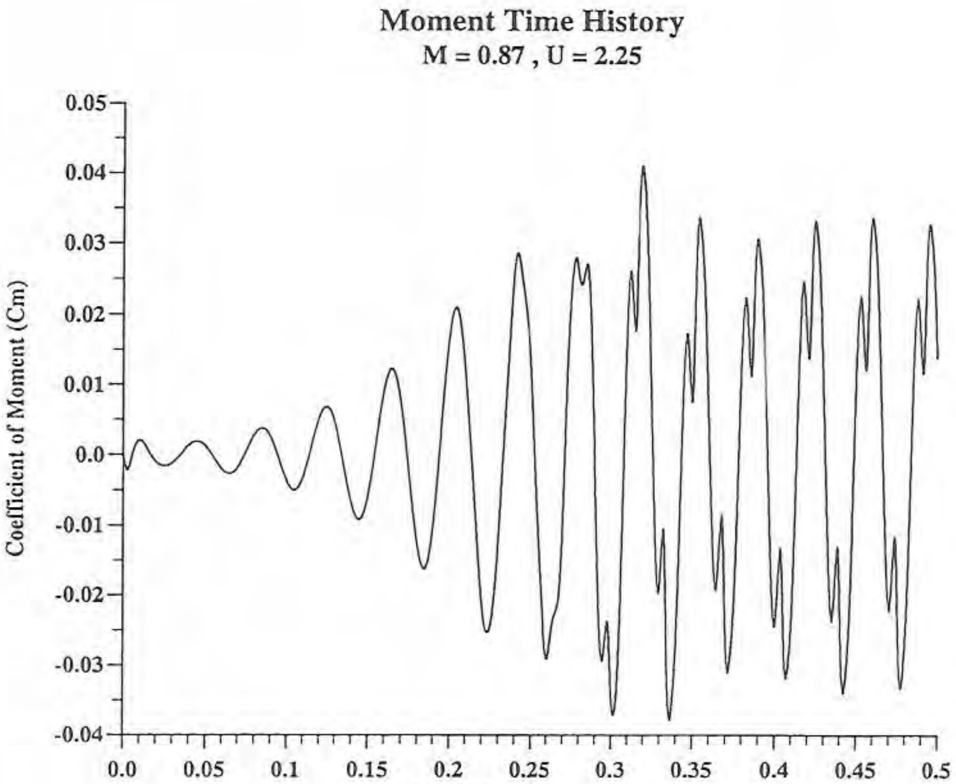

Figure 5.16b

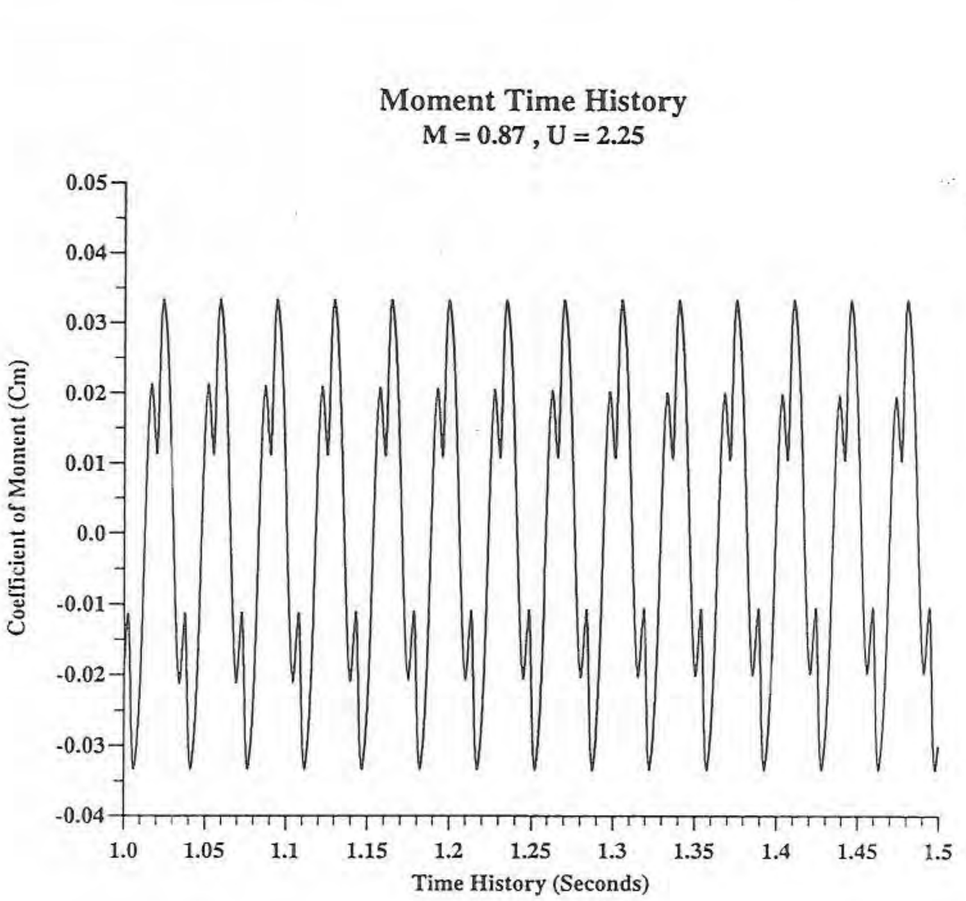
Moment Time History
M = 0.87 , U = 2.25
0.05
0.04
0.03
0.02
0.01
0.0
-0.01
-0.02
-0.03
-0.04
Coefficient of Moment (Cm)
1.0
1.05
1.1
1.15
1.2
1.25
1.3
1.35
1.4
1.45
1.5
Time History (Seconds)

Figure 5.16c

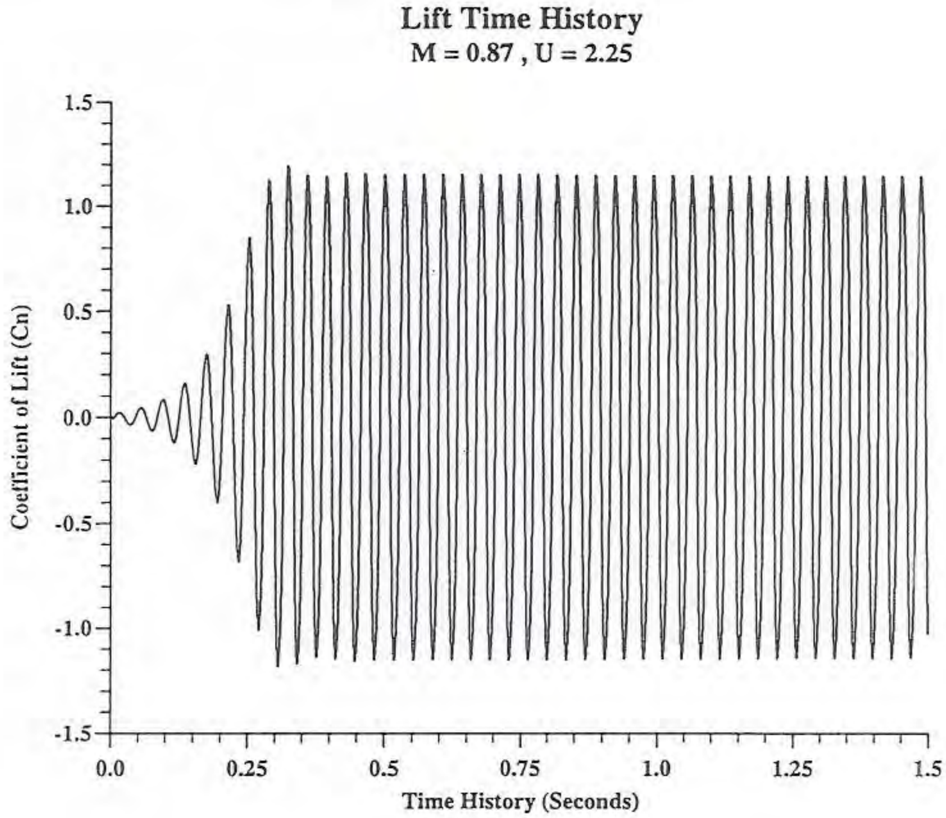

Figure 5.17a

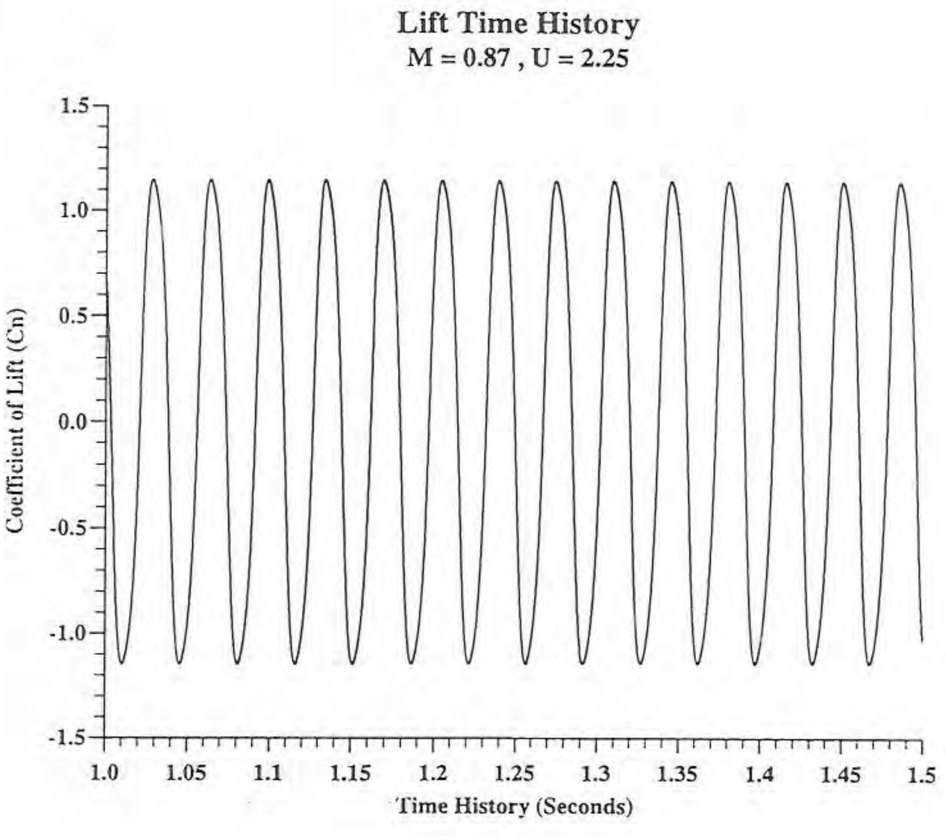

Figure 5.17b

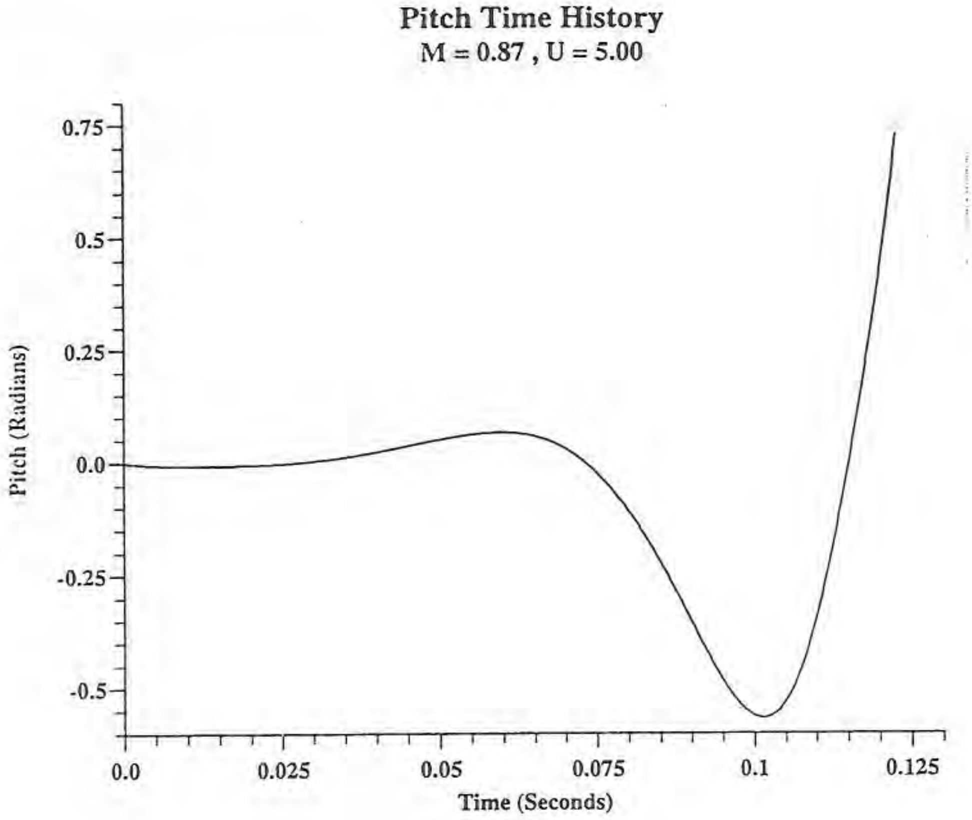

Figure 5.18a

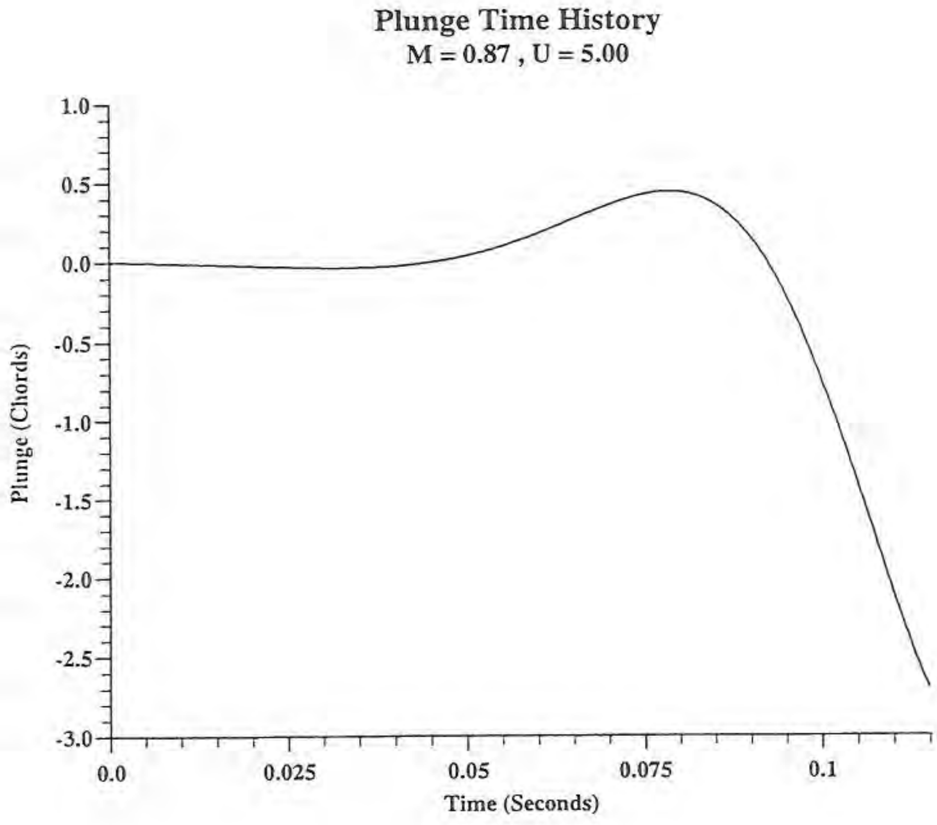

Figure 5.18b

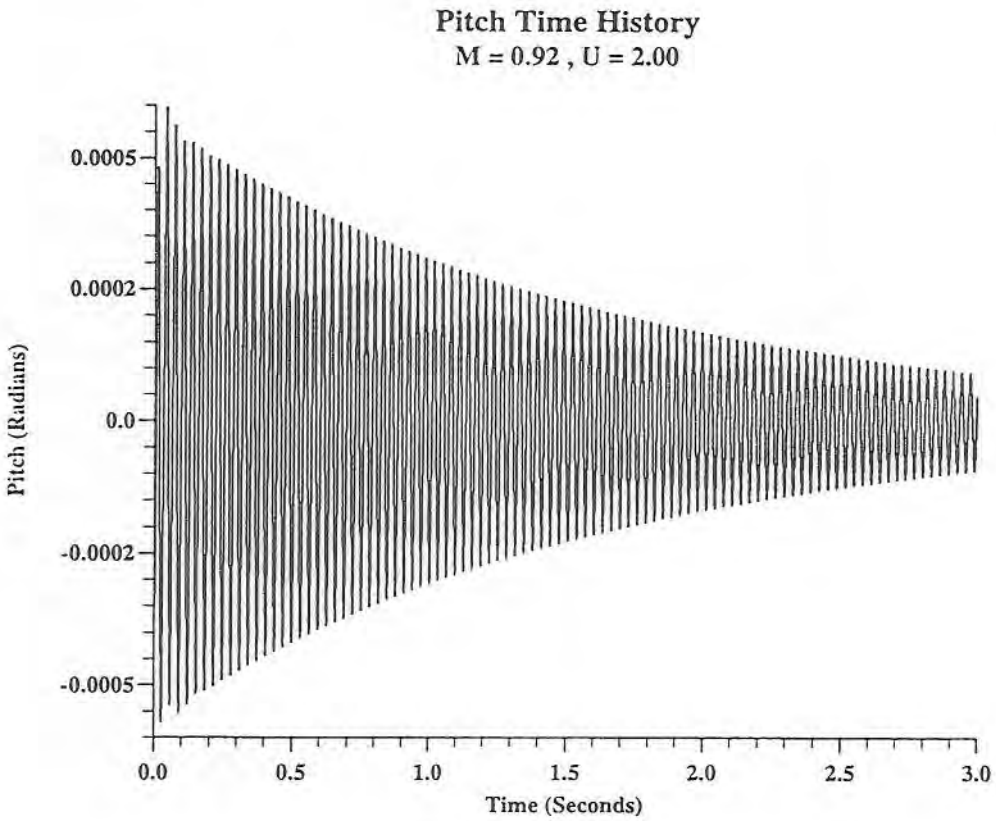

Figure 5.19a

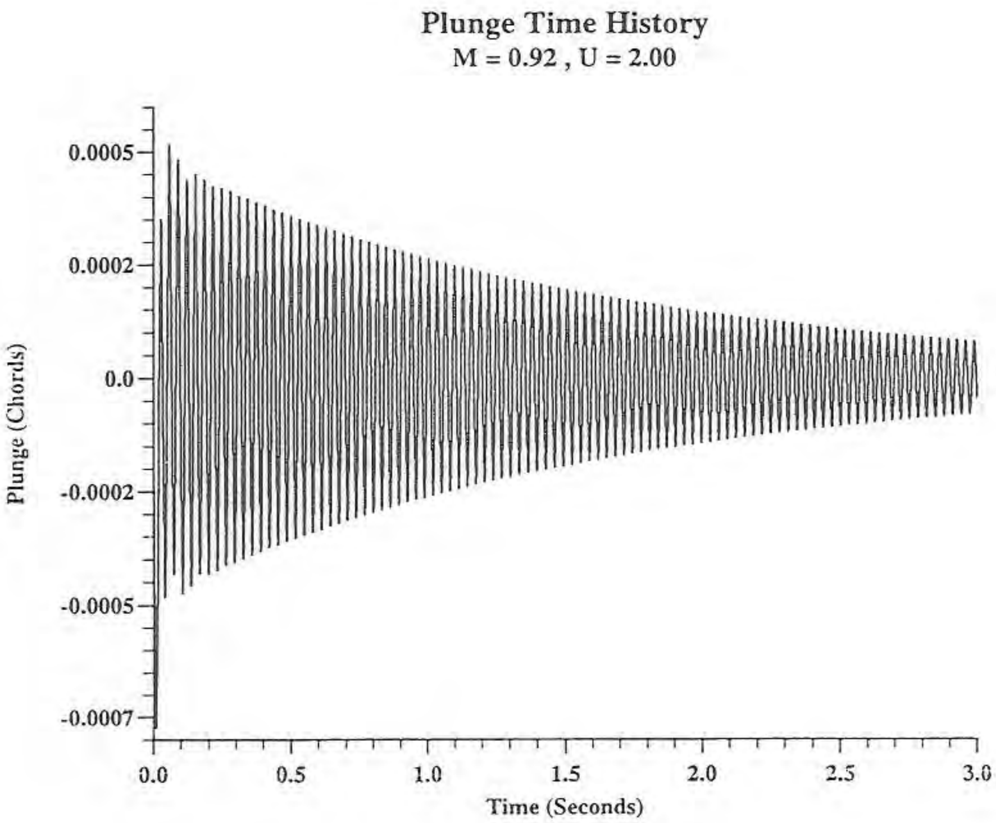

Figure 5.19b

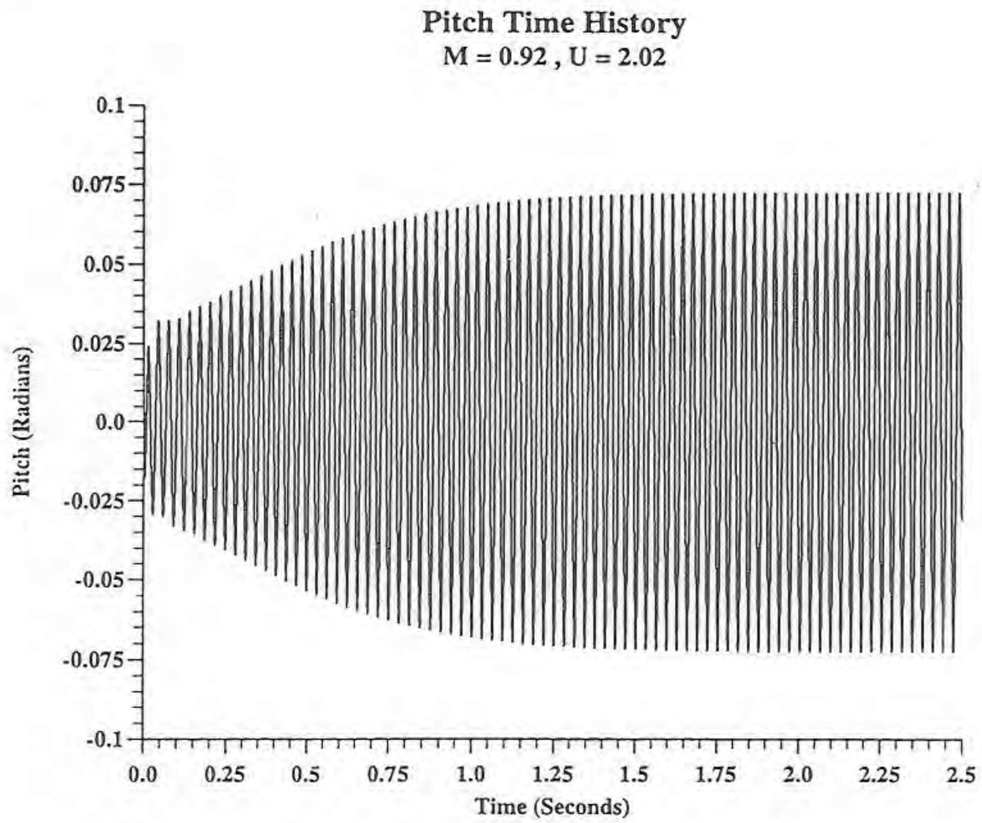

Figure 5.20a

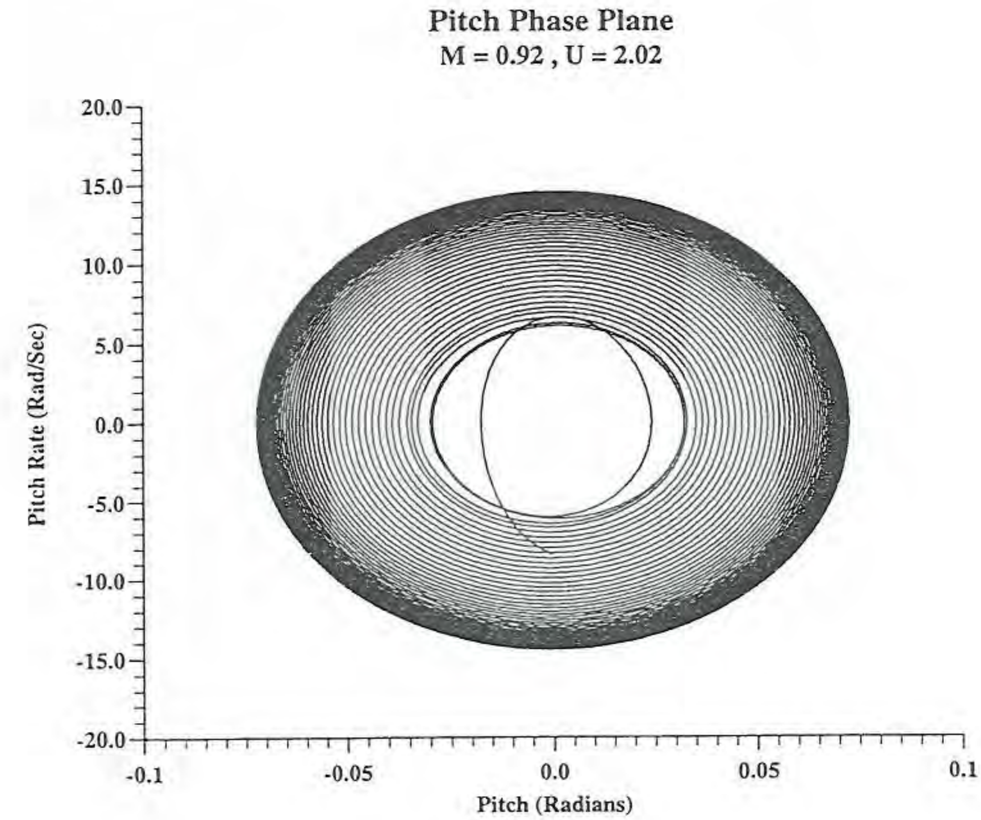

Figure 5.20b

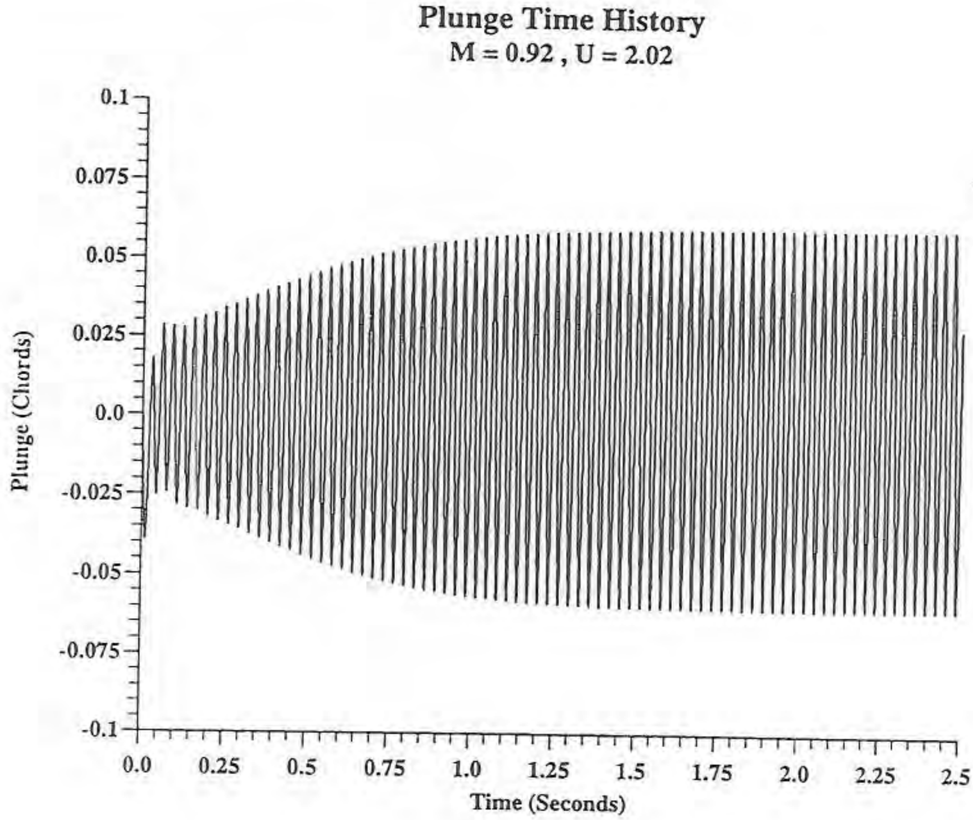

Figure 5.20c

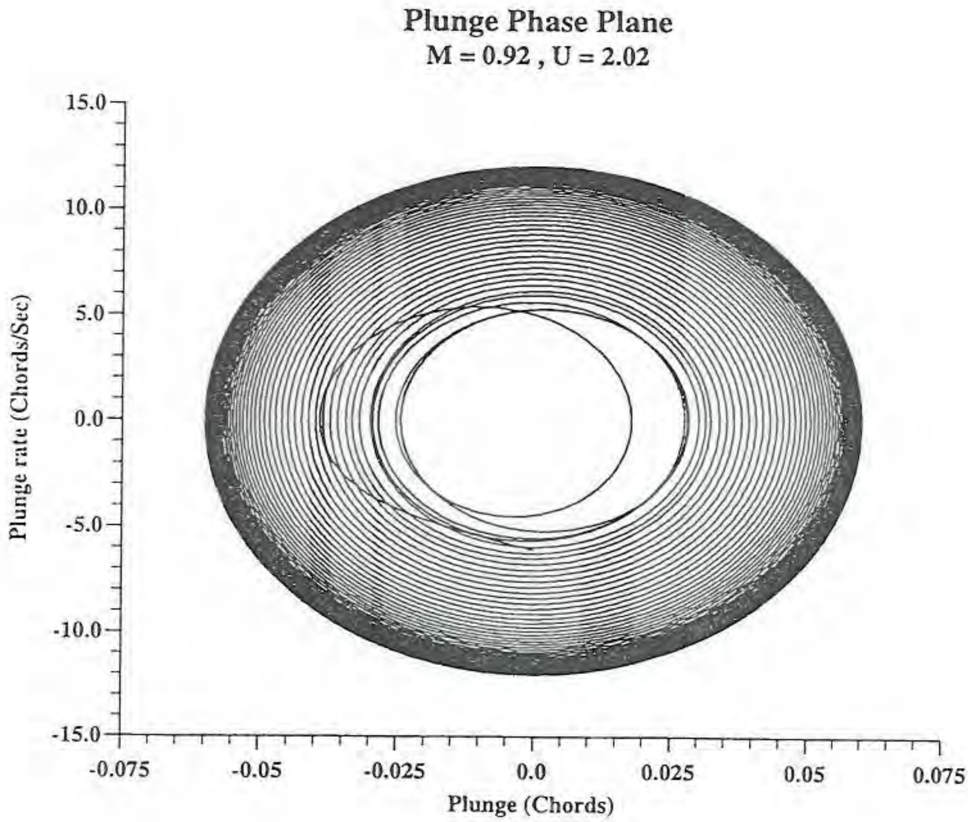

Figure 5.20d

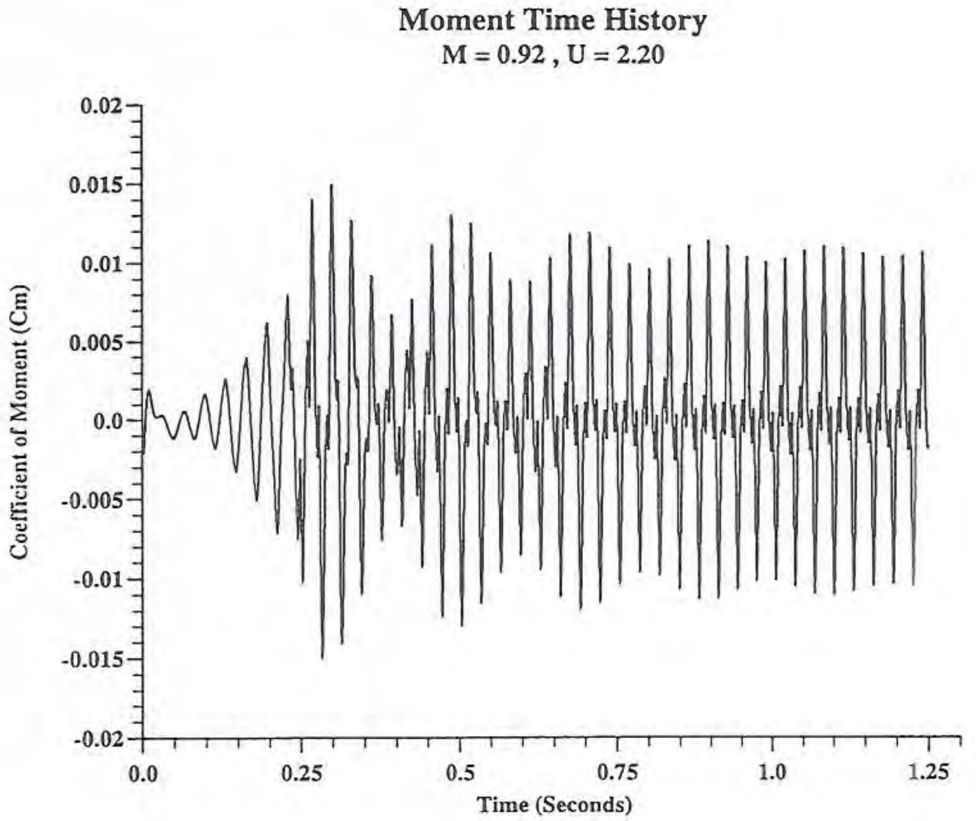

Figure 5.21a

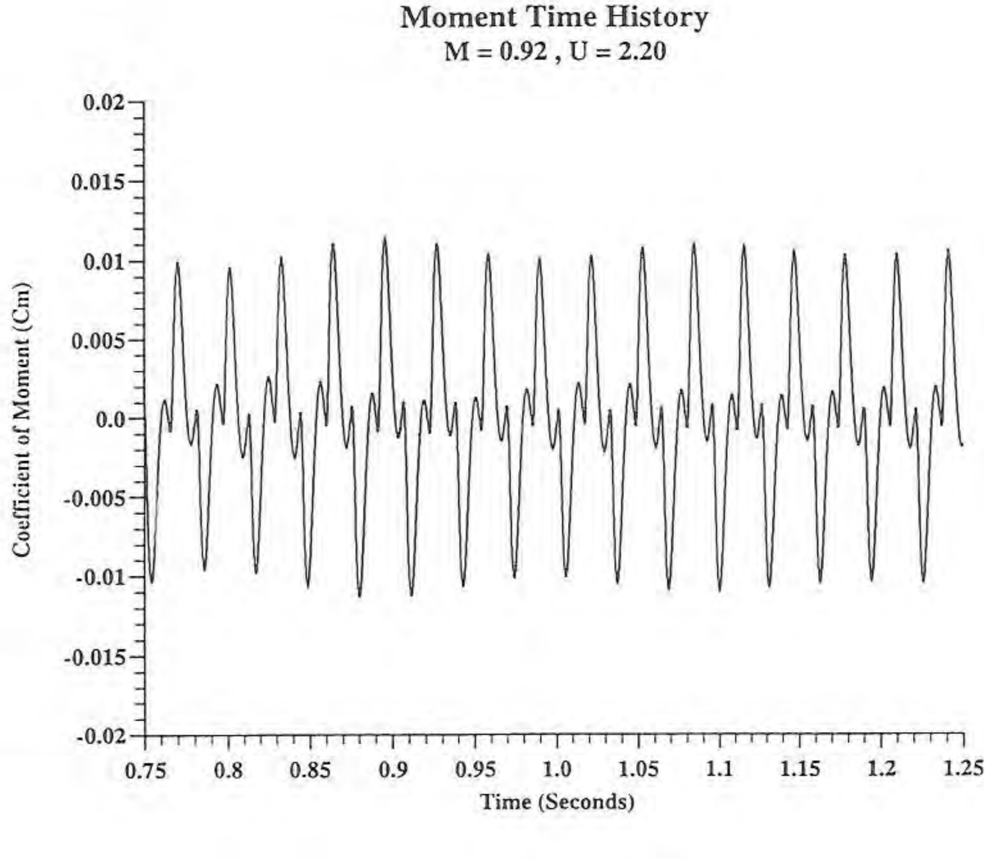

Figure 5.21b

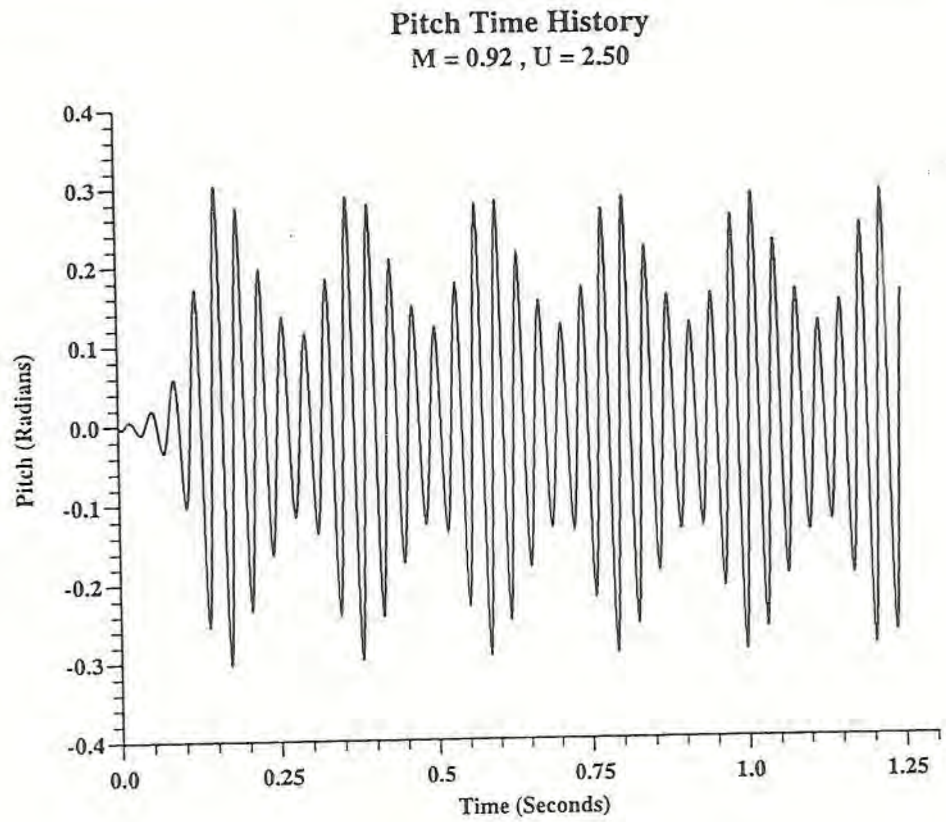

Figure 5.22a

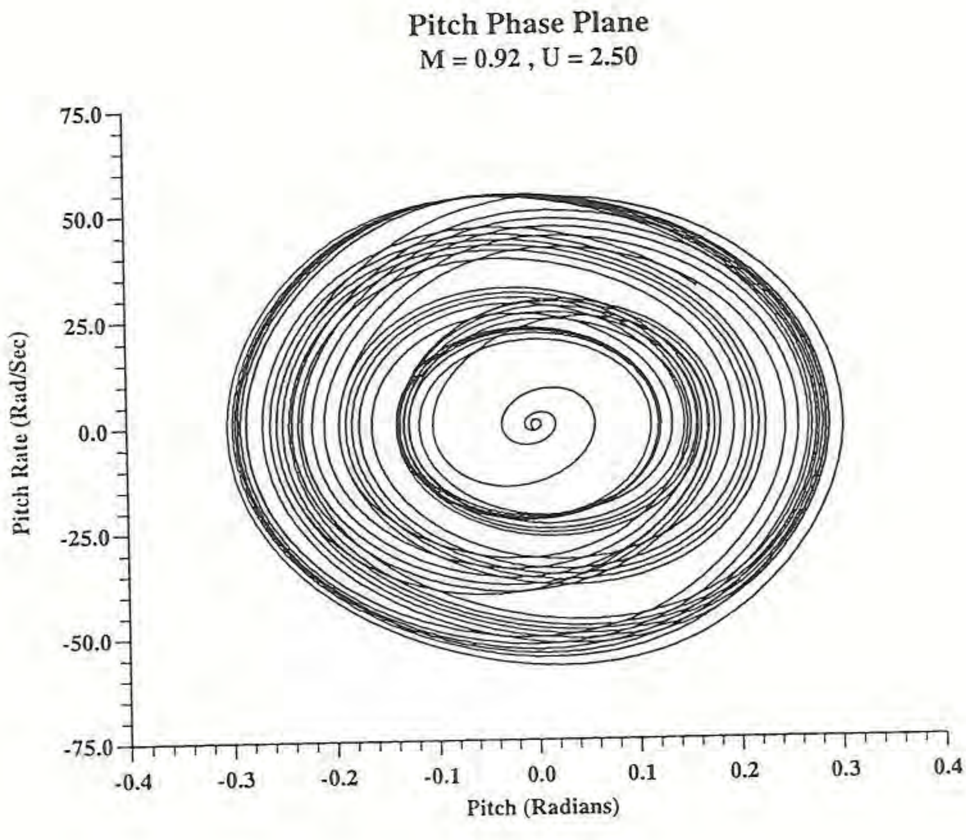

Figure 5.22b

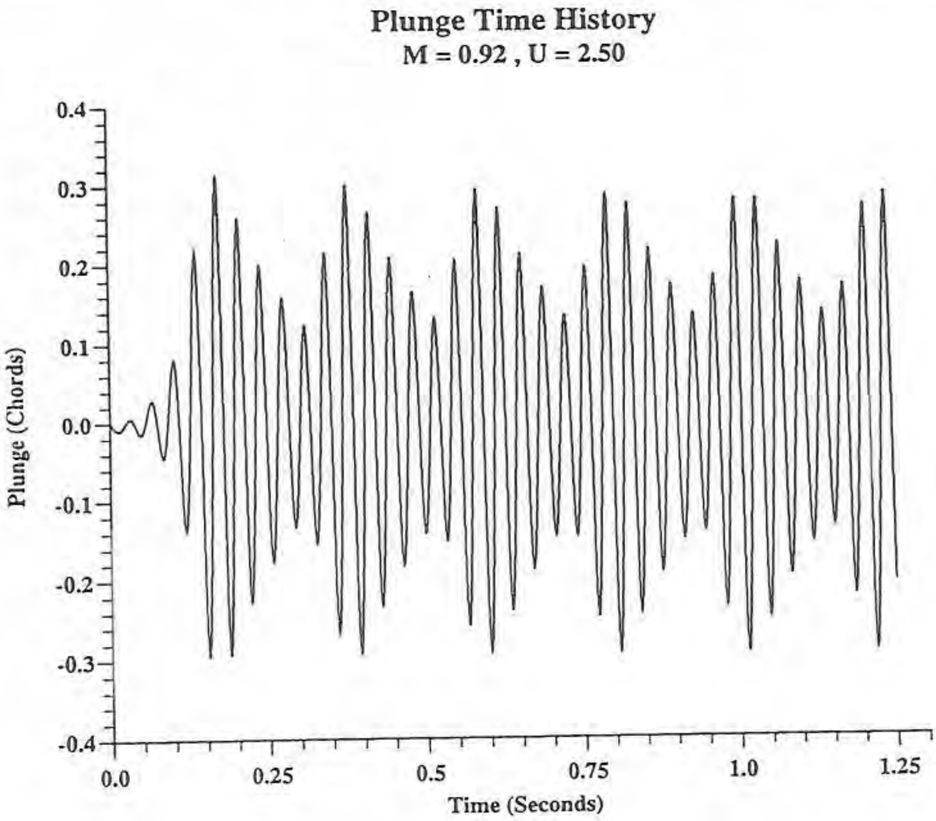

Figure 5.22c

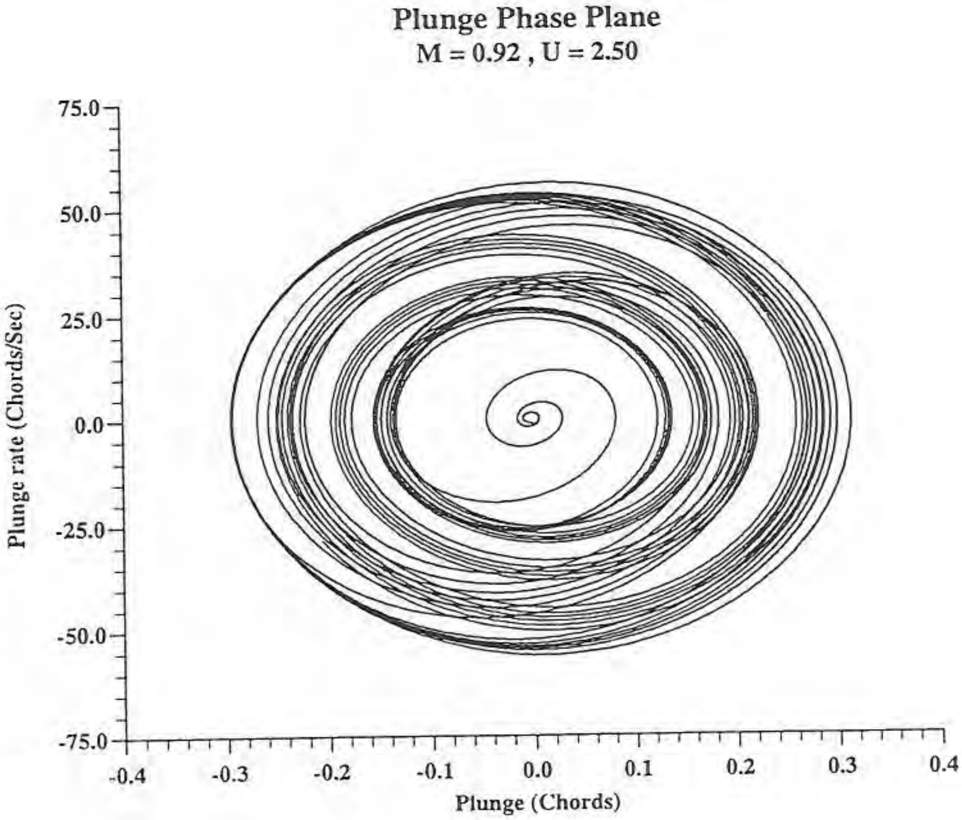

Figure 5.22d

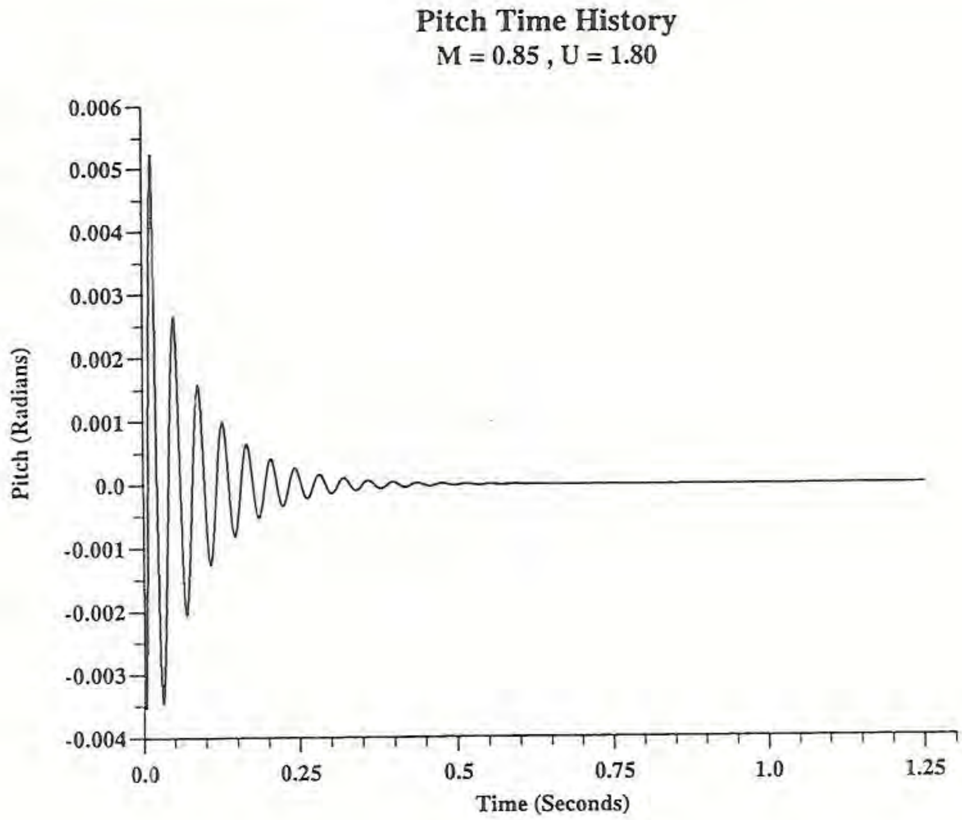

Figure 5.23a

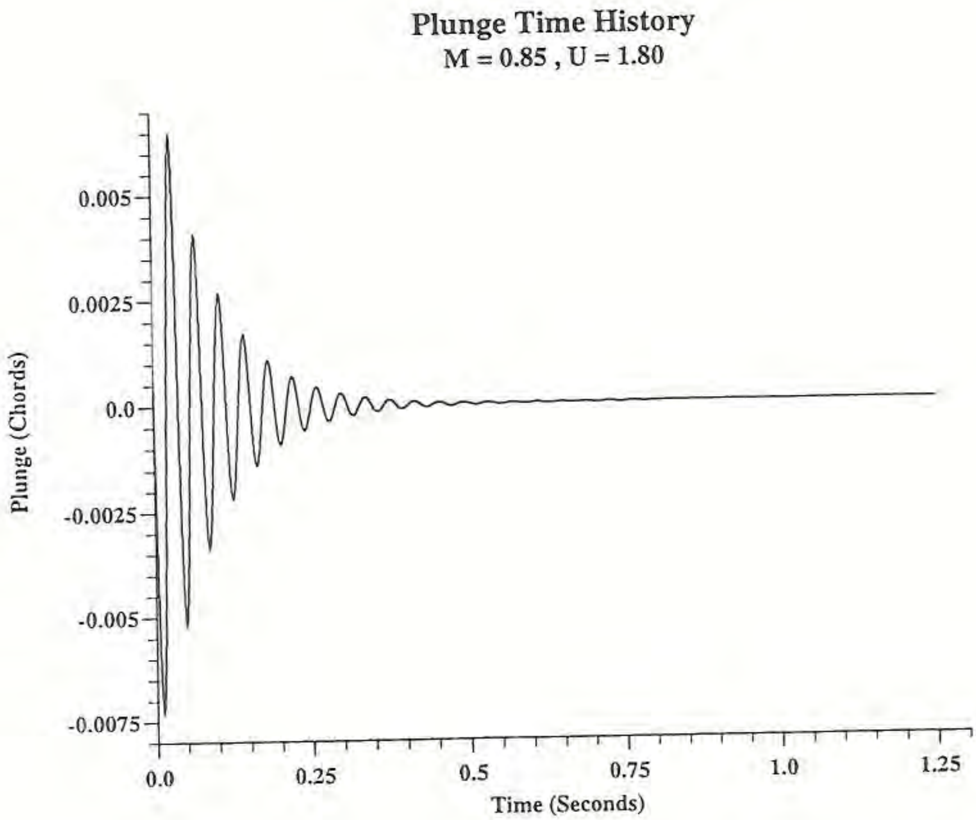

Figure 5.23b

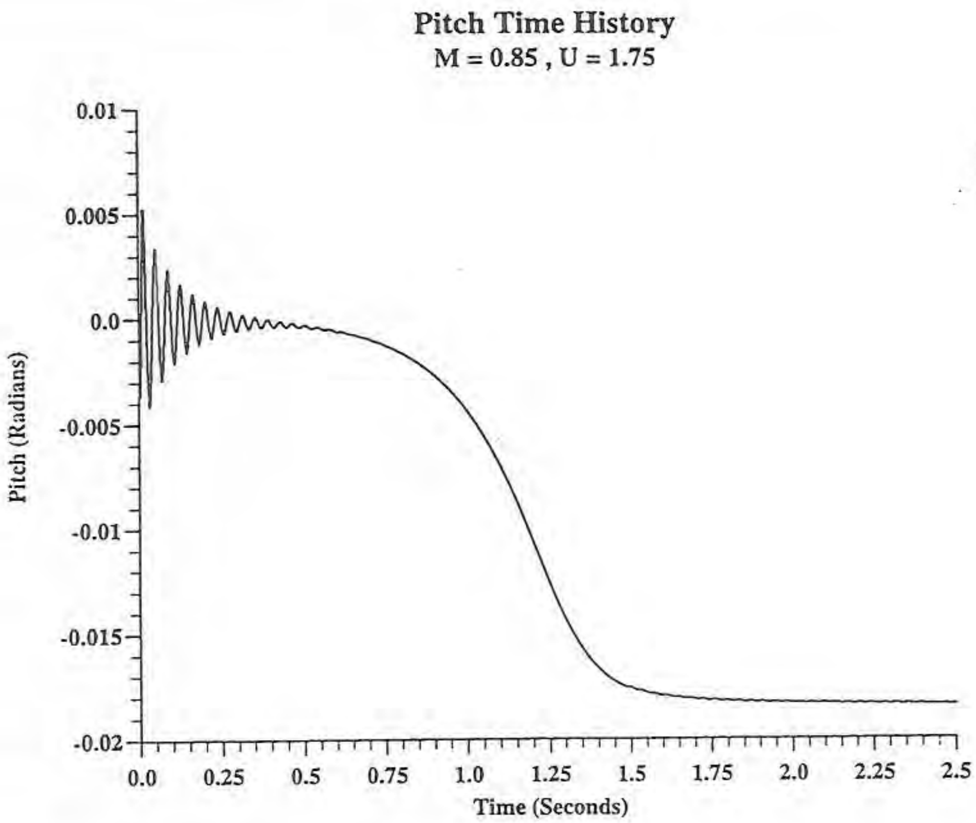

Figure 5.24a

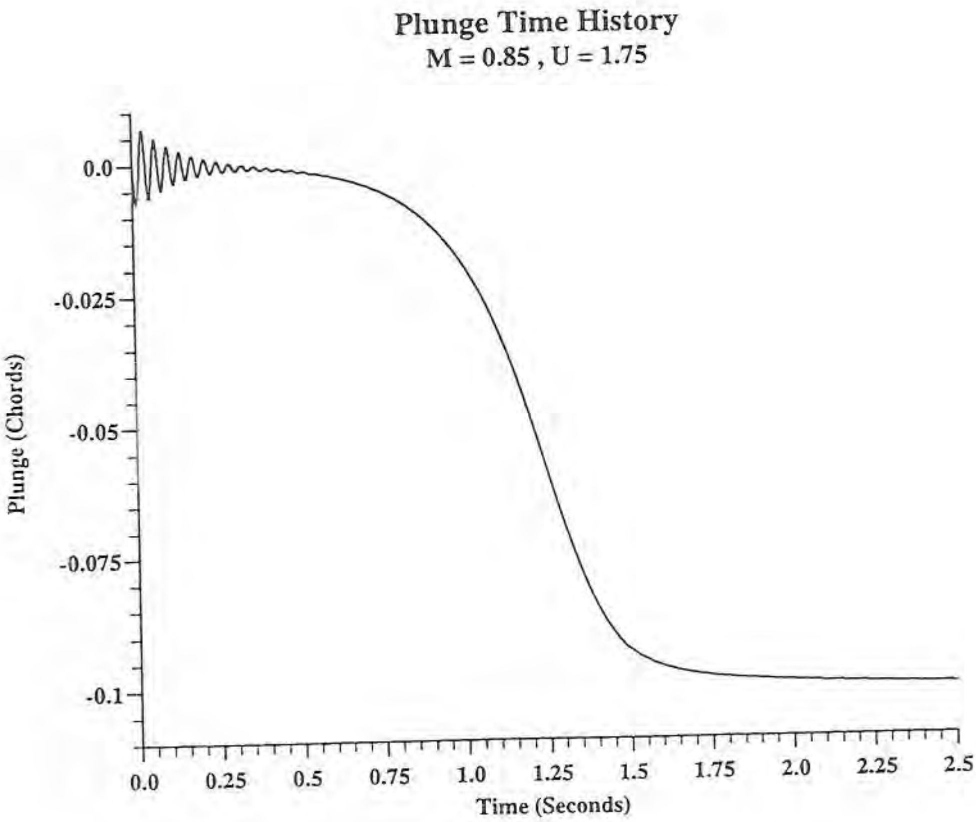

Figure 5.24b

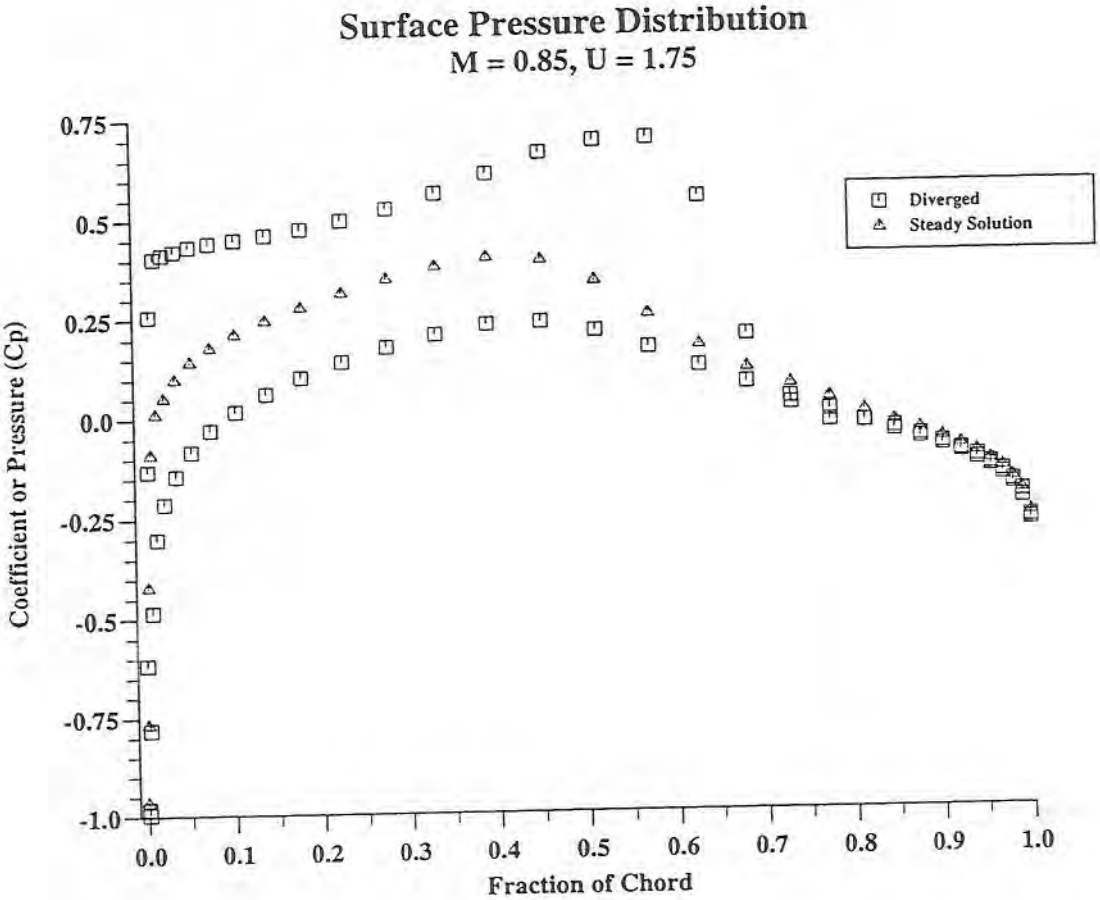
Surface Pressure Distribution
M = 0.85, U = 1.75
Coefficient or Pressure (Cp)
0.75
0.5
0.25
0.0
-0.25
-0.5
-0.75
-1.0
0.0
0.1
0.2
0.3
0.4
0.5
0.6
0.7
0.8
0.9
1.0
Fraction of Chord
Diverged
Steady Solution

Figure 5.25

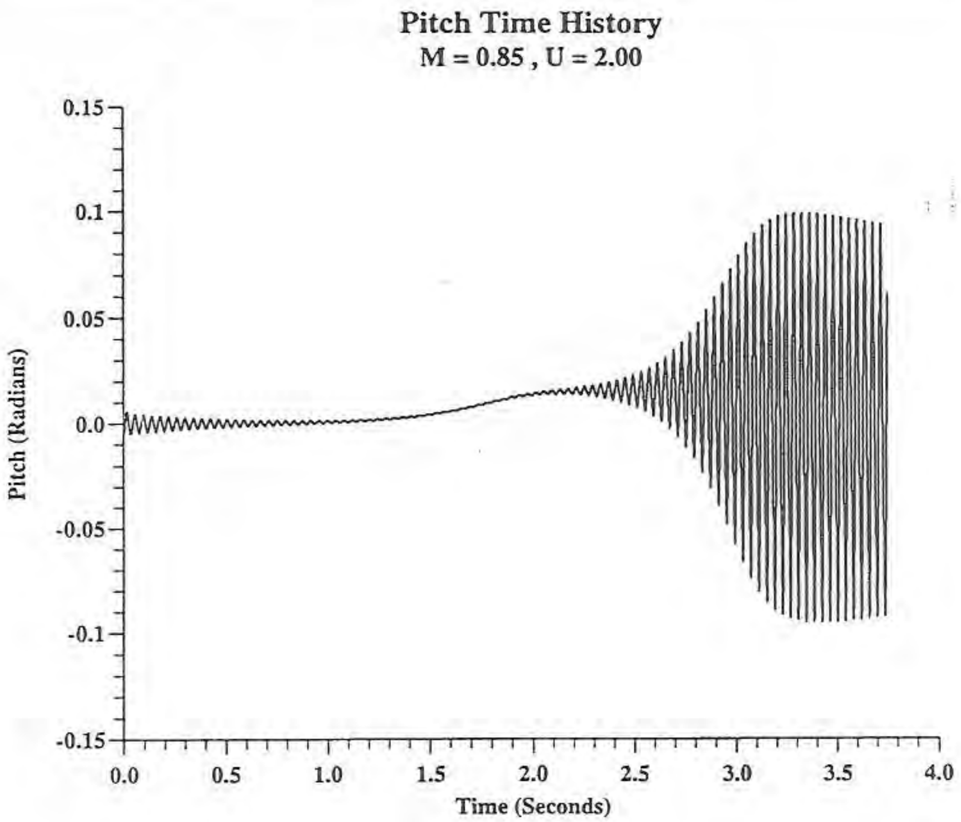

Figure 5.26a

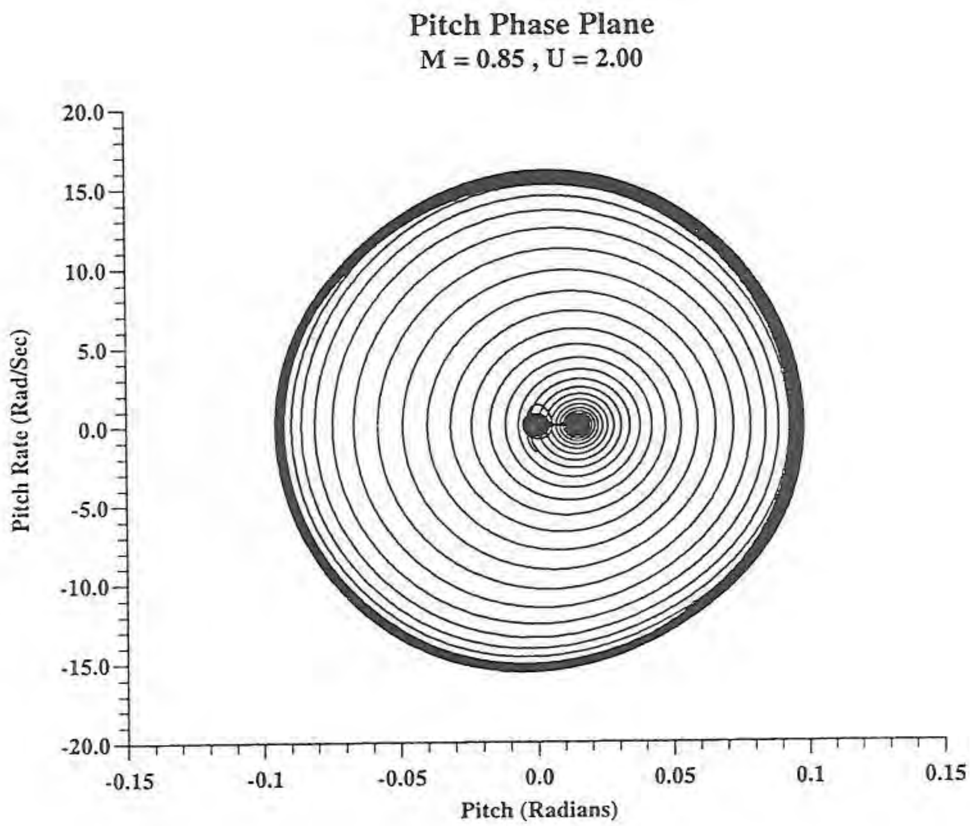

Figure 5.26b

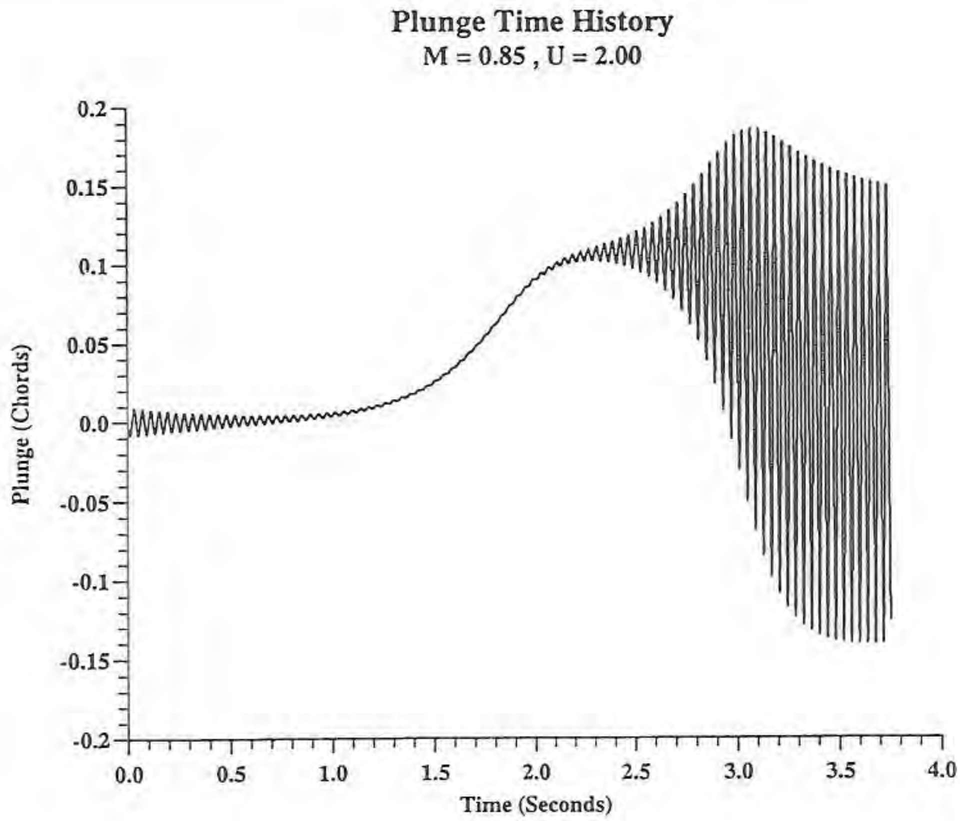

Figure 5.26c

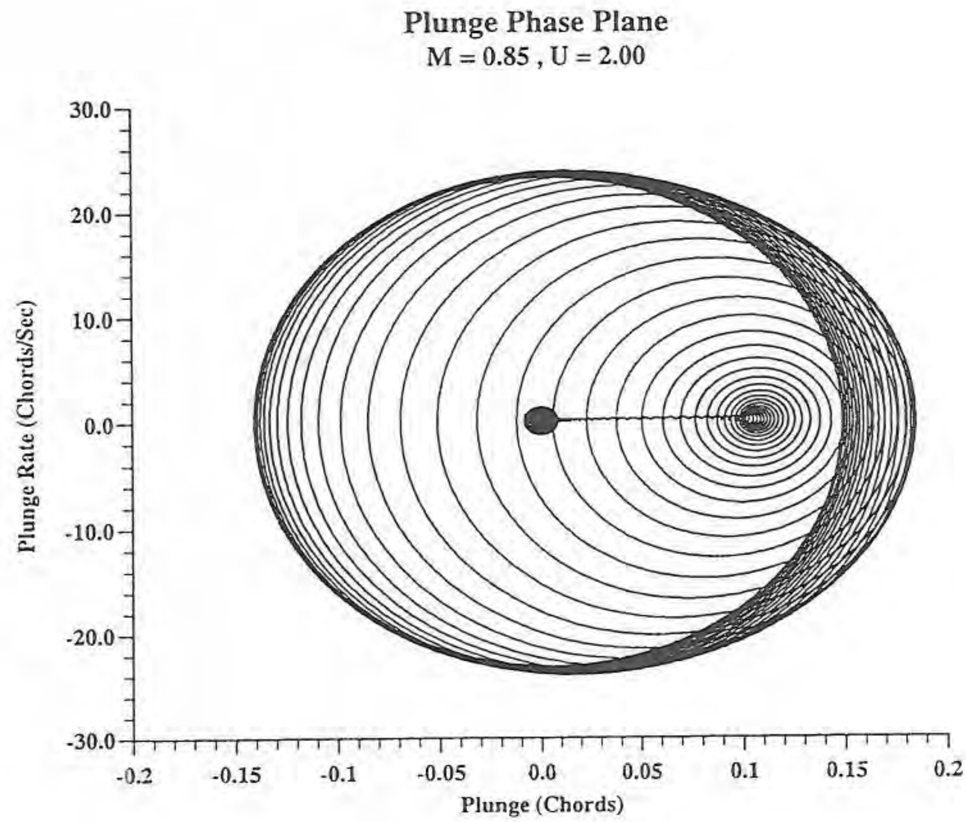

Figure 5.26d

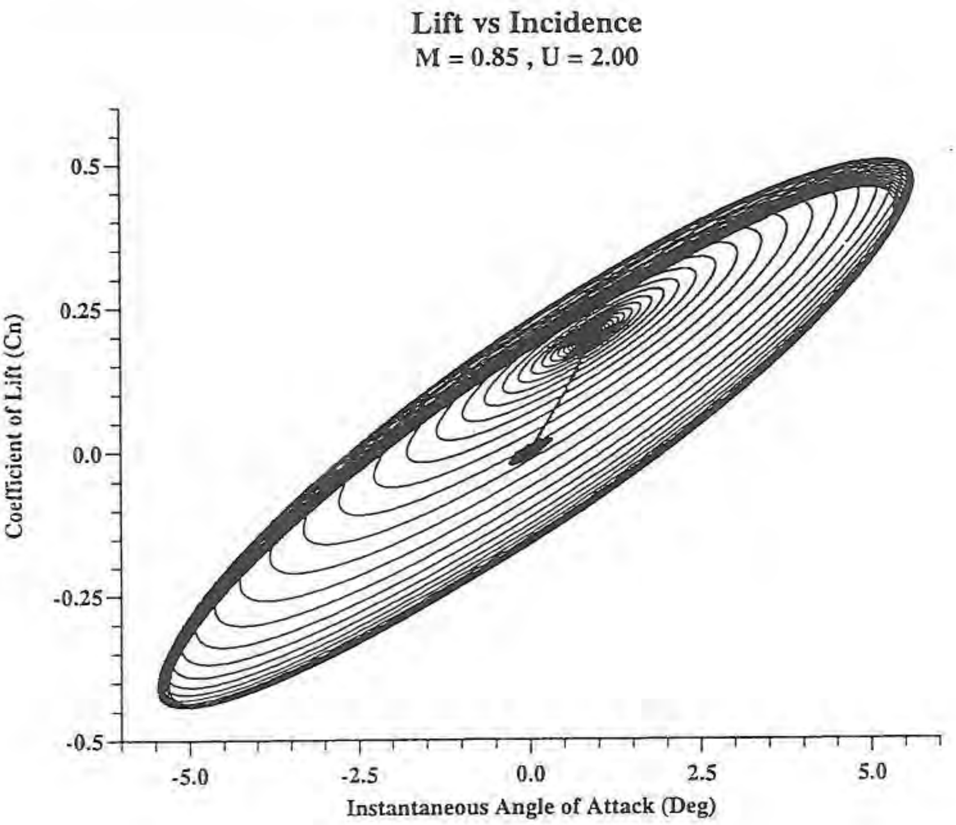

Figure 5.27a

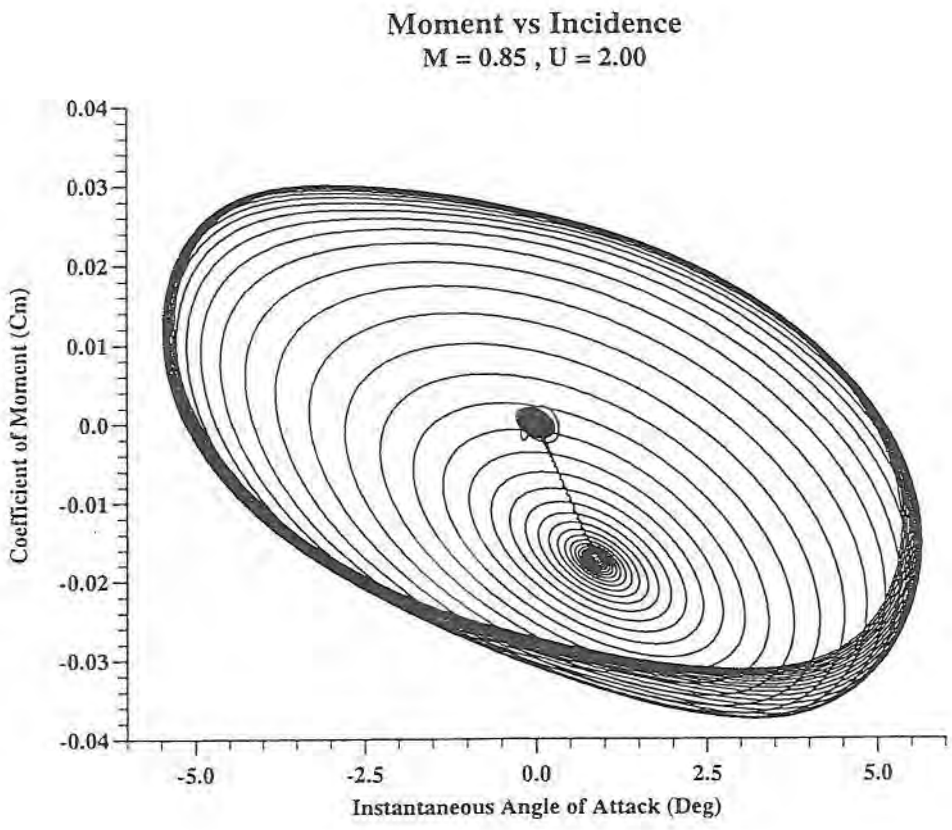

Figure 5.27b

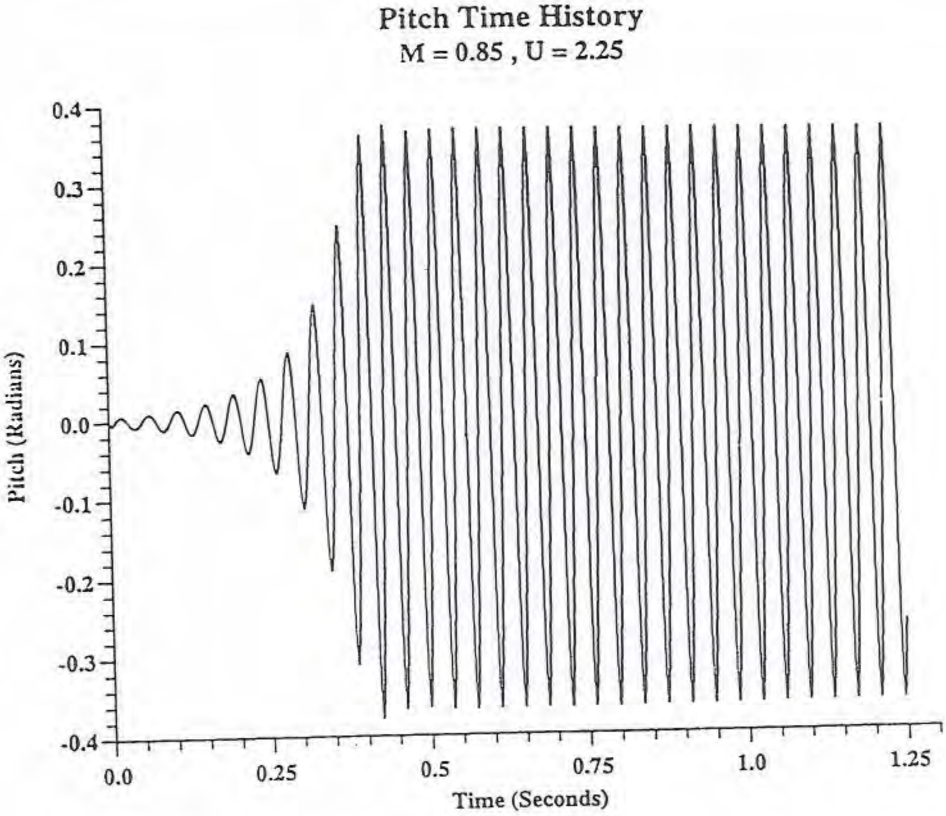

Figure 5.28a

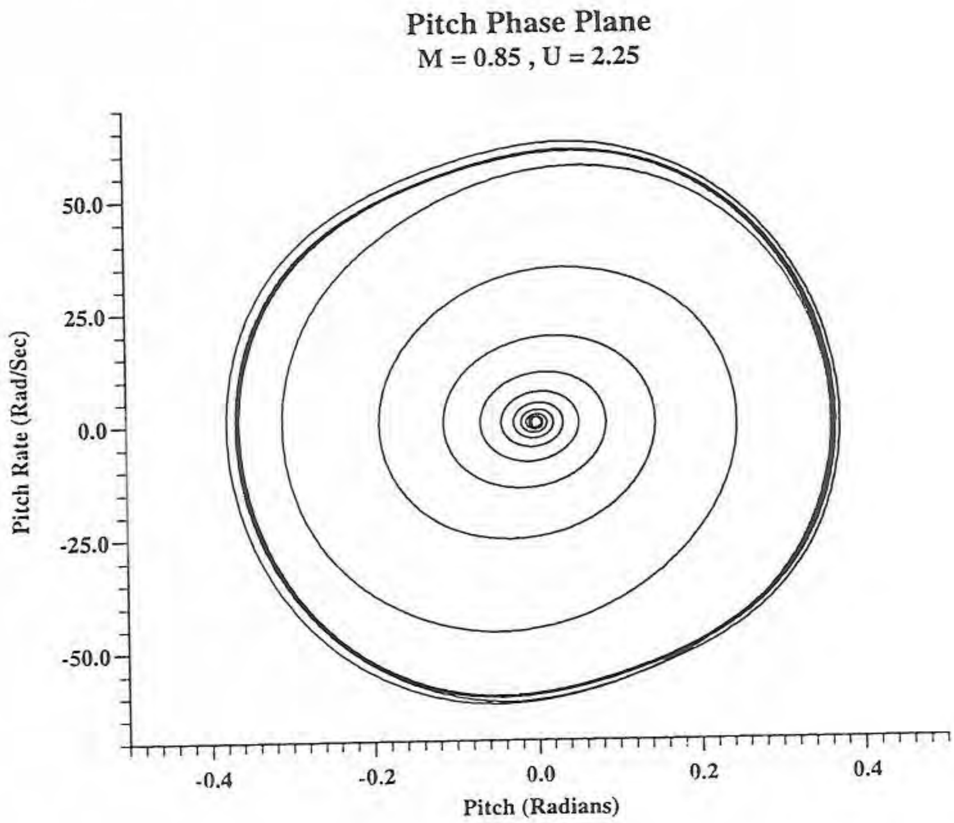

Figure 5.28b

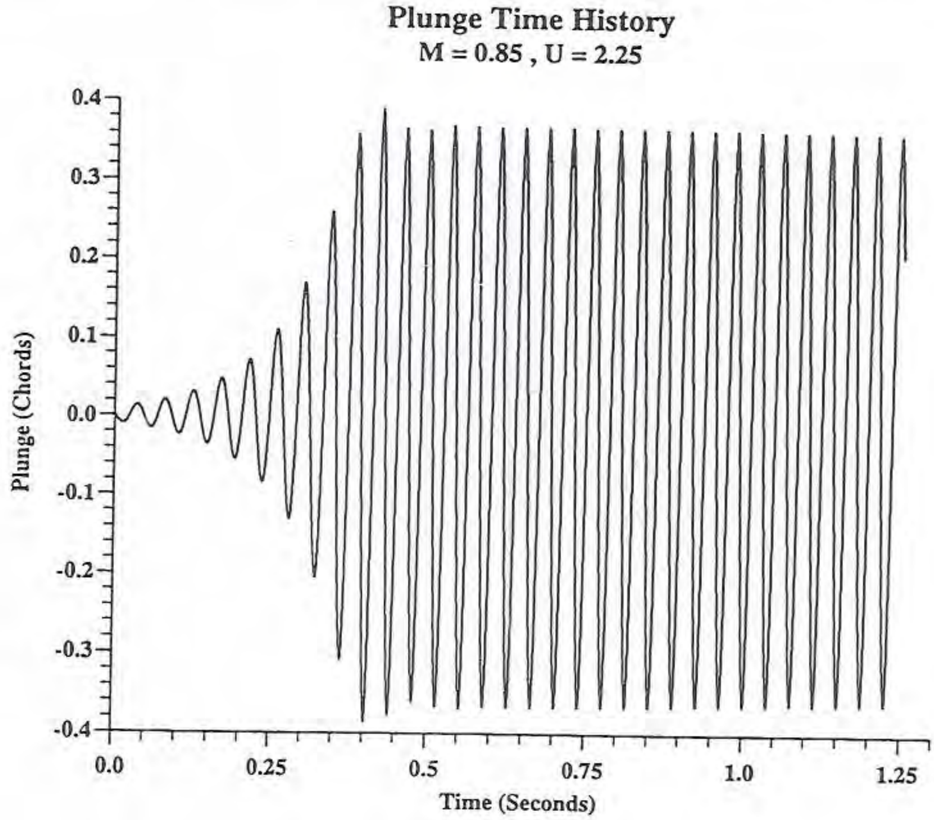

Figure 5.28c

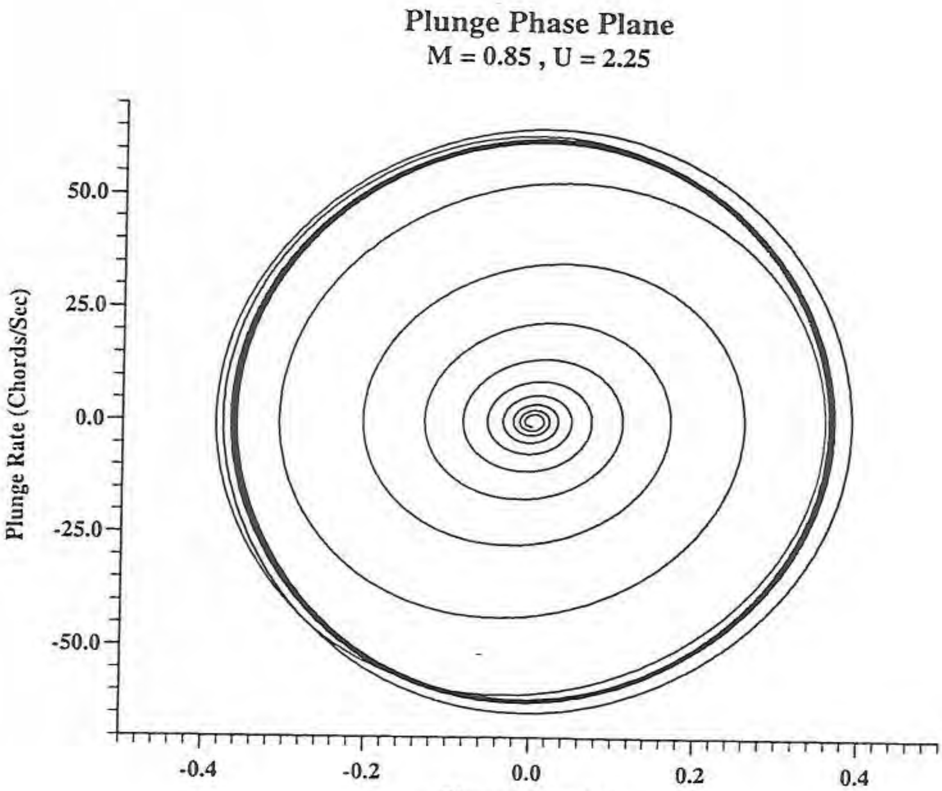

Figure 5.28d

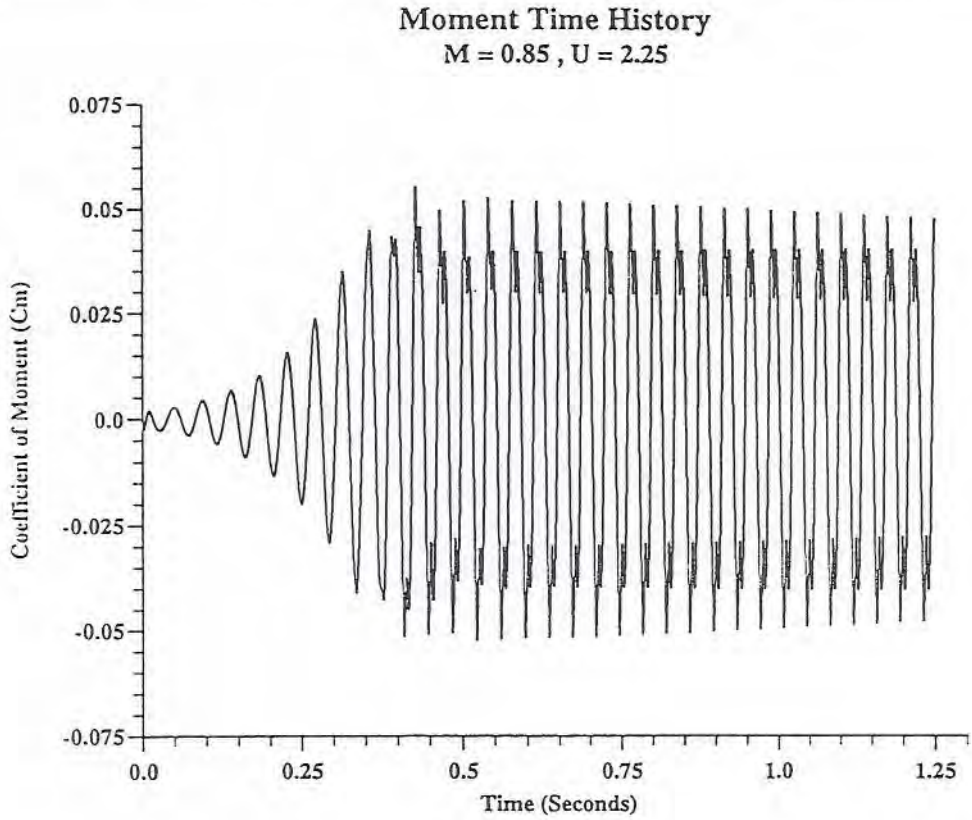

Figure 5.29a

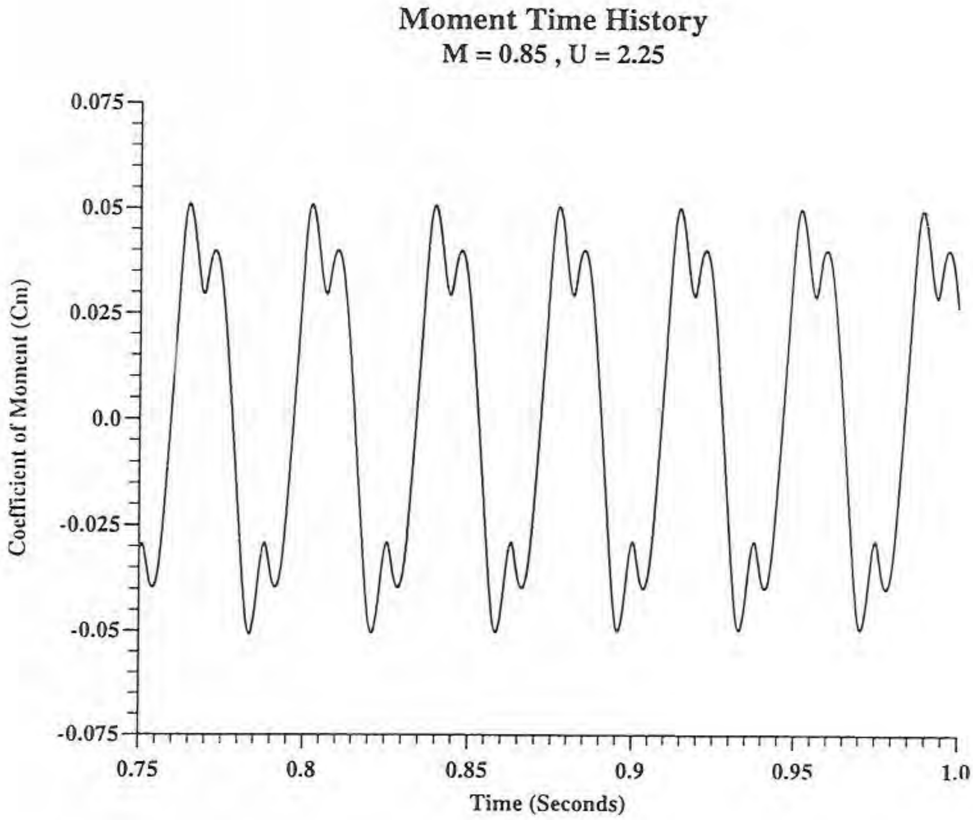

Figure 5.29b

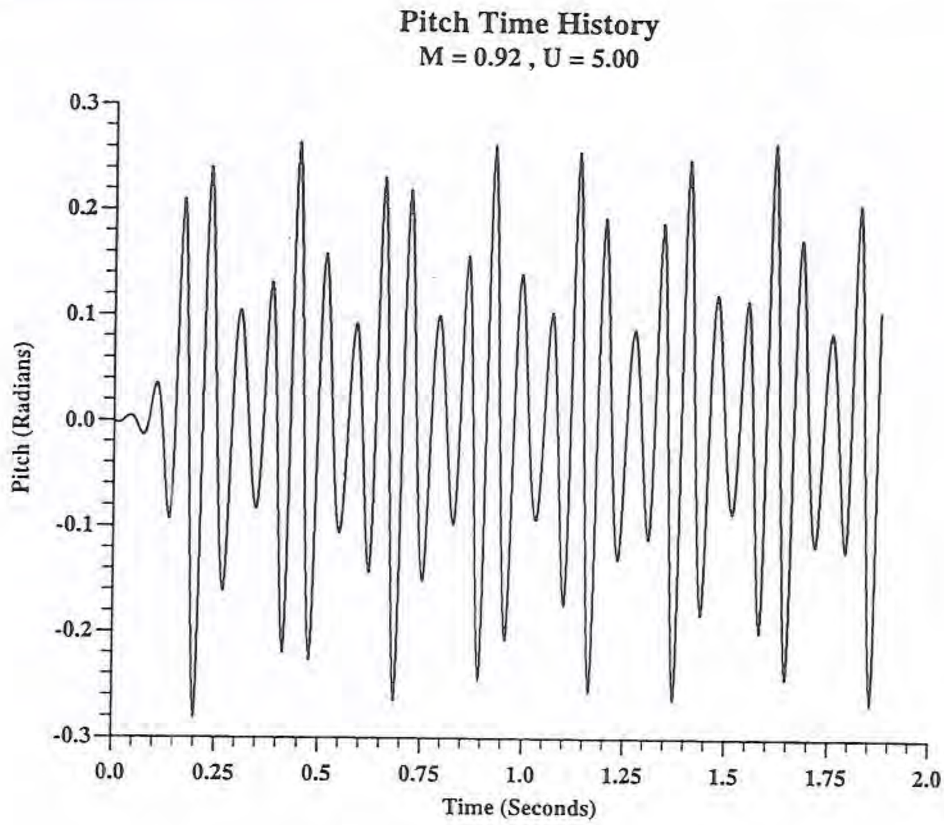

Figure 5.30a

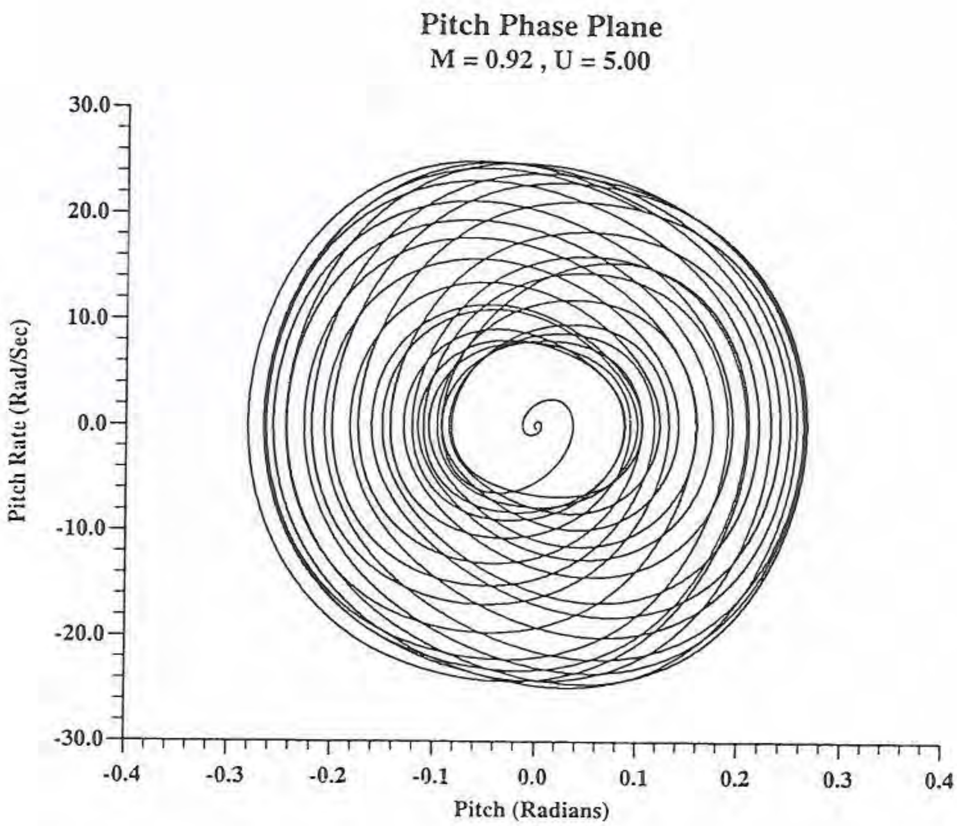

Figure 5.30b

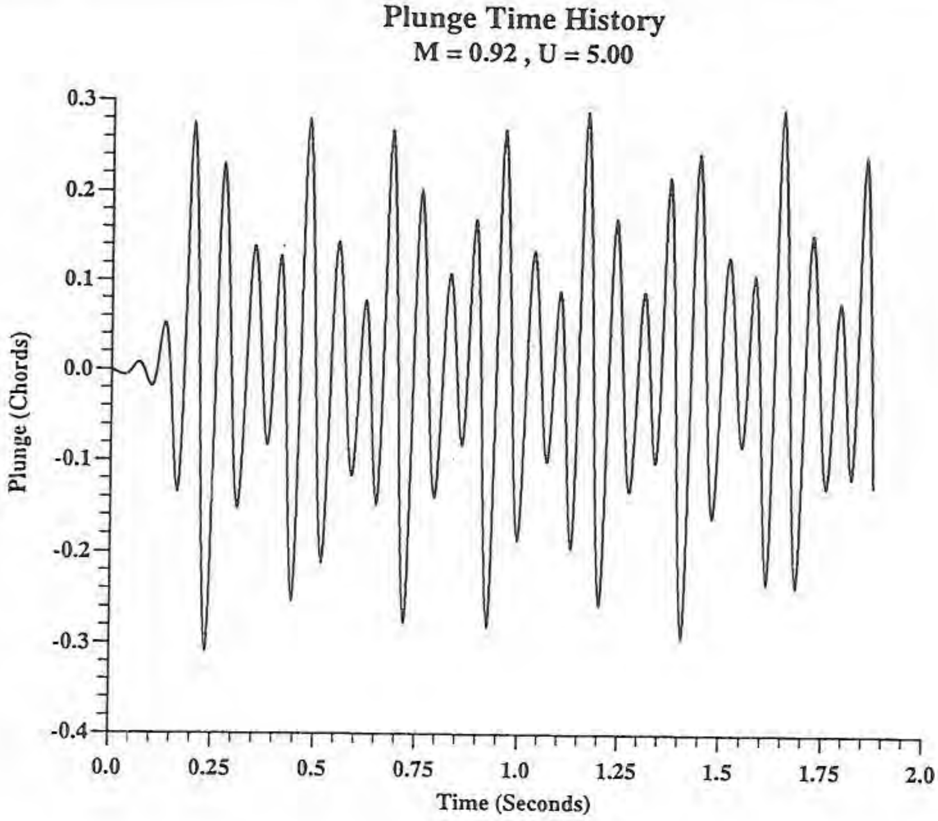

Figure 5.30c

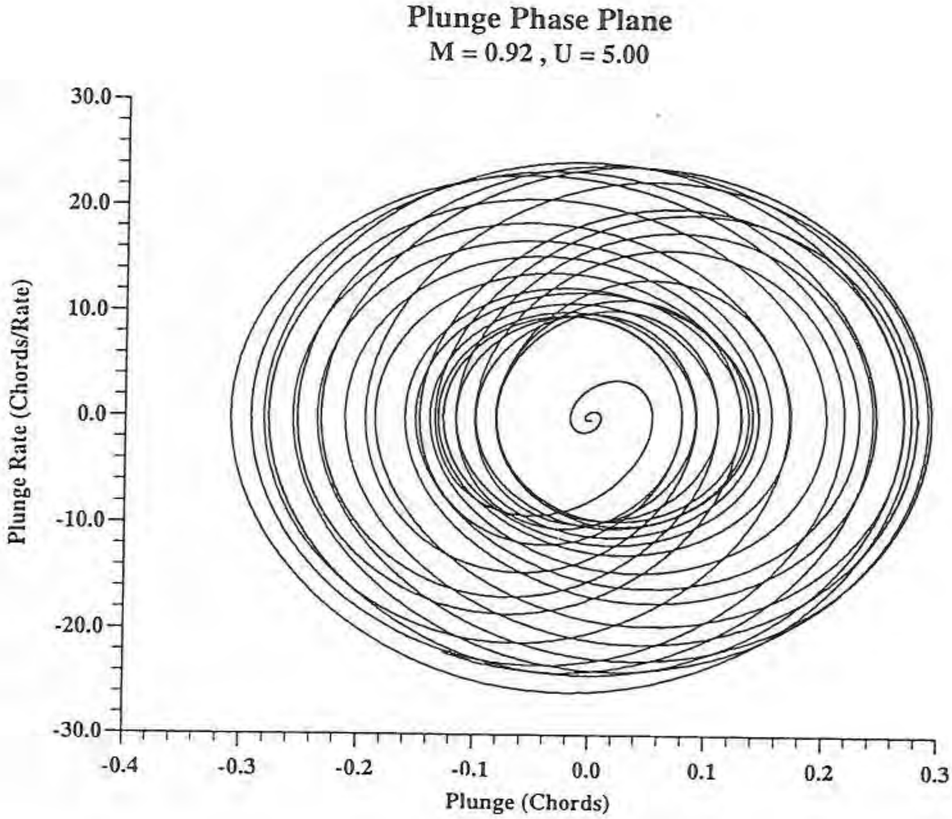

Figure 5.30d

5.5 NACA-64a006 Flutter Boundary

The concept of aerodynamic damping is used to determine the flutter boundary for the NACA-64a006 airfoil. The aerodynamic damping value, based on the first 3 to 4 cycles of airfoil displacement history, at the leading edge point, is used to calculate the aerodynamic Log Dec for two points on either side of the flutter boundary. For example, as shown in figure 5.31, the Log Dec for flow at M = 0.80 is calculated for reduced speeds lying on the either side of the flutter boundary. A simple linear interpolation gives the reduced speed at which the airfoil is neutrally stable with a Log Dec value of zero. This point is taken as the flutter boundary point. So, for M = 0.80, the flutter point is at the reduced speed of 1.615.

This procedure has been repeated for all the cases considered and the result is shown in figure 5.32. From this graph, it can be seen that as the transonic flow regime is approached, a lowering of the flutter boundary limit occurs, a phenomenon known as the transonic dip.

Figures 5.33 and 5.34 show the flutter limit cycle variation with the reduced velocity for Mach numbers 0.87 and 0.92 respectively. Here, the agreement in the actual value of the limit cycle reached is not good between the current results and that of [60]. This discrepancy specially increases at higher reduced speeds. A number of reasons can account for this disagreement, namely: the different fluid discretizations, the different approaches in initialising the flutter solution (this has been discussed earlier in section 5.4) and, the use of different time-marching routines. On the last point, it should be pointed out that the time-marching routines used in reference [60] for the flow and structural solutions are different resulting in a partially-integrated approach, as discussed in detail in chapter 3. Bendikson [24], in his re-examination of these cases with a fully-integrated approach, reports a factor of two increase in the magnitude of limit cycle responses. This observation is in line with the findings of the current work. Also, the use of a flexible section in the present study should be pointed out as a possible source of disagreement.

In any case, flutter boundary predictions are very consistent among themselves, as shown in figure 5.32. This leads the author to conclude that the discrepancy between the current results and those reported in reference [60] is

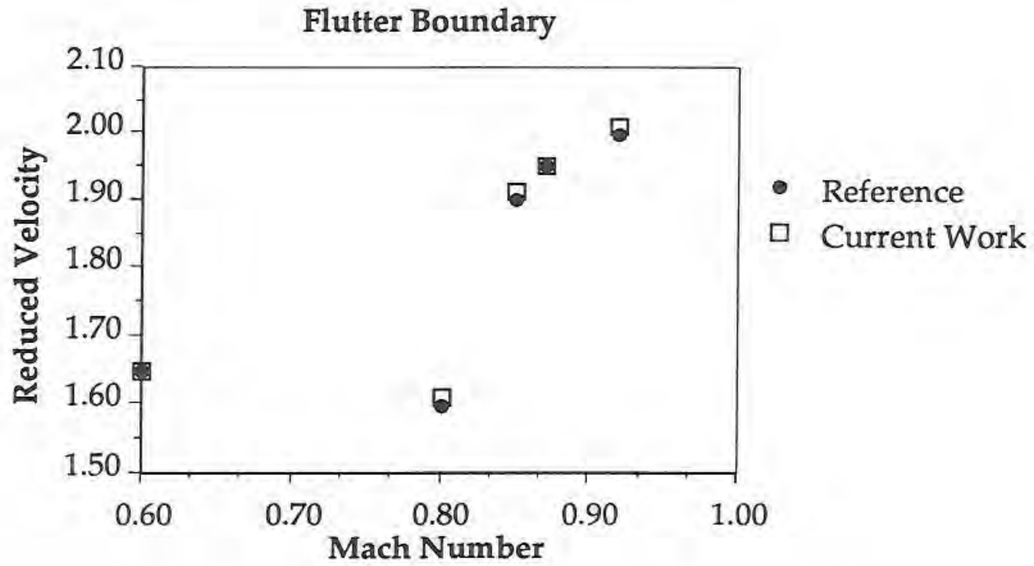

Figure 5.31 - determination of Flutter Boundary

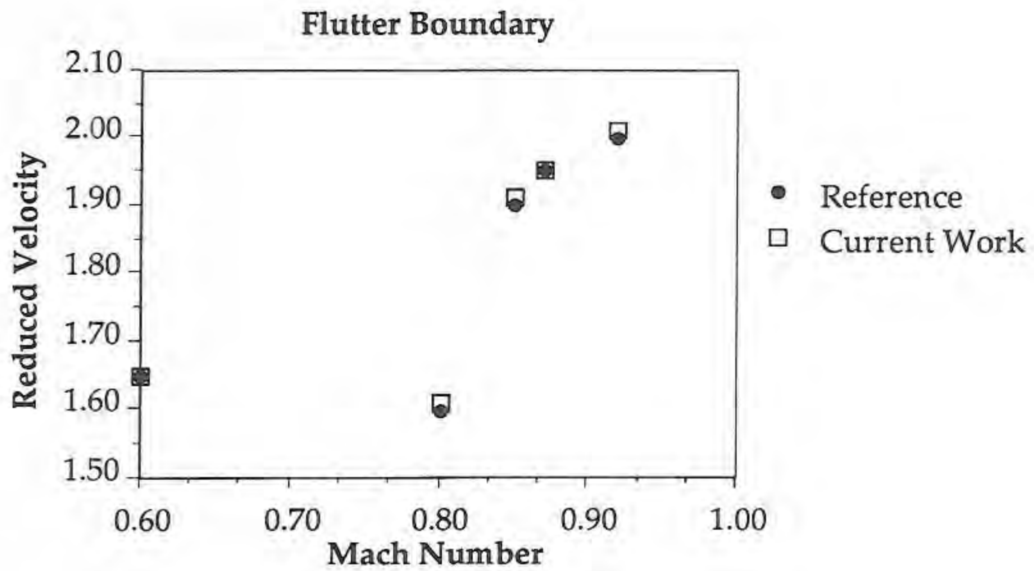

Figure 5.32 - NACA-64a006 Airfoil Flutter Boundary

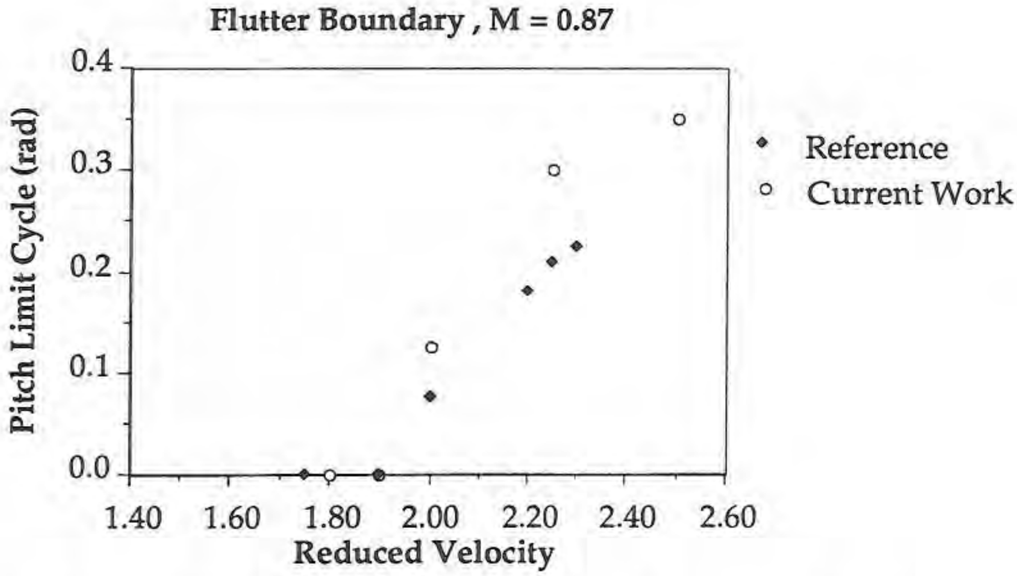

Figure 5.33 - NACA-64a006 Bifurcation Diagram at M = 0.87

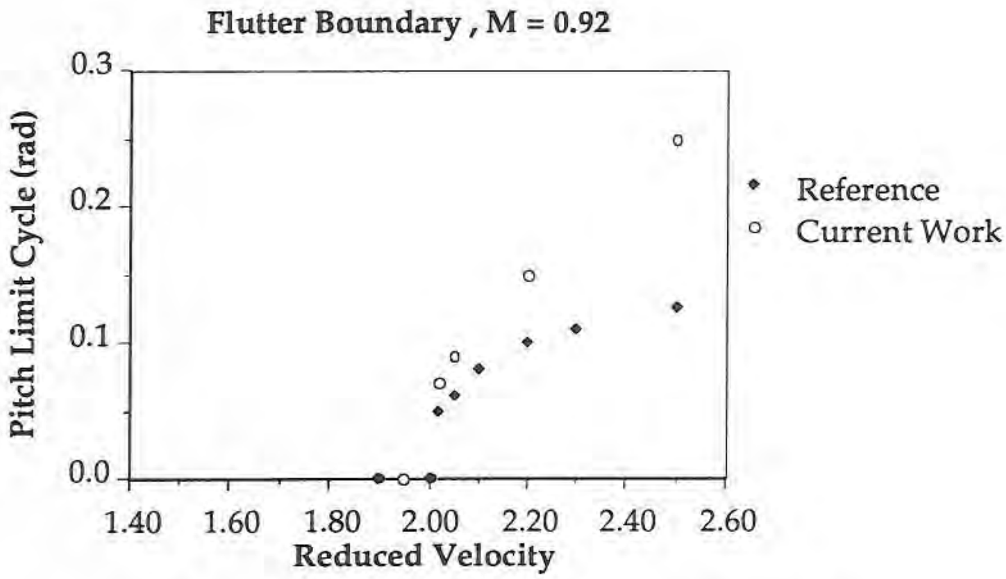

Figure 5.34 - NACA-64a006 Bifurcation Diagram at M = 0.92

mainly of a presentational nature. The results of reference [60] are simply out by a factor of two, probably, due to an error in non-dimensionalisation.

5.6 Conclusions

The main conclusion to be drawn from the above study is that the aeroelasticity model developed in chapter 3 has been satisfactorily implemented and the results obtained are in good agreement with those obtained by other researchers.

More specifically, flutter is not a linear problem but has a variety of non-linear aspects associated with it. The limit cycle behaviour, the weak divergence, divergence/flutter interaction and, the chaotic behaviour at high reduced speeds are some visual manifestations of this non-linearity. Therefore, to be able to predict these features and provide a reliable numerical estimate of flutter behaviour, a non-linear and integrated model of aeroelastic behaviour is required. This requirement is essential not only in terms of understanding the flutter mechanism but also in being able to eliminate flutter instability.

The next step is to show how to transfer this integrated and non-linear flutter model to the field of turbomachinery. This is the task of the following chapters.

Case	Mach Number	Reduced Velocity	Result
1	0.80	1.60	Stable
2		1.65	Stable
3		1.90	Limit Cycle
4		2.00	Limit Cycle
5		2.25	Limit Cycle
6	0.85	1.75	Weak Divergence
7		1.80	Stable
8		2.00	Flutter/Divergence
9		2.25	Limit Cycle
10		2.50	Limit Cycle
11	0.87	1.90	Stable
12		2.00	Limit Cycle
13		2.25	Limit Cycle
14		2.50	Limit Cycle
15		5.00	Divergence
16	0.92	1.90	Stable
17		1.95	Stable
18		2.00	Stable
19		2.02	Limit Cycle
20		2.05	Limit Cycle
21		2.20	Limit Cycle
22		2.50	Limit Cycle
23		5.00	Chaotic Flutter
24	1.00	2.00	Stable
25		2.20	Stable

Table 5.2 - Summary of Cases Studied

Chapter 6

Three-Dimensional Aeroelasticity Modelling in Turbomachinery

A phantom in two dimensions; was ***that*** *the promised angel?*
Gustav Meyrink - The Angel of the WestWindow

6.0 About this Chapter

The strategy and the main features of the proposed aeroelasticity modelling in turbomachinery is introduced in part 6.1. The modelling of the fluid flow in three-dimensional space is described, in detail, in part 6.2. The extra features of structural modelling for a rotating bladed-disc assembly are enumerated in part 6.3. The issues concerning the numerical implementation of the integrated non-linear model are discussed in part 6.4. Finally, part 6.5 is a description of the numerical techniques used for reducing the computational time for aeroelasticity calculations.

6.1 Introduction

The investigation of the flutter phenomenon for turbomachinery blades requires an accurate representation of the flow field and structural properties. In terms of the structural dynamics, a proper modelling of the bladed-disc including rotational effects, as opposed to a single blade representation, are the essential requirements.

For flow modelling, the main features to be considered are the three-dimensional effects and viscosity [62]. In a modern fan or turbine blade, the three-dimensional nature of the and the secondary flow effects are dominant, and two-dimensional or quasi-three-dimensional methods do not represent the flow properly. (The three-dimensional viscous calculation of the steady flow around a single blade is now a routine process for both design and problem solving in industry) However, the prediction of the flutter phenomenon requires the solution of the unsteady flow past not a single blade but the entire bladed-disc assembly. The computational requirements render such calculations unrealistic, at least for the time being. Therefore, a need for simplification arises. In this study, the flow is assumed to be inviscid, a feature that allows the integrated non-linear flutter modelling to become a feasible proposition.

The purpose of the following sections is to explain some of the main features of the aeroelasticity model in the context of turbomachinery blades. The structural dynamics model is the modal representation of the bladed-disc assembly resulting from finite element modelling . The fluid flow model is the three-dimensional Euler model with the appropriate boundary conditions.

The focus of the discussion is on three issues of:

- three-dimensional modelling, in order to represent the real geometry and its effects,

- the complexity of the physics due to blade rotation, and

- the need for fast, time-accurate solution methods.

6.2 Fluid Flow Model

In this study, the fluid flow model is based on the solution of the three-dimensional Euler equations for a 3D blade passage such as shown in figure 6.1. The issue of the blade rotation is tackled by considering a relative frame of reference which has its X-axis along the blade axis of rotation and rotates at the blade speed of rotation (Ω). The governing equations of the fluid flow in this relative frame of reference are:

$$\frac{\partial \mathbf{U}}{\partial t}+\frac{\partial \mathbf{E}}{\partial x}+\frac{\partial \mathbf{F}}{\partial y}+\frac{\partial \mathbf{G}}{\partial z}=\mathbf{S} \qquad (6\text{-}1)$$

where **U**, **E**, **F**, **G** and **S** are vectors given by

$$U = \begin{bmatrix} \rho \\ \rho u \\ \rho v \\ \rho w \\ \rho E \end{bmatrix} \quad E = \begin{bmatrix} \rho(u-\dot{x}) \\ \rho u(u-\dot{x}) + p \\ \rho v(u-\dot{x}) \\ \rho w(u-\dot{x}) \\ \rho E\,(u-\dot{x}) + pu \end{bmatrix} \quad F = \begin{bmatrix} \rho(v-\dot{y}) \\ \rho u(v-\dot{y}) \\ \rho v(v-\dot{y}) + p \\ \rho w(v-\dot{y}) \\ \rho E\,(v-\dot{y}) + pv \end{bmatrix}$$

$$G = \begin{bmatrix} \rho(w-\dot{z}) \\ \rho u(w-\dot{z}) \\ \rho v(w-\dot{z}) \\ \rho w(w-\dot{z}) + p \\ \rho E\,(w-\dot{z}) + pw \end{bmatrix} \quad S = \begin{bmatrix} 0 \\ 0 \\ \rho y\Omega^2 - 2\rho w\Omega \\ \rho z\Omega^2 + 2\rho v\Omega \\ 0 \end{bmatrix}$$

and $\dot{x}$, $\dot{y}$, $\dot{z}$ are the Cartesian velocity components of the moving control volume surface due to blade vibration (**not blade rotation**).

The souce term S represents the body forces (which were set to zero in chapter 3) and now includes both the Coriolis forces and the centripetal forces due to blade rotation. The velocity components (u,v,w) are the relative velocities in the rotating frame of reference and they are related to the absolute velocities according to the following relationship:

$$\begin{aligned} u &= u_{abs} \\ v &= v_{abs} + z\,\Omega \\ w &= w_{abs} - y\,\Omega \end{aligned} \qquad (6\text{-}2)$$

And, finally, to close the system of equations the final relationship is:

$$E = \frac{p}{(\gamma-1)\,\rho} + \frac{1}{2}(u^2 + v^2 + w^2) \qquad (6\text{-}3)$$

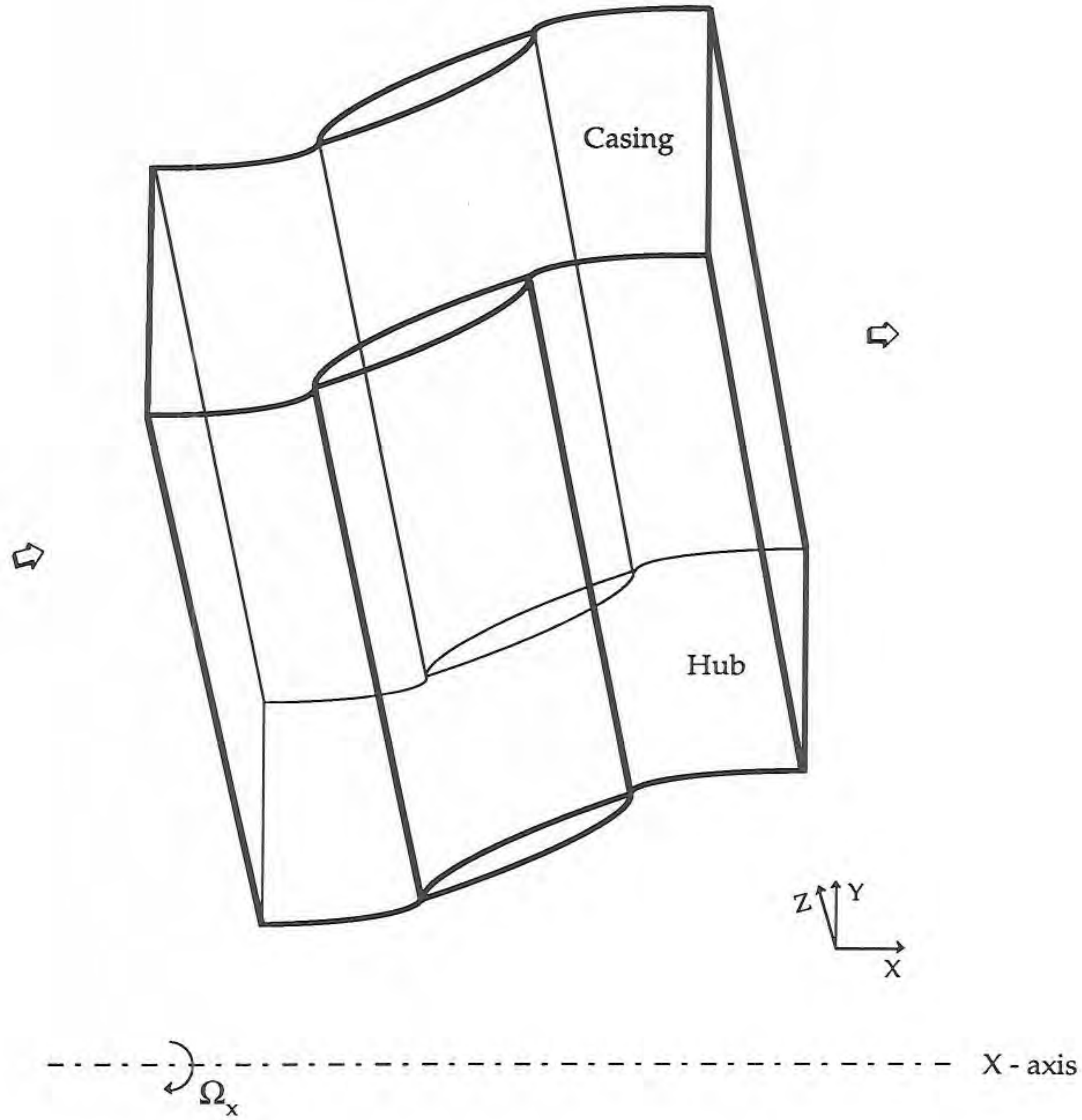

Figure 6.1 - Flow topology

Equations (6-2) and (6-3) are solved on a structured H-grid after a coordinate transformation from the physical domain (x,y,z) to an arbitrary computational domain (ε,η,ζ), as shown in figure 6.2. The integral form of the governing equations is discretized using a cell-vertex scheme on the typical control volume of figure 6.3. The integral form of the above equations in the computational domain are as follows:

$$\frac{d\,(Vol \cdot \rho)}{dt} + \{\, [\rho_n U_n - \rho_s U_s] + [\rho_e V_e - \rho_w V_w] + [\rho_t W_t - \rho_b W_b] \,\} = S(\rho) \qquad \text{(6-4a)}$$

$$\frac{d\,(Vol \cdot \rho u)}{dt} + \{\, [(\rho u_n U_n + p_n \beta_{11n}) - (\rho u_s U_s + p_s \beta_{11s})] +$$

$$[(\rho u_e V_e + p_e \beta_{12e}) - (\rho u_w V_w + p_w \beta_{12w})] +$$

$$[(\rho u_t W_t + p_t \beta_{13t}) - (\rho u_b W_b + p_b \beta_{13b})] \,\} = S(\rho u) \qquad \text{(6-4b)}$$

$$\frac{d\,(Vol \cdot \rho v)}{dt} + \{\, [(\rho v_n U_n + p_n \beta_{21n}) - (\rho v_s U_s + p_s \beta_{21s})] +$$

$$[(\rho v_e V_e + p_e \beta_{22e}) - (\rho v_w V_w + p_w \beta_{22w})] +$$

$$[(\rho v_t W_t + p_t \beta_{23t}) - (\rho v_b W_b + p_b \beta_{23b})] \,\} = S(\rho v) \qquad \text{(6-4c)}$$

$$\frac{d\,(Vol \cdot \rho w)}{dt} + \{\, [(\rho w_n U_n + p_n \beta_{31n}) - (\rho w_s U_s + p_s \beta_{31s})] +$$

$$[(\rho w_e V_e + p_e \beta_{32e}) - (\rho w_w V_w + p_w \beta_{32w})] +$$

$$[(\rho w_t W_t + p_t \beta_{33t}) - (\rho w_b W_b + p_b \beta_{33b})] \,\} = S(\rho w) \qquad \text{(6-4d)}$$

$$\frac{d\,(Vol \cdot \rho E)}{dt} + \{\, [(\rho E_n U_n + p_n U_n^c) - (\rho E_s U_s + p_s U_s^c)] +$$

$$[(\rho E_e V_e + p_e V_e^c) - (\rho E_w V_w + p_w V_w^c)] +$$

$$[(\rho E_t W_t + p_t W_t^c) - (\rho E_b W_b + p_b W_b^c)] = S(\rho E) \qquad \text{(6-4e)}$$

where (see also figure 6.3)

Vol = Volume of control volume for node (P)

$$U_n = \{ (u - \dot{x})_n \beta_{11n} + (v - \dot{y})_n \beta_{12n} + (w - \dot{z})_n \beta_{13n} \}$$
$$V_e = \{ (u - \dot{x})_e \beta_{21e} + (v - \dot{y})_e \beta_{22e} + (w - \dot{z})_e \beta_{23e} \}$$
$$W_t = \{ (u - \dot{x})_t \beta_{31t} + (v - \dot{y})_t \beta_{32t} + (w - \dot{z})_t \beta_{33t} \}$$

$$U_n^c = u_n \beta_{11n} + v_n \beta_{12n} + w_n \beta_{13n}$$
$$V_e^c = u_e \beta_{21e} + v_e \beta_{22e} + w_e \beta_{23e}$$
$$W_t^c = u_t \beta_{31t} + v_t \beta_{32t} + w_t \beta_{33t}$$

and

$$\text{Area of face (n)} = | \beta_{11n}\, i + \beta_{12n}\, j + \beta_{13n}\, k |$$
$$\text{Area of face (e)} = | \beta_{21e}\, i + \beta_{22e}\, j + \beta_{23e}\, k |$$
$$\text{Area of face (t)} = | \beta_{31t}\, i + \beta_{32t}\, j + \beta_{33t}\, k |$$

finally, the source terms become:

$$S = \begin{bmatrix} S(\rho) \\ S(\rho u) \\ S(\rho v) \\ S(\rho w) \\ S(\rho E) \end{bmatrix} = \text{Vol} \begin{bmatrix} 0 \\ 0 \\ \rho y \Omega^2 - 2\rho w \Omega \\ \rho z \Omega^2 + 2\rho v \Omega \\ 0 \end{bmatrix} \qquad (6\text{-}5)$$

The soūrce terms, unlike fluxes and pressure forces which are determined at cell faces, are calculated at node P itself.

The area of each face, such as the top face shown in figure 6.4, is calculated as follows:

$$\text{Area of face (t)} = \frac{1}{2} \vec{GH} \times \vec{DE}$$

The volume of the cell is calculated [63] by breaking the cell into six tetrahedra as shown in figure 6.5. The sum total of the volumes of each of these tetrahedra, which can be calculated exaclty, is equal to the volume of the computational cell. i.e.

$$\mathrm{Vol} = \frac{1}{6}\{ \vec{AD}x\vec{AB} + \vec{AC}x\vec{AD} + \vec{AG}x\vec{AC} + \vec{AB}x\vec{AF} + \vec{AF}x\vec{AE} + \vec{AE}x\vec{AG} \}.\vec{AG}$$

The discretization procedure is the same as that outlined in chapter 3. The final form of the set of ordinary differential equations in terms of the dependent flow variables, after equation (3-31), becomes:

$$\frac{d}{dt}\{ \mathrm{Vol}.\ \Phi \} = -F(\Phi) + D(\Phi) + S(\Phi) \tag{6-6a}$$

or

$$\frac{d}{dt}\{ \Phi \} = \frac{1}{\mathrm{Vol}}\ [-F(\Phi) + D(\Phi) + S(\Phi)] - \frac{\Phi}{\mathrm{Vol}}\ \frac{d}{dt}\{\mathrm{Vol}\} \tag{6-6b}$$

or, equivalently, in a compact form:

$$\frac{d}{dt}\{ \Phi \} = R(\Phi) \tag{6-7}$$

6.2.1 Flow Boundary Conditions

In turbomachinery flow, there are four types of boundary conditions to be imposed, i.e.

- solid boundaries where the no-flow through condition is imposed. This condition is imposed by setting the contra-variant velocity in the direction normal to the solid boundary to zero. Therefore, in the flow geometry of figure 6.1, at the blade surfaces:

$$U(\eta=1) = U(\eta=\eta_{max}) = 0$$

and at the hub and the casing:

$$W(\zeta=1) = W(\zeta=\zeta_{max}) = 0$$

- Periodic boundary conditions resulting from the periodicity of the geometry. Therefore, in figure 6.2b, all physical flow variables at corresponding points T and B are forced to be equal. The numerical treatment of the flow periodicity is detailed in section 6.2.3.

- Inflow/Outflow boundary conditions, where the flow enters or leaves the computational flow domain. The concept of non-reflective boundary condition has been described for two-dimensional flows in chapter 3. Although th implementation of the non-reflective boundary conditions in three-dimensional flow is similar to that in 2D it is useful to summarize the procedure in three-dimensions.

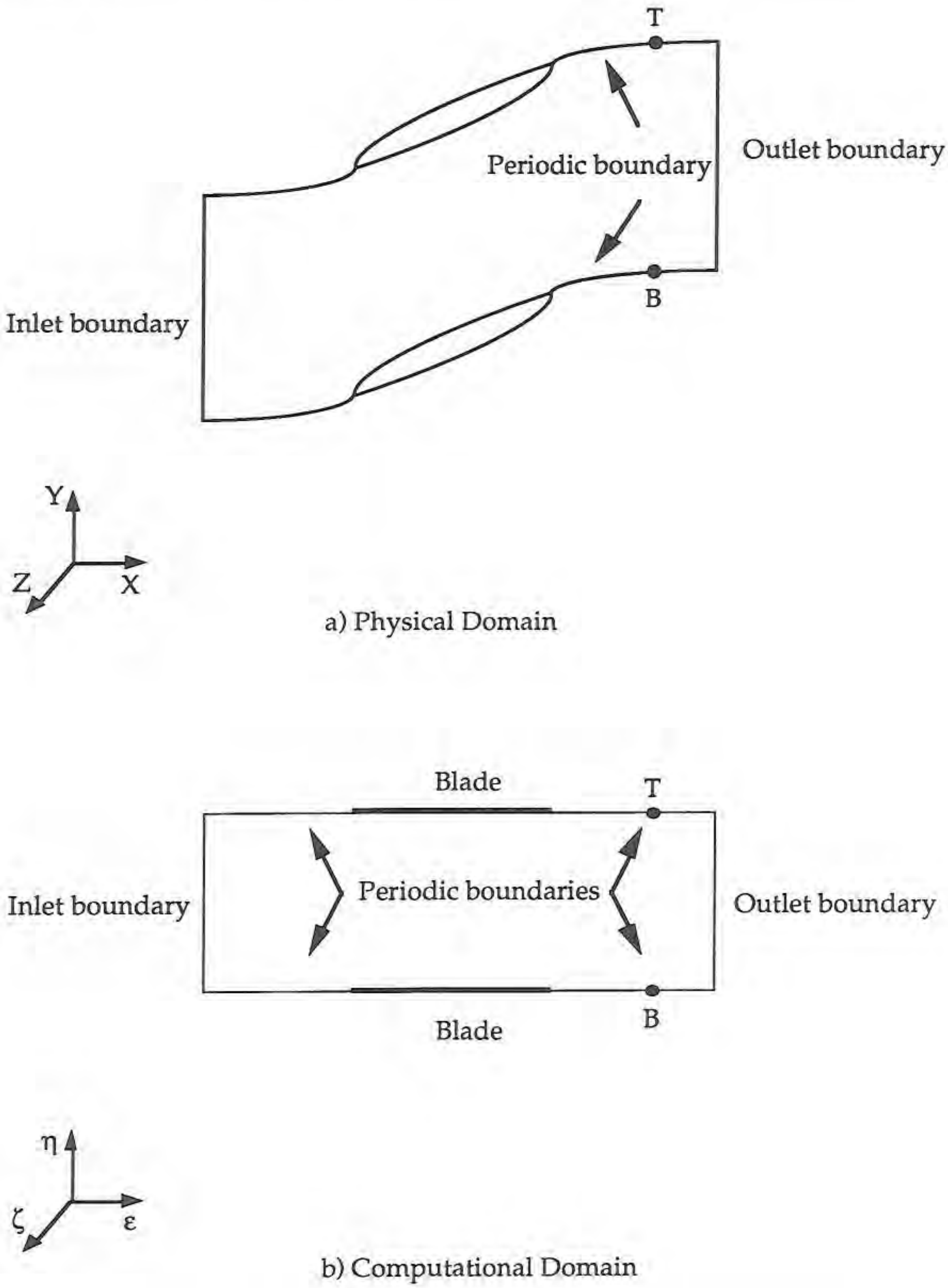

Figure 6.2 - A two-dimensional section of the flow domain

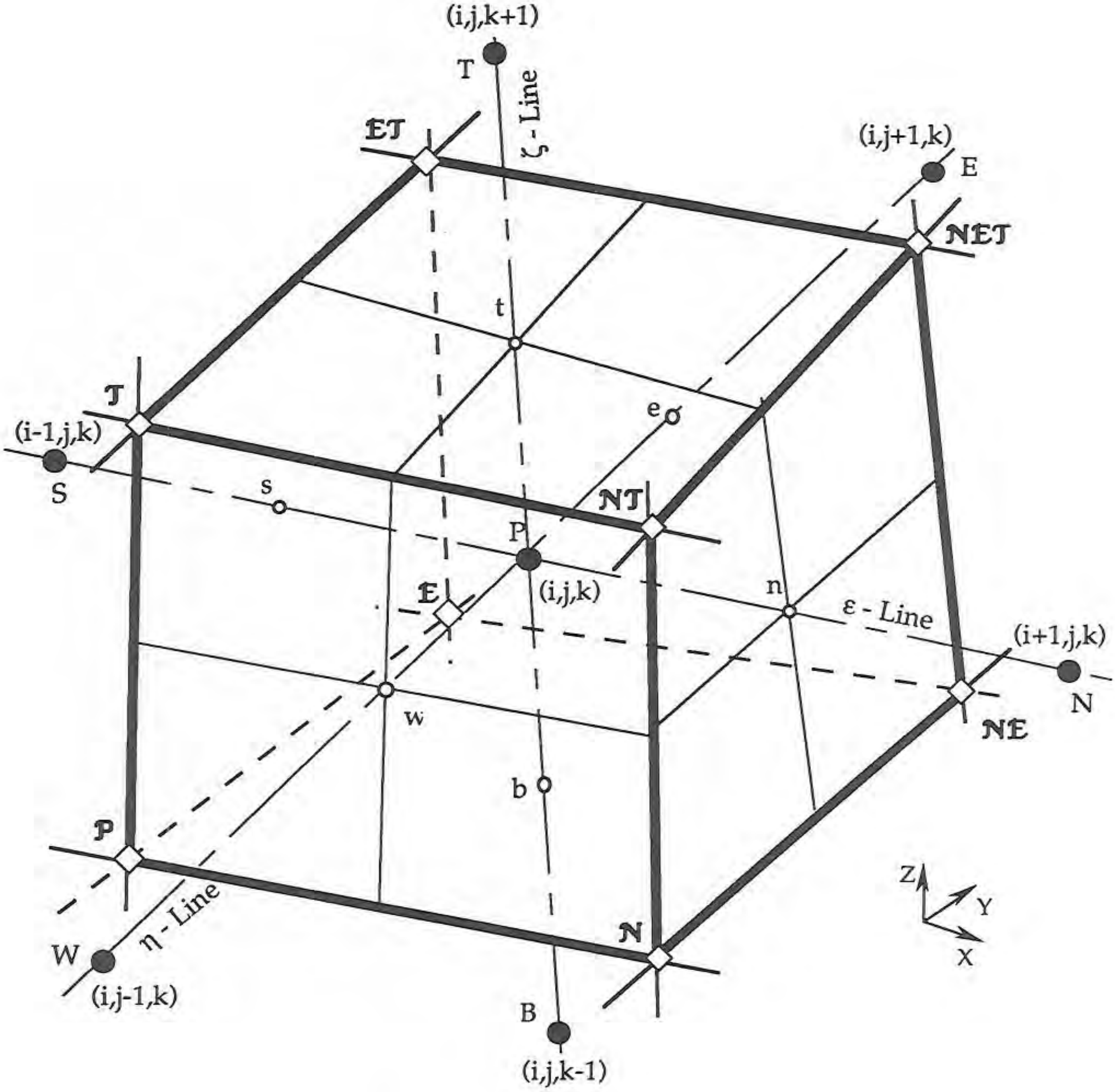

Figure 6.3 - A typical control volume

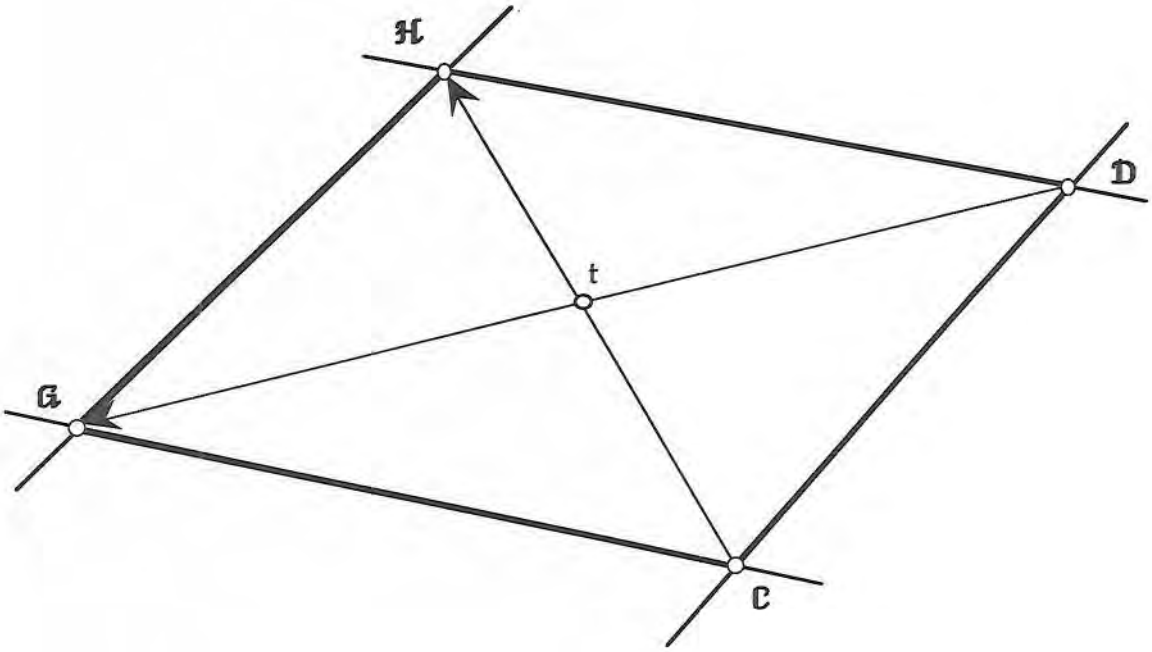

Figure 6.4 - Calculation of control volume area

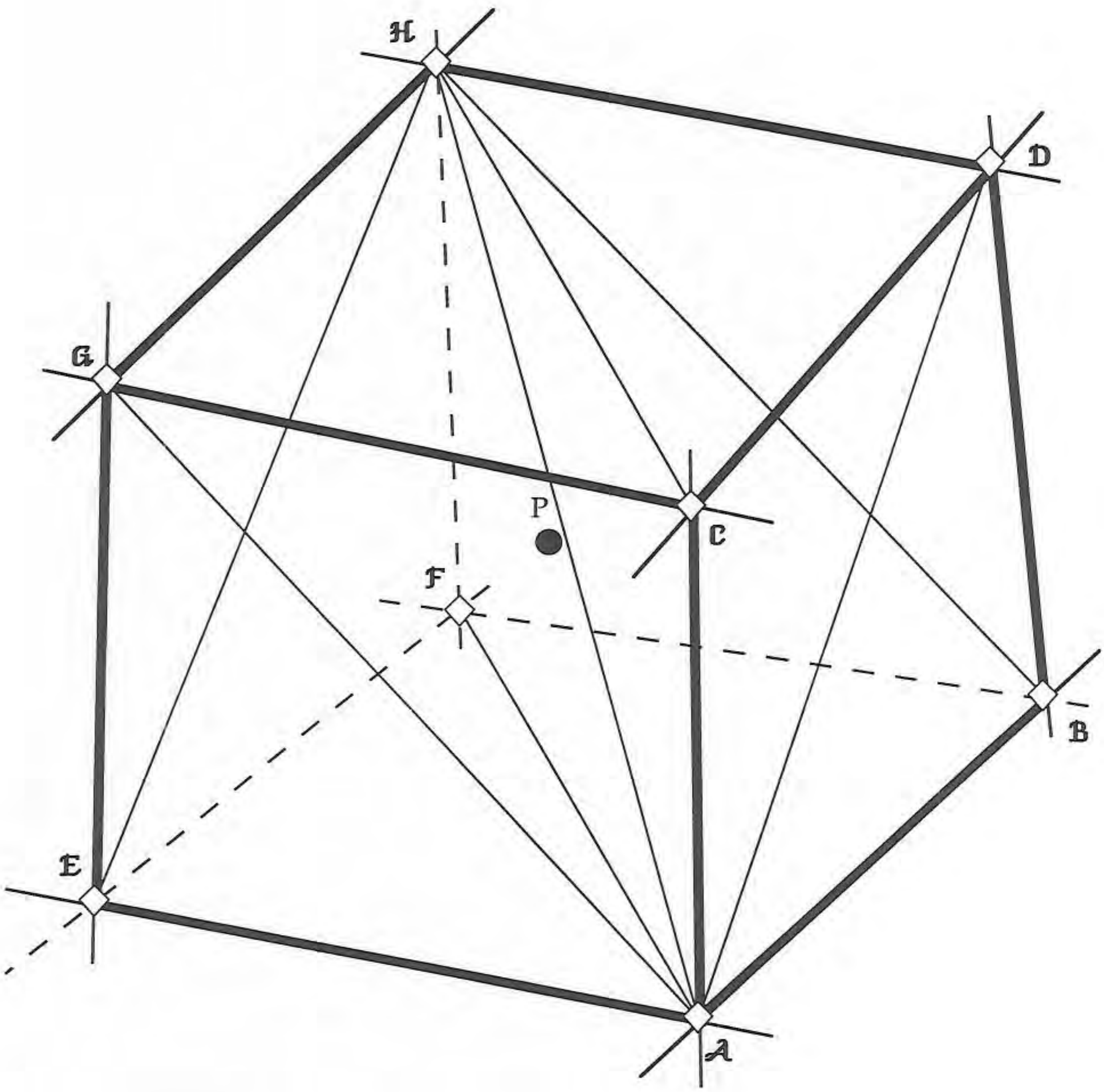

Figure 6.5a - Calculation of Cell Volume

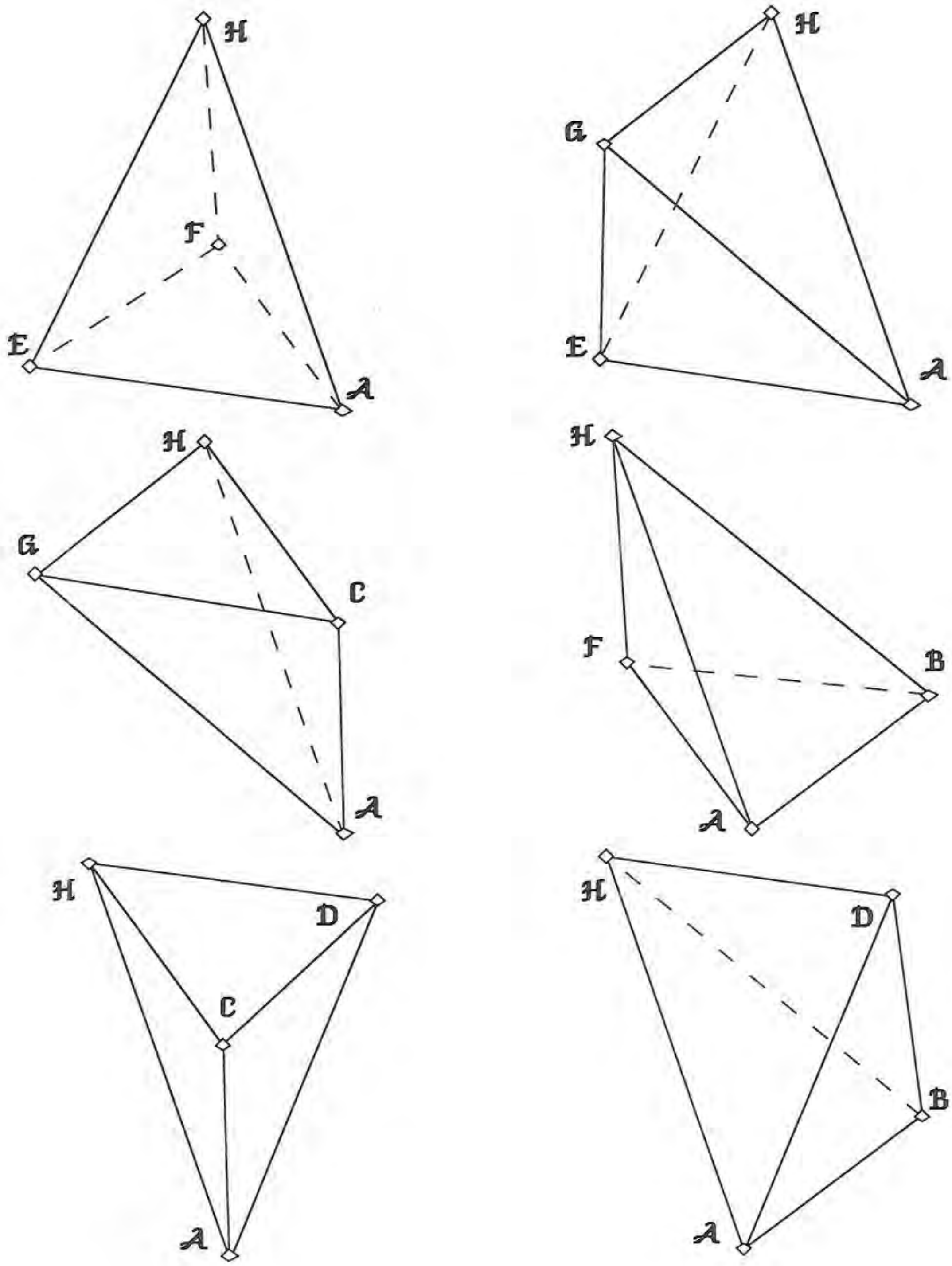

Figure 6.5b - Six tetrahedra froming the control volume

6.2.2 Non-Reflective Boundary Conditions in Three-Dimensional Flow

Here, as in chapter 3, the non-reflective boundary conditions are implemented along the flow characteristic variables and solved in terms of the basic flow variables. The characteristics are the directions along which flow information propagate and , therefore, are the eigenvalues of the system of hyperbolic Euler equations. In three-dimensional flow there are five such eigenvalues, i.e.

$$\lambda_1 = u_\perp \,, \lambda_2 = u_\perp \,, \lambda_3 = u_\perp \,, \lambda_4 = u_\perp + c \,, \lambda_5 = u_\perp - c$$

where c is the local speed of sound and $u_\perp$ is the outgoing flow velocity normal to the boundary **in the relative frame of reference**.

The system of Euler equations governing the fluid flow along these characteristics are:

$$\lambda_1: \qquad \frac{\partial \rho}{\partial t} - \frac{1}{c^2}\frac{\partial P}{\partial t} + \lambda_1 g_1 = 0$$

$$\lambda_2: \qquad n_x \frac{\partial w}{\partial t} - n_z \frac{\partial u}{\partial t} + \lambda_2 g_2 = 0$$

$$\lambda_3: \qquad n_y \frac{\partial u}{\partial t} - n_x \frac{\partial v}{\partial t} + \lambda_3 g_3 = 0 \tag{6-8a}$$

$$\lambda_4: \qquad n_x \frac{\partial u}{\partial t} + n_y \frac{\partial v}{\partial t} + n_z \frac{\partial w}{\partial t} + \frac{1}{\rho c}\frac{\partial \rho}{\partial t} + \lambda_4 g_4 = 0$$

$$\lambda_5: \qquad n_x \frac{\partial u}{\partial t} + n_y \frac{\partial v}{\partial t} + n_z \frac{\partial w}{\partial t} - \frac{1}{\rho c}\frac{\partial \rho}{\partial t} + \lambda_5 g_5 = 0$$

where

$$g_1 = \frac{\partial \rho}{\partial n} - \frac{1}{c^2}\frac{\partial P}{\partial n}$$

$$g_2 = n_x \frac{\partial w}{\partial n} - n_z \frac{\partial u}{\partial n}$$

$$g_3 = n_y \frac{\partial u}{\partial n} - n_x \frac{\partial v}{\partial n} \tag{6-8b}$$

$$g_4 = n_x \frac{\partial u}{\partial n} + n_y \frac{\partial v}{\partial n} + n_z \frac{\partial w}{\partial n} + \frac{1}{\rho c}\frac{\partial \rho}{\partial n}$$

$$g_5 = n_x \frac{\partial u}{\partial n} + n_y \frac{\partial v}{\partial n} + n_z \frac{\partial w}{\partial n} - \frac{1}{\rho c}\frac{\partial \rho}{\partial n}$$

and n is the direction normal to the boundary (outgoing) with the unit vector of $\vec{n} = (n_x, n_y, n_z)$.

The first characteristic equation describes entropy perturbation, The second and the third correspond to vorticity waves and the last two correspond to acoustic pressure waves.

The solution of the above system of Euler equations yields:

$$\frac{\partial \rho}{\partial t} = -\frac{\rho}{2c}(\lambda_4 g_4 + \lambda_5 g_5) - \lambda_1 g_1$$

$$\frac{\partial u}{\partial t} = -\frac{n_x}{2}(\lambda_4 g_4 - \lambda_5 g_5) - n_y \lambda_3 g_3 + n_z \lambda_2 g_2$$

$$\frac{\partial v}{\partial t} = -\frac{n_y}{2}(\lambda_4 g_4 - \lambda_5 g_5) + \frac{(1-n_y^2)}{n_x}\lambda_3 g_3 + \frac{n_y n_z}{n_x}\lambda_2 g_2 \tag{6-9}$$

$$\frac{\partial w}{\partial t} = -\frac{n_z}{2}(\lambda_4 g_4 - \lambda_5 g_5) - \frac{n_y n_z}{n_x}\lambda_3 g_3 - \frac{(1-n_z^2)}{n_x}\lambda_2 g_2$$

$$\frac{\partial P}{\partial t} = -\frac{\rho c}{2}(\lambda_4 g_4 + \lambda_5 g_5)$$

The equations (6-9) have the same form as equation (6-7) and can be integrated simultaneously in time, subject to non-reflective boundary conditions, with the rest of the flow variables in the computational domain. The non-reflective boundary condition means that for each outgoing characteric, $\lambda_i \leq 0$, the corresponding characteristic equation should be solved, i.e. $g_i \neq 0$, while for each incoming wave, the local perturbations are made to vanish, i.e. $g_i = 0$.

As it was pointed out earlier, the numerical implementation of the three-dimensional non-reflective boundary condition is the same as that detailed in the Addendum to chapter 3.

6.2.3 Multi-Passage Flow Modelling

A single-passage flow modelling is adequate for steady flow calculations. However, for flutter calculations, where the blades are vibrating, a single-passage analysis is possible only if all the blades in the stage considered are in-phase. If the inter blade phase angle is not zero, a single passage analysis would not be possible, as the boundary conditions at points T and B in figure 6.2b would not be known. Therefore, in dealing with general inter blade phase angles, enough passages must be included in the analysis, so that the first and the last blades are again in phase. Hence, a multi-passage flow analysis is required.

In multi-passage modelling, extra passages are formed by rotating the original passage about the x-axis, and by an angle equal to a multiple of the pitch angle (θ). So, in figure 6.6, the mesh for passages r+1 and r+2 is created by rotating the mesh of the passage r by $1^*\theta$ and $2^*\theta$, respectively, in order to create a three-passage model is created for a flutter calculation with an inter blade phase angle of $\frac{2\pi}{3}$.

The flow modelling and discretization in each passage is performed independently as for a single-passage analysis. The adjacent passages communicate with each other along their common surfaces only. Flow discretization along these common surfaces is carried out in the normal way in each passage and the resultant residuals are added together prior to each stage of the time-marching process. So, for node P in figure 6.6, the resultant residual for a flow variable Φ becomes:

$$R(\Phi) = 0.5^*(R(\Phi_r) + R(\Phi_{r+1})) \qquad (6\text{-}10)$$

The other important issue is the implementation of the periodic boundary conditions. The obvious procedure would be to calculate the flow at the periodic nodes, e.g. T and B in figure 6.6, separately and then averaging the results, i.e.

$$
\begin{aligned}
&\rho_T = \rho_B = 0.5^*(\ \rho_T + \rho_B) \\
&\rho u_T = \rho u_B = 0.5^*(\ \rho u_T + \rho u_B) \\
&\rho E_T = \rho E_B = 0.5^*(\ \rho E_T + \rho E_B) \\
&\rho v_T = 0.5^* \rho v_T + 0.5^*(\ \cos(n\theta) \cdot \rho v_B + \sin(n\theta) \cdot \rho w_B) \\
&\rho v_B = 0.5^* \rho v_B + 0.5^*(\ \cos(n\theta) \cdot \rho v_T - \sin(n\theta) \cdot \rho w_T) \\
&\rho w_T = 0.5^* \rho w_T + 0.5^*(\ \sin(n\theta) \cdot \rho v_B + \cos(n\theta) \cdot \rho w_B) \\
&\rho w_B = 0.5^* \rho w_B + 0.5^*(-\sin(n\theta) \cdot \rho v_T + \cos(n\theta) \cdot \rho w_T)
\end{aligned}
\tag{6-11}
$$

where n is the number of passages (in figure 6.6, n is equal to 3) and θ is the pitch angle. Also note that because a Cartesian co-ordinate system is used, the momentum variables along y and z directions, i.e. ρv and ρw, are rotated by n*pitch before averaging is performed.

The above procedure, however, was found to lead to numerical instability for unsteady flow calculations. Steady multi-passage flow analyses showed that the above technique considerably slows down the convergence rate and, at times, the flow calculations fail to converge completely.

A more rigourous implemetation of the periodic boundary condition is to add the residuals of the points T and B prior to time marching, i.e.

$$
\begin{aligned}
&R'(\rho_T) = R'(\rho_B) = 0.5^*(\ R(\rho_T) + R(\rho_B)\ ) \\
&R'(\rho u_T) = R'(\rho u_B) = 0.5^*(\ R(\rho u_T) + R(\rho u_B)\ ) \\
&R'(\rho E_T) = R'(\rho E_B) = 0.5^*(\ R(\rho E_T) + R(\rho E_B)\ ) \\
&R'(\rho v_T) = 0.5^* R(\rho v_T) + 0.5^*(\ \cos(n\theta) \cdot R(\rho v_B) + \sin(n\theta) \cdot R(\rho w_B)\ ) \\
&R'(\rho v_B) = 0.5^* R(\rho v_B) + 0.5^*(\ \cos(n\theta) \cdot R(\rho v_T) - \sin(n\theta) \cdot R(\rho w_T)\ ) \\
&R'(\rho w_T) = 0.5^* R(\rho w_T) + 0.5^*(\ \sin(n\theta) \cdot R(\rho v_B) + \cos(n\theta) \cdot R(\rho w_B)\ ) \\
&R'(\rho w_B) = 0.5^* R(\rho w_B) + 0.5^*(-\sin(n\theta) \cdot R(\rho v_T) + \cos(n\theta) \cdot R(\rho w_T)\ )
\end{aligned}
\tag{6-12}
$$

This latter approach was found to be always stable and to perform well. Hence it is recommended for multi-passage modelling.

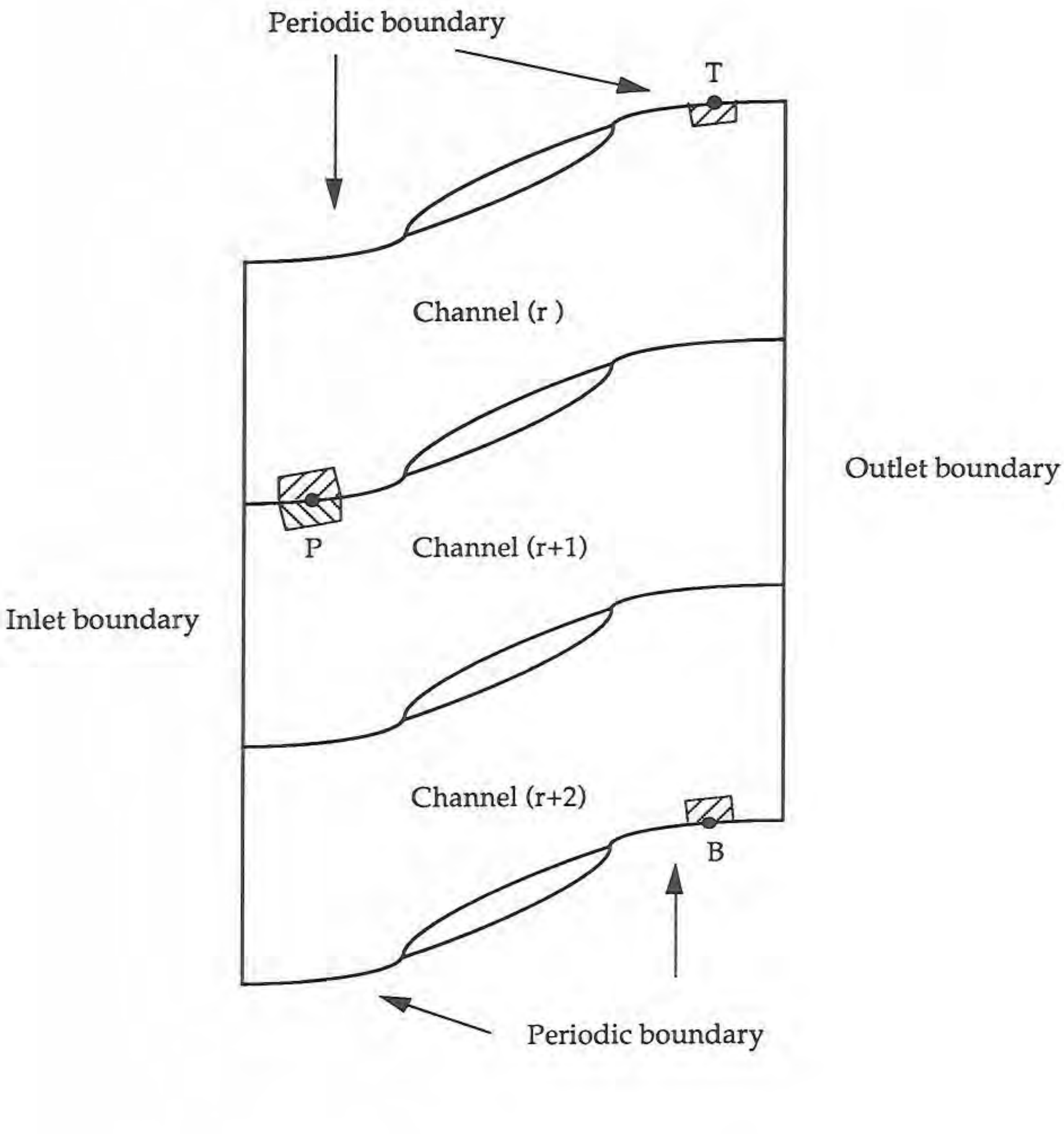

Figure 6.6 - Multi-passage Flow Modelling

In all the discussions above, the talk was that of adding the residuals although at first glance, the equations (6-10) and (6-12) look more like an averaging process. However, the residuals used here are the flow residuals per unit volume in accordance with the final form of equation (6-7). So, the residual term in equation of (6-12), is modified as:

$$R'(\rho_T) = R'(\rho_B) = \frac{R(\rho_T)^*Vol_T + R(\rho_B)^*Vol_B}{Vol_T + Vol_B}$$

But since $Vol_B = Vol_T$,

$$R'(\rho_T) = R'(\rho_B) = \frac{R(\rho_T) + R(\rho_B)}{1+1}$$

$$= 0.5^*(\ R(\rho_T) + R(\rho_B)\ ).$$

It should be pointed out that multi-passage modelling is not the only method for handling flow periodicity in turbomachinery. Refering to figure 6.2b, one could store the flow variables at point B at all time steps (t) and impose the periodicity condition at point T at a later time of ($t+\mathcal{T}$), $\mathcal{T}$ being the period; a process known as the direct store method [64]. The value of the period is calculated as:

$$\mathcal{T} = \frac{2\pi}{IBPA} * \frac{1}{\Omega}$$

where IBPA is the inter-blade phase-angle and Ω is the bladed-disc rotational speed.

The direct store method, however, has the major disadvantage of requiring a lot of storage space and frequent disk access, thus increasing the length of the computation considerably. Hence, a multi-passage implementation has been preferred in this study.

6.3 Structural Dynamics Model

An extra feature in structural dynamics modelling of turbomachinery is the blade annulus rotational effects. The rotation leads to stiffening of the blades and an increase in the natural frequencies of the bladed-disc assembly.

The standard method for including the rotational effects is to perform a stress analysis on the blade annulus prior to the eigen-solution. The resultant stresses are used to modify the assembly stiffness matrix so that the effects of annulus rotation are included. This procedure is easily performed on any standard finite-element package.

However, the above method fixes the blade rotational effects about the equilibrium position of the blades,. However, the centripetal forces acting on blades change according to the instantaneous geometric position as dictated by vibration. This variation is ignored in the above method, an assumption that can only be justifiable if the amplitude of blade vibrations is small.

The alternative approach is to calculate the resulting centripetal forces during the time-marching process. Equation (3-5) can be modified as follows:

$$\{\ddot{q}\} + 2\,\zeta\,[\omega]\,\{\dot{q}\} + [\omega^2]\,\{q\} = [\Psi]^T\,(\{F\}_{flow} + \{F\}_{centripetal}) \qquad (6\text{-}13)$$

where

$$\{F\}_{centripetal} = -\,[M]\,\{r\}\,[\omega^2] \qquad (6\text{-}14)$$

where [M] is the mass matrix and {r} is the distance of each point on the blade from the rotational axis.

It should be pointed out that if rotational effects are included in the eigen-solution, then the modeshapes used in the flutter analysis are at engine speed. However, if the centripetal forces are included in the time-marching process, then the modeshapes are at zero engine speed. Therefore, the modeshapes and natural frequencies of the annulus are entirely different in the two methods outlined above.

6.4 Aeroelasticity Model

Once the above modifications are performed, the flutter calculation procedure is exactly the same as described in chapter 3. The basic steps are

(i) Spatial discretization of the fluid flow and structural dynamics models at each time step.

(ii) Temporal simultaneous solution of the final discretized equations using an explicit Runge-Kutta scheme.

(iii) Imposition of the boundary conditions at each stage of the time-marching process. All the boundary conditions are implemented prior to each stage of the Runge-Kutta solver.

(iv) Adjustment of the fluid mesh to follow the instantaneous blade annulus position. This is performed at the end of the Runge-Kutta time-marching.

Mesh kinematics is implemented for each flow passage independently. The grid nodes on the inlet and outlet boundaries are held fixed. The motion of the grid nodes along the $\eta=1$ and $\eta=\eta_{max}$ lines, i.e. the common boundaries between the adjacent blades is determined from linear interpolation of the blade motion. For example, the displacement of the point P in figure 6.6 becomes:

$$\delta x_P = \frac{\varepsilon_P - 1}{\varepsilon_{LE} - 1} . \delta x_{LE}$$
$$\delta y_P = \frac{\varepsilon_P - 1}{\varepsilon_{LE} - 1} . \delta y_{LE} \qquad (6\text{-}15)$$
$$\delta z_P = \frac{\varepsilon_P - 1}{\varepsilon_{LE} - 1} . \delta z_{LE}$$

where ε_P is the grid node index in the ε direction. Similarly, the displacement of the points lying downstream of the blade are interpolated from the displacement of the trailing edge line.

The above procedure means that the priodic boundary planes are allowed to move. However, since the corresponding blades are in-phase with each other, periodicity of points T and B in figure 6.6 must be maintained when blades move.

In implementing the concept of the spring network, each grid point is connected to all its neighbouring points along the ε,η,ζ directions. So, in figure 6.3, the node P is connected to points N,S,E,W,T,B via springs whose stiffnesses are inversely proportional to the corresponding lengths. It is desirable to include the diagonal nodes in the spring network to avoid mesh shearing. However, this is only needed in external flow calculations where the amplitudes of wing oscillations can be very large. In internal flows, the amplitude of blade vibrations is not large enough to justify this extra computational cost.

Again, as for airfoil flutter calculations, one or two jacobi iterations through the system of the resulting force equlibrium equations leads to the new mesh position. The jacobi sweeps are performed along each of the ε,η,ζ co-ordinate directions in turn.

One final point regarding the flutter modelling in turbomachinery should be explained [1]. In turbomachinery, since the blades are attached to a disc which has its own flexibility, the structural modeshapes are assembly modeshapes with nodal patterns appearing on the bladed-disc assembly. For an N-bladed assembly there are mN assembly modeshapes where m is the number of the structural modes. In the general case, the equations of motion for each blade can be written as:

$$\{\ddot{q}_n\} + 2\zeta_n [\,\omega_n\,] \{\dot{q}_n\} + [\,\omega^2_n\,] \{q_n\} = [\Psi_n]^T \{F\} \qquad \text{for } n = 1,\ldots,N \qquad (6\text{-}16)$$

where each blade has its own set of natural frequencies and damping coefficients which are different for different blades.

However, if the assembly is tuned, all the blades have the same natural frequencies and damping coefficients, so the N equations of (6-15) become identical. This means that the structural data can be obtained from a single blade analysis. However, since there are N possible modeshapes for the assembly corresponding to N different inter blade phase angles, flutter calculations have to be performed for all these inter blade phase angles. The flutter condition, or conditions, will be at the inter blade phase angle which will give an unstable solution.

Therefore, for a tuned assembly, i.e. identical blades, the inter-blade phase-angle is an input to the flutter calculation. Furthermore, for an N-bladed annular, N number of flutter calculations, corresponding to each inter-blade phase-angle, is required.

6.5 Time-Marching Acceleration

A three-dimensional multi-passage formulation with explicit time-marching may make flutter calculations prohibitively expensive. The obvious way of reducing the computational cost is to increase the time step limit, as this is too restrictive and the resulting temporal resolution of the solution is unnecessarily high. It is important to point out that the time step limit in flutter calculations is invariably determined by the fluid flow stability requirements and, therefore, methods in increasing the time step limit are often directed at fluid flow modelling. The time step relaxation of the structural model is, in effect, accomplished by its modal representation which limits the highest natural frequency of the structure, see equation (3-42).

The increase in the allowable time step for the fluid flow model can be achieved in two ways; either by introducing a degree of implicitness in the solution procedure or by performing the calculations on coarser grids which allow larger time steps. The first of these options is achieved by a numerical procedure known as residual averaging technique [47]. The second alternative is to use the multi-grid method [43]. These methods are described below.

6.5.1 Residual Averaging

Residual averaging [43,46] is a technique by which the time step restrictions in explicit schemes can be relaxed by adding a degree of implicitness in the semi-discretized equations of (6-7). This is accomplished by averaging the flow residuals $R(\Phi)$ at each point using values from the neighbouring grid points. So $R(\Phi)$ is replaced in equation (6-7) by the smoothed residual $\bar{R}(\Phi)$ such that, at node P:

$$\bar{R}_P(\Phi) - \nu \nabla^2 . \bar{R}_P(\Phi) = R_P(\Phi) \qquad (6\text{-}17)$$

where ν is a weighting parameter which determines the level of implicitness.

Equation (6-17) is a second-order operator in space, and provided $\bar{R}$ can be solved for exactly, the second-order accuracy is not affected by the averaging process.

Jameson [47] has shown that in the absence of dissipation, the stability can be maintained for any CFL number provided ν satisfies the condition:

$$\nu = \max \left[\frac{1}{4} \cdot \left(\frac{\delta t^2}{\delta t_{CFL}^2} - 1 \right), 0 \right] \tag{6-18}$$

where δt is the time step taken and δt_{CFL} is the local allowable time step. The local allowable time step is determined from equation (3-41) which, in three-dimensional space, can be written as:

$$\delta t_{CFL} \leq CFL \cdot \min \left(\delta t_{\varepsilon}, \delta t_{\eta}, \delta t_{\zeta} \right) \tag{6-19}$$

where

$$\delta t_{\varepsilon} = \frac{Vol}{|U| + c.\sqrt{\beta 11^2 + \beta 12^2 + \beta 13^2}}$$

$$\delta t_{\eta} = \frac{Vol}{|V| + c.\sqrt{\beta 21^2 + \beta 22^2 + \beta 23^2}}$$

$$\delta t_{\zeta} = \frac{Vol}{|W| + c.\sqrt{\beta 31^2 + \beta 32^2 + \beta 33^2}}$$

Vol is the volume of the computational cell and c is the local speed of sound. U, V and W are the local contravariant velocities, and βij are the jacobians of the control volume. As it was described earlier these parameters are calculated on control volume faces so, here, their average values at the grid node concerned is used to determine the local time step.

In practice, by using of the residual averaging method, the unsmoothed time step, i.e. the smallest local allowable time step, can be increased by a factor of 2.5 for cell-centred schemes, and by a factor of 5 for cell-vertex formulation, with no loss of accuracy. These factors have been determined empirically from the experience gained from the flutter calculations on airfoils, described in chapter 5.

It should be pointed out that further increases in the time step does not lead to algorithm failure but results in oscillatory behaviour about the true flow solution. In this case, the predicted flutter behaviour can change from stable to unstable and hence care must be taken when using residual averaging.

Implicit solution of the equation (6-17) in three-dimensional space is computationally very expensive as the LHS matrix to be inverted is a hepta-diagonal matrix. Therefore equation (6-17) is factorised [65] into three tri-diagonal matices, i.e.

$$(1-\nu_\zeta \nabla^2)\cdot(1-\nu_\eta \nabla^2)\cdot(1-\nu_\varepsilon \nabla^2)\cdot \bar{R}_P(\Phi) = R_P(\Phi) \tag{6-20}$$

This equation can now be solved efficiently by an ADI algorithm. This process does produce some additional errors but still remains the only route as there are no viable alternatives.

The implicit coefficients ν_ε , ν_η and ν_ζ can be set equal to ν which is calculated according to equation (6-18). However, in order to take into account the different grid stretching along each co-ordinate direction, an alternative way of determining these coefficients is:

$$\begin{aligned}
\nu_\varepsilon &= \max\left[\ \frac{1}{4}\cdot\left(\frac{\delta t_\varepsilon^2}{\delta t_{CFL}^2} - 1\right), 0\ \right] \\
\nu_\eta &= \max\left[\ \frac{1}{4}\cdot\left(\frac{\delta t_\eta^2}{\delta t_{CFL}^2} - 1\right), 0\ \right] \\
\nu_\zeta &= \max\left[\ \frac{1}{4}\cdot\left(\frac{\delta t_\zeta^2}{\delta t_{CFL}^2} - 1\right), 0\ \right]
\end{aligned} \tag{6-21}$$

The residual averaging method is also used during the steady flow calculations in order to stabilise the solution and increase the rate of convergence but not with a view to increase the allowable time step. In this case the value of the implicit coefficients is set be 0.5.

Residual averaging is performed for each flow passage independently. At the passage boundaries, one-sided differencing is used for implementing equation

(6-20). The boundary conditions at the common surfaces (equations (6-10)) and at periodic boundaries (equations (6-12)) are imposed after the residual averaging is performed. This ensures that the residual averaging process does not interfere with the exact implementation of these boundary conditions.

6.5.2 Multi-Grid Method

Although the five-fold increase in the allowable time step due to residual averaging is a welcome outcome, the resulting CFL number of 16 (5x3.2) is still too restrictive. The need for further efficiency leads us to the multi-grid method.

The multi-grid method is basically a convergence acceleration technique used for steady flow calculations. The concept of multi-grid [66] is to use corrections estimated on a series of succesively coarser meshes to improve the solution on the fine mesh. The idea is that each successive coarser mesh is able to quickly remove a band of residual wavelengths which is of the same order as its mesh spacing. This avoids the handling of residual wavelengths that are larger than the fine mesh spacing which tends to slow down the convergence [50].

In the present work the multi-grid approach is used for increasing the allowable time step for flutter calculations. The basic idea is to perform one time-marching calculation on each of the successively coarser mesh, starting from the fine mesh itself, and then to update the solution on the fine mesh. So, at the end of the multi-grid process the total time step taken becomes:

$$\delta t_{total} = \delta t_h + \delta t_{2h} + \delta t_{4h} \dots \qquad (6\text{-}22)$$

For a one-dimensional flow and with three uniform mesh levels the total time step is:

$$\begin{aligned} \delta t_{total} &= \delta t_h + \delta t_{2h} + \delta t_{4h} \\ &= \delta t_h + 3 * \delta t_h + 9 * \delta t_h \\ &= 13 * \delta t_h \end{aligned}$$

However, the overheads required for computing on the coarse meshes needs to be taken into account for a representative comparison. If the amount of computational work required on the finest mesh is W, the computational effort on the next two mesh levels are about 0.5W and 0.25W respectively. Therefore, an overall increase of about 8 times for the same amount of computational work is achieved. The use of residual averaging along with the multi-grid technique therefore leads to an increase of about 40 times in the allowable time step. Of course, this is only an estimate and the actual acceleration is subject to the problem being investigated and the original mesh density being used. However, the benefits of reducing the computational cost for flutter calculations are clear. On the other hand, the drawback of the multi-grid technique is that it does not retain the second-order accuracy in time. Therefore, in using the method care should be taken not to "over-use" it. The number of the mesh levels to be used is subject to the density of the fine mesh. If the original grid is very fine, then more multi-grid levels can be included. In most flutter calculations in this work, a two level multi-grid usually results in a time step which is comparable in magnitude to that of the structural model. This acts as a natural limit to the number of multi-grid levels that can be allowed.

The multi-grid method used in this study is a standard V-cycle [43]. The procedure is to perform one Runge-Kutta time-stepping on each grid level. The next coarser mesh is created by removing alternative grid lines along each co-ordinate direction. A two-dimensional representation of the process is shown in figure 6.7a. There is no need for a variable transfer from the fine mesh to the coarse mesh although this is an option that has been explored by other researchers [38]. So, node P, in figure 6.7a, retains its own flow variables during the mesh transfer. The flow discretization on the coarse mesh control volumes is performed in exactly the same form as for the fine mesh. However, in order to drive the solution on the coarse mesh by the fine mesh residuals, the residuals on the fine mesh are introduced into the time-marching algorithm in the form of a forcing function. Therefore, the Runge-Kutta scheme, i.e. equation (3-36), is modified in the following form:

$$\Phi^{0}_{2h} = \Phi^{t=t_o}$$

$$\Phi^{i+1}_{2h} = \Phi^{0}_{2h} + \alpha_i\, \delta t\,(R^{i}_{2h} + P_{2h}) \tag{6-23}$$

$$\Phi^{t=t_o+\delta t}_{2h} = \Phi^{t=t_o} + \alpha_n\, \delta t$$

The forcing function, P_{2h}, is determined as:

$$P_{2h} = \frac{\sum R_h \, vol_h}{\sum vol_h} - R^0_{2h} \tag{6-24}$$

The form of the forcing function means that if the flow variables satisfy the governing equations, i.e. the residuals on the fine mesh are zero, the solution is no longer updated on the coarse mesh. Therefore, flow solution on the coarse mesh is controlled by the residuals on the fine mesh.

The process of the residual transfer of equation (6-24) is shown in figure 6.7b. The fine mesh residuals at all the points within the control volume of node P for coarse mesh are added together and are used for calculating the forcing function for node P. The nodes concerned are W , SW , S , SE , E , NE , N , NW and P itself, nine nodes in total. In three-dimensional space, there are 27 grid points of the fine mesh that are used for calculating the forcing function.

Having calculated the updated flow variables on the coarse mesh, the corrections, not the actual flow values, i.e.

$$\delta\Phi_{2h} = \Phi^{t=t_o+\delta t}_{2h} - \Phi^{t=t_o}_{2h}$$

are transfered back to the fine mesh (this process also includes the corrections for pressure and temperature). The corrections for the nodes present on both meshes, i.e. points P , EE, etc., are straightforward. For the other nodes a linear interpolation process is used. Corrections for nodes E and NE are calculated as:

$$\delta\Phi(E)_{2h} = 0.5 * (\delta\Phi(P)_{2h} + \delta\Phi(EE)_{2h})$$

and

$$\delta\Phi(NE)_{2h} = 0.25 * (\delta\Phi(P)_{2h} + \delta\Phi(EE)_{2h} + \delta\Phi(NN)_{2h} + \delta\Phi(NNEE)_{2h})$$

In three-dimensional space, there are four extra corner points whose correction are obtained by eight-point averaging.

Finally, the solution on the fine mesh is updated by these corrections, i.e.

$$\Phi(P)^{n+1}_{2h} = \Phi(P)^n_{2h} + \delta\Phi(P)_h + \delta\Phi(P)_{2h} \tag{6-25}$$

where the superscript (n) represents the previous solution on the fine mesh and (n+1) the new solution.

If there are more than two grid levels present equation (6-25) becomes:

$$\Phi(P)_{2h}^{n+1} = \Phi(P)_{2h}^{n} + \delta\Phi(P)_h + \delta\Phi(P)_{2h} + \delta\Phi(P)_{4h} + \ldots \qquad (6\text{-}26)$$

The updating of the flow solution on the fine mesh completes the multi-grid cycle.

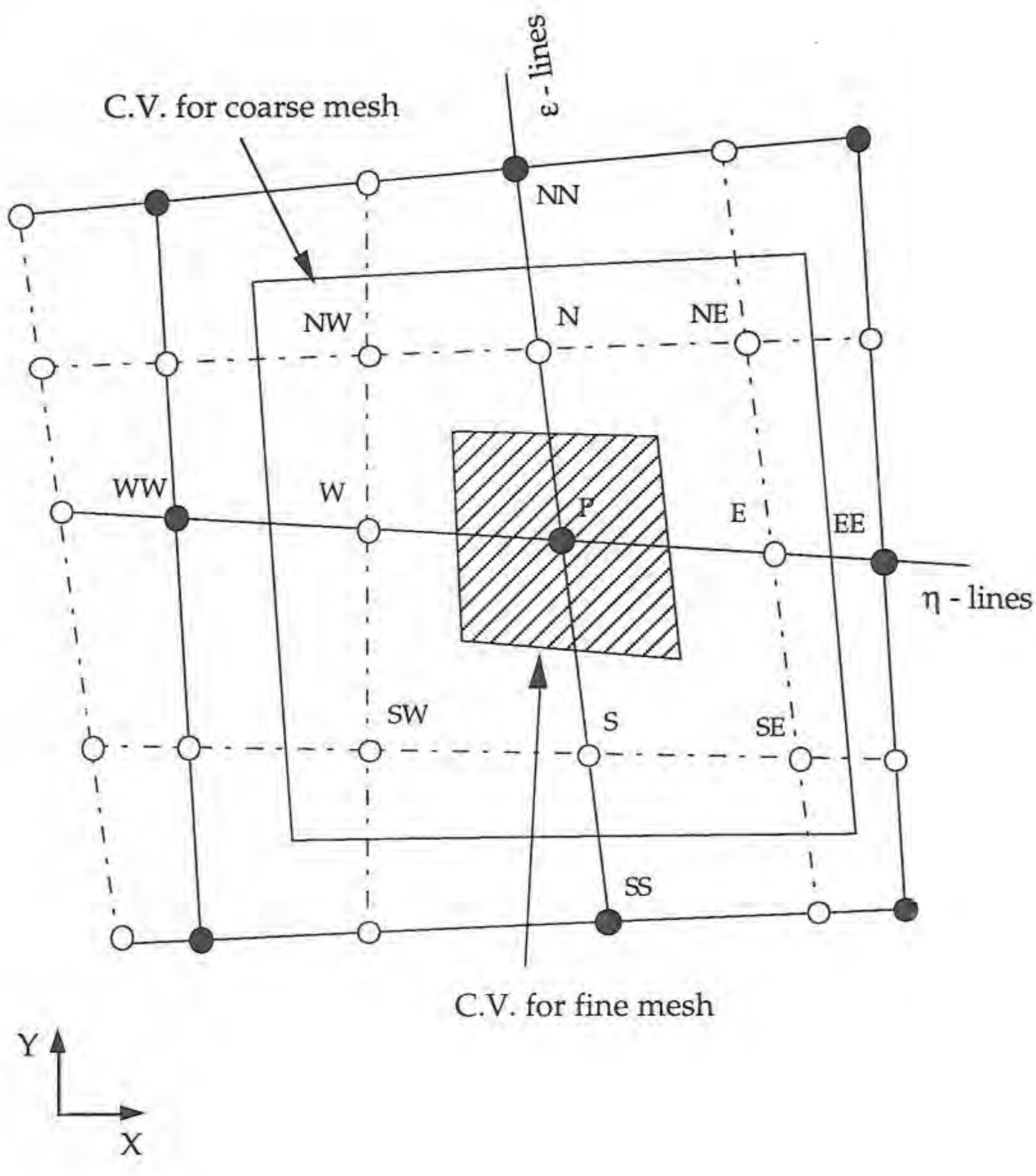

Figure 6.7a - Multi-grid Method

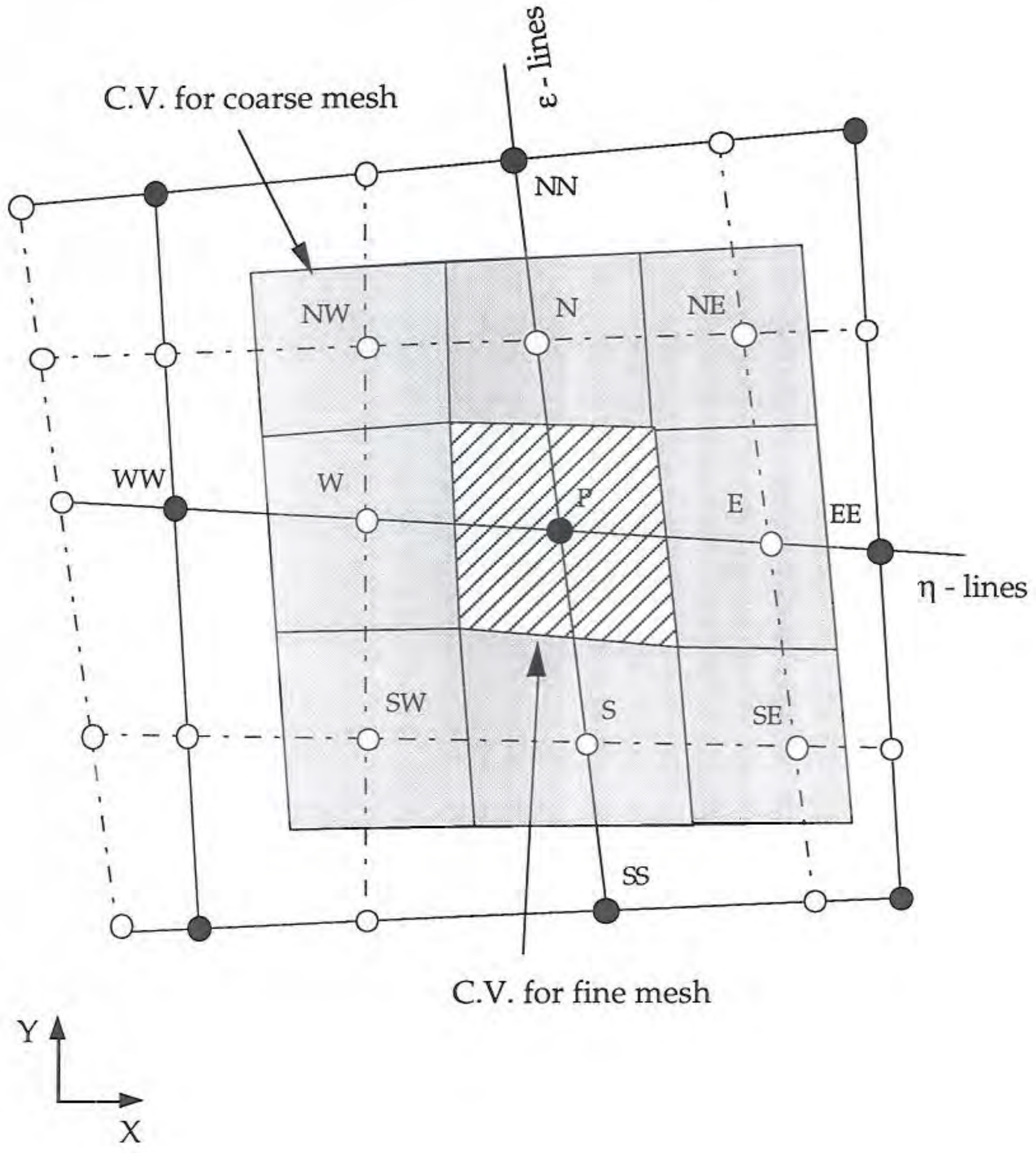

Figure 6.7b - Residual Transfer in Multi-grid

Chapter 7

Blade Untwist

You see how I have thought of everything.
Dostoyevsky - The Brothers Karamazov

7.0 About this Chapter

In part 7.1, the blade untwist problem is introduced. The solution procedure to the untwist problem by the integrated method is demonstrated on a real fan blade geometry in part 7.2. In part 7.3, the issue of time accuracy of the untwist solution process is discussed. The effect of mesh sensitivity on untwist results are investigated in part 7.4. The geometrical nonlinearity effects are detailed in part 7.5. In part 7.6, a general solution to the blade unrunning problem is introduced. Finally, in part 7.7, the general conclusions that can be drawn from this study are outlined.

7.1 Introduction

One important aspect of investigation of blade stability analysis is the question of blade untwist. The treatment of the untwist problem is often limited to a structural analysis only. However, with integrated aeroelastic models, untwist analysis can be performed as a fluid/structure coupling problem and blade untwist can be determined by incorporating both the fluid and the structural effects simultaneously.

The essence of the untwist problem is to determine the running geometry of the blade from its cold shape. This is to ensure that the manufactured blade performs as intended by the designer at operating conditions. Therefore, the correct solution to this problem is of paramount importance.

The forces acting on the blade which result in its geometry to be different from its manufactured geometry are blade rotational forces and fluid pressure forces. In a coupled analysis these forces are included in a time marching process which results in the final blade geometry and the corresponding flow field at a specific operating condition.

Of course, if the blade happens to be unstable the untwist calculation turns into a flutter calculation and the untwist results become irrelevant. However, in this study, we avoid the flutter problem by critically damping the blade so that the blade untwist is obtained regardless of the stability considerations. If required, the blade stability analysis can then be performed about this untwisted geometry. This separation of the two problems is for convenience, therefore, the untwist calculations have no bearing on the integrity of the blade which has to be investigated separately.

7.2 Case Study

A real, lightweight, fan blade geometry, fan B, has been chosen to investigate the validity of the integrated untwist calculation procedure. This allows the method to be evaluated for real geometries and operating conditions. The operating condition investigated is the maximum takeoff point at 85% engine speed at sea level static.

7.2.1 Structural Model

The structural analysis is performed on the finite element package SC03. The blade is modelled using 20 node brick elements. There are, in total, 2100 elements and 11700 nodes present in the blade structural model. The structural analysis is restricted to a single blade and the blade root is assumed to be rigid. Furthermore, disc flexibility is ignored. This single blade modelling implies that all the blades in the assembly are identical to each other, an assumption which is not quite true because of mistunning. However, as the untwist problem is a check on the blade design, the same assumption is used here. An untwist calculation for non-identical blades would require the whole bladed-disc assembly to be modelled.

A standard feature of the structural finite element modelling is the inclusion of the centripetal effects due to the blade rotation in the form of extra stiffness. This approach has been used here and the resultant displacements on the cold geometry are then added to the blade. Therefore, the outcome of the eigensolution is the blade geometry, including rotational effects, as well as the blade modeshapes and natural frequencies. The blade natural frequencies at 0% and 85% speeds are given in Table 7.1 and some of the modeshapes are shown in figure 7.1.

In the untwist calculation the first twelve modes of the blade have been used.

Mode	Static Frequency (Hz)	80% Speed Frequency (Hz)
First Bending	34.41	70.83
First Edgewise	84.40	149.23
First Torsion	199.13	203.17
Second Bending	225.82	299.94
Second Torsion	368.85	389.59

Table 7.1 - Blade Frequencies

7.2.2 Steady Flow

The second step in the untwist procedure is the calculation of the steady flow around the cold blade geometry which has been modified to account for rotation. This steady flow calculation is to speed up the untwist calculation. It is also a reference point against which the final flow results can be compared with. For the steady flow calculations and the untwist calculations a two-level multi-grid process is employed along with residual smoothing. The overall increase in the allowable time step is ten-fold.(based on the first time step)

A 99x16x16 fluid mesh is used for the flow calculations. For the steady flow calculations the exit pressure is imposed. Figure 7.2 shows the steady pressure contours on the blade suction and pressure surfaces. The shock wave is located at the blade tip trailing edge and it weakens and moves inside the passage as it approaches the hub section. The overall shock formation and its location are effectively determined at the tip section. In reality, the position of the shock at the tip would be further upstream and inside the passage due to viscous effects which are significant for a fan blade. This effect can, in theory, be simulated in an inviscid model by increasing the back pressure. This increase takes into account the losses which are not present in the Euler flow model. However, in practice, such a remedy does not work, as in an inviscid model a shock wave inside the passage is unstable. Therefore, an incremental increase in the back pressure does not move the shock wave from the trailing edge point until the increase is large enough to move the shock to the leading edge; again outside the passage. Therefore, such a modification was not attempted and the results of the flow calculations are for the correct back pressure.

Figure 7.3 shows the steady pressure contours for different heights along the blade. It can be seen that the shock strength increases as we move towards the blade tip and the shock moves towards the trailing edge line. It can also be seen that the shock wave tends to be stronger on the suction surface and it persists towards the hub section.

7.2.3 Blade Untwist

The final stage of the blade untwist calculation is the coupled fluid/structure analysis. The blade is allowed to move due to flow pressure field and the calculation proceeds in time until the blade reaches its final position. As it was pointed out earlier, since the main interest in the untwist calculations is to determine the blade design geometry, the blade motion is critically damped to remove possible blade instabilities. Damped blade motion also means that the untwist calculation in time would be quicker as the blade reaches its final position without any vibratory motion.

Figure 7.4 shows the modal contributions of the blade displacement in time. In can be seen that the main components of the blade displacement are in the first bending mode and the first torsion mode, the effect of the higher modes being insignificant. Figure 7.5 shows the resultant displacement of the blade. It can be seen that the effect of flow pressure on the blade is predominantly a bending displacement and perhaps the term "untwist" is somewhat misleading. Figure 7.6 shows the time history of the blade tip motion at the leading and trailing edge lines which represents the torsional component of the blade deformation; the blade torsion being the difference in the displacement of the tip leading edge and trailing edge points divided by the blade chord.

Figure 7.7 shows the comparison between steady flow results before and after the blade untwist. It can be seen that the shock wave motion is virtually non-existent at the blade tip while at lower blade heights there is a shock wave motion downstream of the flow towards the blade trailing edge line.

7.3 Time Accuracy for Untwist Calculations

The untwist results shown above are the result of a time-accurate calculation. However, it appears that the whole untwist process is a procedure that starts from a steady, or static, state and arrives at another steady-state condition. Therefore, it seems that time accuracy for such a procedure may not be required and, regardless of the actual path taken, one should arrive at the final solution. To investigate such a possibility, an untwist calculation is performed in which the flow solution proceeds by local time stepping and the blade displacements are calculated using the allowable time step for the structure, i.e. the time step allowed by the highest natural frequency. In this case no multi-grid or residual smoothing is used. The results of this calculation is given in figure 7.8 along with the results from the time-accurate calculation. It can be seen that while the time histories are not identical, the final results are the same. This means that untwist calculations can be performed with local time-stepping resulting in a substantial reduction in the computation time. A more important conclusion to be drawn is that blade untwist is a static problem unlike the divergence case studied in chapter 5.

7.4 Effects of Mesh Density

The effect of mesh density for the untwist calculations has also been investigated. Here, mesh density does not only refer to the fluid mesh but also the structural mesh, as there is a one-to-one correspondence between the fluid and structural nodes.

Three sets of flow meshes with 99x16x16, 99x16x31, and 99x31x31 nodes have been used. (a 99x16x31 mesh means 99 mesh points along the blade axis direction, 16 mesh points in the blade-to-blade direction and 31 points along the blade height). The last of these grids is really a viscous mesh and some inviscid flow models have difficulty in handling such a high mesh density because of anti-diffusion occurring due to high aspect ratios in the grid spacing. No such difficulties have been observed in the flow model used in this study.

The results of the three sets of untwist results, all obtained by local time stepping, are given in figure 7.9. It can be seen that the untwist results for the medium and fine meshes are identical. However, these are somewhat different from the results obtained on the coarse mesh, furthermore, the difference is more pronounced in the torsion mode. This dicrepancy can be explained by figure 7.10 which shows the final steady flow pressure distributions for the three meshes at different blade heights. While the pressure distributions for the medium and fine meshes are almost identical, they are markedly different from the pressure distribution obtained on the coarse mesh due to the poor shock capturing by the latter. This difference in shock strength and its position has a significant effect on the resultant moment on the blade; hence the differences in the untwist results of figure 7.9.

It is important to note that this case of mesh sensitivity is entirely due to the low number of grid points along the blade height. The medium mesh, which has the same number of mesh points in the blade passage but more points along the blade height than the coarse mesh, gives exactly the same results as that obtained on the fine mesh.

7.5 Effects of Geometrical Non-linearity

The inclusion of the rotational effects, i.e. the centripetal forces, in the eigensolution analysis although very convenient, has the disadvantage of neglecting the change in these forces as the blade moves under the flow pressure. This effect which has been termed "geometrical nonlinearity" can be significant if the amount of blade displacement is large enough (what constitutes a large displacement is a moot point). To take account of this extra feature in the untwist problem, one can include the centripetal forces in the time marching process itself and use the blade modal data at the zero speed. The centripetal forces on the blade are simply (chapter 6):

$$F_{centripetal} = -\Omega^2 [M] \{r\}$$

where {r} is a vector comprising the instantaneous position of each point on the blade, [M] is the mass matrix, and Ω is the blade rotational speed. As the blade rotational axis is along the x-axis, the above force at each point on the blade becomes:

$$F_{centripetal} = \begin{Bmatrix} \cdot \\ f_x \\ f_y \\ f_z \\ \cdot \end{Bmatrix} = -\Omega^2 [M] \begin{Bmatrix} \cdot \\ 0 \\ y_i \\ z_i \\ \cdot \end{Bmatrix}$$

Now, as the blade position in time changes the corresponding rotational forces acting on the blade are also modified.

The results of the untwist calculations with the above modification is shown in figure 7.11. It can be seen that the contribution of the first and the second mode is very small and, in fact, the third mode dominates the blade motion. The contribution of the first torsional mode is now very significant and corresponds to the blade twisting due to the combined centripetal and fluid flow forces. To be able to compare this result with that of section 7.2, the centripetal forces should be removed from the results of figure 7.11. Therefore, a structure alone analysis is performed and the resultant modal displacements are subtracted from those of figure 7.11. The outcome is shown in figure 7.12 which shows the untwist due to the pressure forces alone. Also given in figure 7.12 are the modal results of section 7.2. Figure 7.12 shows the effect of the geometrical non-linearity on the blade untwist calculation. It can be seen that while the first bending modal displacements are very similar (but not identical) the torsional modal displacements are somewhat different. The conclusion that can be drawn from this comparative study is that the inclusion of geometrical nonlinearity leads to a somewhat lower blade untwist corresponding to a smaller torsional modal displacement. Of course, one should bear in mind that such a conclusion is not general and is dependent on the specific case being studied. However, a more general conclusion that can be drawn is that the effect of geometrical nonlineariy is not negligible even at small blade displacements.

7.6 Blade Unrunning

While the above untwist procedure is a major step forward compared to the current procedures in use, the fact is that the untwist problem remains as only a check on the much more important procedure of blade unrunning. This is the procedure by which the designer obtains the cold blade geometry from the design geometry. Blade unrunning is an inverse problem with no exact solution and its accuracy is of paramount importance. Here, a possible procedure for blade unrunning calculations is proposed based on the results of sections 7.3 and 7.5 outlined above.

A simple procedure for blade unrunning would be to first calculate the steady flow field at the design condition. The pressure field obtained is the desired flow field corresponding to the desired blade geometry under operating conditions. The second step is to form the structural model for this desired blade geometry.

The blade rotation is not included in the model so the structural eigensolution is performed at zero speed. The third and final step is a static analysis to determine the blade displacement under the centripetal and pressure forces, i.e.

$$[K]\{x\} = F_{flow} + F_{centripetal}$$
$$= F_{flow} + -\Omega^2 [M]\{r\} \qquad (7\text{-}1)$$

The flow pressures are due to the desired flow field and hence determined. The mass and stiffness matrices are for the structure at the operating geometry (but zero speed) and also determined. So the above equation is a linear static problem to determine how much blade motion {x} is required to cancel the effect of fluid and centripetal forces. Subtracting the blade displacements {x} from the design geometry {r} gives the cold blade shape. This analysis can be performed in one step if it is assumed that blade stiffness does not change (linear solution) or can be performed iteratively if [K] is allowed to vary (non-linear solution). However, the non-linearity is only on the LHS of the equation and does not effect the RHS forces.

The conclusion of section 7.3 that the untwist problem is path independent means that the resultant cold geometry returns to the design position when subjected to the same centripetal and fluid forces.

The result of the blade unrunning calculation for the above test case is identical with the untwist results and hence not shown here (using the untwisted geometry and equation (7-1) results in the cold geometry used for the untwist). The differences might begin to appear if blade stiffness is allowed to vary. This however, is beyond the scope of this work.

7.7 Conclusions

At first sight, referring to the untwist calculation procedure, outlined above, as an integrated method seems to be an anachronism. After all the centripetal forces and the fluid flow forces are considered separately so the talk of integrated fluid/structure coupling is out of place. The integrated feature of the untwist calculation is in the inclusion of the flow forces. Here an uncoupled method can not determine the final flow field which acts on the blade. An integrated method enables us to find out what the final flow field is going to be, and how this differs from the design flow field. The matching pair of the final blade geometry and the final steady flow field can only be obtained by an integrated time-marching fluid/structure model.

The main conclusions derived from the use of the integrated method in solving the untwist problem are three-fold. First of all the blade untwist is characterised by blade bending under the flow pressure forces and blade twist, though more significant, is numerically much smaller. The second conclusion is that the effect of geometrical nonlinearity in blade untwist is not negligible even for small displacements. Finally, it has been demonstrated that the untwist problem is a static problem and independent of the dynamic fluid/structure features that are dominant in blade flutter.

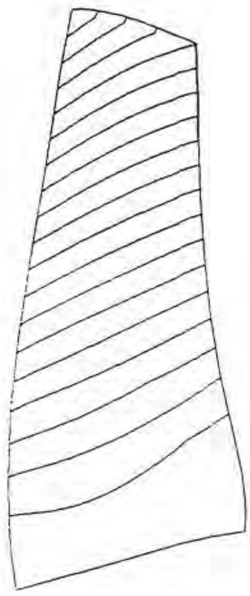

1)First Flap

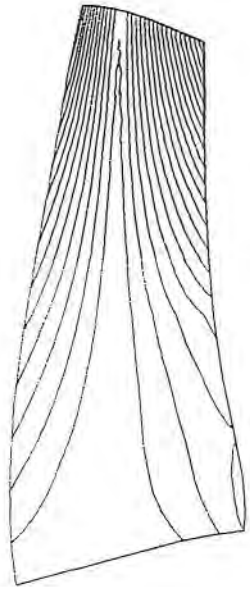

3)First Torsion

4)Second Flap

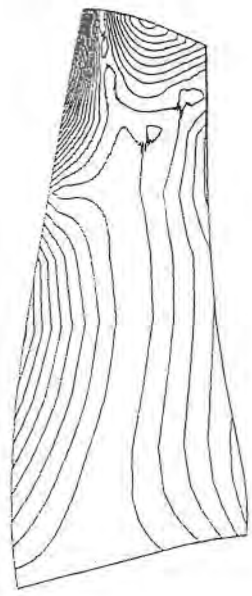

5)Second torsion

Figure 7.1 - Blade modeshapes

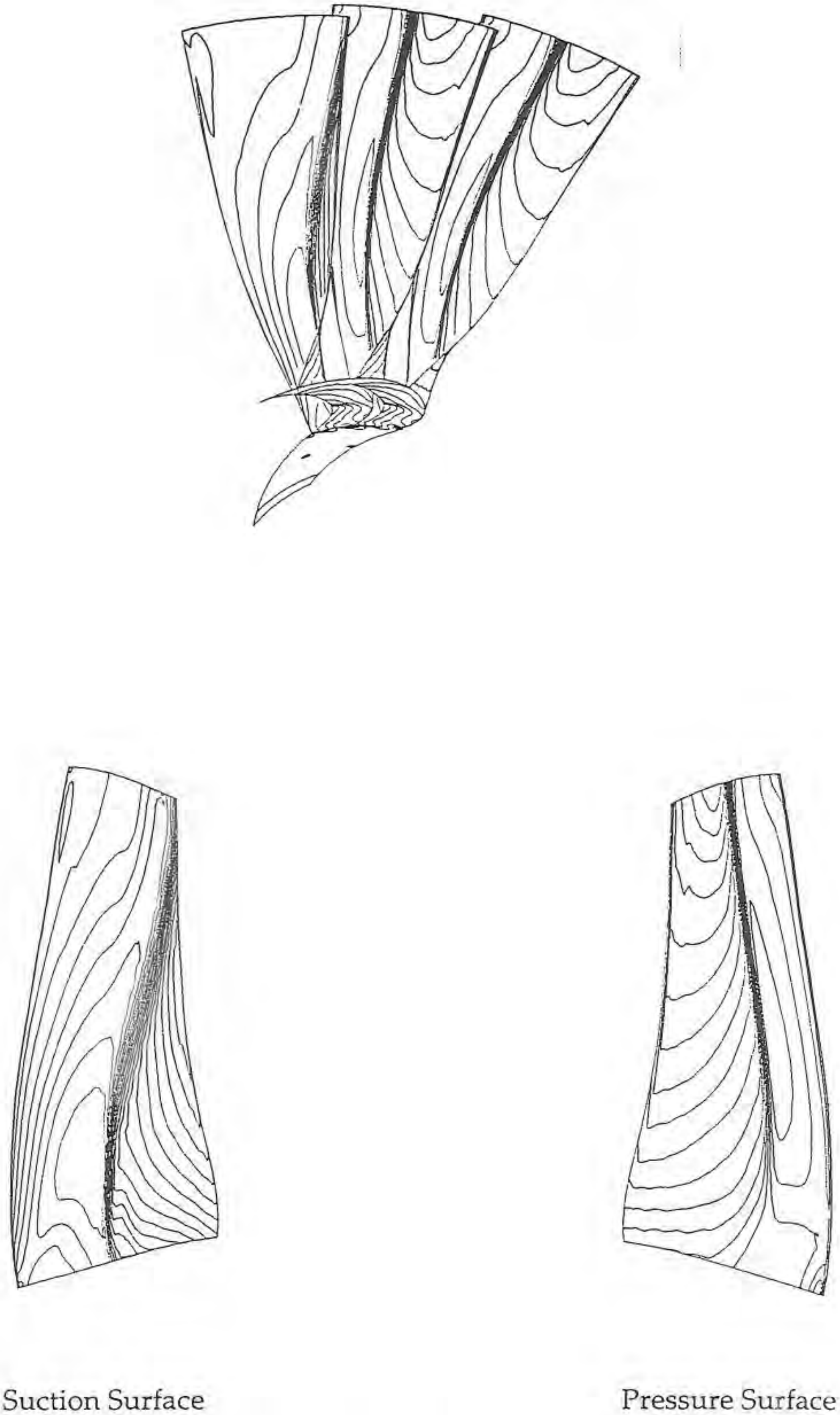

Suction Surface Pressure Surface

Figure 7.2 - Steady pressure contours

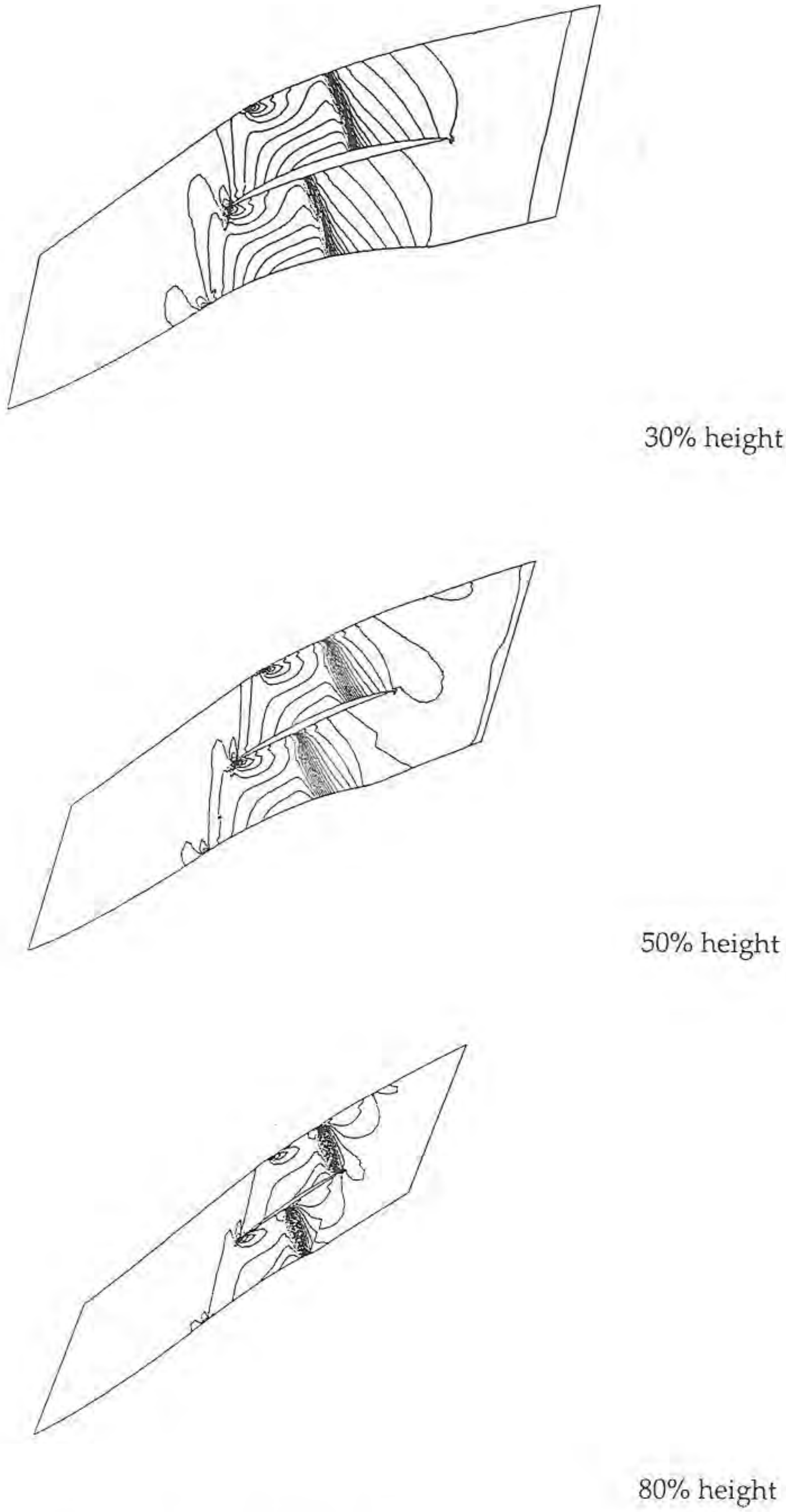

Figure 7.3 - Steady passage pressure contours

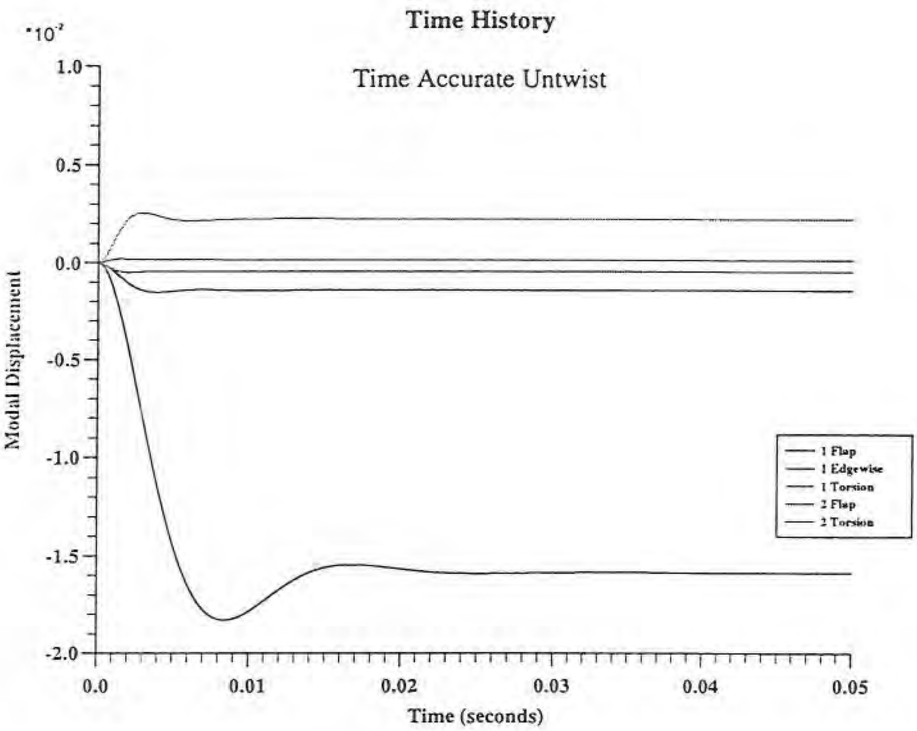

Figure 7.4 - Blade modal displacements

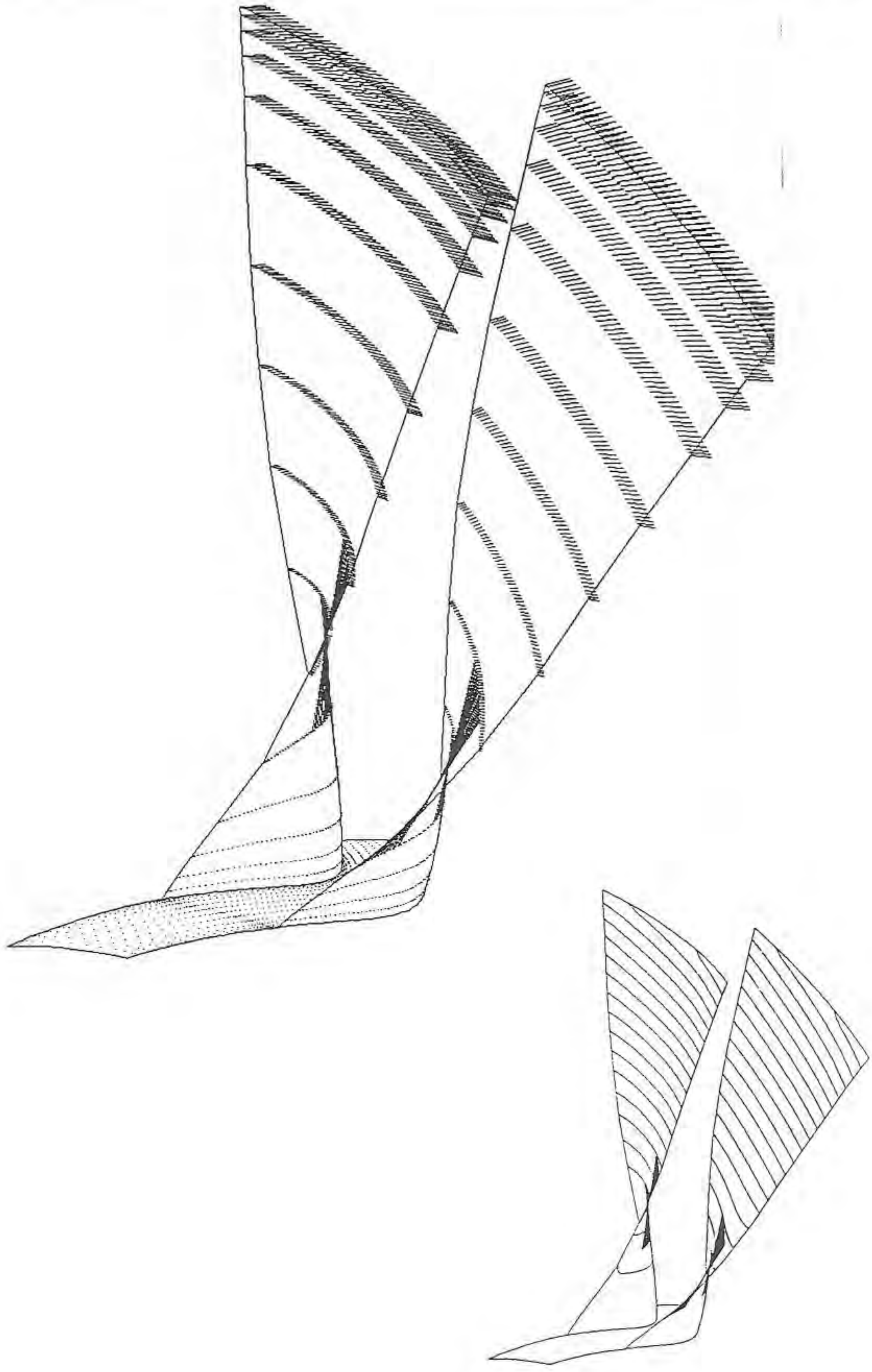

Figure 7.5 - Blade untwist displacement

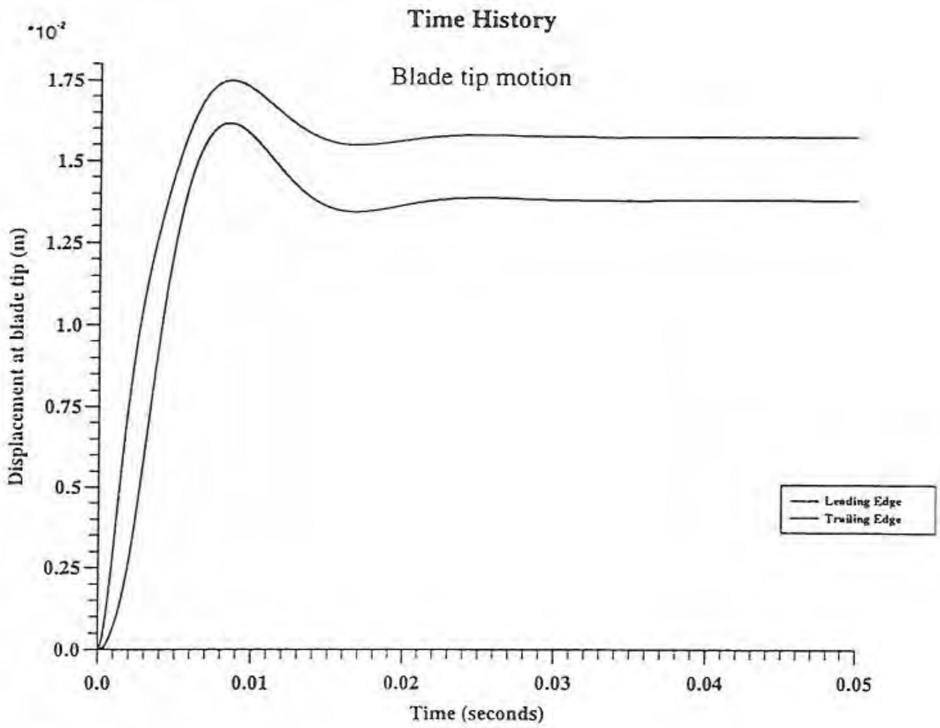
Time History
Blade tip motion
*10^-2
Displacement at blade tip (m)
Time (seconds)
Leading Edge
Trailing Edge
1.75
1.5
1.25
1.0
0.75
0.5
0.25
0.0
0.0
0.01
0.02
0.03
0.04
0.05

Figure 7.6

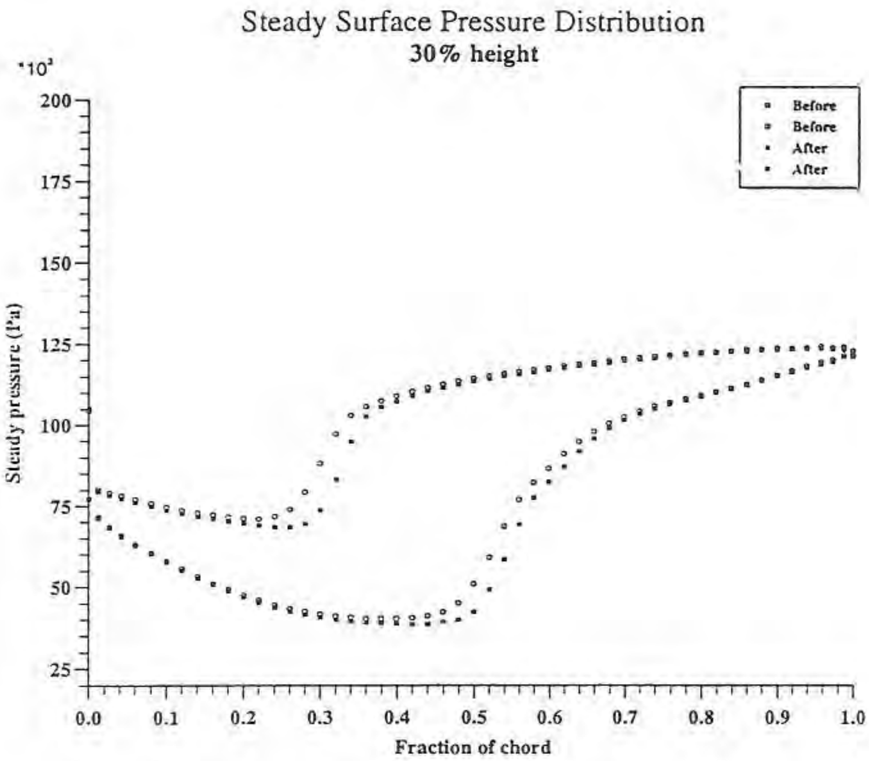

Figure 7.7a - Steady flow before and after untwist

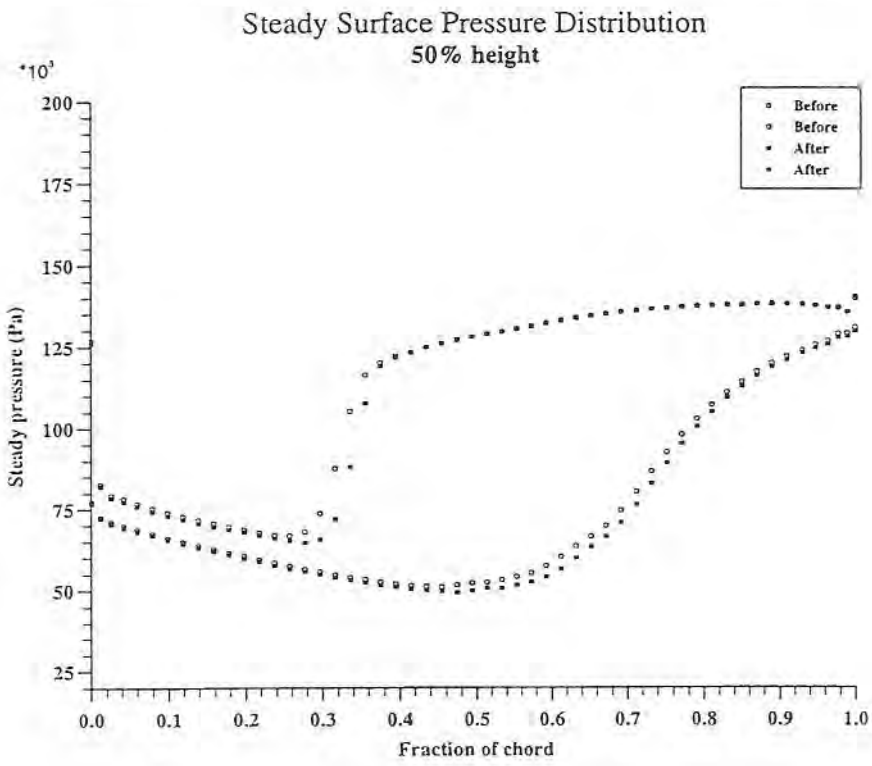

Figure 7.7b - Steady flow before and after untwist

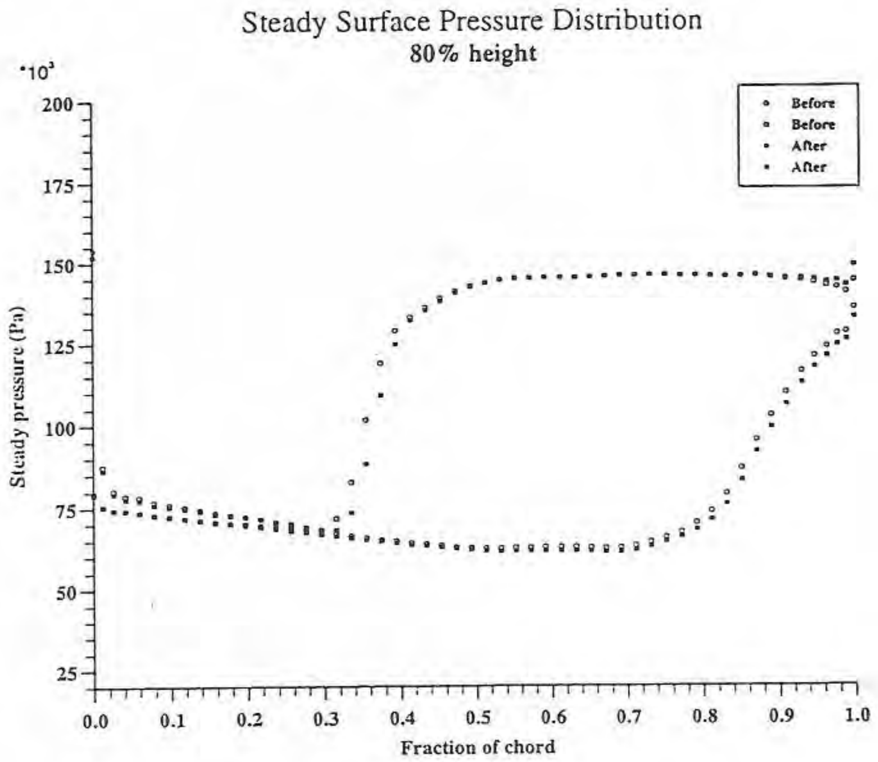

Figure 7.7c - Steady flow before and after untwist

Time History

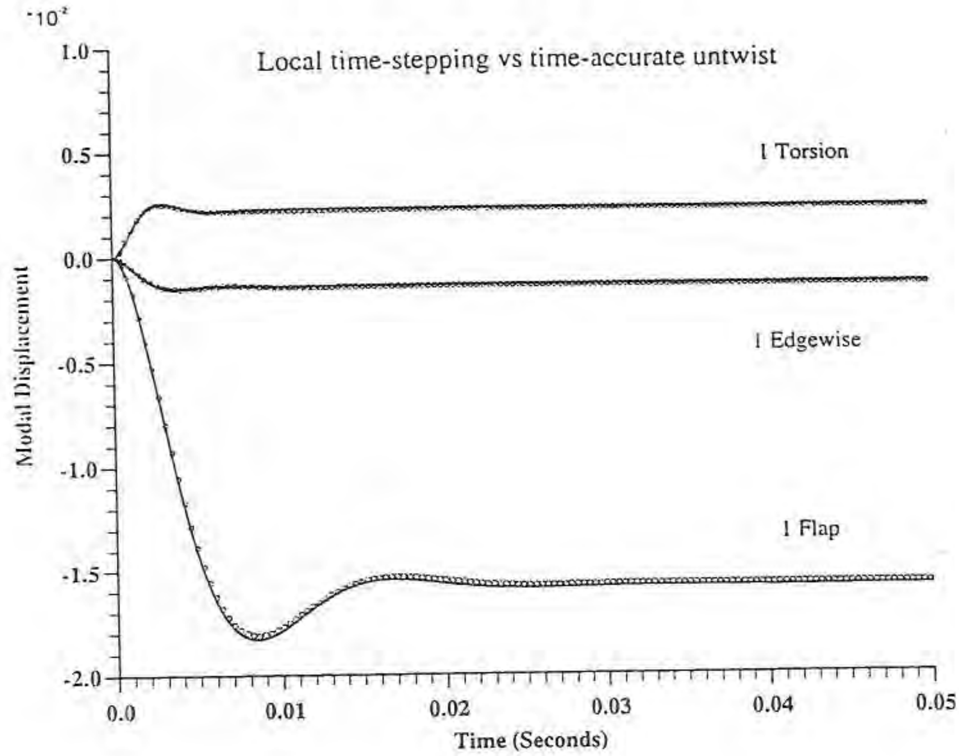

Figure 7.8

Time History

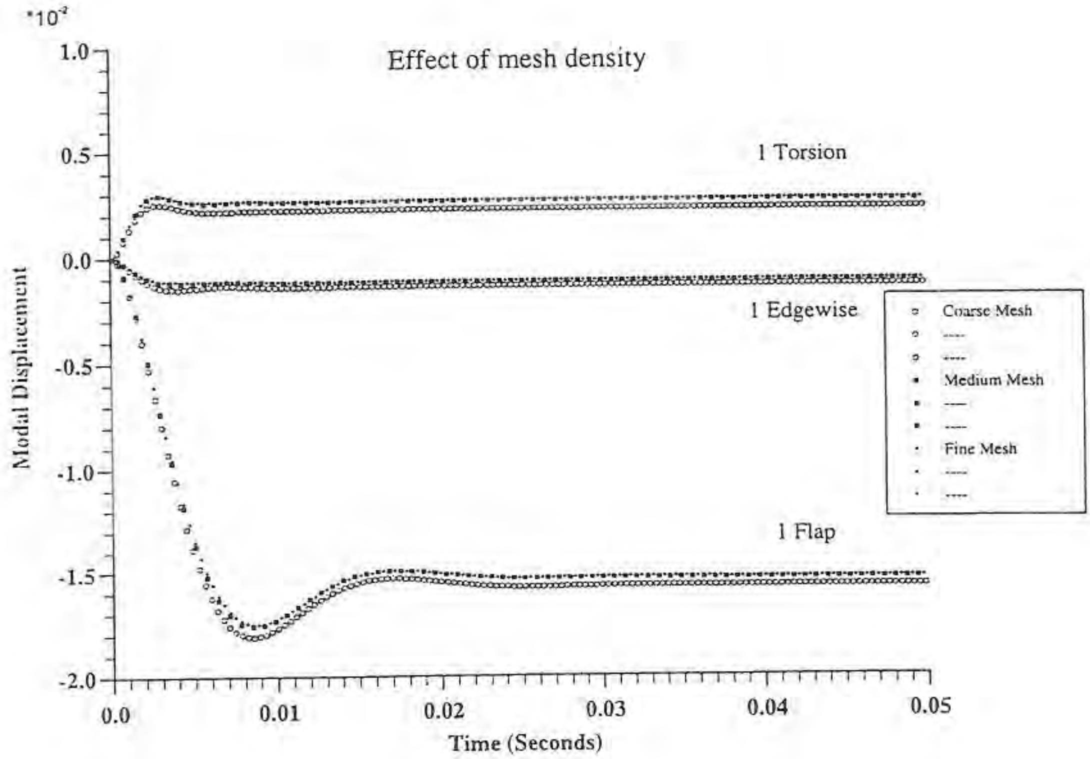

Figure 7.9

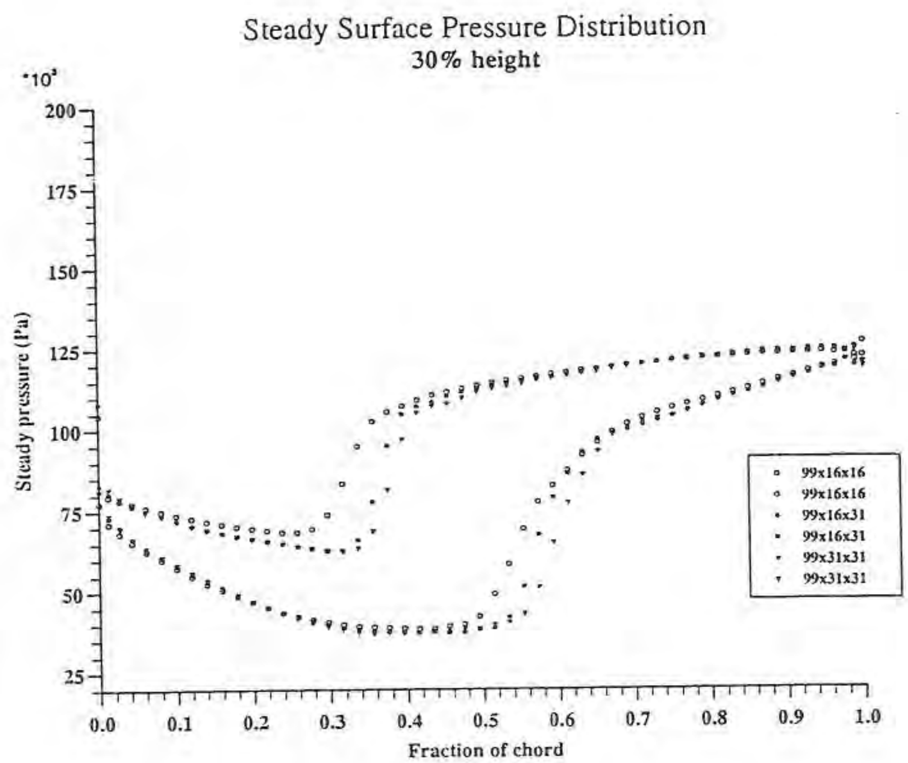
Steady Surface Pressure Distribution
30% height
*10³
200
175
150
125
100
75
50
25
Steady pressure (Pa)
0.0
0.1
0.2
0.3
0.4
0.5
0.6
0.7
0.8
0.9
1.0
Fraction of chord
99x16x16
99x16x16
99x16x31
99x16x31
99x31x31
99x31x31

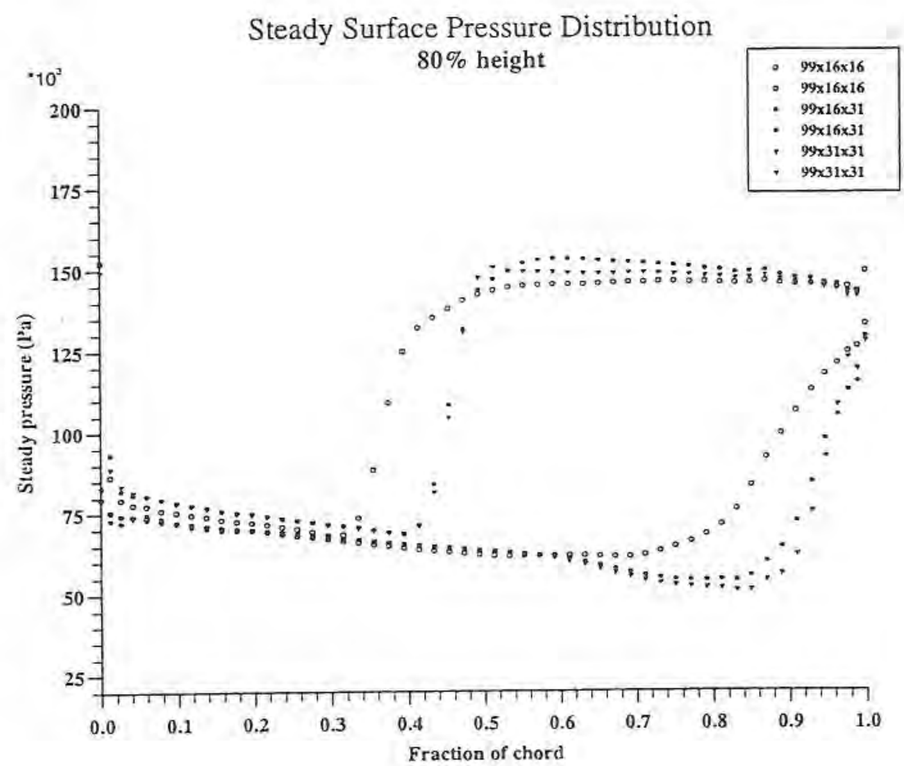
Steady Surface Pressure Distribution
80% height
*10³
200
175
150
125
100
75
50
25
Steady pressure (Pa)
0.0
0.1
0.2
0.3
0.4
0.5
0.6
0.7
0.8
0.9
1.0
Fraction of chord
99x16x16
99x16x16
99x16x31
99x16x31
99x31x31
99x31x31

Figure 7.10

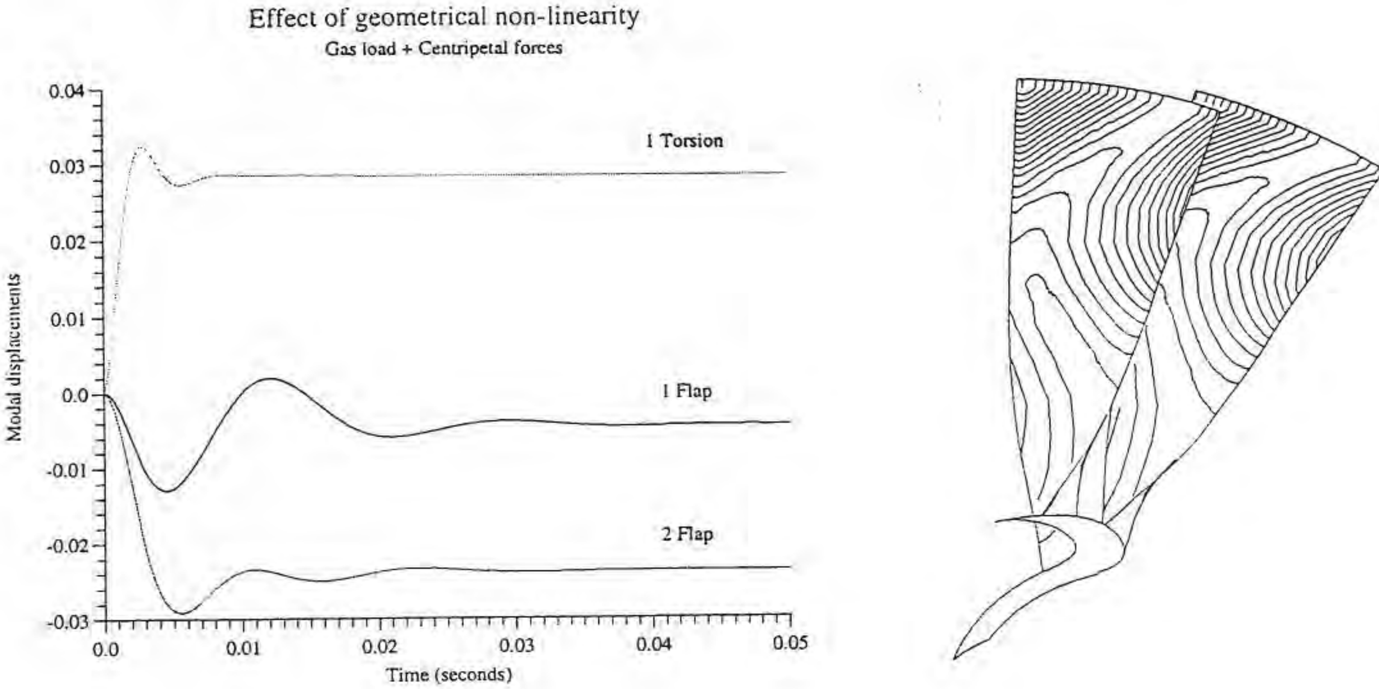

Figure 7.11

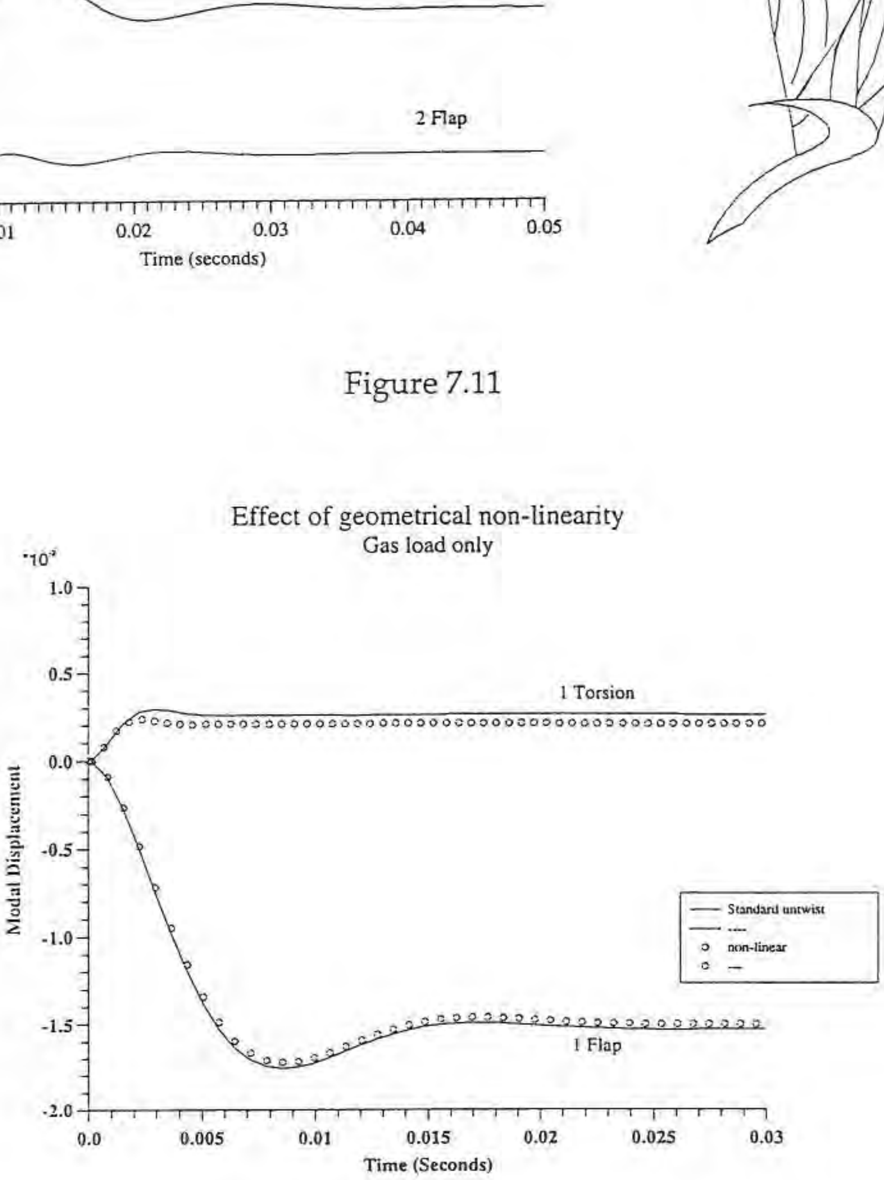

Figure 7.12

Chapter 8

Blade Flutter

AND THAT MORROW HAS COME.
Denis Diderot - Jacques the Fatalist

8.0 About this Chapter

The flutter problem being investigated is introduced in part 8.1. The specific case study is outlined in part 8.2. In part 8.3, the blade structural model is described. The steady flow results are given in part 8.4. In part 8.5, the results of the aeroelastic analysis are given. Finally, the flutter results obtained, are discussed in part 8.6

8.1 Introduction

To demonstrate the integrated non-linear method's ability to deal with fan blade flutter, in this section, a re-examination of the flutter boundaries of the fan A studied in chapter 2 is carried out.

As it was pointed out in chapter 2, the traditional method used in the study of the fan A failed to predict the onset of stall flutter because of the linear assumption implicit in the model and the decoupling of the fluid and the structural dynamics. The non-linear response of the fluid flow to the finite amplitude vibrations of the blade was judged to be the real cause behind the various flutter regimes. In the case of stall flutter, the non-linear fluid response may involve partial- or complete flow separation from the blade surfaces which is not taken into account in the fluid flow modelling in most of the current traditional methods. The linear assumption in flutter modelling implies that the flow remains attached at all times.

In this chapter, the stall flutter inception point at 85% engine speed is investigated using the integrated non-linear model. It should be borne in mind that if the stall flutter mechanism is, as often stated, the flow separation then the current integrated method cannot predict stall flutter either, as an inviscid flow model is employed in the present investigation. This, however, is not a major obstacle since the inclusion of the viscous effects can be readily added to the current technique if it is deemed to be essential. The inviscid flow modelling is only a way of reducing the problem size in the context of a research environment.

Therefore, the interest in this study is to find out the extra features that can be predicted by the inegrated method and an investigation of the feasibility of its use.

8.2 Case Study

The case study is that of the real fan blade, fan A, [ref 32 & chapter2]. The condition investigated is the onset of the flutter above the SLS working line, condition 4 in figure 2.4, at 85% engine speed.

As the flutter is observed to occur at 30 degrees inter blade phase angle, only the foreward travelling waves, corresponding to inter blade phase angles 0-180 degrees, are used in the study.

8.3 Structural Model

The structural model of the blade is the same as that given in chapter 2. Initially, the first five modes of the blade were used for the flutter calculations. However, as it became clear that the higher modes do not play a part in the blade stability, only the first three modes of the blade free-vibrations are retained. For the sake of completeness, the blade natural frequencies and their description are reproduced in Table 8.1 for the case of 85% engine speed. The annulus rotation effects are included in the eigensolution of the blade structural model, therefore, the effects of the geometrical non-linearity of the blade are ignored.

The structural model is based on a single blade analysis. For each blade mode, there are N possible inter blade phase angles, corresponding to the different assembly modes, where N is the total number of blades in the assembly; in this case 24 blades. This would imply that for each blade mode, N different flutter analyses should be performed. The alternative approach, which reduces the number of possible cases, is to impose the inter blade phase angle on the physical displacements of the blades. So for a general inter blade phase angle of IBPA, the physical displacements for the successive blades are obtained from the reference blade multiplied by a transformation matrix, i.e.

$$\{\delta x\}_n = \begin{bmatrix} 1 & 0 & 0 \\ 0 & \cos\theta & -\sin\theta \\ 0 & \sin\theta & \cos\theta \end{bmatrix} \{\delta x\}_1$$

where $\{\delta x\}_1$ is the displacement of a point on the reference blade, $\{\delta x\}_n$ is the displacements of the corresponding node on blade n, and θ is the rotation angle equal to n*IBPA.

The number of blades included in the flutter analysis, of course, depends on the value of the inter blade phase angle, so that the first and the last blades in the analysis are in phase with each other.

Mode	Frequency (Hz)
First Flap	180.521
First Flap & Second Edgewise	417.936
First Torsion	675.320
Second Flap	915.233
Second Torsion	1303.980

Table 8.1 - Natural frequencies for fan A at 85% Speed

8.4 Steady Flow

The steady flow calculations are performed on a 65x13x13 mesh. Calculations are performed for a single passage only, and the flow field in the extra passages are generated from the single passage solution. Figure 8.1 shows the pressure contours along the blade surfaces and figure 8.2 gives the pressure contours at the flow passage at different blade heights. It can be seen that there is a stand-off shock outside the flow passage. Figure 8.3 gives the surface Mach number distribution at different blade heights. For comparison purposes, the results from the FINSUP calculations given in chapter 2 are reproduced here in figure 8.4. This is only a rough comparison, as there is no exact matching between the blade sections used for the FINSUP calculations and the stream-heights in the current

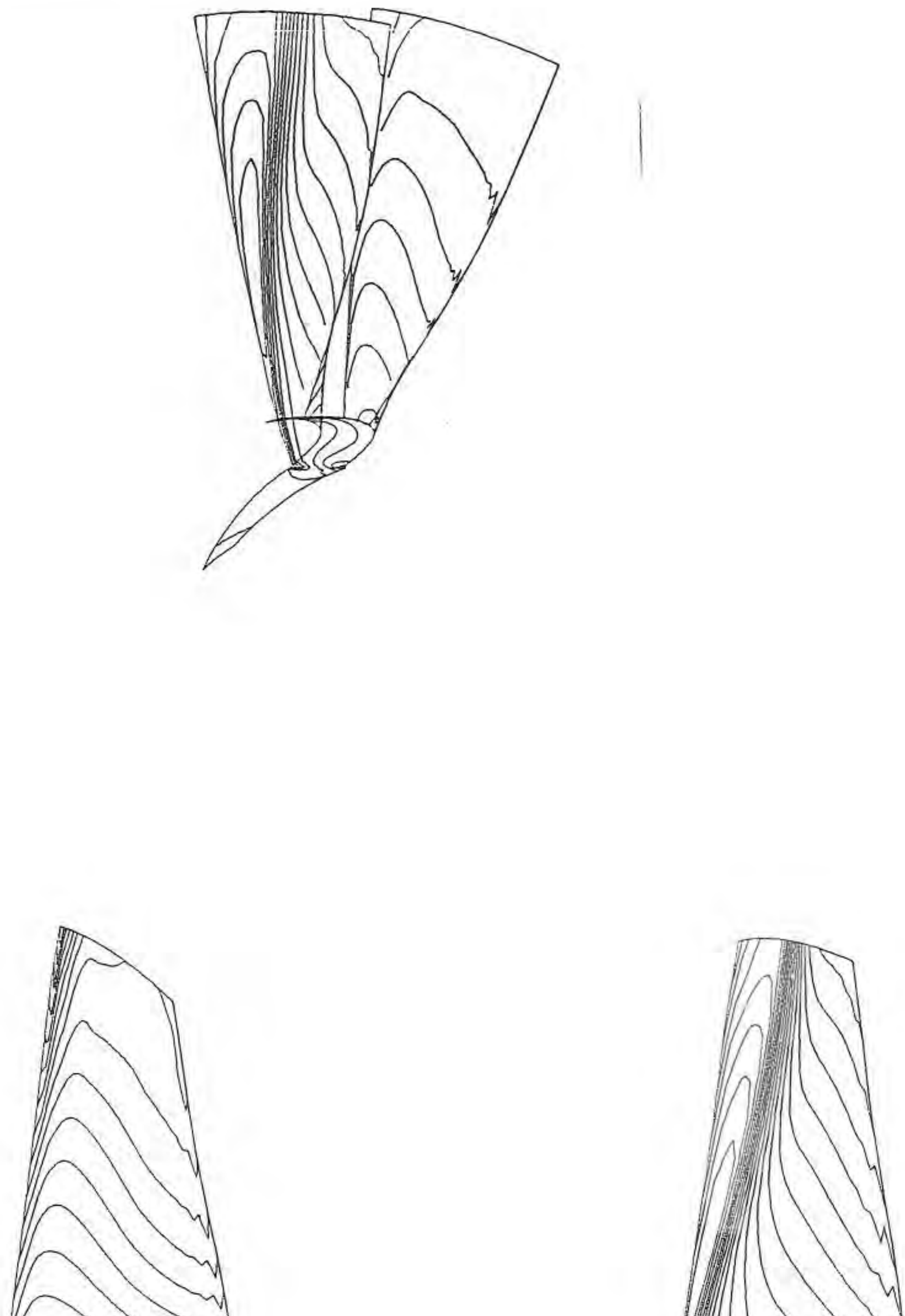

Suction Surface

Pressure Surface

Figure 8.1 - Steady pressure contours

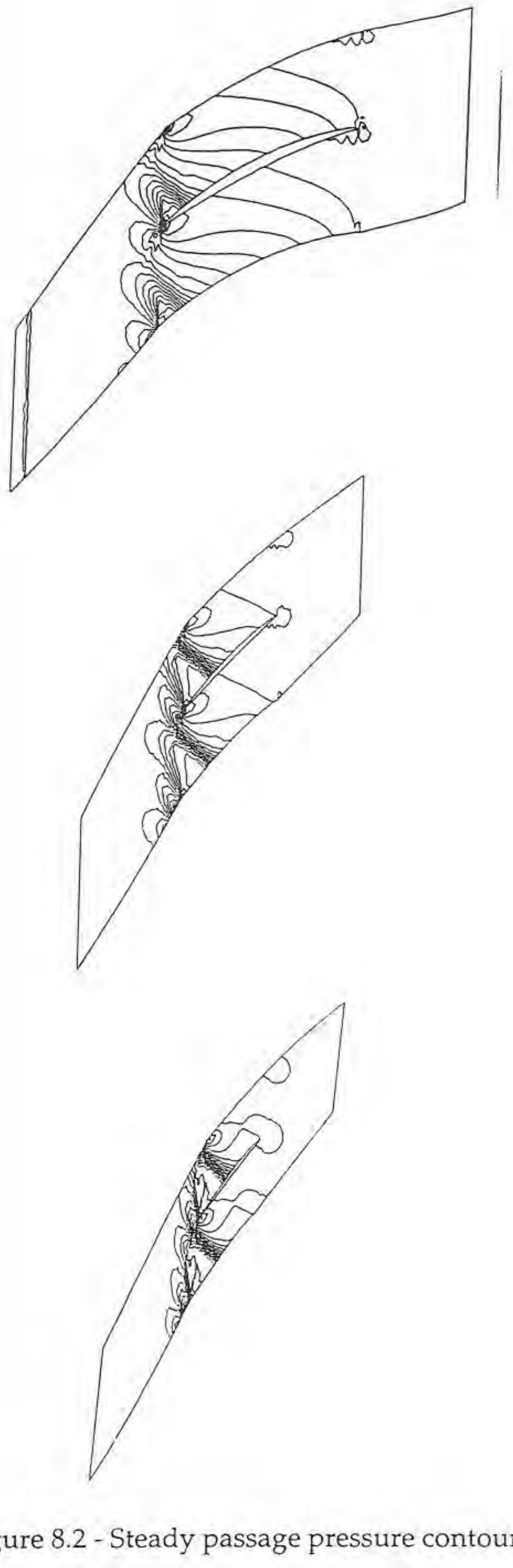

33% height

66% height

100% height

Figure 8.2 - Steady passage pressure contours

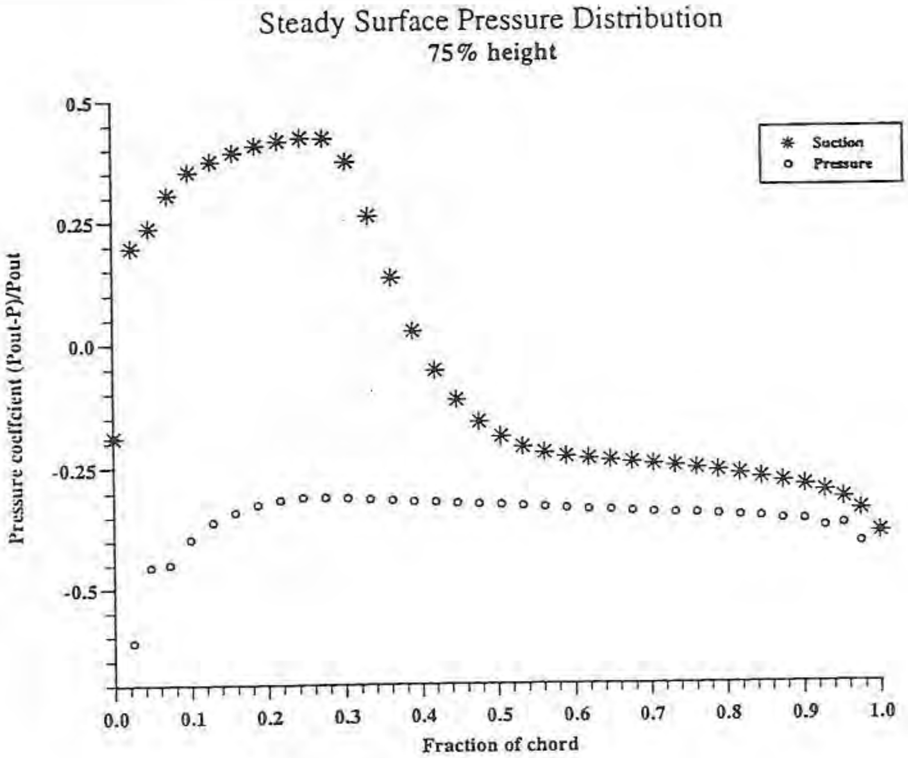

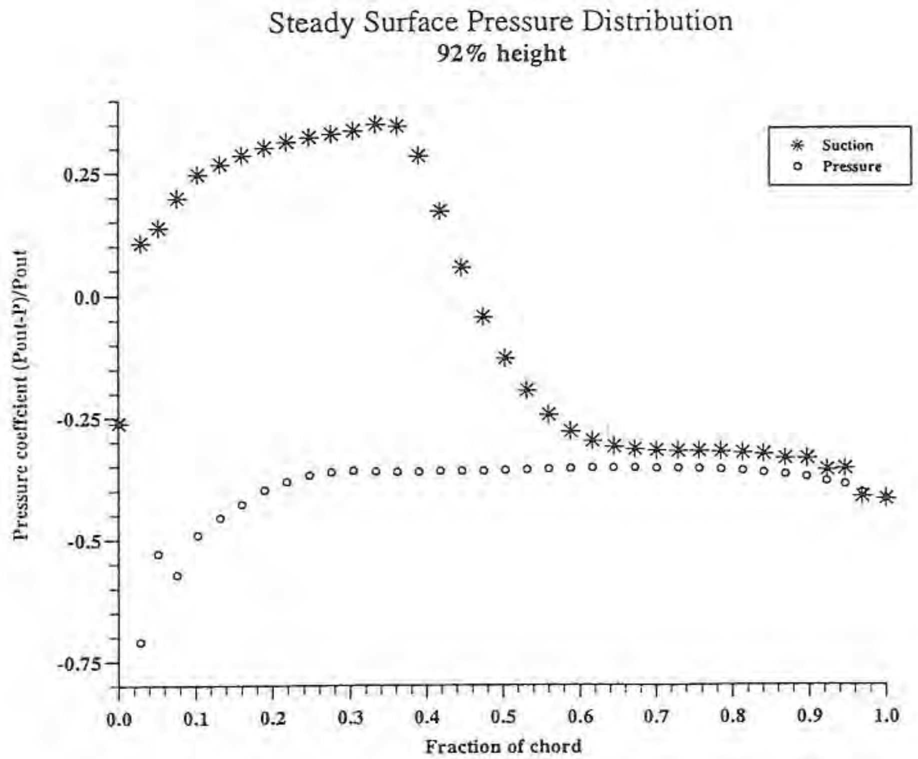

Figure 8.3 - Surface Mach Number Distributions

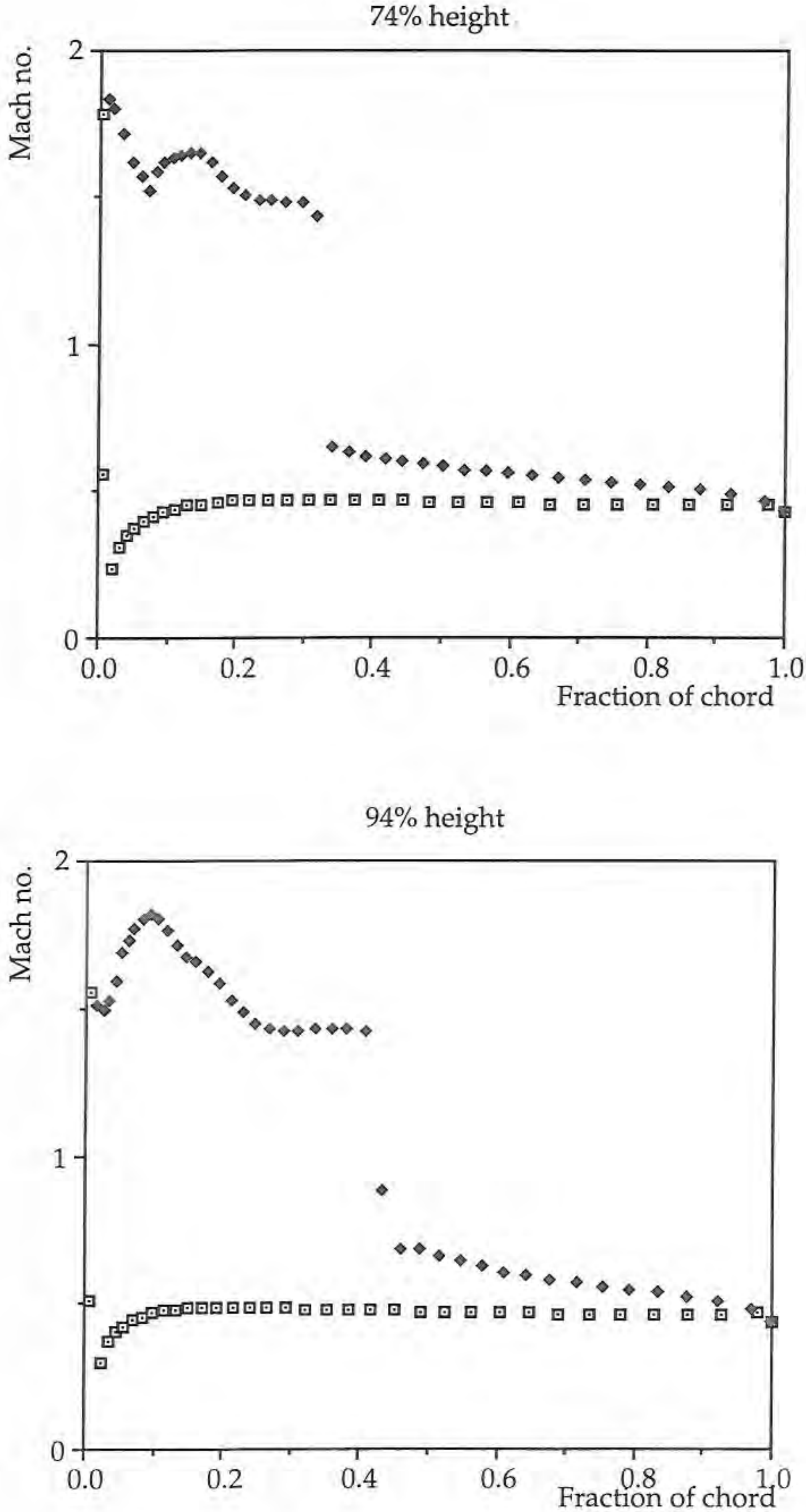

Figure 8.4 - Surface Mach Number Distributions (FINSUP)

results. However, it can be seen that the shock in both cases is outside the blade passage at about 40% chord length. The discrepancy at the leading esge line is due to the sharp cusp used in the FINSUP calculations which is not required in an Euler model. Therefore, the leading edge geometry for the two sets of results are effectively different from each other.

8.5 Blade Flutter Results

As the experimental results show that flutter occurred at 30 degrees inter blade phase angle, the flutter calculations are performed at about this value. In total, 6 cases of 0.0, 15.0, 30.0, 45.0, 60.0, and 180.0 degrees inter blade phase angles have been investigated. The phase angles corresponding to the backward travelling waves, i.e the negative inter blade phase angles, are always stable. The flutter calculations are triggered by an initial impulse of 10 N force applied at the blade tip mid-section along the y-direction.

Figure 8.5 shows the modal displacement history at the zero inter blade phase angle. It can be seen that the first mode is marginally stable, i.e. the decay rate is small, while the higher modes, including the first torsion are very stable. The modes 4 and 5 are practically of no significance and hence have been dropped from the subsequent analyses.

Figure 8.6 shows the modal displacements for the 180 degrees inter blade phase angle. This corresponds to a two-blade flutter analysis. It can be seen that the blade is unstable in its first bending mode, but the higher modes are stable. It is important to note the numerical predominance of the first bending mode in the results.

Figure 8.7 shows the modal time histories for the 15 degrees inter blade phase angle. The blade is stable. Figure 8.8 gives the time history of the blade modal displacements at an interblade phase angle of 30 degrees. Twelve blades have been used in the calculation. It can be seen that the blade is unstable in its first bending mode, but the other two modes present in the computation are both very stable. Therefore, the blade is unstable at 30 degrees inter blade phase angle. The same is true for inter blade phase angle of 45 degrees, figure 8.9, and, furthermore, it can be seen that the rate of energy transfer from the flow is higher judging from the faster growth in the blade amplitudes. Finally, in the case of 60 degrees inter blade phase angle, the blade is again unstable in its first bending

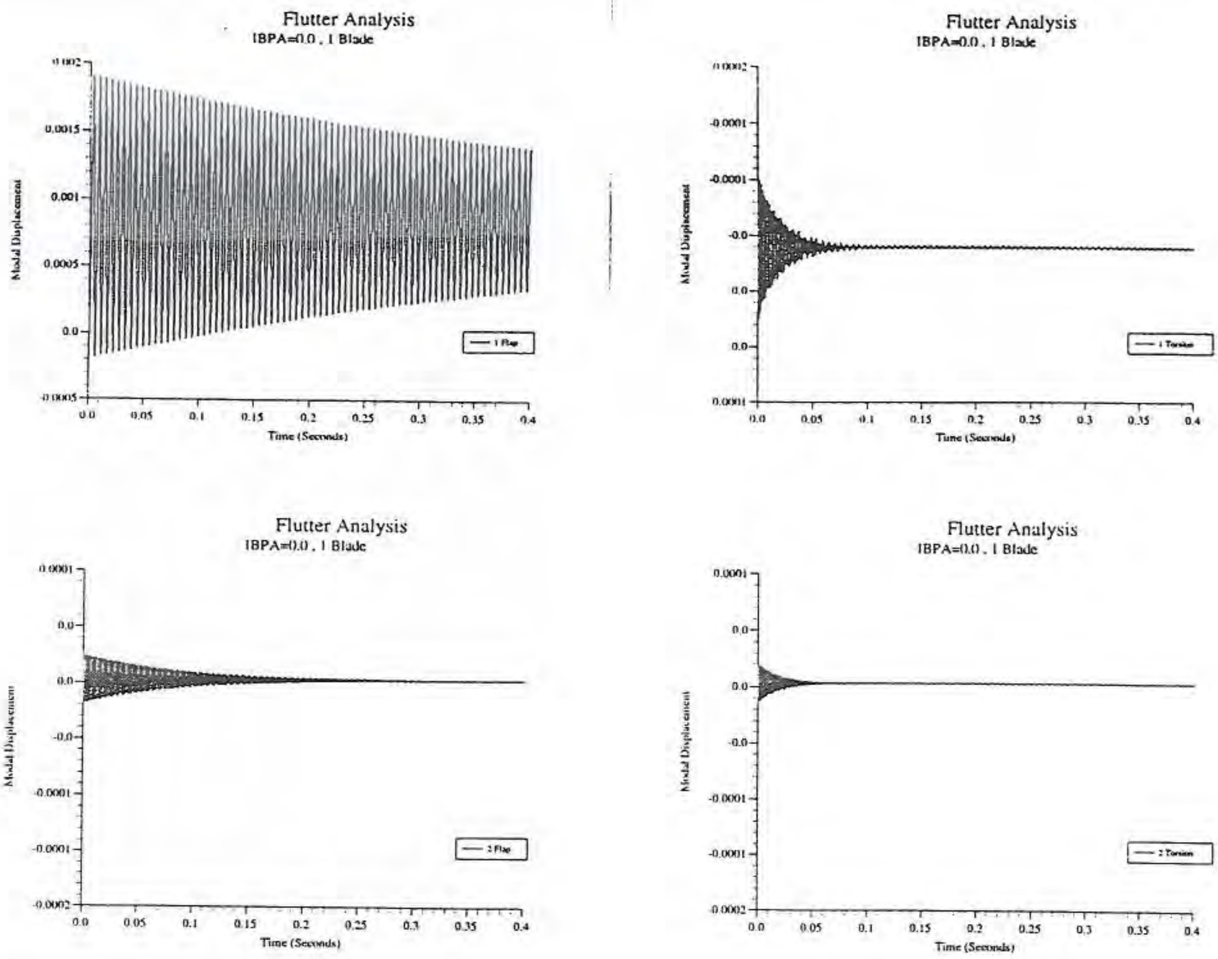

Figure 8.5

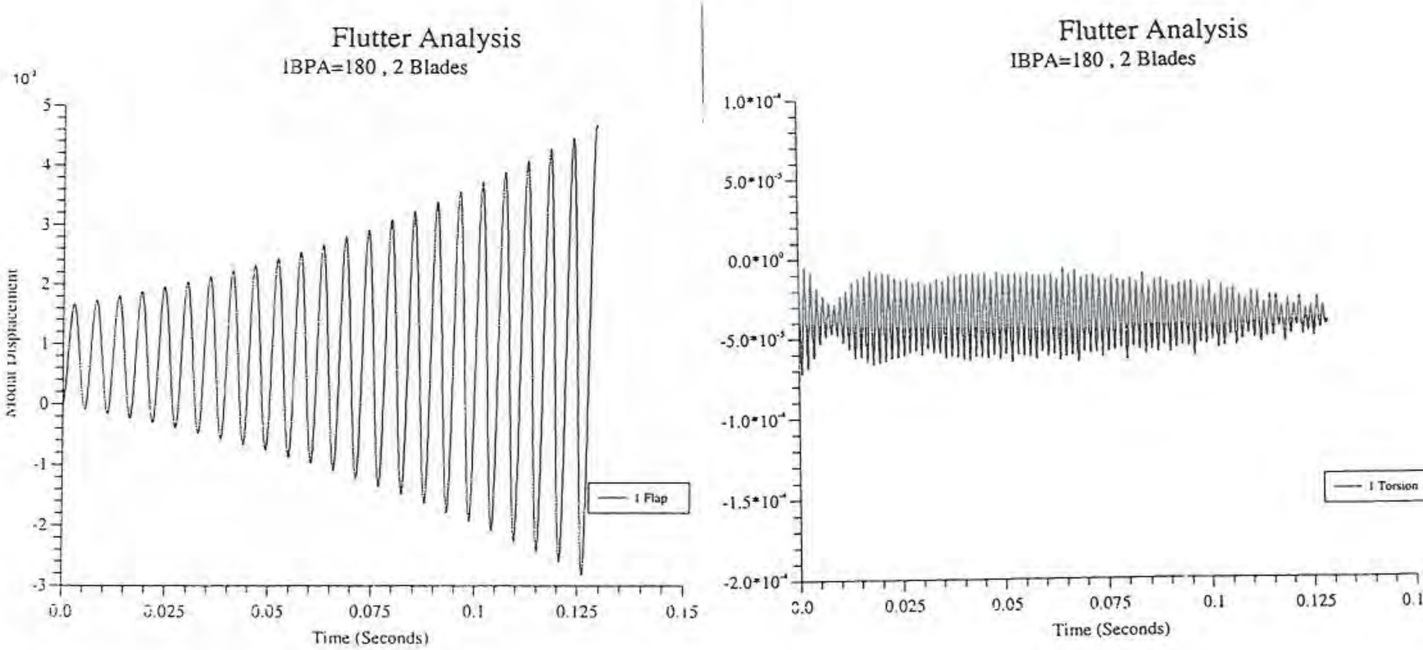

Figure 8.6

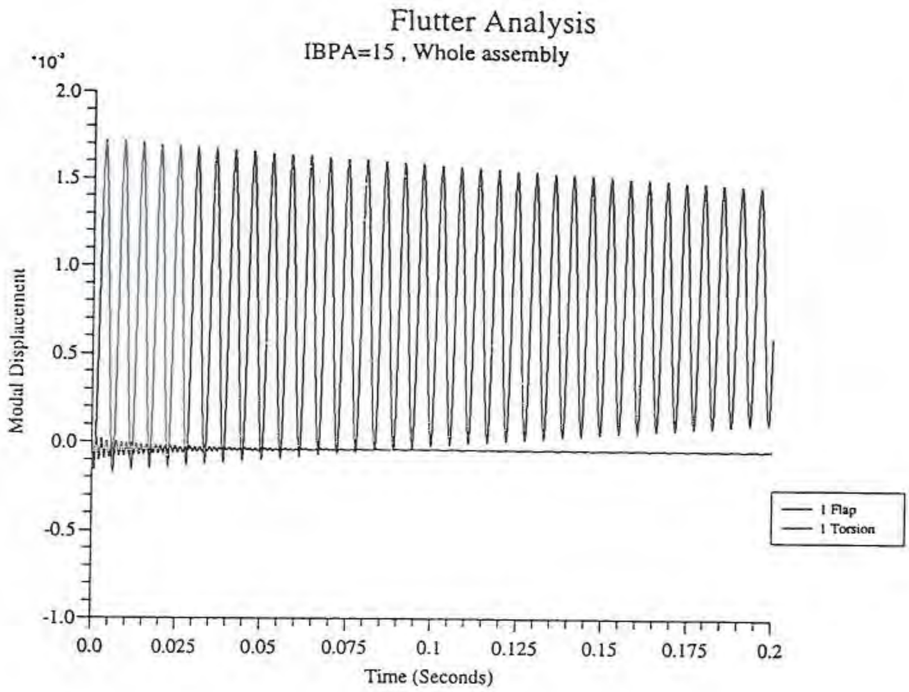

Figure 8.7

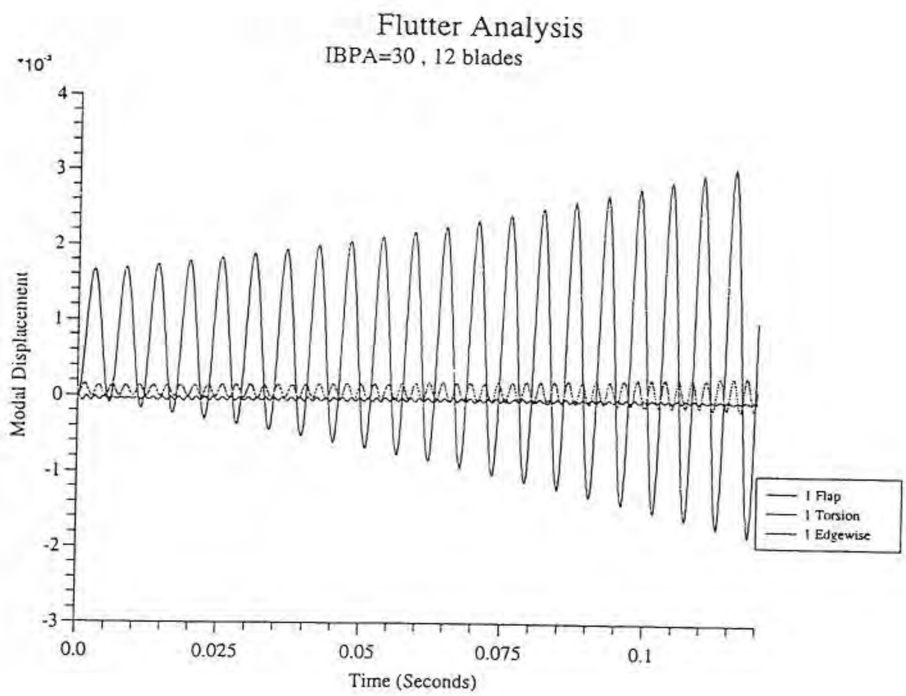

Figure 8.8

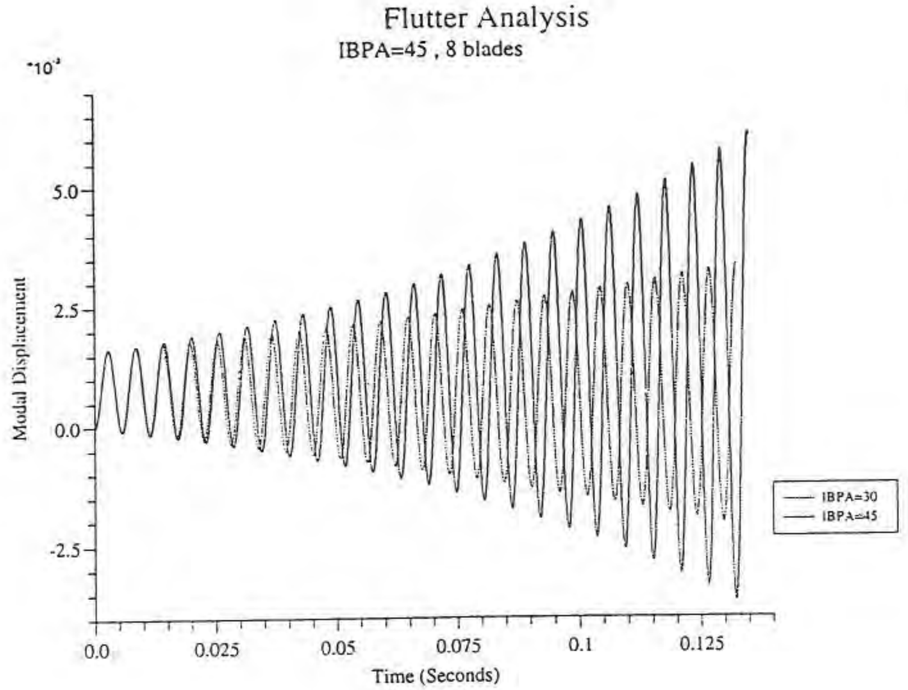

Figure 8.9

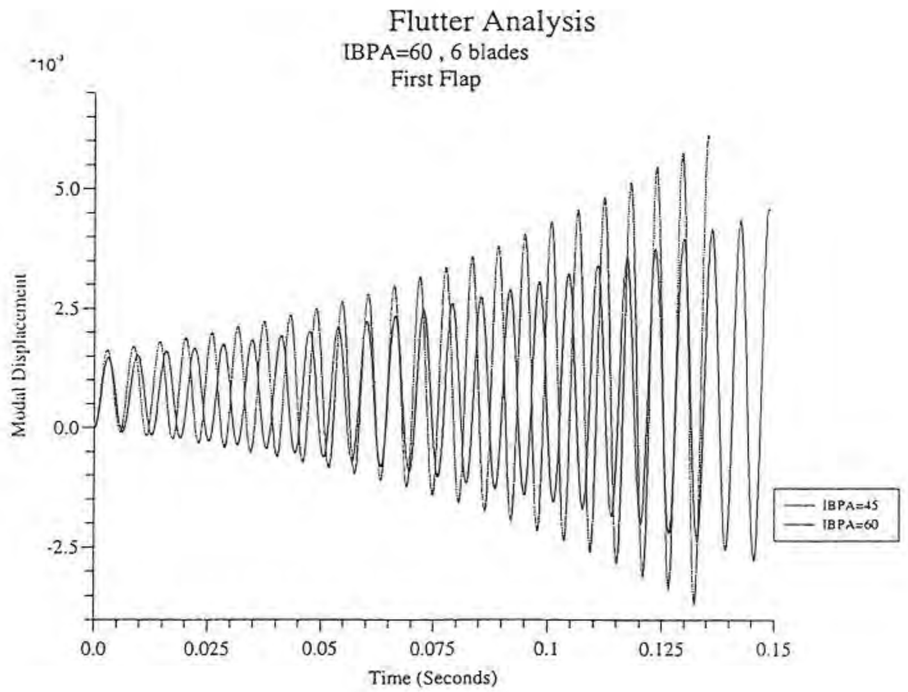

Figure 8.10

mode as shown in figure 8.10, however, the rate of growth in the blade amplitude is again lower than that for the 45 degrees inter blade phase angle.

Therefore, it seems that the blade assembly is unstable in its first flap mode for inter blade phase angles 30 to 180 degrees with the 45 degrees inter blade phase angle being the least stable combination.

8.6 Discussion and Conclusions

The above results are not very easy to explain. It seems that the calculations have resulted in a prediction of the stall flutter without the stall mechanism being present in the flow model! A possible explanation is that the mode of flutter predicted is imaginary and appears beyond the stall flutter boundary. And, in reality, the stall flutter mechanism occurs before the flutter regime predicted here.

This explanation, however, is not fully satisfactory. The problem lies in the fact that the very concept of bending mode instability does not tie in with the inviscid model used in the study. For a bending mode instability to occur, flow separation must take place. This can be easily demonstrated as shown in figure 8.11a: as the blade goes through a bending motion, the blade velocity reduces the overall flow incidence, and hence, the lift on the blade decreases, i.e. the fluid flow lift acting on the blade acts in the opposite direction to the motion of the blade. Therefore, in an inviscid model, the bending motion is invariably stable. Of course, this explanation only applies to a single blade and is most applicable to the case corresponding to 0.0 degrees inter blade phase angle. In fact, the case of zero inter blade phase angle corresponds very well to the single airfoil calculations in chapter 5. There, the mode of flutter was the coupling between the bending and torsion modes. Therefore, for the 0.0 inter blade phase angle, we are below the flutter boundary of a single blade. Reducing the back pressure which correponds to a reduction in the flow Mach number, of course, might lead to flutter instability. It was shown in chapter 5 that a reduction in the incoming Mach number lowers the flutter boundary margin for the same reduced speed. Therefore, the qualitative blade aeroelastic behaviour at these two inter blade phase angles can be fully explained from the two-dimensional airfoil calculations. In fact, the well known mode coupling flutter regime shown in figure 2.4 occurs below the SLS working line and corresponds to a reduction in the back pressure.

Appendix

A Dictionary of Aeroelasticity

A Dictionary of Aeroelasticity

Contents

The Aeroelasticity Dictionary consists of two main parts. The first part, which forms the main body of the Dictionary, gives the definitions of the terms used in aeroelasticity literature. The second part of the Dictionary is a list of the principal references, selected for their suitability when a more thorough discussion of the related topic is desired.

To summarise, the contents of the **Aeroelasticity Dictionary** are as follows:

i. Definitions
ii. References

Structure

The entries in the dictionary are classified alphabetically. Each entry is defined in the following format:

Word/Phrase, Notation (If any)
Context
Definition
Related topics
Reference
Comments

The **Context** of each entry specifies the relevant aeroelasticity discipline from which the term has arisen. All entries in the dictionary are classified in terms of the following four categories:

Aeroelasticity (**Aeroelasticity**)
Fluid Dynamics (**Fluid**)
Structural Dynamics (**Structural**)
Numerical Methods (**Numerical**)

The **Definition** of the item is a brief and concise meaning of the entry. This is neither a full description nor an explanation of the term: the main purpose is to help the reader to understand the relevance of the term when met in aeroelasticity literature.

The **Related topics** are other entries in the dictionary which are considered to be relevant to the specific entry defined. Related topics are there to help the reader to gain an insight into the broader inter-relation of the aeroelasticity terminology.

The **Reference** given for each entry is the **principal** source which can be used by the user who is keen to gain a fuller insight to the entry defined. The listing of all the references is given in part ii of the dictionary.

Comments at the end are brief remarks on the usage of the term defined in practice.

Index

Accelerance 1
Admissible Function 1
Admittance 1
Advancing-Front Method 1
Aerodynamic Damping 1
Aeroelastic Eigenvalues 1
Aeroelasticity 1
Alternating-Direction Implicit Method (ADI) 1
Apparent Mass 1
Artificial Compressibility 1
Artificial Viscosity 1
Assembly Modes 1
Assumed Modes Method 2

Beam-Warming Scheme 2

Cantilever Modes 3
Cell-Centre Scheme (CCS) 3
Cell-Vertex Scheme (CVS) 3
Central Differencing (CD) 3
Chaotic Flutter 3
Choking Flutter 3
Cholesky Factorisation 3
Complex Mode 3
Compliance 3
Component Mode Synthesis 3
Computational Domain 3
Conjugate Gradient Method (CGM) 4
Consistent Mass 4
Convergence Acceleration 4
Convolution Integral 4
Coulomb Damping 4
Coupled Vibration 4
Coupling (disc) 4
Courant-Friedrichs-Lewy Number (CFL) 4
Cyclically Symmetric Structures 4

D'Alembert Principle 5
Damping 5
Degree of Freedom (DOF) 5
Dependent Variables 5
Detuning 5
Distributed Mass 5
Divergence 5
Double Modes 5
Dry Friction 5
Duffing's Equation 5
Duhamel Integral 5
Dynamic Flexibility 5
Dynamic Stiffness 5

Eigenvalue 6
Eigenvalue Problem 6
Eigenvector 6
Engine-Order 6
Enthalpy Damping 6
Explicit Solution Techniques 6

Far-Field Boundary Conditions 7
Finite Difference Method (FDM) 7
Finite Element Method (FEM) 7
Finite Volume Method (FVM) 7
Fixed Interface Coupling 7
Flutter 7
Flutter-Divergence Interaction 7
Flux Splitting 7
Forced Response Vibration 7
Forced Vibration 7
Fourier Transform 7
Free Interface Coupling 8
Free Vibration 8
Frequency Domain Analysis 8
Frequency Response Function (FRF) 8

Galerkin Method 8
Galloping 8
Gauss-Seidel Method (GSM) 8
Generalised Co-ordinates 8
Godunov Schemes 8
Guyan Reduction 9

Hamilton Principle 9
Harmonic Balance Method (HBM) 9
Householder Method 9
Hysteretic Damping 9

Implicit Solution Techniques 10
Independent variables 10
Inertance 10
Inter-Blade Phase Angle (IBPA) 10

Jacobi Method 10

Kutta-Joukowski Condition 11

Lagrange's Equation 11
Lanczos Method 11
Lax-Wendroff Schemes 11
Limit Cycle 11
Lumped Mass 11

Material Damping 12
Matrix Stability Analysis Method 12
Mechanical Impedance 12
Mesh Kinematics 12
Mistuning 12
Mixtuning 12
Mobility 12
Modal Analysis 12
Modal Model 12
Modal Testing 12
Mode Localisation 12

Mode Shape 13
Mode Splitting 13
Mode Superposition 13
Modes 12
Multi-Grid Methods 13

Natural Frequency 13
Newmark Method 13
Nodal Diameter 13
Non-reflecting Boundary Conditions 13
Normal Modes 13
Numerical Boundary Conditions 13

Orthogonal modes 14
Orthogonality of Modes 14
Over-Relaxation Methods 14

Periodic Structures 14
Periodic Vibration 14
Periodically Stalled Flow 14
Physical Boundary Conditions 14
Physical Domain 14
Predictor-Corrector Schemes 14
Principal Co-ordinates 15
Principle of Superposition 15
Principle of Virtual Displacement 15
Principle of Virtual Work 15

Random Vibrations 15
Rayleigh Damping 15
Rayleigh's Quotient 15
Rayleigh-Ritz Method 15
Receptance 15
Residual Modes 16
Residual Smoothing 16
Response Model 16
Runge-Kutta Schemes 16

Shape Function 16
Shock/Boundary-Layer Interaction 16
Solution Domain 16
Spatial Model 16
Spectral Analysis 16
Spectral Method 17
Standing Waves 17
State -Space Equation 17
Structural Damping 17
Subsonic Stall Flutter 17
Subspace Iteration 17
Substructure 17
Supersonic Flutter 17
Supersonic Stall Flutter 17
Supersonic Unstalled Flutter 17

Time Domain Analysis 18
Total Pressure (P0) 18
Total Temperature (T0) 18
Total Variational Diminishing Schemes (TVD) 18
Travelling Waves 18
Trial Function 18
Tuned Systems 18
Turbulence Modelling 18

Unit-Impulse Response Function 19
Upwind Schemes 19

Variational Principle 19
Vibration 19
Viscous Damping 19
Von-Neumann Stability Analysis Method 19

Weak Divergence 20
Weighted Residual Methods 20

I. Definitions

A

Accelerance

Context Structural
Definition Acceleration per unit force (harmonic)
See Also Inertance
Reference 10
Comments -

Admissible Function

Context Numerical
Definition A function that satisfies the geometric boundary conditions of a given domain
See Also Assumed Modes, Galerkin Method, Weighted Residual Method
Reference 14
Comments -

Admittance

Context Structural
Definition Displacement per unit force (harmonic)
See Also Compliance, Dynamic Flexibility, Receptance
Reference 10
Comments -

Advancing-Front Method

Context Numerical
Definition A method for generating unstructured meshes
See Also -
Reference -
Comments -

Aerodynamic Damping

Context Aeroelasticity
Definition The effect of the fluid flow on structural vibration represented as a damper
See Also -
Reference 6
Comments Applicable to linear aeroelastic models only

Aeroelastic Eigenvalues

Context Aeroelasticity
Definition Natural frequencies of the coupled fluid/structure system
See Also Aeroelasticity
Reference 8
Comments Confined to linear models of fluid/structure interaction

Aeroelasticity

Context Aeroelasticity
Definition Study of interaction of a structure with the surrounding flow
See Also Flutter, Forced Vibration
Reference 8
Comments -

Alternating-Direction Implicit Method (ADI)

Context Numerical
Definition An implicit method for solving a system of differential equations
See Also Implicit Solution Techniques
Reference 9
Comments ADI is second-order accurate in time and space, in three-dimensional space, stability is conditional

Apparent Mass

Context Structural
Definition Force per unit acceleration (harmonic)
See Also -
Reference 10
Comments -

Artificial Compressibility

Context Fluid/Numerical
Definition Upwinding of density in fluid flow modelling which incorporates the parabolic nature of fluid flow at high speeds
See Also Upwind Differencing
Reference 13
Comments -

Artificial Viscosity

Context Fluid/Numerical
Definition Addition of dissipative type terms to the discretization of the flow field equations to dampen unwanted oscillations or help shock capturing
See Also -
Reference 13
Comments Also known as artificial dissipation or numerical viscosity

Assembly Modes

Context Structural
Definition Vibration modes of a complete bladed-disc assembly
See Also Cantilever Modes
Reference 11
Comments -

Assumed Modes Method

Context	Structural/Aeroelasticity
Definition	Assumes deformation of a structure to be a combination of its modes
See Also	Galerkin Method, Rayleigh-Ritz Method
Reference	5
Comments	-

B

Beam-Warming Scheme

Context	Fluid/Numerical
Definition	A fully-implicit method for the solution of hyperbolic differential equations
See Also	Implicit Solution Techniques
Reference	1
Comments	Second-order accurate in time

C

Cantilever Modes

Context	Structural
Definition	Modes of a single blade with clamped root
See Also	Assembly Modes
Reference	11
Comments	-

Cell-Centre Scheme (CCS)

Context	Fluid/Numerical
Definition	Stores the dependent variables at the centre of each element
See Also	Dependent Variable, Cell-Vertex Scheme
Reference	13
Comments	-

Cell-Vertex Scheme (CVS)

Context	Fluid/Numerical
Definition	Stores the dependent variables at the vertices of each element
See Also	Dependent Variable, Cell-Centre Scheme
Reference	13
Comments	Tends to have higher accuracy and better stability on stretched grids than the Cell-Centre Scheme

Central Differencing (CD)

Context	Numerical
Definition	A second-order unbiased differencing of a variable at the elemental level
See Also	-
Reference	12
Comments	Accuracy is defined in terms of Taylor Series Truncation Error (TSTE) on a uniform element size distribution

Chaotic Flutter

Context	Aeroelasticity
Definition	A type of flutter regime observed for wings at high reduced speeds with no periodicity observed in structural response but which is not random
See Also	Flutter
Reference	-
Comments	This flutter regime has been observed numerically, there are no experimental data available mainly due to violent mode of flutter occurring

Choking Flutter

Context	Aeroelasticity
Definition	Flutter regime occurring at a negative incidence at below design speed
See Also	Flutter
Reference	6
Comments	Mainly confined to subsonic flows

Cholesky Factorisation

Context	Numerical
Definition	Decomposition of a matrix to upper and lower triangular matrices which are transposes of each other
See Also	-
Reference	16
Comments	Only applicable to symmetric matrices

Complex Mode

Context	Structural
Definition	A mode in which the amplitude of each co-ordinate has both a magnitude and a phase angle which is not identical for all co-ordinates
See Also	Mode Shape
Reference	10
Comments	-

Compliance

Context	Structural
Definition	Displacement per unit force (harmonic)
See Also	Admittance, Dynamic Flexibility, Receptance
Reference	10
Comments	

Component Mode Synthesis

Context	Structural/Numerical
Definition	A method for coupling of substructures/components
See Also	Substructures
Reference	5
Comments	-

Computational Domain

Context	Numerical
Definition	Solution domain in the computational orthogonal system
See Also	Physical Domain, Solution Domain
Reference	13
Comments	-

Conjugate Gradient Method (CGM)

Context Numerical
Definition A method for accelerating the convergence of steady-state solution of finite-difference equations
See Also -
Reference 16
Comments Coupled with the Cholesky factorisation, CGM is a very efficient solution technique

Consistent Mass

Context Structural/Numerical
Definition A method for formulating the mass matrix from the variational principle as opposed to using lumped masses
See Also Variational Principle, Lumped Mass, Distributed Mass
Reference 14
Comments -

Convergence Acceleration

Context Numerical
Definition A family of methods for speeding up the rate of convergence of the steady-state solution of a given set of differential equations
See Also Multi-Grid Methods
Reference 13
Comments -

Convolution Integral

Context Structural
Definition Computing the response of a structure to an arbitrary loading in the time domain using the unit-impulse response function
See Also Duhamel Integral, Unit -Impulse Response Function
Reference 4
Comments -

Coulomb Damping

Context Structural
Definition Damping of structures caused by dry friction
See Also Damping, Dry Friction
Reference 10
Comments -

Coupling (disc)

Context Structural
Definition The interaction between blades which is provided by the disc or stator to which they are attached
See Also -
Reference 11
Comments -

Coupled Vibration

Context Structural
Definition Two or more vibrating systems connected in such a way that energy can be transferred from one to the other
See Also Coupling
Reference 7
Comments -

Courant-Friedrichs-Lewy Number (CFL)

Context Numerical
Definition Limit of stability for time-marching techniques
See Also Explicit Solution Techniques, Implicit Solution Techniques
Reference 12
Comments -

Cyclically Symmetric Structures

Context Structural
Definition Structures made up of repeated identical substructures with the first and the last substructures being connected
See Also Periodic Structures
Reference -
Comments -

D

D'Alembert Principle

Context	Structural
Definition	The concept that a mass develops an inertia force proportional to its acceleration
See Also	-
Reference	1
Comments	-

Damping

Context	Structural
Definition	A mechanism by which structures dissipate energy when set in motion
See Also	-
Reference	10
Comments	Many mathematical models are available but none is totally satisfactory

Degree of Freedom (DOF)

Context	Structural
Definition	Ability to move in a given co-ordinate direction
See Also	Principal Co-ordinates, Generalised Co-ordinates
Reference	10
Comments	-

Dependent Variables

Context	Numerical
Definition	Variables for which the solution of the governing equations is sought
See Also	Independent Variable
Reference	1
Comments	-

Detuning

Context	Structural
Definition	Deliberate mistuning of blades in an assembly
See Also	Mistuning, Mixtuning
Reference	11
Comments	-

Distributed Mass

Context	Structural
Definition	Mass matrix of a continuous system formed by the variational method
See Also	Lumped Mass
Reference	14
Comments	Also known as consistent mass

Divergence

Context	Aeroelasticity
Definition	Deviation of a structure from its equilibrium position without any oscillatory behaviour
See Also	-
Reference	16
Comments	Divergence is equivalent to flutter with zero frequency

Double Modes

Context	Structural
Definition	A pair of modes having the same natural frequency but different mode shapes
See Also	-
Reference	11
Comments	-

Dry Friction

Context	Structural
Definition	Force caused by sliding surfaces
See Also	Coulomb Friction
Reference	7
Comments	-

Duffing's Equation

Context	Structural
Definition	Non-linear equation of motion with a cubic stiffness term
See Also	-
Reference	18
Comments	-

Duhamel Integral

Context	Structural
Definition	Used to evaluate response of single degree-of-freedom system under arbitrary loading by using superposition principle
See Also	Convolution integral
Reference	15
Comments	-

Dynamic Flexibility

Context	Structural
Definition	Displacement per unit force
See Also	Receptance, Admittance
Reference	10
Comments	-

Dynamic Stiffness

Context	Structural
Definition	Force per unit displacement (harmonic)
See Also	-
Reference	10
Comments	-

Residual Modes

Context	Structural
Definition	The so-called out-of-range modes which are below and/or above the analysis range
See Also	-
Reference	5
Comments	-

Residual Smoothing

Context	Fluid/Numerical
Definition	A technique to increase the stability limit of explicit time-marching models by introducing a degree of implicitness to the discretized equations
See Also	Explicit Solution Techniques, Time Domain Analysis
Reference	13
Comments	Should be used with moderation, specially in unsteady calculations

Response Model

Context	Structural
Definition	A dynamic model defined in terms of frequency response data
See Also	Frequency Response Function
Reference	-
Comments	-

Runge-Kutta Schemes

Context	Numerical
Definition	A family of explicit time-marching schemes for solving a system of differential equations
See Also	Explicit solution methods
Reference	1
Comments	Conditionally stable; has excellent damping properties for damping noise and high frequency components in the time response

S

Shape Function

Context	Numerical
Definition	Linear interpolation functions at the elemental level
See Also	Trial Function
Reference	14
Comments	-

Shock/Boundary-Layer Interaction

Context	Fluid/Aeroelasticity
Definition	Growth of boundary layer behind a shock wave
See Also	-
Reference	19
Comments	This effect is more pronounced at higher flow speeds leading to a separation bubble or a complete flow separation. This phenomenon if not directly responsible for the flutter regime, has generally a detrimental effect on the flutter stability

Solution Domain

Context	Numerical
Definition	Part of the physical space for which the equations of motion are solved
See Also	Computational Domain, Physical Domain
Reference	13
Comments	-

Spatial Model

Context	Structural
Definition	Description of a structure's physical characteristics in terms of mass, stiffness and damping elements
See Also	Modal Model, Response Model
Reference	10
Comments	-

Spectral Analysis

Context	Structural/Numerical
Definition	The Study of the frequency content of a signal
See Also	-
Reference	10
Comments	-

Spectral Method

Context Numerical
Definition A weighted-residual method to obtain an approximation to the solution of the governing equations of motion
See Also Weighted-Residual Methods, Galerkin Method
Reference 12
Comments Unlike Galerkin method, orthogonal trial functions are employed.

Standing Waves

Context Structural
Definition Vibration amplitude of blades around the disc with all blades in or out of phase with each other
See Also Travelling Wave
Reference 11
Comments -

State -Space Equation

Context Structural
Definition Transformation of governing equations of a damped system to a generalised eigenvalue problem
See Also Eigenvalue Problem
Reference 4
Comments -

Structural Damping

Context Structural
Definition Energy dissipation due to internal resistance of the material
See Also Hysteretic Damping, Material Damping
Reference 10
Comments -

Subsonic Stall Flutter

Context Aeroelasticity
Definition Flutter regime occurring at above design speeds in subsonic flow conditions
See Also Flutter
Reference 6
Comments Occurs due to flow separation, it is the upper limit to the operational pressure ratio

Subspace Iteration

Context Numerical
Definition A reduction method to solve the eigenproblem along with an iterative process
See Also -
Reference 9
Comments -

Substructure

Context Structural
Definition A component of a complex and large structure
See Also Component Mode Syntheses, Coupling
Reference 5
Comments -

Supersonic Flutter

Context Aeroelasticity
Definition Flutter regime due to high blade loading arising from strong passage shocks
See Also Flutter
Reference 6
Comments -

Supersonic Stall Flutter

Context Aeroelasticity
Definition See Subsonic Stall Flutter
See Also Flutter
Reference 6
Comments -

Supersonic Unstalled Flutter

Context Aeroelasticity
Definition Flutter regime at supersonic flows due to blade coupling
See Also Flutter
Reference 6
Comments It is the effective operational limit to shrouded fan blades as it occurs along the operational line

T

Time Domain Analysis

Context Numerical
Definition Solution of governing equations of motion in time
See Also -
Reference 8
Comments Mainly used for non-linear systems

Total Temperature (T_0)

Context Fluid
Definition Temperature of a fluid isentropically reduced to stagnation
See Also -
Reference 2
Comments Also known as stagnation temperature

Total Pressure (P_0)

Context Fluid
Definition Pressure of a fluid isentropically reduced to stagnation
See Also -
Reference 2
Comments Also known as stagnation pressure

Total Variational Diminishing Schemes (TVD)

Context Fluid/Numerical
Definition A discretization technique for obtaining a physically realistic and bounded solution without the use of artificial viscosity
See Also Upwind Schemes, Central Differencing Schemes, Artificial Viscosity
Reference 13
Comments A TVD scheme is locally monotonic; Second-order accuracy is achieved at the expense of lower stability limit; It is roughly 40% more expensive than the corresponding CD schemes with artificial viscosity

Travelling Waves

Context Structural
Definition The response for every blade exhibits the same amplitude as its neighbours but with a phase lag between them
See Also Standing wave
Reference 11
Comments -

Trial Function

Context Numerical
Definition A function which satisfies the required boundary conditions and is used to approximate the solution via a minimisation procedure
See Also Admissible Function, Shape Function
Reference 14
Comments -

Tuned Systems

Context Structural
Definition A bladed assembly with identical blades
See Also Mistuning
Reference 11
Comments -

Turbulence Modelling

Context Fluid/Numerical
Definition An empirical model that attempts to include the effects of turbulent unsteadiness of the flow in terms of extra viscous effects
See Also -
Reference 13
Comments Variety of empirical turbulence models are available, each suitable for a particular type of flow; The above definition does not include the family of Reynolds Stress Models for Turbulence

U

Unit-Impulse Response Function

Context	Structural
Definition	A function describing the motion of a structure due to a unit impulse
See Also	Convolution Integral
Reference	4
Comments	-

Upwind Schemes

Context	Fluid/Numerical
Definition	Incorporation of the local flow direction into the discretization of the fluid flow equations
See Also	-
Reference	13
Comments	Applicable generally to parabolic differential equations which are directionally biased

V

Variational Principle

Context	Structural
Definition	Approximate solution to the governing equations by minimising a function
See Also	Rayleigh-Ritz Method
Reference	14
Comments	-

Vibration

Context	Structural
Definition	Energy transfer between elastic and inertia status of a mechanical system
See Also	-
Reference	7
Comments	-

Viscous Damping

Context	Structural
Definition	Damping proportional to the velocity of the motion
See Also	-
Reference	10
Comments	-

Von-Neumann Stability Analysis Method

Context	Numerical
Definition	A linear method for determining the stability of the solution procedure of initial-value problems
See Also	Matrix Stability Analysis Method
Reference	17
Comments	-

W

X Y Z

Weak Divergence

Context	Aeroelasticity
Definition	A form of divergence behaviour in which structure slowly deviates from its original equilibrium position and reaches a new position. No oscillatory pattern is observed
See Also	Divergence
Reference	-
Comments	This form of divergence is due to non-linear fluid/structure interaction and can occur at flow speed below the flutter point; Also known as sub-critical divergence or mild divergence

Weighted Residual Methods

Context	Numerical
Definition	A family of numerical techniques for obtaining an approximate continuous solution of the governing equations of motion
See Also	-
Reference	12
Comments	Generally is more accurate than finite-differencing techniques which provide a discrete solution

II. References

[1] Anderson, D. A. & Tannehill, J. C. and Pletcher, R. H.
Computational Fluid Mechanics and Heat Transfer
Hemisphere Publishing Corporation, 1990

[2] Anderson, J. D.
Modern Compressible Flow
McGraw-Hill International, 1990

[3] Bisplinghoff, R. L. & Ashley, H.
Principles of Aeroelasticity
Dover, 1962

[4] Clough, R. W. and Penizen, J.
Dynamics of Structures
McGraw-Hill International 1975

[5] Craig, R. R.
Structural Dynamics
John Wiley & Sons, 1981

[6] Cumpsty, N. A.
Compressor Aerodynamics
Longman Scientific & Technical, 1989

[7] Den Hartog, J. P.
Mechanical Vibrations
Dover, 1985

[8] Dowell, E. H., Curtiss, H. C., Scanlan, R. H., and Sisto, F.
A Modern Course in Aeroelasticity
Kluwer Academic Publishers, 1989

[9] Doyle, J. F.
Static and Dynamic Analysis of Structures
Kluwer Academic Publishers, 1991

[10] Ewins, D. J.
Modal Testing: Theory and Practice
Research Studies Press, 1984

[11] Carta, F. O., Platzer., M. F.
AGARD Manual on Aeroelasticity in Axial-flow Turbomachines
AGARD-AG-298
North Atlantic Treaty Organization, 1988

[12] Fletcher. C. A. J.
Computational Techniques for Fluid Dynamics
Springer-Verlag, 1991

[13] Hirsch, C.
Numerical Computation of Internal and External Flows
John Wiley & Sons, 1988

[14] Huges, T. J. R.
The Finite Element Method
Prentice Hall International, 1987

[15] Meirovitch, L.
Elements of Vibrations Analysis
McGraw-Hill International 1986

[16] Press, W. H. et. al.
Numerical Recipes
Cambridge University Press, 1992

[17] Richtmyer, R. D.
Difference Methods for Initial-Value Problems
Interscience Publishers, 1956

[18] Weaver, W., Timoshenko, S. P. and Young, D. H.
Vibration Problems in Engineering
John Wiley & Sons, 1990

[19] White, F. M.
Viscous Fluid Flow
McGraw-Hill International, 1991

[20] Zenkenwiciz, O. J. and Talyor, R. L.
The Finite Element Method
Prentice Hall International, 1987